



UNIVERSITY COLLEGE LONDON

Faculty of Mathematics and Physical Sciences

Department of Physics & Astronomy

HERSCHEL STUDIES OF CORE
COLLAPSE SUPERNOVA REMNANTS
AT INFRARED WAVELENGTHS

Thesis submitted for the Degree of Doctor of
Philosophy of the University of London

by
Patrick James Owen

Supervisors:

Prof. Michael J. Barlow
Prof. Bruce M. Swinyard

Examiners:

Dr. David A. Green
Prof. Jonathan M. C. Rawlings

September 28, 2015

In Memory of Prof. Bruce Swinyard 1962-2015

I, Patrick James Owen, confirm that the work presented in this thesis is my own. Where information has been derived from other sources, I confirm that this has been indicated in the thesis.

Abstract

Core collapse supernovae play a vital role in the evolution of the universe. They are major producers of metals and the only place where elements heavier than Iron can be made. These metals can then combine to form molecules and dust, enriching the interstellar medium to provide cooling to form new stars. These molecules and dust, as well as metal cooling lines can all be observed in the infrared, making it a very interesting wavelength range in which to study supernovae and their remnants.

This investigation of supernova remnants in the infrared has been made possible by the European Space Agency's *Herschel* Space Observatory. *Herschel* studied the universe between 60 and 670 μm , covering the peak of dust emission, a large range of atomic fine structure cooling lines, a large portion of the Carbon Monoxide rotation ladder and other more exotic molecular line transitions.

This thesis presents spectroscopic observations of the Cassiopeia A and Crab supernova remnants using two of the *Herschel* instruments to investigate their structure, physics and chemistry. It also presents the results of radiative transfer models based on photometric *Herschel* data to investigate more physical measurements of the mass of dust in supernova remnants. These models, along with others are then used to investigate the nature of dust formation in supernovae and the composition of this dust.

Observations of the Crab Nebula with *Herschel* SPIRE made the first ever observation of a molecule containing a noble gas in space. Within the dense filaments of the nebula, two rotational lines of $^{36}\text{ArH}^+$ were observed. This discovery was followed up with the

VLT to try to find vibrational lines in the near infrared as well as an investigation of the potential presence of HeH^+ . Unfortunately these were unsuccessful. PACS and LWS observations were used to diagnose the conditions in the remnant, density, oxygen to nitrogen ratio and the ionic abundances of Nitrogen. Velocity information was also investigated and emitting regions compared to optical emission.

Cassiopeia A was observed with *Herschel* PACS-IFU and SPIRE-FTS spectrometry instruments. The PACS observations were used to look at the structure of the bright ring of the remnant. The $63 \mu\text{m}$ [O I] detected line emission along with upper limits on $146 \mu\text{m}$ [O I] emission were used to diagnose the temperature in the remnant using neutral hydrogen as a collision partner, found to be within a range of 100-1000K . Along with the SPIRE-FTS observations they were also used to investigate the formation of CO in the remnants. These CO observations were also used to diagnose conditions in the remnant. The temperature determined from CO in the neutral regions of the remnant was 300-500 K which is in agreement with the temperatures determined using the [O I] line ratios.

By using photoionisation models of the Crab Nebula we were about to determine the mass of dust in the remnant. This measurement takes in to account realistic heating of the dust, density distribution of the dust, the gas in the nebula and the size and species of the dust grains. We found that the dust mass is larger when these physical conditions are taken in to account. With our favoured geometry, distribution and grain species optical constants, we find a mass of $0.18 \pm 0.3 M_\odot$ of dust, as opposed to the $0.1 M_\odot$ determined empirically, and a gas mass of $7.0 \pm 0.5 M_\odot$ for the remnant.

Acknowledgements

Firstly massive thanks to Mike for giving me this opportunity and for putting up with me for the past few years. I couldn't have done it without his help and advice. Also really couldn't have done it without the help from Bruce, who also provided a large amount of useful input. Antonia has to get thanks for sanity checks and science chats. Mikako also gets a science and sanity mention. Roger and Oskar for their better than mine knowledge of MOCASSIN and its *usability*.

I'd like to apologise to everyone who had the misfortune of sharing an office with me in my first few years here. I was a bit noisy at times (although I did actually work too!). I think an extra special mention has to go to Emma who really bore the brunt of the shenanigans of G18 and Beca who bore the brunt of the planes! (and was generally awesome). Barney and Bambam and Cris and Sree and Walter and Lucy and Antonia (again, you get thanked twice) and all the visitor who came to play Nicolas Cage. Thanks to everyone in the basement. Especially my OB22 peoples for all the popcorn. Rich, Deej, Little Paul (who?) and GeorgeKelly. Thank you. Tea break?

Thanks to mum and dad for being mum and dad.

Jen for putting up with me and generally being amazing.

For the chemical aids to sanity, those good people at the Euston Tap and the Algerian Coffee Company - without these I'd really not have made it through to the end. Swing Patrol Waterloo and Kings Cross peoples for general awesomeness and dancing and dancing and awesomeness.

Cheers.

*Something in the way he said it made Lyra imagine dust with a capital letter, as if
this wasn't ordinary dust.*

Philip Pullman in Northern Lights

Contents

Table of Contents	6
List of Figures	11
List of Tables	23
List of Acronyms	31
1 Introduction	35
1.1 Dust in the Universe	35
1.2 What is dust?	37
1.3 Dust Properties	37
1.3.1 Optical and UV properties	38
1.3.2 X-Ray Properties	42
1.3.3 Infrared and Sub-millimetre Properties	42
1.3.4 Identifying Dust Species	42
1.4 The Standard Dust Model	43
1.5 How we observe Dust at Infrared Wavelengths	44
1.5.1 The <i>Herschel</i> Space Observatory	45
1.5.2 The <i>Spitzer</i> Space Telescope	46
1.5.3 Other Infrared and Sub Millimetre Observatories	47
1.6 Supernovae and their Remnants	48
1.7 Types of Core-Collapse Supernovae	48
1.8 Supernova Remnants	50
1.8.1 Shell Supernova Remnants	50

1.8.2	Centre-Filled Supernova Remnants	50
1.9	Dust Formation in Supernovae and Supernova Remnants	52
1.9.1	Theories of Formation	52
1.9.2	Isotopic Ratios	53
1.9.3	Observed Dust Masses	53
1.9.4	Recent Observations with Herschel	53
1.10	Infrared atomic lines in Supernova Remnants	57
1.10.1	Fine Structure Lines	57
1.11	Molecules in Supernova Remnants	58
1.12	This Thesis	60
2	Herschel Spectroscopy of the Crab Nebula	61
2.1	The Crab Nebula with the PACS-IFU Spectrometer	62
2.1.1	Nebula Diagnostics	63
2.1.2	Velocity Structure	67
2.2	The Crab Nebula with SPIRE-FTS	69
2.2.1	Unidentified Lines	70
2.2.2	Identifying the Line	71
2.2.3	ArH ⁺ Line Fluxes	73
2.2.4	Fomation and Destruction Mechanisms for ArH ⁺	73
2.2.5	Argon Nucleosynthesis	76
2.2.6	The search for ArH ⁺ with PACS	77
2.2.7	Temperature	77
2.3	Follow-up with IRTF CSHELL AND VLT-CRIRES	77
2.3.1	IRTF CSHELL observations of H ₂ 2.122 μ m line.	77
2.3.2	Observations of H ₂ knots	79
2.3.3	CSHELL Data Reduction	80
2.3.4	H ₂ Line Width Results	83
2.4	VLT-CRIRES observations of ArH ⁺ and HeH ⁺	83
2.4.1	The VLT-CRIRES Observations	85
2.4.2	CRIRES Data Reduction	87
2.4.3	Results	90
2.4.4	CRIRES Line Flux Upper Limits	91

2.5	HeH ⁺ line flux upper limits with PACS	102
2.6	Conclusions	102
3	<i>Herschel Spectroscopy of Cassiopeia A</i>	107
3.1	Cassiopeia A with PACS-IFU spectrometer	107
3.2	PACS Spectra	108
3.2.1	Oxygen Fine Structure Lines	108
3.2.2	Upper Limits to the [O I] 146 μm line flux	120
3.2.3	The 158 μm [C II] line	128
3.3	Cas A with SPIRE-FTS	131
3.4	CO and [C II]	135
3.5	Conclusions	137
4	Dust in the Crab Nebula	141
4.1	The Models	144
4.1.1	Geometry and Spectrum	146
4.1.2	Spectral Energy Distribution	147
4.1.3	Optical Lines	148
4.1.4	Grain species and optical properties	149
4.1.5	Density distributions	151
4.1.6	Nucleosynthesis	160
4.2	Results	160
4.2.1	Elemental Abundances and Ionisation	160
4.2.2	Dust Masses	173
4.3	Discussion	188
4.3.1	The importance of using both gas and dust	188
4.3.2	Clumping	188
4.3.3	Optical Properties	189
4.3.4	Grain Size Distribution	191
4.3.5	Continuous Distribution of Ellipsoids	195
4.3.6	Optical Depths of the Clumps	197
4.3.7	Predicting Photometric Fluxes	198
4.4	Alternative Dust Mass Estimates	198
4.4.1	The Temim and Dwek 2013 Estimate	198

4.4.2 Empirical Dust Masses	199
4.5 Conclusions	200
5 Conclusions and Future Work	205
5.1 The Crab Nebula	205
5.2 Cassiopeia A	208
5.3 Other future work	209
A Appendix A	211
B Appendix B	217
B.1 SP1	218
B.2 SP3	219
B.3 SP4	222
B.4 SP5	223
B.5 SP7	226
B.6 SP8	228
B.7 SP9	230
C Appendix C	233
Bibliography	235

This page was intentionally left blank

List of Figures

1.1	SDSS J114816.64+525150.3, a quasar at $z = 6.42$ observed with IRAM 30 m telescope showing a rest frame IR excess corresponding to $10^8 M_\odot$ of dust taken from Bertoldi et al. (2003).	36
1.2	A Hubble Space Telescope optical image of the Andromeda Galaxy	38
1.3	An infrared image of the Andromeda galaxy taken with the Herschel Space Observatory (Fritz et al. 2012)	39
1.4	FIR to UV extinction curves taken from Fitzpatrick (1999) based on parameterisations by Cardelli, Clayton, & Mathis (1989) for $R = 2.3, 3.1, 4.0$ and 5.5 . $R = 3.1$, the Milky Way average is shown as a solid line with the others being dotted/dashed.	40
1.5	The opacity of the Earth's atmosphere vs wavelength to show regions where it is not possible to make observations from the ground.	45
1.6	Example light curves of Type II-P and II-L supernovae.	49
1.7	Multi wavelength observations of Cas A showing the synchrotron continuum at 6 cm (VLA) and $3.6 \mu\text{m}$, warm dust at $24 \mu\text{m}$ (Spitzer) and $70 \mu\text{m}$ (Herschel), cool dust $100 \mu\text{m}$ (Herschel) and $70 \mu\text{m}$ (Herschel) and $160, 350$ and $500 \mu\text{m}$ foreground dust taken from Barlow et al. (2010).	54
1.8	<i>Herschel</i> Observation of 1987A at $100, 160, 250$ and $350 \mu\text{m}$ taken from Matsuura et al. (2011).	56
1.9	ALMA (mm and sub-mm), ATCA (mm), Hubble (visible) and Chandra (x-ray) observations of SN1987a showing the structure of the supernova remnant and location of the dust. Taken from Indebetouw et al. (2014). . .	57
1.10	The fine structure splitting of the ground state of doubly ionised oxygen. . .	59

2.1	The position of the PACS-IFU observations of the Crab Nebula plotted on a PACS 70 μm image.	62
2.2	The position of the ISO-LWS observations of the Crab Nebula plotted on a PACS 70 μm image.	63
2.3	The 25 individual PACS spaxels plotted in velocity space. The 88 μm [O III] line is in black, the 63 μm [O I] line is in red and the 158 μm [C II] line is in green.	68
2.4	A brightness map of the blue and red shifted emission components of the 88 μm [O III] line for each PACS-IFU spaxel, plotted over the PACS 70 μm map plotted as a contour plot.	69
2.5	A brightness map of the blue and red shifted emission of the 63 μm [O I] line for each PACS-IFU spaxel, plotted over the PACS 70 μm map plotted as a contour plot.	70
2.6	A brightness map of the blue and red shifted emission of the 158 μm [C II] line for each PACS-IFU spaxel, plotted over the PACS 70 μm map plotted as a contour plot. Note the scale is an order of magnitude less than the plots for the [O I] and [O III] maps.	71
2.7	The SPIRE-FTS detectors for the Crab Nebula observations shown on a 70 μm PACS broadband image. Green circles are the SSW detectors, white circles are the SLW detectors. Circles with a cross denote the detectors in which the unidentified lines were observed.	72
2.8	SLW D4 spectrum showing one of the initially unidentified lines at 618 GHz.	72
2.9	SSW B1 spectrum showing one of the initially unidentified lines at 1235 GHz.	73
2.10	A <i>Herschel</i> PACS 70 μm image with the size and locations of the Loh et al. (2011) H ₂ knots shown as green circles.	75
2.11	PACS-IFU observations of the region of the J=3-2 161.98 μm $^{36}\text{ArH}^+$ line.	78
2.12	The rotation diagram used to determine the temperature of $^{36}\text{ArH}^+$ in the SLW-C3 SSW D4 and PACS-IFU observations	79
2.13	The CSHELL spectral image - position vs wavelength plot for Loh et al. (2011) knots 1 and 2 taken by the IRTF.	80
2.14	The position wavelength plot star HD 1791	81

2.15 The cuts made perpendicular to the spectral direction for the observation of HD 1791 to investigate the need for rotational correction in the angle of the observations of the Crab knots. The cut through the short wavelength end shown in blue and the cut through the long wavelength end of the spectrum shown in green.	82
2.16 The extracted spectrum for Loh et al. (2011) knots 1 and 2 of the Crab Nebula in radial velocity units of km s ⁻¹	82
2.17 The extracted spectrum of the Loh et al. (2011) knots 1 and 2 of the Crab Nebula in velocity units with the gaussians fitted to determine the central velocity and line width using two gaussians for one knot and one for the other. There is no baseline as the central region between the two knots goes to zero.	83
2.18 The extracted spectrum of the Loh et al. (2011) knots 1 and 2 of the Crab Nebula in velocity units with the gaussians fitted to determine the central velocity and line width using two gaussians to the slower/shorter wavelength knot and three gaussian to the faster/longer wavelength knot. There is no baseline as the central region between the two knots goes to zero	84
2.19 The location of the Loh et al. (2011) knot 1 (magenta circle) and nearby <i>Herschel</i> SPIRE-FTS detectors that detected $^{36}\text{ArH}^+$ (the two green circles are the SSW detectors, the blue circle is the SLW detector).	85
2.20 Finding chart for the VLT observations showing the slit position of the CRIRES spectrometer in blue on the 2MASS catalogue image of the Crab Nebula. The Loh et al. (2011) knot 1 position is shown as a green circle. the red crosses are the locations of objects in the 2MASS catalogue	86
2.21 The targeting of the VLT showing the spectrograph slit over the central knots. The black line in the centre of the image is the slit, with the edges of the knot being region the bright which points at the side of the centre of the slit.	88
2.22 The raw spectral data from CRIRES observations of the Crab Nebula before any processing has taken place	89

2.23 The spectral data from CRIRES observations of the Crab Nebula after they have been processed using a median filtering technique to remove cosmic rays from the data. The darker vertical bands correspond the the sky emission lines.	90
2.24 The spectrum of the observation of HeH ⁺ R(1) (blue) and model sky from the ETC (green).	91
2.25 The modelled blackbody spectrum of ι Tau used for flux calibration.	92
2.26 The spectrum of the region of the HeH ⁺ R(0) 3364.09 nm line taken with VLT-CRIRES.	92
2.27 The spectrum of the region of the HeH ⁺ R(1) 3302.10 nm line taken with VLT-CRIRES.	93
2.28 The spectrum of the region of the ArH ⁺ ($v=1-0$, $J=2-1$) 3799.99 nm line taken with VLT-CRIRES.	93
2.29 The spectrum of the region of the ArH ⁺ ($v=1-0$, $J=1-0$) 3827.75 nm line taken with VLT-CRIRES.	94
2.30 The 8 coadded spectra of the whole slit of the spectrograph in the region encompassing the HeH ⁺ R(1) 3302.10 nm line taken with VLT-CRIRES based on an assumed radial velocity of $+140 \text{ km s}^{-1}$ for the knot (Barlow et al. 2013).	94
2.31 The 8 coadded spectra of the whole slit of the spectrograph in the region encompassing the HeH ⁺ R(0) 3364.09 nm line taken with VLT-CRIRES based on an assumed radial velocity of $+140 \text{ km s}^{-1}$ for the knot (Barlow et al. 2013).	95
2.32 The 8 coadded spectra of the whole slit of the spectrograph in the region encompassing the ArH ⁺ ($v=1-0$, $J=1-0$) 3827.75 nm line taken with VLT-CRIRES based on an assumed radial velocity of $+140 \text{ km s}^{-1}$ for the knot (Barlow et al. 2013).	95
2.33 The 8 coadded spectra of the whole slit of the spectrograph in the region encompassing the ArH ⁺ ($v=1-0$, $J=2-1$) 3799.99 nm line taken with VLT-CRIRES based on an assumed radial velocity of $+140 \text{ km s}^{-1}$ for the knot (Barlow et al. 2013).	96

2.34 The spectrum of the region encompassing the HeH ⁺ R(1) 3302.10 nm line taken with VLT-CRIRES based on an assumed radial velocity of +140 km s ⁻¹ for the knot (Barlow et al. 2013). Negative features are due to sky subtractions.	97
2.35 The spectrum of the region encompassing the HeH ⁺ R(0) 3364.09 nm line taken with VLT-CRIRES based on an assumed radial velocity of +140 km s ⁻¹ for the knot (Barlow et al. 2013).	97
2.36 The spectrum of the region encompassing the ArH ⁺ (v=1-0, J=1-0) 3827.75 nm line taken with VLT-CRIRES based on an assumed radial velocity of +140 km s ⁻¹ for the knot (Barlow et al. 2013).	98
2.37 The spectrum of the region encompassing the ArH ⁺ (v=1-0, J=2-1) 3799.99 nm line taken with VLT-CRIRES based on an assumed radial velocity of +140 km s ⁻¹ for the knot (Barlow et al. 2013).	98
2.38 The coadded spectrum of the whole slit of the spectrograph in the region of the HeH ⁺ R(1) 3302.10 nm line taken with VLT-CRIRES with a gaussian of width of the H ₂ as measured by the IRTF. The red line shows the observed spectrum with what a 3- σ detection of a line of width 20 km s ⁻² would look like and the blue line shows the observed spectrum with what a 3- σ detection of a line of width 10 km s ⁻² . The black line shows the actual observational data.	100
2.39 The coadded spectrum of the whole slit of the spectrograph in the region of the HeH ⁺ R(0) 3364.09 nm line taken with VLT-CRIRES with a gaussian of width of the H ₂ as measured by the IRTF. The red line shows the observed spectrum with what a 3- σ detection of a line of width 20 km s ⁻² would look like and the blue line shows the observed spectrum with what a 3- σ detection of a line of width 10 km s ⁻² . The black line shows the actual observational data.	100

2.40 The coadded spectrum of the whole slit of the spectrograph in the region of the ArH ⁺ ($v=1-0$, $J=1-0$) 3827.75 nm line taken with VLT-CRIRES with a gaussian of width of the H ₂ as measured by the IRTF. The red line shows the observed spectrum with what a 3- σ detection of a line of width 20 km s ⁻² would look like and the blue line shows the observed spectrum with what a 3- σ detection of a line of width 10 km s ⁻² . The black line shows the actual observational data.	101
2.41 The coadded spectrum of the whole slit of the spectrograph in the region of the ArH ⁺ ($v=1-0$, $J=2-1$) 3799.99 nm line taken with VLT-CRIRES with a gaussian of width of the H ₂ as measured by the IRTF. The red line shows the observed spectrum with what a 3- σ detection of a line of width 20 km s ⁻² would look like and the blue line shows the observed spectrum with what a 3- σ detection of a line of width 10 km s ⁻² . The black line shows the actual observational data.	101
2.42 PACS-IFU observations of the region of the $J=1-0$ 149.25 μ m HeH ⁺ line.	103
2.43 PACS-IFU observations of the region of the $J=2-1$ 74.83 μ m HeH ⁺ line.	104
3.1 The positions of the observations of Cas A made with the <i>Herschel</i> PACS-IFU plotted on a PACS 70 μ m image.	109
3.2 The 5x5 PACS-IFU observation SP1 of Cas A in velocity space. The black line shows the 88 μ m [O III] line, the red line shows the 63 μ m [O I] line and the green shows the 158 μ m [C II] line.	111
3.3 The 5x5 PACS-IFU observation SP2 of Cas A in velocity space. The black line shows the 88 μ m [O III] line, the red line shows the 63 μ m [O I] line and the green shows the 158 μ m [C II] line.	112
3.4 The 5x5 PACS-IFU observation SP3 of Cas A in velocity space. The black line shows the 88 μ m [O III] line, the red line shows the 63 μ m [O I] line and the green shows the 158 μ m [C II] line.	113
3.5 The 5x5 PACS-IFU observation SP4 of Cas A in velocity space. The black line shows the 88 μ m [O III] line, the red line shows the 63 μ m [O I] line and the green shows the 158 μ m [C II] line.	114

3.6	The 5x5 PACS-IFU observation SP5 of Cas A in velocity space. The black line shows the 88 μm [O III] line, the red line shows the 63 μm [O I] line and the green shows the 158 μm [C II] line.	115
3.7	The 5x5 PACS-IFU observation SP6 of Cas A in velocity space. The black line shows the 88 μm [O III] line, the red line shows the 63 μm [O I] line and the green shows the 158 μm [C II] line.	116
3.8	The 5x5 PACS-IFU observation SP7 of Cas A in velocity space. The black line shows the 88 μm [O III] line, the red line shows the 63 μm [O I] line and the green shows the 158 μm [C II] line.	117
3.9	The 5x5 PACS-IFU observation SP8 of Cas A in velocity space. The black line shows the 88 μm [O III] line, the red line shows the 63 μm [O I] line and the green shows the 158 μm [C II] line.	118
3.10	The 5x5 PACS-IFU observation SP9 of Cas A in velocity space. The black line shows the 88 μm [O III] line, the red line shows the 63 μm [O I] line and the green shows the 158 μm [C II] line.	119
3.11	The relative flux of the red shifted emission of the [O III] 88 μm in Cas A plotted over a contour map of the PACS 70 μm image.	121
3.12	The relative flux of the blue shifted emission of the [O III] 88 μm in Cas A plotted over a contour map of the PACS 70 μm image.	122
3.13	The relative flux of the red shifted emission of the [O I] 63 μm in Cas A plotted over a contour map of the PACS 70 μm image.	123
3.14	The relative flux of the blue shifted emission of the [O I] 63 μm in Cas A plotted over a contour map of the PACS 70 μm image.	124
3.15	[O I] Fine-structure energy levels	125
3.16	Temperature vs log density for the I_{63}/I_{146} ratio of 42.1 to illustrate the method for temperature determination.	126
3.17	The temperature determined from the I_{63}/I_{146} ratio against that ratio to show the range of temperatures and the decrease in sensitivity as the ratio decreases.	128
3.18	The relative flux of the red shifted emission of the [C II] 158 μm in Cas A plotted over a contour map of the PACS 70 μm image.	129
3.19	The relative flux of the blue shifted emission of the [C II] 158 μm in Cas A plotted over a contour map of the PACS 70 μm image.	130

3.20 Positions of the SSW detectors of the three <i>Herschel</i> SPIRE-IFU on Cas A plotted on a 70 μm image. The "Central" observation is shown in top left, top right is the "North West" and bottom left is the "North" observation.	132
3.21 Blue circles show SPIRE SSWC4 and C5 in which CO was detected. Red square shows the locations of the PACS CO detections of Wallström et al. (2013) plotted on a 70 μm Herschel PACS image of the northern half of the remnant.	133
3.22 the observed spectrum of Cas A with detector SSWC5 of the Herschel SPIRE-FTS - lines from CO rotational transitions are labelled.	134
3.23 A CO rotation excitation to determine temperature and column density using Herschel SPIRE-FTS observations of Cas A-NW with detector SSW C4.	135
3.24 A CO rotation excitation to determine temperature and column density using Herschel SPIRE-FTS observations of Cas A-NW with detector SSW C5. $T_{ex} = 554 \pm 25 \text{ K}$ $N_{CO} = 4.0 \pm 0.5 \times 10^{17} \text{ cm}^{-2}$.	136
3.25 A CO rotation excitation to determine temperature and column density using Herschel SPIRE-FTS observations of Cas A-NW with detector SSW C5 and the <i>Herschel</i> PACS observations from Wallström et al. (2013). $T_{ex} = 540 \pm 25 \text{ K}$ $N_{CO} = 4.3 \pm 0.5 \times 10^{17} \text{ cm}^{-2}$.	136
3.26 <i>Herschel</i> PACS 70 μm map of Cas A shows the regions with where broad CO emission has been detected shown in green and the regions where the broad [C II] lines have been observed shown in red.	137
4.1 Left: Modern infrared observations of the Crab Nebula from <i>Spitzer</i> (red circles), <i>Herschel</i> (purple circles) and <i>Planck</i> (light blue circle) as used by Gomez et al. (2012) with modelled SED. Right: Archival/previous IR observations of the Crab Nebula taken from WISE (black circles), ISO (dark blue circles), IRAS (green circles), KAO (orange circles), IRAM (black square), Archeops (purple squares) and SCUBA (red square) also shown with a modelled fitted to the modern data for comparison.	142

4.2 Composite image of the Crab Nebula, obtained by combining a <i>Hubble Space Telescope</i> optical emission line image (blue-white) with a <i>Herschel Space Observatory</i> 70- μm dust emission image (red), showing the emitting dust to be closely aligned with the optical knots and filaments. The image is 5.65 arcmin on a side; north is up and east is to the left. Credits: Oli Usher (UCL); <i>Herschel Space Observatory</i> , <i>Hubble Space Telescope</i> : ESA, NASA.	145
4.3 The input Spectrum used to heat the dust and ionise the gas, taken from Hester (2008) and adjusted for Planck Collaboration (2011) in the sub-mm.	146
4.4 A cartoon schematic of geometry I	151
4.5 A cartoon schematic of geometry II	152
4.6 A cartoon schematic of geometry III	152
4.7 A cartoon schematic of geometry IV	153
4.8 A cartoon schematic of geometry V	154
4.9 A cartoon schematic of geometry VI	154
4.10 A cartoon schematic of geometry VII	155
4.11 A cartoon schematic of geometry VIII	156
4.12 A cartoon schematic of geometry IX	157
4.13 A cartoon schematic of geometry X	157
4.14 A cartoon schematic of geometry XI	158
4.15 A cartoon schematic of geometry XII	159
4.16 A cartoon schematic of geometry XIII	159
4.17 Best fit models plotted with observed SEDs for the six different sets of optical constants using a smooth isotropic density distribution with a density of 775 cm^{-3} (Model I).	174
4.18 Best fit models plotted with observed SEDs for the six different sets of optical constants using a smooth isotropic density distribution in a shell in the outer third of the nebula with a density of 850 cm^{-3} outside the diffuse radiation source (Model II)	175
4.19 Best fit Models plotted with observed SEDs for the six different sets of optical constants using a smooth isotropic density distribution in a shell 0.5 pc thick and a inner diameters of $2.1 \times 1.4 \text{ pc}$ entirely inside the diffuse radiation source (Model III).	176

4.20 Best fit models plotted with observed SEDs for the six different sets of optical constants using a smooth isotropic density distribution in a shell all the way to the edge of the nebula and a inner diameters of 2.1×1.4 pc entirely inside the diffuse axes source (Model IV).	177
4.21 Best fit models plotted with observed SEDs for the six different sets of optical constants using a smooth isotropic density distribution in a shell all the way to the edge of the nebula and a inner axes of 2.3×1.7 pc entirely inside the diffuse radiation source (Model V).	178
4.22 Best fit models plotted with observed SEDs for the six different sets of optical constants using a smooth isotropic density distribution in a shell 0.1 pc thick and a inner diameter of 1.1 pc entirely inside the diffuse radiation source (Model VI).	179
4.23 Best fit dust models plotted with the observed SEDs for six different sets of optical constants using a density distribution when all of the matter is in clumps with radius 0.111 pc and a density of 1400 cm^{-3} (Model VII). . .	180
4.24 Best fit dust models plotted with observed SEDs for the six different sets of optical constants using a density distribution when all of the matter is in clumps of radius 0.037 pc with a H number density of 1900 cm^{-3} (Model VIII).	181
4.25 Best fit dust models plotted with observed SEDs for the six different sets of optical constants using a density distribution when all of the matter is in clumps of radius 0.037 pc with a H number density of 1900 cm^{-3} (Model IX).182	
4.26 Best fit models plotted with observed SEDs for the six different sets of optical constants using a density distribution when all of the matter is in clumps of radius 0.037 pc with a density of 1900 cm^{-3} . (model X)	184
4.27 Best fit models plotted with the observed SEDs for the six different sets of optical constants using a density distribution starting at radius 0.55 pc in a 0.1 pc thick shell with a diffuse source going up to the inner radius of the dust shell (Model XI).	185

4.28 Best fit dust models plotted with observed SEDs for the six different sets of optical constants using a density distribution when all of the matter is in clumps of radius 0.037 pc with a H number density of 1900 cm^{-3} with a diffuse radiation source going up to the inner radius of the dust shell (Model XII).	186
4.29 Best fit models plotted with observed SEDs for the six different sets of optical constants using a density distribution when all of the matter is in clumps of radius 0.037 pc with a density of 1900 cm^{-3} (Model XIII).	187
4.30 Synchrotron-subtracted infrared SEDs of the best fit dust mass for the gas and dust model (black line) and for a model with the same parameters with no gas, just dust (red line) Model XII.	188
4.31 The ultraviolet SED for models with gas and dust (black), gas only (red) and dust only (blue) for Model XII	189
4.32 $Q_{\text{abs}}(\lambda)$ against Wavelength for amorphous carbon grain optical constants and a grain size of $0.1 \mu\text{m}$	190
4.33 the effect on the SED of varying the power law slope α . The black line shows the best fit Model x with Zubko et al. (1996) BE dust properties. The green line is the same parameters but with $\alpha = 3.1$ and the blue line has the same parameters but $\alpha = 2.7$	193
4.34 the effect of varying the maximum grain size, a_{max} on the fitted SED. The black line gives the best fits for Model x using Zubko et al. (1996) BE amorphous carbon, the green line uses the same parameters but has an a_{max} of $1.5 \mu\text{m}$ and the blue line has a maximum grain radius of $0.5 \mu\text{m}$. . .	194
4.35 the effect of varying the minimum grain size, a_{min} on the fitted SED. The black line gives the best fits for Model x using Zubko et al. (1996) BE amorphous carbon, the green line uses the same parameters but has an a_{min} of $0.0001 \mu\text{m}$ and the blue line has a maximum grain radius of $0.01 \mu\text{m}$. . .	194
4.36 Best fit models plotted with the observed SED for the six different sets of optical constants using a density distribution where all of the matter is in clumps of radius 0.037 pc with a density of 1900 cm^{-3} using a continuous distribution of ellipsoids rather than modelling dust as a sphere using Mie scattering. (model x - with CDE)	196

4.37 The dust temperature with grain size for Model XI using Rouleau & Martin (1991) amorphous carbon optical constants at 0.55 pc (red) and Temim & Dwek (2013) (blue) both of which use the Čadež et al. (2004) geometry as their basis.	199
5.1 The results for Model XII. A clumpy geometry with clumps starting at radii of 2.3×1.7 pc decreasing with r^{-2} with a diffuse radiation source going up to the inner radius of the dust shell using the <i>Planck</i> "Gaussian" fitted Full Release Compact Source Catalogue fluxes.	207

List of Tables

1.1	The different types of core collapse supernovae.	51
2.1	Information on the position and integration time of spectroscopic measurements of the Crab Nebula using <i>Herschel</i> PACS-IFU and ISO-LWS.	64
2.2	Crab Nebula far-infrared line fluxes, electron densities and relative ion abundances. Line intensities relative to [O III] F _(88 μm) =100.	66
2.3	Details of the <i>Herschel</i> SPIRE-FTS observation of the Crab Nebula.	69
2.4	SPIRE-FTS radial velocity and line surface brightness measurements for the J = 1-0 and 2-1 rotational lines of ³⁶ ArH ⁺ from the Crab Nebula. The table is laid out so that SLW and SSW detectors that correspond to one another spatially are next to each other.	74
2.5	The velocity and line widths of the Loh et al. (2011) knots 1 and 2 in the Crab Nebula, by fitting one gaussian to each line as shown in 2.17.	83
2.6	The velocity and line widths of the Loh et al. (2011) knots 1 and 2 in the Crab Nebula, by fitting two gaussians to the slower/shorter wavelength and knot and 3 gaussians to the faster/longer wavelength knot as shown in Figure 2.18.	84
2.7	Information about the VLT-CRIRES observations of the Crab Nebula ArH ⁺ and HeH ⁺	87
2.8	The factors used in calculating the upper limits of detection in the CRIRES spectra. Heliocentric correction for motion of the earth taken from ESO Sky Calendar Tool http://www.eso.org/sci/observing/tools/calendar/airmass.html	96

2.9	The upper limits of detection of the HeH ⁺ R(0), R(1) and ArH ⁺ (v=1-0, J=1-0) and (v=1-0, J=2-1) lines with VLT-CRIRES	99
2.10	The temperature that the gas would be at if the line widths were purely from the thermal motion.	99
2.11	The upper limits of detection of the HeH ⁺ R(0), R(1) and ArH ⁺ (v=1-0, J=1-0) and (v=1-0, J=2-1) lines with VLT-CRIRES using the IRTF measured H ₂ line widths. Also included are the upper limits based purely on the standard deviation of the noise in the CRIRES data	102
3.1	The positions of the PACS Spectroscopic observations of Cas A	110
3.2	The upper limits on the red shifted component of the [O I] 146 μm emission [O I] 63 μm observed fluxes along with the lower limit on the ratio between them and the upper limit on observed temperature in the observations of Cas A by PACS-IFU	126
3.3	The upper limits on the blue shifted component of the [O I] 146 μm emission and [O I] 63 μm observed fluxes along with the lower limit on the ratio between them and the upper limit on observed temperature in the observations of Cas A by PACS-IFU	127
3.4	The measured fluxes, radial velocity and FWHM of the CO rotation lines observed with <i>Herschel</i> SPIRE-FTS. $T_{ex} = 305 \pm 15 \text{ K}$ $N_{CO} = 8.7 \pm 0.5 \times 10^{16} \text{ cm}^{-2}$	134
3.5	Temperatures measured in Cas A, using CO rotational temperatures and 63 μm [O I] line emission and upper limits placed on 146 μm [O I] line emission.	138
4.1	Continuum IR Fluxes from the Crab Nebula	147
4.2	A summary of the density distributions of the different models.	161
4.3	The masses of emitting gas phase elements in the Crab Nebula determined by the MOCASSIN models	163
4.4	Derived elemental abundances of emitting gas in the Crab Nebula relative to hydrogen	164
4.5	Observed and modelled absolute H _{β} fluxes. Observed and modelled line strengths are relative to H _{β} . All observed lines are taken from Smith (2003), except for [C I] 9824+9850 from Rudy et al. (1994), [Ar III] 7136+7751 from Davidson & Fesen (1985) and [Ar III] 89911 from Temim et al. (2012).	165

4.6	Observed and modelled absolute H_{β} fluxes. Observed and modelled line strengths are relative to H_{β} . All observed lines are taken from Smith (2003), except for [C I] 9824+9850 from Rudy et al. (1994), [Ar III] 7136+7751 from Davidson & Fesen (1985) and [Ar III] 89911 from Temim et al. (2012). . . .	166
4.7	Observed and modelled absolute H_{β} fluxes. Observed and modelled line strengths are relative to H_{β} . All observed lines are taken from Smith (2003), except for [C I] 9824+9850 from Rudy et al. (1994), [Ar III] 7136+7751 from Davidson & Fesen (1985) and [Ar III] 89911 from Temim et al. (2012). . . .	167
4.8	Observed and modelled absolute H_{β} fluxes. Observed and modelled line strengths relative are to H_{β} . All observed lines are taken from Smith (2003), except for [C I] 9824+9850 from Rudy et al. (1994), [Ar III] 7136+7751 from Davidson & Fesen (1985) and [Ar III] 89911 from Temim et al. (2012). . . .	168
4.9	Observed and modelled absolute H_{β} fluxes. Observed and modelled line strengths are relative to H_{β} . All observed lines are taken from Smith (2003), except for [C I] 9824+9850 from Rudy et al. (1994), [Ar III] 7136+7751 from Davidson & Fesen (1985) and [Ar III] 89911 from Temim et al. (2012). . . .	169
4.10	Observed and modelled absolute H_{β} fluxes. Observed and modelled line strengths are relative to H_{β} . All observed lines are taken from Smith (2003), except for [C I] 9824+9850 from Rudy et al. (1994), [Ar III] 7136+7751 from Davidson & Fesen (1985) and [Ar III] 89911 from Temim et al. (2012). . . .	170
4.11	Observed and modelled absolute H_{β} fluxes. Observed and modelled line strengths are relative to H_{β} . All observed lines are taken from Smith (2003), except for [C I] 9824+9850 from Rudy et al. (1994), [Ar III] 7136+7751 from Davidson & Fesen (1985) and [Ar III] 89911 from Temim et al. (2012). . . .	171
4.12	Global ionisation fractions of elements in model x.	172
4.13	The results for model i, the smooth isotropic density distribution.	174
4.14	The results for model ii. the smooth isotropic density distribution with outer diameters of 4.0×2.9 pc and inner diameters of 3.0×2.0 pc outside the radiation source.	175
4.15	The results for model iii. the smooth isotropic density distribution in a shell 0.5 pc thick and a inner axes of 2.1×1.4 pc entirely inside the diffuse radiation source.	177

4.16 The results for Model iv. the smooth isotropic density distribution with outer diameters of 4.0×2.9 pc and inner axes of 2.1×1.4 pc entirely inside the diffuse radiation source.	178
4.17 The results for model v. the smooth isotropic density distribution with outer diameters of 4.0×2.9 pc and inner axes of 2.13×1.7 pc entirely inside the diffuse radiation source.	179
4.18 The results for Model vi. the smooth isotropic density distribution in a shell 0.1 pc thick and a diameter of 1.1 pc entirely inside the diffuse radiation source..	180
4.19 The results for model vii. A clumpy geometry with clumps starting at radii of 3.0×2.0 pc decreasing with r^{-2} entirely outside the radiation source. The clumps have a of radius 0.111 pc with a density of 1400 cm^{-3}	181
4.20 The results for Model viii. A clumpy geometry with clumps starting at radii of 3.0×2.0 pc decreasing with r^{-2} entirely outside the radiation source. The clumps have a of radius 0.037 pc with a H number density of 1900 cm^{-3}	182
4.21 The results for model ix. A clumpy geometry with clumps starting at radii of 2.1×1.4 pc decreasing with r^{-2} entirely inside the radiation source (Model IX).	183
4.22 The results for model x. A clumpy geometry with clumps starting at radii of 2.3×1.7 pc decreasing with r^{-2} entirely inside the radiation source.	183
4.23 The results for Model xi. A geometry with clumps starting at radius 0.55 pc in a 0.1 pc thick shell with a diffuse source going up to the inner radius of the dust shell.	185
4.24 The results for Model xii. A clumpy geometry with clumps starting at radii of 2.3×1.7 pc decreasing with r^{-2} with a diffuse radiation source going up to the inner radius of the dust shell.	186
4.25 The results for Model xiii. A clumpy geometry with clumps starting at radii of 2.1×1.4 pc decreasing with r^{-2} with a diffuse radiation source going up to the inner radius of the dust shell.	187
4.26 The results for Model x using a CDE scattering routine rather than a Mie scattering routine. A clumpy geometry with clumps starting at diameters of 2.3×1.7 pc with a clump number density decreasing with r^{-2} entirely inside the radiation source.	196

4.27	The mass of dust, gas and the v-band optical depth of each clump from centre to surface for the models with the clumps outside the radiation field and a clump radius of 0.11 pc.	197
4.28	The mass of dust, gas and the optical depth of each clump from centre to surface for the models with the clumps embedded in the radiation field with a clump radius of 0.037 pc.	197
4.29	Observed and predicted photometric fluxes for the <i>Herschel</i> wave bands and their colour correction factors for Model XII.	198
4.30	Amorphous carbon dust masses in the Crab Nebula calculated empirically using equation 4.1.	200
4.31	The dust mass results for all of the models with the Zubko et al. (1996) BE amorphous carbon optical properties, the numbers in bold are the values for Model XII, the preferred model.	201
4.32	The results for model XII. A clumpy geometry with clumps starting at radii of 2.3×1.7 pc decreasing with r^{-2} with a diffuse radiation source going up to the inner radius of the dust shell.	201
5.1	The results for Model XII using the Zubko BE amorphous carbon optical constants to compare the differences between different available <i>Planck</i> fluxes.	208
A.1	The red shifted component of the [O I] 63 μm emission in the Crab Nebula measured by PACS-IFU	212
A.2	The blue shifted component of the [O I] 63 μm emission in the Crab Nebula measured by PACS-IFU	213
A.3	The red shifted component of the [O III] 88 μm emission in the Crab Nebula measured by PACS-IFU	214
A.4	The blue shifted component of the [O III] 88 μm emission in the Crab Nebula measured by PACS-IFU	215
A.5	The red shifted component of the [C II] 158 μm emission in the Crab Nebula measured by PACS-IFU	215
A.6	The red shifted component of the [C II] 158 μm emission in the Crab Nebula measured by PACS-IFU	216

B.1	The blue shifted component of the [O I] 63 μm emission in the SP1 obser-	
	vations of Cas A measured by PACS-IFU	218
B.2	The red shifted component of the [O I] 63 μm emission in the SP1 observa-	
	tions of Cas A measured by PACS-IFU	218
B.3	The blue shifted component of the [O III] 88 μm emission in the SP1 obser-	
	vations of Cas A measured by PACS-IFU	219
B.4	The red shifted component of the [O III] 88 μm emission in the SP1 obser-	
	vations of Cas A measured by PACS-IFU	220
B.5	The red shifted component of the [O III] 88 μm emission in the SP3 obser-	
	vations of Cas A measured by PACS-IFU	221
B.6	The blue shifted component of the [O III] 88 μm emission in the SP3 obser-	
	vations of Cas A measured by PACS-IFU	221
B.7	The red shifted component of the [C II] 157 μm emission in the SP3 obser-	
	vations of Cas A measured by PACS-IFU	222
B.8	The blue shifted component of the [C II] 157 μm emission in the SP3 ob-	
	servations of Cas A measured by PACS-IFU	222
B.9	The red shifted component of the [O III] 88 μm emission in the SP4 obser-	
	vations of Cas A measured by PACS-IFU	223
B.10	The blue shifted component of the [O III] 88 μm emission in the SP4 obser-	
	vations of Cas A measured by PACS-IFU	224
B.11	The blue shifted component of the [O I] 63 μm emission in the SP4 obser-	
	vations of Cas A measured by PACS-IFU	224
B.12	The blue shifted component of the [O I] 63 μm emission in the SP4 obser-	
	vations of Cas A measured by PACS-IFU	224
B.13	The red shifted component of the [C II] 157 μm emission in the SP4 obser-	
	vations of Cas A measured by PACS-IFU	225
B.14	The blue shifted component of the [C II] 157 μm emission in the SP4 ob-	
	servations of Cas A measured by PACS-IFU	225
B.15	The red shifted component of the [O III] 88 μm emission in the SP5 obser-	
	vations of Cas A measured by PACS-IFU	226
B.16	The blue shifted component of the [O III] 88 μm emission in the SP5 obser-	
	vations of Cas A measured by PACS-IFU	226

B.17 The blue shifted component of the [O I] 63 μm emission in the SP5 obser-	
vations of Cas A measured by PACS-IFU	226
B.18 The blue shifted component of the [O I] 63 μm emission in the SP5 obser-	
vations of Cas A measured by PACS-IFU	227
B.19 The red shifted component of the [C II] 157 μm emission in the SP5 obser-	
vations of Cas A measured by PACS-IFU	227
B.20 The blue shifted component of the [C II] 157 μm emission in the SP5 ob-	
servations of Cas A measured by PACS-IFU	227
B.21 The red shifted component of the [O III] 88 μm emission in the SP7 obser-	
vations of Cas A measured by PACS-IFU	228
B.22 The blue shifted component of the [O III] 88 μm emission in the SP7 obser-	
vations of Cas A measured by PACS-IFU	228
B.23 The red shifted component of the [O I] 63 μm emission in the SP7 observa-	
tions of Cas A measured by PACS-IFU	229
B.24 The blue shifted component of the [O I] 63 μm emission in the SP7 obser-	
vations of Cas A measured by PACS-IFU	229
B.25 The red shifted component of the [O III] 88 μm emission in the SP8 obser-	
vations of Cas A measured by PACS-IFU	230
B.26 The blue shifted component of the [O III] 88 μm emission in the SP8 obser-	
vations of Cas A measured by PACS-IFU	230
B.27 The red shifted component of the [O I] 63 μm emission in the SP8 observa-	
tions of Cas A measured by PACS-IFU	231
B.28 The blue shifted component of the [O I] 63 μm emission in the SP8 obser-	
vations of Cas A measured by PACS-IFU	231
B.29 The red shifted component of the [O III] 88 μm emission in the SP9 obser-	
vations of Cas A measured by PACS-IFU	232
B.30 The blue shifted component of the [O III] 88 μm emission in the SP9 obser-	
vations of Cas A measured by PACS-IFU	232
B.31 The red shifted component of the [O I] 63 μm emission in the SP9 observa-	
tions of Cas A measured by PACS-IFU	232

C.1 Values of n and k measured by Uspenskii et al. (2006) between 2.8 nm and 30 nm for an amorphous carbon sample and extrapolated n and k for Zubko et al. (1996) ACAR and BE amorphous carbon samples	234
---	-----

List of Acronyms

ACAR - An interstellar amorphous carbon dust analogue

ADU - Analogue to Digital Converter

AGB - Assymtotic Giant Branch

ALMA - Atacama Large Millimetre/Sub-Millimetre Array

BE - An interstellar amorphous carbon dust analogue

Cas A - Cassiopeia A

CDE - Continuous Distribution of Ellipsoids

CRIRES - Cryogenic Infrared Echelle Spectrograph - A VLT instrument

DDT - Directors Discretionary Time

ESA - European Space Agency

ESO - European Southern Observatory

ETC - Exposure Time Calculator

FIR - Far Infrared

FTS - Fourier Transform Spectrometer

IFU - Ingrated Field Unit

IR - Infrared

IRAC - Infrared Array Camera - A *Spitzer* instrument

IRAS - Infrared Astronomy Satellite

IRAM - Institut de Radioastronomie Millimétrique

IRS - Infrared Spectrometer - A *Spitzer* instrument

IRTF - Infrared Telescope Facility

ISM - Interstellar Medium

ISO - Infrared Space Observatory

JCMT - James Clarke Maxwell Telescope

KAO - Kuiper Airborne Observatory

LBV - Luminous Blue Variable

LTE - Local Thermodynamic Equilibrium

LWS - Long Wavelength Spectrograph - An ISO Instrument

MIPS - Multiband Imaging Photometer for Spitzer - A *Spitzer* Instrument

MRN - Mathis, Rumpl, & Nordsieck (1977) - a widely used grain size distribution

NASA - National Aeronautics and Space Administration

NIR - Near Infrared

NuSTAR - Nuclear Spectroscopic Telescope Array

PACS - Photodetecting Array Camera and Spectrometer - A *Herschel* Instrument

PAH - Poly Aromatic Hydrocarbon

PWN - Pulsar Wind Nebula

QSO - Quasi Stellar Object or Quasar

RSRF - Relative Spectral Response Function

SCUBA - Submillimeter Common User Bolometer Array - a JCMT instrument

SED - Spectral Energy Distribution

SLW - SPIRE Long Wavelength - A Spire Detector Array

SN - Supernova

SN1987A - Supernova 1987A

SNe - Supernovae

SNR - Supernova Remnant

SPIRE - Spectral and Photometric Imaging Receiver - A *Herschel* Instrument

SSW - SPIRE Short Wavelength - A Spire Detector Array

SWS - Short Wavelength Spectrograph - An ISO Instrument

UV - Ultraviolet

VLT - Very Large Telescope

WISE - Wide-field Infrared Survey Explorer

This page was intentionally left blank

Chapter 1

Introduction

For dust thou art, and unto dust shalt thou return

Genesis 3:19

1.1 Dust in the Universe

Cosmic dust plays a vital role in the evolution of the universe. It plays an essential role in the formation of molecules (Hirashita & Ferrara 2002). It is needed to cool down star forming clouds to allow second generation stars to be born (Schneider et al. 2004). It is vital in the formation of planets (Boehler et al. 2013) and is one of the biggest causes of uncertainty in cosmological observations (Wood-Vasey et al. 2007).

The origin of dust in the universe is currently a topic of great debate in astrophysics. Recent sub-millimetre and millimetre observations of galaxies and quasars (QSO's) out to redshifts of around 6 have found these objects to be very dusty. These observations have found around $10^8 M_\odot$ of dust, adopting a 50 K dust temperature from the peak in the emission for the dust species used(Bertoldi & Cox 2002; Omont et al. 2001; Carilli et al. 2001) as illustrated in Figure 1.1 which shows the rest frame sub millimetre observation of SDSS J114816.64+525150.3, a quasar at $z = 6.42$. The first stars are believed to have formed somewhere between $z = 10 - 50$ (Greif & Bromm 2006) and the youngest galaxies

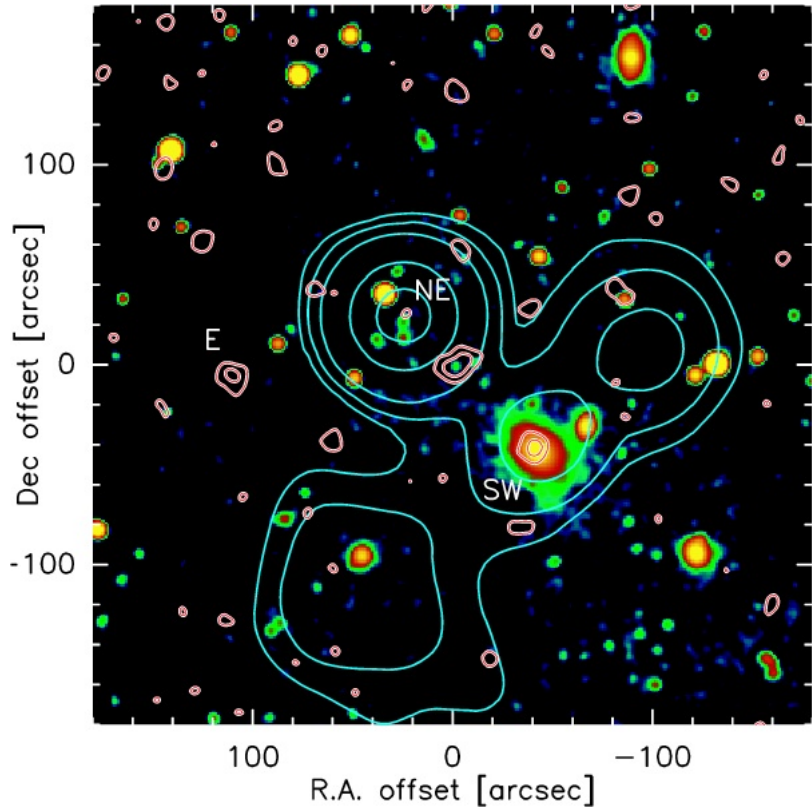


Figure 1.1. SDSS J114816.64+525150.3, a quasar at $z = 6.42$ observed with IRAM 30 m telescope showing a rest frame IR excess corresponding to $10^8 M_\odot$ of dust taken from Bertoldi et al. (2003).

observed at around $z = 10$ (Bouwens et al. 2011) giving a time of around 500 megayears for the dust observed at $z = 6$ to have formed.

In the local universe Assymtotic Giant Branch (AGB) stars are considered to be the most significant source of dust. AGB stars are those stars which had a mass of $0.85\text{--}8 M_\odot$ on the main sequence and finished hydrogen and helium core burning. AGB stars have a low surface temperature (usually around 3500 K) but high luminosity ($>10^3 L_\odot$) caused by a degenerate oxygen or carbon core surrounded by hydrogen and helium burning layers. As AGB stars evolve they develop strong winds which lead to them losing up to 80% of their mass which forms an envelop of gas and dust. AGB stars are unlikely to be the main source of the dust observed at high redshift, as the universe is too young then for most stars of low enough mass (less than $8 M_\odot$) to become AGB stars to have been formed and evolved far enough to become dust producing. Additionally, the dust budgets of local metal poor galaxies show a discrepancy between the total amount of dust observed and

that which has been produced by AGB stars(Matsuura et al. 2009, 2013).

1.2 What is dust?

When we discuss dust, we are talking about small particles ranging in size from a few molecules to a radius of $\sim 1 \mu\text{m}$. Dust can be divided into two major different species, silicates and carbonaceous materials. Broadly speaking these can be considered analogous to sand and soot particles, although the astronomical samples are much smaller than either of these.

Silicates are made up of stable condensates of silicon and oxygen along with other elements such as Iron and magnesium in complex molecules such as olivine (MgFeSiO_3) and pyroxene (MgFeSiO_4). These molecules then clump together to form dust grains. In the interstellar medium (ISM) it is nearly all amorphous (Li & Draine 2002) although in the regions where it forms it appears to be more crystalline (Kemper et al. 2004).

Carbonaceous dust is made up of many different kinds of carbon containing material. It includes everything from small poly aromatic hydrocarbons (PAHs) and fullerenes to large chunks of glassy, amorphous carbon and also includes graphite and diamonds (Draine 2011).

Which species of dust dominates is determined by the ratio of carbon to oxygen. Carbon monoxide (CO) is formed with the available oxygen and carbon, and whichever is left over from this formation of CO then forms dust. If the $\frac{\text{C}}{\text{O}} > 1$ then carbon chemistry dominates and the majority of dust formed will be carbonaceous. Conversely if $\frac{\text{C}}{\text{O}} < 1$ then the chemistry is dominated by oxygen and silicate dusts will form.

1.3 Dust Properties

Dust absorbs light at ultraviolet and optical wavelengths and re-emits in the infrared. This thermal emission can be observed allowing direct observation of dust. This emission peaks at around $100 \mu\text{m}$ for cold dust ($T \sim 30 \text{ K}$) so to measure masses and characterise dust properties a range of observations is needed to build up a spectral energy distribution (SED) at these wavelengths. In addition to this dust does not absorb light in the infrared

allowing us to observe emission lines from atoms and molecules where optical emission lines would not be visible due to their absorption by the dust. Figure 1.2 shows a Hubble



Figure 1.2. A Hubble Space Telescope optical image of the Andromeda Galaxy

Space Telescope optical image of the Andromeda galaxy. Dust in its spiral arms can clearly be seen silhouetted against the emitted light from the galaxy. Figure 1.3 shows the same galaxy in the far infrared. The orangey colour is the same dust seen in silhouette emitting the optical/uv energy it has absorbed in the infrared.

1.3.1 Optical and UV properties

Interstellar dust was first discovered by its ability to obscure starlight, known as extinction (Trumpler 1930). Much of our knowledge of dust is based on studies of the wavelength dependence of this attenuation. It is often referred to as reddening, as bluer wavelengths

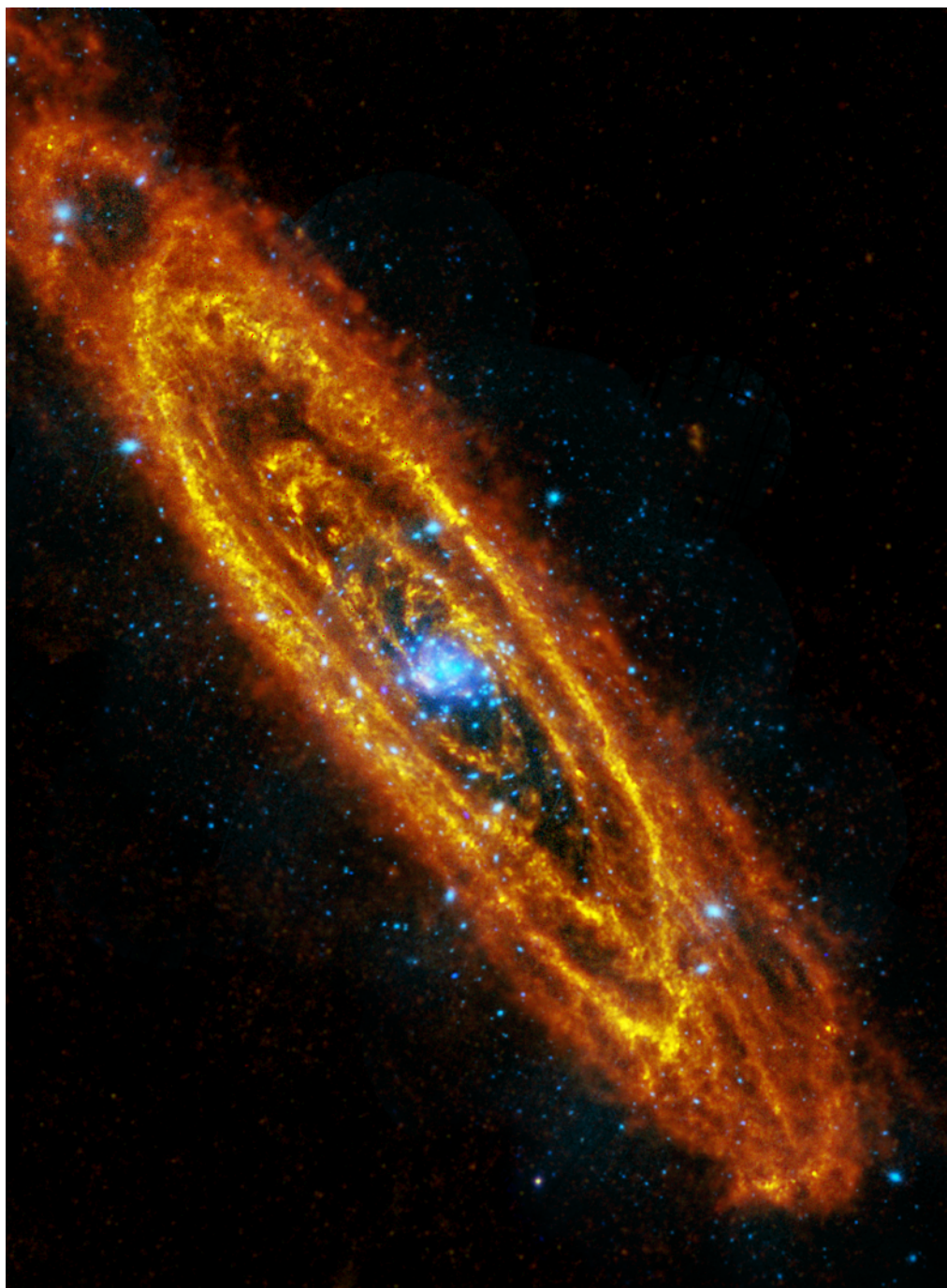


Figure 1.3. An infrared image of the Andromeda galaxy taken with the Herschel Space Observatory (Fritz et al. 2012)

are preferentially extinguished over redder ones. This change in extinction with wavelength allows us to study dust populations. A curve plotting the different extinctions at different wavelengths can built up from the observations. This curve can be used to diagnose dust properties such as the size distribution of grains (Mathis et al. 1977) and the grain species. Examination of these curves gives rise to a dimensionless quantity called R_V . R_V is a measure of the slope of an extinction curve in the optical region, it relates to the size distribution of dust grains, and is given by

$$R_V = A_V / (A_B - A_V) \quad (1.1)$$

where A_V and A_B are the measured extinctions in the V (540 nm) and B (442 nm) photometric bands.

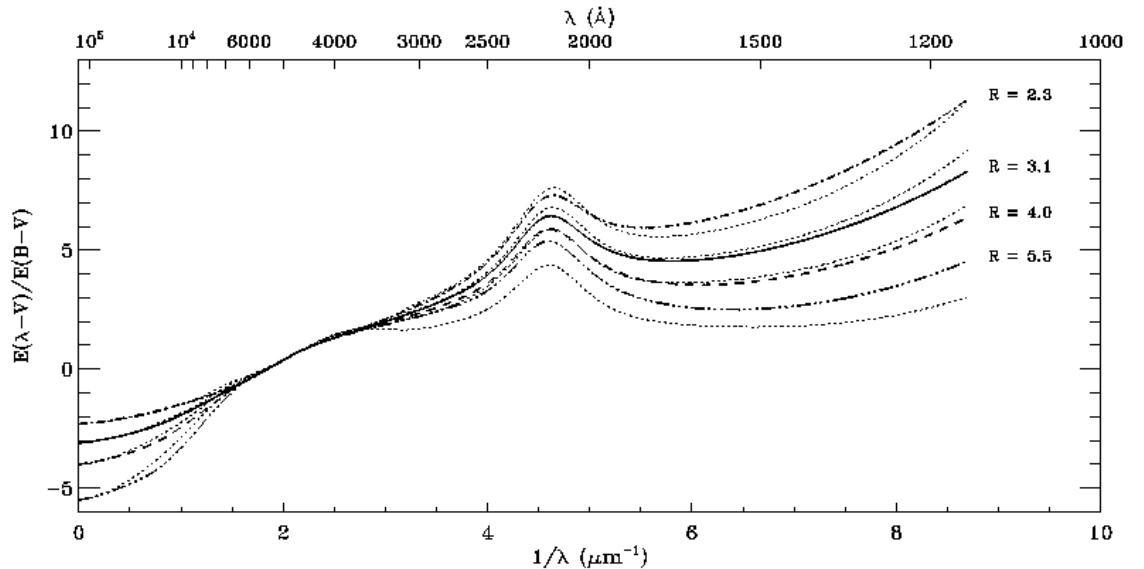


Figure 1.4. FIR to UV extinction curves taken from Fitzpatrick (1999) based on parameterisations by Cardelli, Clayton, & Mathis (1989) for $R = 2.3, 3.1, 4.0$ and 5.5 . $R = 3.1$, the Milky Way average is shown as a solid line with the others being dotted/dashed.

Figure 1.4 shows a series of different extinction curves of different R_v . The shape of the

interstellar extinction curve can be entirely described using this one parameter (Cardelli, Clayton, & Mathis 1989). A low value of R_V gives a steep slope, particularly towards the UV and is caused by scattering by very small dust grains. Rayleigh scattering (scattering by particles much smaller than the wavelength of the light being scattered) would produce an $R_V \approx 1.2$. As R_V increases, the extinction curve gets flatter and extinction becomes dominated by larger grains acting as grey bodies. A grey body is a black body that has been modified to take in to account the optical properties of the object absorbing and emitting the radiation. There is also a prominent bump at around 2175 Å, attributed to carbon ring structures (see section 1.3.4). The average interstellar extinction in our galaxy is $R_V = 3.1$ (Savage & Mathis 1979), shown as a solid line in Figure 1.4.

Light reaching us from reddened stars is often linearly polarised because the emission from dust depends on the polarisation mode. The polarisation comes from different levels of extinction due to dust grains being aligned with one another in a magnetic field. This depends on the degree of alignment of the dust grains with the local magnetic field and it's direction. Observing this polarisation can teach us a lot about the magnetic field in a region of space.

Dust also scatters light at optical and UV wavelengths. This scattering can be used to observe past events via a phenomenon called a Light Echo. Light echoes occur when the light from a bright blast such as a supernova or luminous blue variable (LBV) eruption is reflected off surrounding dust. These echoes can be used to investigate previous events in greater detail than they could be at the time, for example the classification of the supernova that gave rise to the Cassiopeia A supernova remnant was done by observing its light echo (Krause et al. 2008) and the circumstellar environment of the progenitor of 1987A was probed using light echoes (Sugerman et al. 2005). They have also been used to identify the stellar conditions pre- and post-outburst for the eruptions of η Car (Rest et al. 2012). Light scattered by dust also give rise to reflection nebulae. Starlight that is not of high enough energy to ionise gas can be scattered and reflected off a cloud of dust, thus making that dust visible.

1.3.2 X-Ray Properties

Dust can both absorb and scatter X-rays. X-ray absorption and scattering usually takes the form of excitation of an electron of a single heavy metal atom within the dust at the K-edge. The K-edge is the binding energy of an inner K-shell electron, so there is a sudden increase in the interaction of photons with the atoms at these energies. Significant scattering and absorption by dust take place around the K-edge of carbon, oxygen, silicon, magnesium as well as the K and L edges of iron (Draine 2003).

1.3.3 Infrared and Sub-millimetre Properties

The energy from absorbed optical and UV photons heats the dust grains. This causes them to emit light at infrared wavelengths, as that is where the black body peak lies for the temperatures to which the dust grains are heated to lies. It is estimated that 50% of the light energy in the universe is reprocessed starlight from galaxies, increasing to as much as 80% for gas rich galaxies (da Cunha et al. 2008). As with the polarisation at UV/optical wavelengths, the light emitted dust grains aligned to a magnetic field is also linearly polarised at infrared and sub-millimetre wavelengths. The different amounts of polarisation depend on the magnetic field strength in the region where the dust is located. This can be used to differentiate between different dust populations within a single line of sight, for example towards Cassiopeia A supernova remnant, where there is a large dust cloud between us and the remnant (Krause et al. 2004). Polarised dust emission has recently been mistaken as evidence for primordial B-modes on the CMB which might otherwise have provided observational proof for hyperinflation in the early universe (Ade et al. 2014).

The small dust grains that are required to fit the observed IR emission from the ISM will rotate. This rotation of grains leads to emission in the microwave. Observations consistent with the expected frequencies have been correlated with dust emissions towards the galactic plane (Finkbeiner et al. 2004).

1.3.4 Identifying Dust Species

The composition of dust is difficult to determine. There are several spectroscopic features in absorption and emission which can be used to help diagnose what grain species are present.

Carbon Features

The most prominent feature attributed to carbonaceous dust species is a broad bump in the interstellar extinction curve (see the large bump in the centre of the curves in Figure 1.4 in Section 1.3.1) at around 2175 Å. Carbon rings, as well as having a C-C bond have a cloud of shared electrons in the centre of the ring called π electrons. These π electrons can be excited by absorption at around 2175 Å, giving rise to the feature. The width and strength of the feature vary depending on the type of carbon dust present, with the majority of the feature being attributed to graphitic dust species and PAH clusters (Li & Draine 2001).

In addition to this broad feature, there is emission in the wavelength range 3-15 μm , which is also much greater than would be expected for purely thermal emission by dust grains in that wavelength range. A lot of this emission is concentrated around 3.3, 3.6, 6.2, 7.7, 8.6, and 11.3 μm . These bands have been attributed to stretching modes of C-H and C-C bonds in Poly Aromatic Hydrocarbons (PAHs) (Leger & Puget 1984). There are also pairs of infrared lines at 7.0, 8.5, 17.4, and 18.9 μm which can be attributed to Fullerene species such as C-60 and C-70 (Cami et al. 2010).

Silicate Features

The infrared extinction includes a strong absorption feature peaking at around 9.7 μm . Silicate minerals have an absorption feature at around 10 μm due to a Si-O stretching mode (Chiar & Tielens 2006). There is also a SiC emission feature at \sim 11 μm (Speck et al. 1997). This 10 μm feature is observed in emission in the outflows of cool oxygen stars, where silicate dusts are thought to form, but not in the outflows from carbon stars (Habing 1996). In addition to this there is a regularly observed broad feature at 18 μm which is attributed to O-Si-O bending modes in silicate dusts (Chiar & Tielens 2006). The strengths of these features appear to be strongly dependent on the shape of the grains (Min et al. 2007).

1.4 The Standard Dust Model

The standard model used as a dust model is based on the work of Mathis, Rumpl, & Nordsieck (1977). It was developed by attempting to fit observational data on interstellar

extinction between 0.1 and 1 μm using particle size distributions of different materials in such a way that all the features in the extinction curve are replicated. They used various mixtures consisting of graphite, silicates, iron, and iron oxides to fit this curve finding them all acceptable. The grains size distribution used by them was a power law distribution with grain radii $a_{max} = 1 \mu\text{m}$, $a_{min} = 0.005 \mu\text{m}$ with a power law index, α , of $\alpha = -3.3$ to -3.6 for graphite grains. For silicate materials the power law index was found to be the same but there is a much narrower range of sizes $a_{max} = 0.25 \mu\text{m}$, $a_{min} = 0.025 \mu\text{m}$. This model is the bases of all subsequent dust models.

The Mathis, Rumpl, & Nordsieck (1977) model has been developed to include more modern dust optical properties including several types of amorphous carbon species (Zubko et al. 2004) as well as improved silicate models (Weingartner & Draine 2001). Recently there has been a move away from the use of power law distributions with curves such as skewed gaussians (Sarangi & Cherchneff 2013) and log normal type distributions (Jones et al. 2013) to give distributions that better fit specific dust populations and better take in to account formation and destruction mechanisms.

1.5 How we observe Dust at Infrared Wavelengths

A lot of modern dust research takes place in infrared wavelengths, particularly towards the far infrared where dust is re-emitting the starlight it has absorbed.

Although astronomy in the infrared is very good at seeing through clouds of dust, far infrared light can not pass through the water vapour in the Earth's atmosphere. As a result the most effective way of doing infrared astronomy is to use space based observatories. The most powerful of these observatories have been the European Space Agency (ESA) *Herschel* Space Observatory in the far infrared and sub millimetre (60-670 μm) and NASA's *Spitzer* space telescope in the near and mid infrared (3-160 μm). Some IR astronomy can be done from earth, in the near and mid-IR and then towards the sub-millimetre as there are "windows" in the atmosphere, through which light at infrared wavelengths can pass through, shown in Figure 1.5 which also clearly shows the complete opacity in the wavelengths in which the *Herschel* Space Observatory operates.

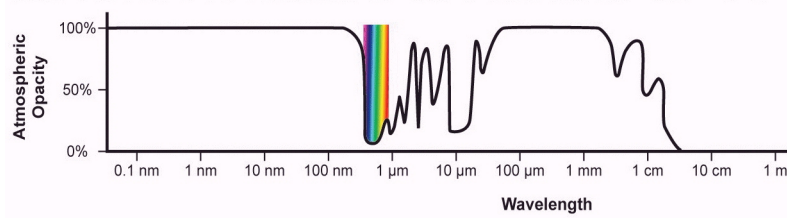


Figure 1.5. The opacity of the Earth's atmosphere vs wavelength to show regions where it is not possible to make observations from the ground.

1.5.1 The *Herschel* Space Observatory

The Herschel Space Observatory (Pilbratt et al. 2010) was a space observatory run by the European Space Agency (ESA), with involvement from the National Aeronautics and Space Agency (NASA), to explore the universe in the far infrared and sub millimetre regions of the spectrum. The satellite was launched on the 14th of May 2009 along with ESA's *Planck* mission. It operated until the 29th of April 2013, when it ran out of liquid helium, used to cool the detectors to cryogenic temperatures. It was in an orbit around the L2 Lagrange point meaning that the Earth was always between it and the sun. Its mirror diameter was 3.5 m, the largest to have been put in to space. Despite this, because of the relationship between angular resolution and wavelength (equation 1.2) *Herschel* has a similar resolving power to early telescopes developed by Galileo.

$$\theta = \frac{1.22\lambda}{D} \quad (1.2)$$

Herschel had three instruments on board, PACS - a camera and spectrometer operating from 55 to 210 μm, SPIRE a camera and spectrometer for wavelengths of 194 to 672 μm and HIFI, A heterodyne detector giving a very high spectral resolution between 157-212 μm and 240-625 μm.

PACS (Photodetector Array Camera and Spectrometer)

The Photodetector Array Camera and Spectrometer (PACS) (Poglitsch et al. 2010) was an imaging camera and low-resolution spectrometer covering wavelengths from 55 to 210 μm. Its spectrometer has a resolving power of between R = 1000 and R = 5000 and worked simultaneously in two bands as it can use two of its three gratings at a time. The PACS spectrometer is an Integrated Field Unit (IFU). An IFU is an instrument that combines spectrographic and imaging capabilities to obtain spectra that are spatially resolved. The

PACS-IFU is made up of 5×5 square spaxels with 9.4 arcsec sides, giving a 47×47 arcsec field of view. There are a number of important atomic and ionic fine structure transition lines within this wavelength range which can be used to diagnose the temperature, density and composition of gaseous regions including supernova remnants. The spectrometer also has a high enough resolution to be able to obtain velocity information about these components allowing us to look at the 2D+velocity structure of objects. The camera has three imaging bands at 70, 100 and 160 μm .

SPIRE (Spectral and Photometric Imaging Receiver)

The Spectral and Photometric Imaging Receiver (SPIRE) (Griffin et al. 2010) instrument was also a photometer (camera) and spectrometer operating between 200 and 670 μm . The spectrometer was an imaging Fourier Transform Spectrometer consisting of two arrays of bolometer detectors; one array of 35 detectors (originally 37, but 2 of the bolometers were non-detecting) detectors covering the 194-313 μm wavelength range (SSW - SPIRE Short Wavelength) and the other an array of 19 detectors covering the 303-671 μm wavelength range (SLW - SPIRE Long Wavelength). This wavelength range contains a large number of molecular rotational lines including many carbon monoxide lines as well as OH⁺ and other more exotic species. The camera images simultaneously at 250, 350 and 500 μm , so when combined with the PACS camera can provide a full spectral energy distribution at far infrared wavelengths, covering the peak of cool dust emission, which allows the measurement of dust masses.

1.5.2 The *Spitzer* Space Telescope

The 85-cm Spitzer Space Telescope (Werner et al. 2004) was an infrared space observatory launched by NASA in 2003. Originally it covered a wavelength range of 3-100 μm , but ran out of its cryogenic coolant in May 2009 meaning that it currently only operates in with the detectors that do not require cryogenic cooling, two photometric bands at 3.6 μm and 4.5 μm .

In its full mission Spitzer had three instruments: IRAC, IRS and MIPS. IRAC (Infrared Array Camera) (Fazio et al. 2004) is a camera which operates at 3.6, 4.5, 5.8 and 8 μm . IRS (Infrared Spectrograph) (Houck et al. 2004) was a spectrometer which operated in four wavelength ranges at different resolutions. It covered 4.3-14 and 14 to 40 μm at low

resolution (60-120) and 10-19.5 and 19-37 μm at high resolution (600). MIPS (Multiband Imaging Photometer for Spitzer) (Rieke et al. 2004) was a three detector photometer array which operated at 24, 70 and 160 μm . This wavelength range gave information about the peak of dust emission but did not constrain the SED as well as *Herschel* due to not providing information beyond the peak where cold dust emission occurs, nor was it as sensitive.

1.5.3 Other Infrared and Sub Millimetre Observatories

Planck

The *Planck* (The Planck Collaboration 2006) space craft was operated by ESA and was designed to observe anisotropies in the Cosmic Microwave Background. Although primarily a cosmology mission, *Planck* made all sky maps in 9 sub-millimetre and millimetre wavelengths. These maps can be used to investigate the interstellar medium of our galaxy as well as observations of point sources within the map which can be used to constrain their spectral energy distributions in this wavelength range (e.g. Crab Nebula (Gomez et al. 2012), see chapter 5). These maps can also be used to investigate effects such as the polarisation of dust (Planck Collaboration 2014) on very large scales which in turn can give information about large scale magnetic field structures .

ISO

The Infrared Space Observatory (ISO) (Kessler et al. 1996) was a cryogenically cooled 60-cm space telescope for infrared astronomy that operated between 1995 and 1998. It was designed and operated by ESA and covered a wavelength range from 2.5-240 μm . ISO had four scientific instruments

- ISOCAM - a camera imaging between 2.5 and 17 μm (Cesarsky et al. 1996)
- ISOPHOT - a photometer-polarimeter to measure the amount of radiation emitted in wavelength range 2.5-240 μm (Lemke et al. 1996)
- SWS - a short wavelength spectrometer operating between 2.5 and 45 μm (de Graauw et al. 1996)
- LWS - a long wavelength spectrometer operating between 45 and 196 μm (Clegg et al. 1996)

ALMA

The Atacama Large Millimetre/Sub-Millimetre Array (ALMA) is an interferometer array of up to 54 12-metre radio antennae and 12 7-metre antennae, located 5000 meters above sea level in the Atacama desert of northern Chile. It operates in between $350\ \mu\text{m}$ and 10mm (although coverage is not complete due to absorption and emission in the Earths atmosphere). The array has a much higher sensitivity than both single dish sub-millimeter observatories such as the 15m James Clerk Maxwell Telescope and the SMA and IRAM Plateau de Bure interferometers. The distance between the antennae can be varied between 150 m and 14 km to allow it to obtain a range of angular resolutions. Because of this long baseline it has almost unparalleled spatial and velocity resolution. ALMAs observation bands include one at $450\ \mu\text{m}$ (band 9) and one at $870\ \mu\text{m}$ (band 7) which can be used for the observation of cold dust as well as other bands useful for constraining line emission and background emission and synchrotron spectra in SEDs.

1.6 Supernovae and their Remnants

Core collapse supernovae represent the violent deaths of massive stars. They produce explosions incredibly luminous explosions which often brighter than their host galaxies, SN 2006gy, the brightest ever observed had a visual magnitude of about -22 (Smith et al. 2007). Once the core of a star reaches a point where it requires more energy per nucleon for fusion to occur than the reaction will release, at 56 nucleons (^{56}Ni , ^{56}Co , and ^{56}Fe), fusion stops. This unbalances the hydrostatic support against gravity in the star which then collapses in on itself and explodes.

There is another type of supernova (Type Ia) which is caused by thermonuclear runaway of carbon/oxygen white dwarf stars. These do not seem to create dust (Gomez et al. 2012), and are beyond the scope of this thesis.

1.7 Types of Core-Collapse Supernovae

Supernovae are typically characterised by their properties in the visible part of the electromagnetic spectrum. Type I supernovae do not have hydrogen present in their spectra,

whereas Type II do not. Each of these classes contains multiple subclasses depending on features in their spectra and the shape of their light curves (the light intensity over time) which are summarised in Table 1.1.

There are two classes of type I (hydrogen poor) core-collapse supernovae, Ib and Ic (Wheeler & Harkness 1990). Progenitors are thought to be massive stars that have lost their outer layer of hydrogen and helium, either via winds or mass transfer to a companion. They are observationally distinct from Ia (thermonuclear) supernovae due to the lack of Si lines in their optical spectra. The light curves of Ib and Ic are initially very similar, but Ib's decline at a slower rate to Ic's (Filippenko 2005).

Type II supernovae can be separated into four classes (with one of these classes also being split into two subclasses). Type IIb supernovae are observationally very similar to Type Ib supernovae, but have a weak hydrogen line in their initial spectrum (Filippenko 1988). Type II-L supernovae are so called because of the linear decrease in time of their light curve following the peak brightness. By contrast, Type II-P supernovae have a distinctive flat plateau stage during the decline after peak brightness (Filippenko 1997). The contrast between these light curves is shown in Figure 1.6.

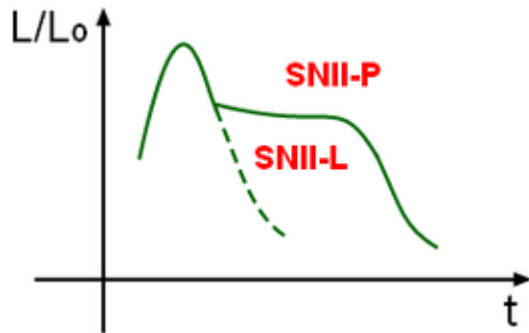


Figure 1.6. Example light curves of Type II-P and II-L supernovae.

Type IIn supernovae are characterised by the much narrower emission lines in their spectra (Schlegel 1990). It is hypothesised that these come about due to a strong interaction between the supernova explosion and a dense circumstellar environment caused by mass ejections (Chugai 1991) such as Luminous Blue Variable (LBV) eruptions or AGB

mass ejections. Type IIn supernovae can also be divided into two sub-classes based on their luminosity. Type IIn's can be super luminous, these are thought to have massive LBVs as their progenitors. The combination of the massive progenitor and the interaction between the supernova explosion and the dense circumstellar envelope leads to a very bright supernova event (Smith et al. 2008). Conversely, very low luminosity Type IIn supernovae are thought to have Super AGB stars as progenitors which are only just large enough to become supernovae (Smartt 2009).

There can be overlap in these types of supernova, for example II-L and II-P type supernovae can also have narrow line emission, giving rise to IIn-L and IIn-P type supernovae.

1.8 Supernova Remnants

1.8.1 Shell Supernova Remnants

Supernovae evolve through several stages between their explosion and their merging entirely with the surrounding interstellar medium. Initially the remnant expands freely sweeping up interstellar and circumstellar material. This phase lasts until the supernova has swept up its own mass in external material. At this point the remnant enters what it known as the Sedov phase (Chevalier 1974). During this phase a strong reverse shock also propagates back through the ejecta heating it. This phase ends when the shocks are slow enough that significant radiative cooling can take place. This can take hundreds to thousands of years. The remnant becomes a cool dense shell around a hot interior, which continue as a pressure driven expansion known as the snowplough phase. Finally as the interior cools, the shell expands from its own momentum from the explosion, eventually merging with the ISM. This whole process takes approximately 30,000 years from the initial explosion.

1.8.2 Centre-Filled Supernova Remnants

In addition to the “traditional” shell supernova remnants, there are another class that have a filled centre. There are several different explanations for these. Some are much older remnants that the shell has cooled while the interior has remained hotter, allowing emission to reach us (Seward et al. 1995). This may be caused by evaporation of interstellar clouds (White & Long 1991). Some, such as the Crab Nebula, are driven by a central heating

Supernova Type	Defining Characteristics	Progenitor Mass (M_{\odot})	Progenitor Type	Examples
Type I	Hydrogen deficient			
Ib	Helium rich	25	Wolf-Rayet Stars	
Ic	Helium Poor, no Si II	25	Wolf-Rayet Stars, Binaries	
Type II	Hydrogen Present			
IIb	similar to Type Ib SN	25-30	Wolf-Rayet Stars	
II-L	Light curve decreases linearly in magnitude	15-25		
IIIn (narrow)	narrow emission lines on a broad base can be split in to two subclasses		SAGB stars	
IIIn Low Luminosity		8-10	LBV stars	
IIIn Super luminous		25-30	RSG	
II-P (plateau)	blue, almost featureless spectrum	8-25		

Table 1.1. The different types of core collapse supernovae.

source such as a pulsar, which enhances the central emission (Hester 2008).

1.9 Dust Formation in Supernovae and Supernova Remnants

Fast and efficient dust formation is required to explain observations of large reservoirs of dust in high redshift galaxies. Due to their short life times and the large amounts of metals they produce, core collapse supernovae have been suggested as this source (Morgan & Edmunds 2003). For supernovae to be able to produce enough dust to fit observations, they must be efficient producers of dust, requiring as much as $1 M_{\odot}$ to be produced per supernova event for the required amounts to be injected in to the interstellar medium after destruction rates are taken in to account (Dwek et al. 2007).

1.9.1 Theories of Formation

Supernovae have long been suggested as potential sources of interstellar dust (Dwek & Scalo 1980). Metallic elements in interstellar clouds can be trapped on the surfaces of graphitic and iron based dust grains leading to a gas phase depletion (Barlow 1978). The particularly high depletion of Al, Ca and Ti can only be explained if condensation takes place in supernovae (Clayton 1978). There are two main theories of dust formation in stellar outflows supernovae, those based on classical nucleation theory and those which use a chemical kinetic approach.

Nucleation theory assumes that when a gas is supersaturated; particles form seeds which then accrete more particles. This method has been used to model dust formation in supernovae by Todini & Ferrara (2001) and Bianchi & Schneider (2007). Using these models in conditions found in supernovae of different sizes they find that supernovae of progenitor size $12-40 M_{\odot}$ are capable of forming $0.1-0.6 M_{\odot}$ of dust, which is enough to account for the dust masses observed in the early universe.

The chemical kinetic description of the ejecta is based on the initial chemical composition of the gas and a set of chemical reactions describing the chemical processes in the ejecta. Cherchneff & Dwek (2009, 2010) used these techniques to investigate the masses of dust formed in primordial pair instability supernovae and a $20 M_{\odot}$ core collapse su-

pernova. These was then extended by Sarangi & Cherchneff (2013) to investigate Type II core collapse supernovae in the local universe. Chemical kinetic models tend to predict far less dust than models using classical nucleation theory. They tend predict to the order $10^{-2} M_{\odot}$ of dust.

1.9.2 Isotopic Ratios

The ratios of isotopes in interstellar dust are important in determining the origins of interstellar dust. This can be investigated by investigating so called "pre-solar grains" from interplanetary dust samples (Messenger et al. 2003). Supernovae and AGB stars have very different isotopic ratios, and whether dust comes from one or another of these sources can be investigate. Several dust grains have found to of supernova origin (Messenger et al. 2005).

1.9.3 Observed Dust Masses

Prior to *Herschel*, observations of dust formed in supernova ejecta had only found 10^{-4} - $10^{-2} M_{\odot}$ of hot (200-900 K) dust (Wooden et al. 1993; Sugerman et al. 2006; Kotak et al. 2009; Fabbri et al. 2011). These observation were mostly taken in the near infrared and of dust formed very close to the supernova event. This view of supernova dust formation is being challenged by recent observations of older supernovae and remnants in the far infrared and submillimetre wavelengths leading to the discovery of much larger masses of cold dust.

1.9.4 Recent Observations with Herschel

Cassiopeia A

Cassiopeia A (Cas A) is a young oxygen rich supernova remnant (SNR). It is approximately 3.4 kpc away (Reed et al. 1995) and around 330 years old (Fesen et al. 2006). Cas A is one of the most-studied objects in the sky, having been observed in all wavelengths from radio waves through to γ -rays. Recent optical observations of light echoes due to scattering by interstellar dust show that it is the remnant of a Type IIb supernova, with a probable initial mass of around $15 M_{\odot}$ (Krause et al. 2008).

The mass of dust in Cas A has been much studied and has been a controversial topic. Dunne et al. (2003) reported as much as $4 M_{\odot}$ of dust in the remnant. This was later challenged by Krause et al. (2004) who showed that most of this emission was not actually in the remnant, but in foreground molecular clouds by associating the dust emission with emission from OH molecules. Using the *Spitzer* Space Telescope, Rho et al. (2008) measured between 0.02 and 0.05 M_{\odot} of warm dust (between 65–265 K). Although the strong interstellar foreground emission prevents direct observation of cold dust, observations with *Herschel* were able to identify a cool dust component with a mass of $0.08 M_{\odot}$ (Barlow et al. 2010) leading to a total mass of $\sim 0.10 M_{\odot}$ of dust.

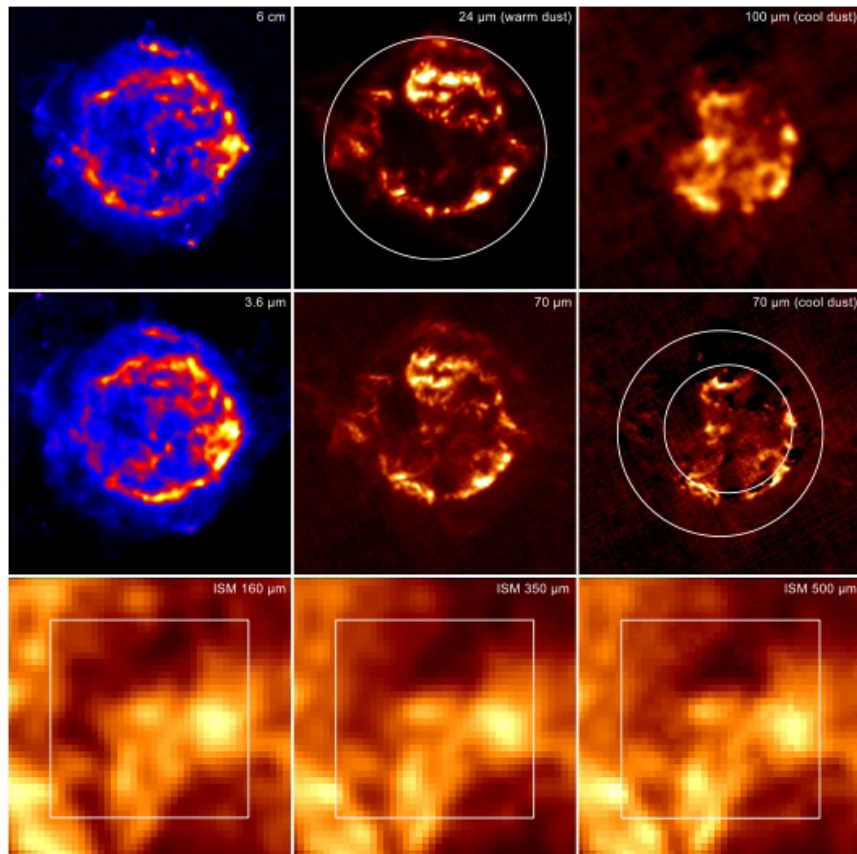


Figure 1.7. Multi wavelength observations of Cas A showing the synchrotron continuum at 6 cm (VLA) and 3.6 μm , warm dust at 24 μm (*Spitzer*) and 70 μm (*Herschel*), cool dust 100 μm (*Herschel*) and 70 μm (*Herschel*) and 160, 350 and 500 μm foreground dust taken from Barlow et al. (2010).

Figure 1.7 shows multi wavelength observations of Cas A used to constrain its dust. The top left and middle left show the 6 cm and 3.6 μm observations used to constrain the

background spectrum. The top central and central image show the contributions to from the warm dust component at 24 μm (top central) and 70 μm (central). The top right and central right show the emissions from the cool dust component at 100 μm (top right) and 70 μm (centre right). The bottom row shows the ISM foreground at 160, 250 and 500 μm . These foreground emission features are present in all three of these wavelength ranges and completely obscure any emission from within the remnant. It may be possible to identify a cold dust reservoir in the remnant by investigating the effect of extinction on optical lines emitted from the front and back of the shell of the remnant. The lines which have been emitted from the front of the remnant will have been extinguished by dust between the remnant and observer, whereas the emission from the back of the nebula will have the additional extinction from dust formed within the remnant itself. Because of the foreground dust there is no way of identifying it using the infrared/sub-millimetre excess. The warm and cool dust components combined give a dust mass of approximately 0.1 M_\odot of dust in the Cassiopeia A supernova remnant.

Supernova 1987A

First observed on the 23rd of February 1987, SN1987A is the nearest core collapse supernova in modern times. It is approximately 51 kpc away in the Large Magellanic Cloud (LMC), a dwarf galaxy orbiting our own. Given previous indications that young supernovae ejecta only produced $\sim 10^{-3} M_\odot$ of dust, it was not chosen as a target for the *Herschel* Space Observatory, as it was predicted to not be detectable at far infrared and sub-millimetre wavelenghts. During the HERITAGE survey (Meixner et al. 2013), a *Herschel* survey of the LMC, an unexpected signal was detected in 2010 coincident with the location of SN1987A, at 100, 160, 250 and 350 μm wavelengths, shown in Figure 1.8. This turned out to come from a large reservoir of previously unobserved cold dust. Analysis of the data showed between 0.4 and 0.7 M_\odot of dust, depending on which dust species assumed to make up the majority of this dust (Matsuura et al. 2011). Observations at much earlier epochs had found $\sim 10^{-4}$ solar masses of dust (Bouchet & Danziger 1993; Wooden et al. 1993; Ercolano et al. 2007). This result was considered controversial, with some people questioning whether the dust was located in the ejecta, or if it was pre-existing dust that had been formed by the progenitor star. Supernova progenitors such as η Carina have been shown to produce similar amounts of dust (Gomez et al. 2010). Follow up 450 μm

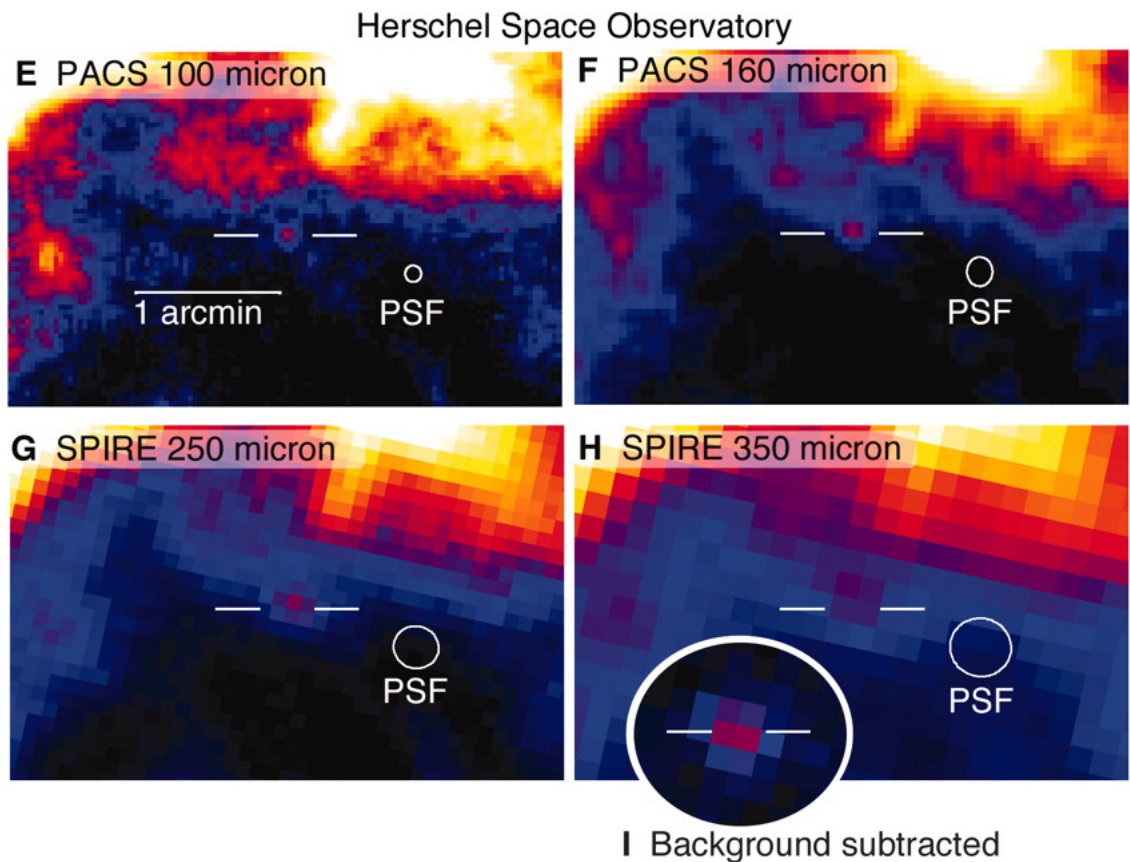


Figure 1.8. *Herschel* Observation of 1987A at 100, 160, 250 and 350 μm taken from Matsuura et al. (2011).

observations of SN1987A with ALMA (Indebetouw et al. 2014) were able to resolve the location of the dust in the remnant showing that the cold dust was located entirely within the central ejecta region rather than in the circumstellar ring of pre-supernova material, as shown in Figure 1.9. As well as the 450 μm image, Figure 1.9 shows observations of SN1987A at other wavelengths to demonstrate its structure, which includes a bright ring of material that was ejected by the progenitor before going supernova and a central ejecta region. The ejecta region is expanding and has begun to interact with the outer ring. This will form shockwaves travelling back inward towards the central ejecta region. This may have an impact on the amount of surviving dust in the remnant. It will be observed over the coming decades with interest to see how much of the dust survives, and whether any more dust forms in the shocked regions and in the cold regions formed in between shocks.

With these results for SN1987A and Cas A along with those for the Crab Nebula,

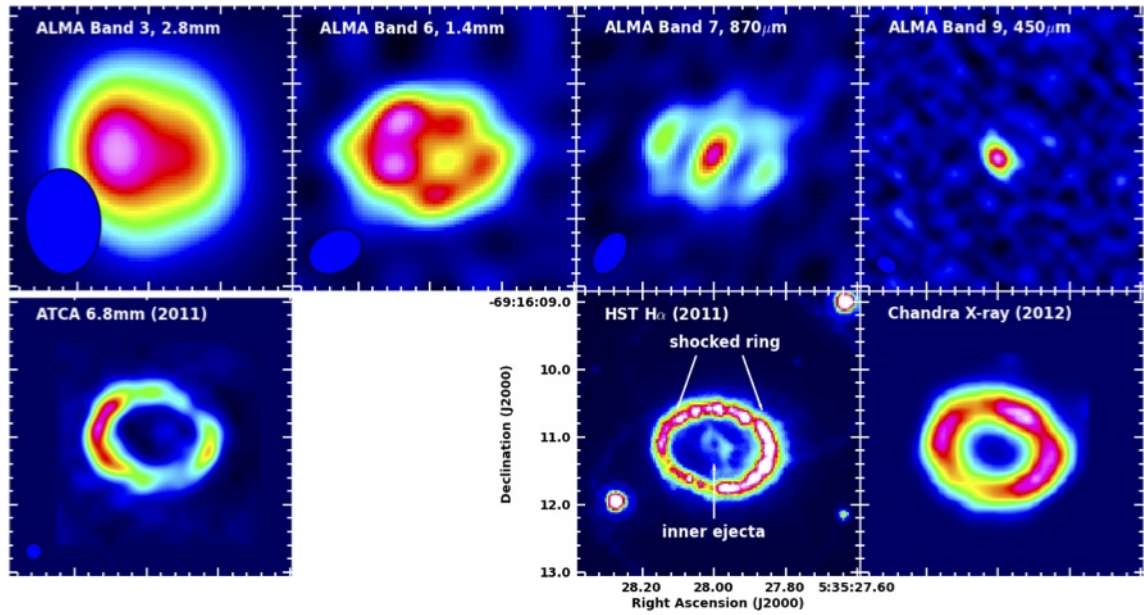


Figure 1.9. ALMA (mm and sub-mm), ATCA (mm), Hubble (visible) and Chandra (x-ray) observations of SN1987a showing the structure of the supernova remnant and location of the dust. Taken from Indebetouw et al. (2014).

which will be discussed in more detail in Chapter 5, we are starting to build up a body of evidence for highly efficient condensation of dust by supernovae and their remnants. The masses of dust formed are potentially enough to account for the large masses of dust observed in high redshift galaxies (Dwek et al. 2007).

1.10 Infrared atomic lines in Supernova Remnants

1.10.1 Fine Structure Lines

When some spectral lines are examined at a very high resolution they display a splitting. Lines split into closely spaced doublets and triplets rather than a single line. This small splitting of the spectral lines is caused by an interaction between an electron's spin, S , and its orbital angular momentum, L . This is called the spin-orbit interaction.

In the frame of reference where the electron is stationary with the nucleus orbiting it, the motion of the nucleus generates a magnetic field. The electron also has an intrinsic magnetic field caused by its spin. These two magnetic fields couple giving a difference in

energy depending on their orientation.

These fine structure lines can be excited by collisions with electrons and other atoms. When the levels de-excite they emit a photon which carries away energy, cooling the region. These fine structure lines of ground state atoms and ions are usually in the near to far infrared. Figure 1.10 shows a schematic energy level diagram of the O^{2+} ion including this line ground state splitting. This is the same structure as the isoelectronic N^+ and C species. The energies of the transitions are different for the different species. For the neutral oxygen ground state, the J-sequence energy levels is reversed.

These lines are known as forbidden lines. This is because they are not excited electronically, so must be excited collisionally or thermally, which is why they make such good diagnostic tools for physical conditions.

1.11 Molecules in Supernova Remnants

Studies of local supernova remnants have shown that they can form both dust and molecules. Herschel observations of Cassiopeia A (Cas A) show that it has formed CO (Rho et al. 2009; Wallström et al. 2013) (see Chapter 4) while the Crab Nebula has been observed to have formed OH^+ and $^{36}ArH^+$ (Barlow et al. 2013) (see Chapter 3). Supernova 1987A has also been observed to have formed SiO and CO molecules (Kamenetzky et al. 2013).

Carbon monoxide (CO) is an important coolant. As a fast forming molecule it also plays a vital role in controlling the chemistry and dust formation of a region by looking up all of whichever species, C or O, is less abundant. If more carbon is left after CO has formed then the chemistry will be carbon based and amorphous carbon dust species will form where as if there is more oxygen is left over then that will drive the chemistry and O-rich molecules and silicate dusts will be more likely to form.

As well as being an important coolant, and of interest in its own right, CO, and other molecules, can be used to help diagnose conditions in regions where it is observed by looking at its rotational temperature.

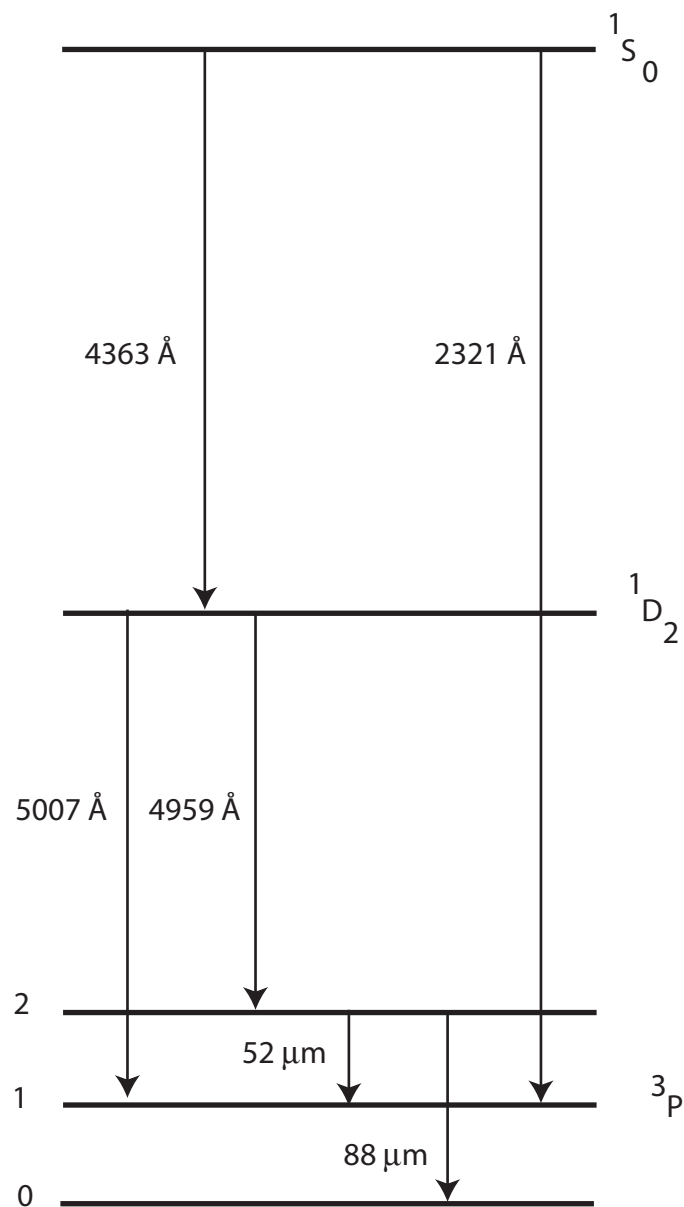


Figure 1.10. The fine structure splitting of the ground state of doubly ionised oxygen.

Observations of the strengths of different rotational transitions can be tied to physical conditions within an object. A excitation temperature can be determined from the column densities of several rotational energy states, utilising the upper energy level of that state and the statistical weight of that energy level using Equation 1.3.

$$\frac{N_u}{g_u} = \frac{N_{\text{tot}}}{Q(T_{\text{rot}})} e^{\frac{-E_u}{T_{\text{rot}}}} \quad (1.3)$$

where N_u is the population at a given upper energy level g_u is the statistical weight of the level, N_{tot} is the total column density of the molecule, $Q(T_{\text{rot}})$ is the rotational partition function. For diatomic molecules, which all molecules observed in supernova remnants so far have been, the rotational partition function is $Q(T) = kT/hB$ when kT is the Boltzmann temperature, B is the rotational constant, $\frac{h}{8\pi^2 I}$ where I is the moment of inertia, and h is the Planck constant. By plotting this logarithmically a straight line slope fitted to this gives $\frac{-1}{T_{\text{rot}}}$, which can then give us the rotational temperature within the system (Goldsmith & Langer 1999). The column density, the number of absorbers/molecules per unit area, can be determined from the intercept of this slope. To do this correctly, the solid angle of the telescope beam filled by the source of the emission needs to be taken in to account.

1.12 This Thesis

This thesis presents infrared spectroscopic observations of two galactic supernova remnants the Crab Nebula in Chapter 2 and Cassiopeia A in Chapter 3 using the *Herschel* PACS-IFU and SPIRE-FTS spectrometers. These observations are used to investigate the structure and conditions within these supernova remnants. In addition to the *Herschel* observations, Chapter 3 contains follow up observations of the Crab Nebula made with ESO's Very Large Telescope (VLT) and NASA's Infrared Telescope Facility (IRTF). Chapter 4 contains a full 3D radiative transport model treating gas and dust in the Crab Nebula. This model is fitted to photometric data from *Herschel* taken from Gomez et al. (2012) to measure the dust mass of the nebula, as well as using optical emission line fluxes taken from Smith (2003) to investigate the gas properties and atomic abundances in the Crab Nebula.

Chapter 2

Herschel Spectroscopy of the Crab Nebula

OOOOOOG! THE CLAW

Those aliens in Toy Story

The Crab Nebula is the remnant of a supernova that was observed by the Chinese in 1054. It is measured to be around 2 kpc away (Trimble 1968). The is one of the most-studied objects in the sky, having been observed at all wavelengths from radio waves through to γ rays. It is hypothesised that it was an Type IIn-P core-collapse supernova of a progenitor with an initial mass of around $10 M_{\odot}$ (Smith 2013). It consists of a central pulsar that drives a pulsar wind nebula (PWN) (Hester 2008). The synchrotron radiation from this PWN in turn ionises the dense filaments of ejecta. It is a good choice for investigating the formation of dust in supernovae and supernova remnants as it is close enough to be resolved so the supernova and interstellar/circumstellar components can be separated. It is also young enough that the thermal emission from the remnant is dominated by its ejecta rather material that has been swept up. In addition to this, it is located a long way from the Galactic plane and away from the Galactic centre so it is not subject to much interstellar reddening and is not obscured by much foreground dust.

2.1 The Crab Nebula with the PACS-IFU Spectrometer

A spectrum was taken of the central region of the Crab Nebula on the 4th of April 2011 with the PACS instrument centred at RA 5h 34m 29.44s DEC 22° 0' 32.52". This position is shown in Figure 2.1 plotted over a 70μm image of the Crab Nebula. These observations were made as part of MESS (Mass-loss of Evolved StarS), a guaranteed time key program (Groenewegen et al. 2011). Two observations have been made at this position; one for the wavelength range 51-72 μm and 102-146 μm (Range Mode SED B2A + Short R1) and one for the 70-105 μm and 140-220 μm (Range Mode SED B2B + Long R1). Data was reduced to level 2 using the standard PACS ranged SED pipeline in HIPE version 8.0.1 (Ott 2010), this is the level of reduction at which validation has taken place and the observations are ready to be used for scientific purposes. Additional data were taken from the ISO-LWS archive covering a similar wavelength range (shown in Figure 2.2). Information on these observations can be found in Table 2.1.

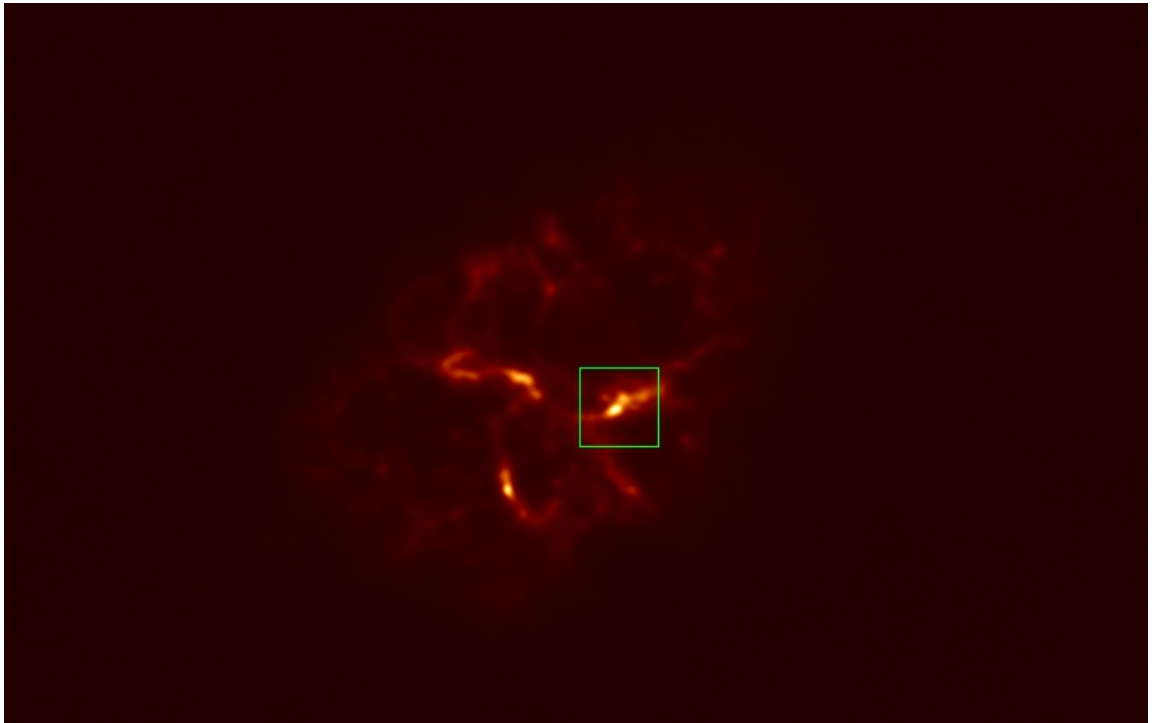


Figure 2.1. The position of the PACS-IFU observations of the Crab Nebula plotted on a PACS 70 μm image.

HIPE (Herschel Interactive Processing Environment) is a data retrieval and processing

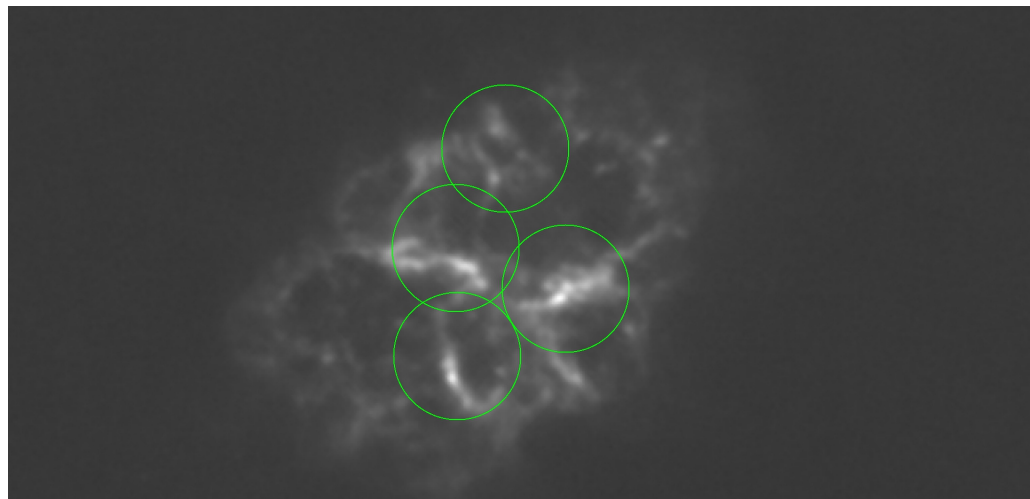


Figure 2.2. The position of the ISO-LWS observations of the Crab Nebula plotted on a PACS 70 μm image.

package for the *Herschel* Space Observatory. It provides access to the Herschel Science Archive and allows for processing and reduction and calibration of data for export as well as some analysis tools.

2.1.1 Nebula Diagnostics

Determining physical conditions such as temperature and density in nebulae, including supernova remnants can be done by comparing line flux ratios of atomic transitions. This can be done by taking the intensity ratio of two lines of the same ion. If the different levels have similar excitation energies then the relative excitation rates of these two levels depend on the collision strengths and electron densities. If the two levels have different critical densities, the relative population between these two levels will be dependent on the density, therefore the ratio of the line intensities they emit will also be density dependent.

The critical density of a level i is given by

$$n_{cr}(i) = \frac{\sum_{i>j} A_{ij}}{\sum_{i \neq j} c_{ij}} \quad (2.1)$$

A_{ij} is the Einstein A coefficient, the probability of the transition occurring spontaneously

Instrument	Date	Time	RA	DEC	TDT/ObsID	Time
ISO-LWS	1997-10-09	01:18:54	05h 34m 34.27s	22° 01' 02.4"	69501241	1124s
ISO-LWS	1997-10-09	01:29:10	05h 34m 32.02s	22° 02' 04.6"	69501242	1126s
ISO-LWS	1997-10-09	01:48:46	05h 34m 29.31s	22° 00' 37.0"	69501243	1124s
ISO-LWS	1997-10-09	02:08:20	05h 34m 34.19s	21° 59' 54.7"	69501244	1630s
PACS	2011-04-04	12:40:19	05h 34m 29.44s	22° 00' 32.52"	1342217847	2267s
PACS	2011-04-04	13:20:18	05h 34m 29.42s	22° 00' 47.17"	1342217847	1139s

Table 2.1. Information on the position and integration time of spectroscopic measurements of the Crab Nebula using *Herschel* PACS-IFU and ISO-LWS.

between levels i and j , and c_{ij} is the collisional excitation or de-excitation rate. When the density is much larger than the critical density, collisions dominate and the system can be represented by a Boltzmann population of energy levels.

The 52 and 88 μm fine structure lines of [O III] provide good diagnostic lines for determining electron density, as they have low excitation energies (both much lower than typical nebula temperatures) but different critical densities. This means that there is only a very small temperature dependence but strong density dependence for the ratio of their intensities so that $I_{88 \mu\text{m}}/I_{52 \mu\text{m}}$ ratio is a good diagnostic for the electron density for densities between 10^2 and a few 10^3 cm^{-3} . The energy difference between the fine structure lines and the [O III] optical 5007 Å line means that there is a strong temperature dependence on the ratio of line intensities, so $I_{88 \mu\text{m}}/I_{5007\text{\AA}}$ can be used as a diagnostic for temperature. By measuring the 52 and 88 μm and the 5007 Å [O III] lines the density and temperature of a nebula can be diagnosed.

Using the *Herschel* PACS spectral observations along with archive data from the Infrared Space Observatory Long Wavelength Spectrometer (ISO-LWS) some of the conditions in the nebula have been determined as shown in Table 2.2. A polynomial background is fitted and then integrated line fluxes are measured by fitting a gaussian to each line. The PACS fluxes are from the coadding of all 25 spaxels. A spaxel is a spectral pixel in an integrated field unit (IFU). All of the line fluxes are relative to the 88 μm [O III] line flux. There is an obvious line with the same profile as the μm oxygen line at around 52 μm in the PACS spectra. While this is likely to be the 52 μm [O III] line, the wavelength is below the official PACS wavelength limit and the calibration is poor, so we rely on the ISO-LWS measurements for the 52 μm [O III] line.

Using the 88/52 μm [O III] line ratio, we determined the electron densities to be between $135\text{-}485 \text{ cm}^{-3}$. These values are systematically lower than the electron densities measured using optical [S II] lines by MacAlpine et al. (1996) and from 18.7 and 33.5 μm [S III] lines by Temim et al. (2006), who found values ranging from $830\text{-}1230 \text{ cm}^{-3}$. Sankrit et al. (1998) from observations with the Hubble Space Telescope (HST) found that while the [S II] emission comes from the dense filaments, a lot of the [O III] emission comes

	Coadded LWS	LWS #1	LWS #2	LWS #3	LWS #4	Coadded PACS
[O III] 52 μm	116 ± 9	168 ± 12	109 ± 2	140 ± 9	91 ± 4	(75 ± 4)
[N III] 57 μm	11 ± 2	14 ± 2	5 ± 1	18 ± 4		
[O I] 63 μm	46 ± 2	69 ± 3	39 ± 1	58 ± 2	S 36 ± 2	46 ± 2
[O III] 88 μm	100 ± 10	100 ± 10	100 ± 10	100 ± 10	100 ± 10	100 ± 10
[N II] 122 μm	3.4 ± 0.2	8 ± 1	2.5 ± 0.3	2.9 ± 0.3	2.6 ± 0.3	2.0 ± 0.2
[O I] 146 μm	2.2 ± 0.1	4.0 ± 0.2	1.9 ± 0.1	1.5 ± 0.3	1.9 ± 0.3	2.8 ± 0.2
[C II] 158 μm	7.8 ± 0.3	12.4 ± 0.8	6.9 ± 0.4	12 ± 1	5.9 ± 0.3	9.3 ± 0.5
$F_{(88 \mu\text{m})} (\times 10^{-14} \text{ W m}^{-2})$	14.9 ± 0.4	1.94 ± 0.08	5.9 ± 0.1	2.19 ± 0.05	4.64 ± 0.09	3.6 ± 0.1
$F(52)/F(88)$	1.16 ± 0.09	1.68 ± 0.12	1.1 ± 0.03	1.4 ± 0.09	0.91 ± 0.04	
$N_e(\text{O III}) (\text{cm}^{-3})$	240 ± 30	485 ± 30	220 ± 20	350 ± 30	135 ± 20	
$F(52+88)/F(57)$	18.5 ± 1	18.9 ± 0.7	42.8 ± 3	12.8 ± 1		
O^{2+}/N^{2+}	15.0 ± 0.9	14.4 ± 0.5	35 ± 3	17 ± 1		
$F(122)/F(57)$	0.29 ± 0.05	0.54 ± 0.1	0.51 ± 0.1	0.16 ± 0.04		
N^+/N^{2+}	2.3 ± 0.4	5.3 ± 1	3.9 ± 1	1.4 ± 0.4		

Table 2.2. Crab Nebula far-infrared line fluxes, electron densities and relative ion abundances. Line intensities relative to [O III] $F_{(88 \mu\text{m})}=100$.

from sheaths around the filaments, which is consistent with the lower electron densities determined by using the doubly ionised oxygen emission.

By looking at the ratio of [O III] to [N III] lines we can also determine the ratio of oxygen to nitrogen. This ratio ranges between 10 and 35, showing the Crab Nebula to be very nitrogen poor. MacAlpine & Satterfield (2008) split the Crab Nebula in to three domains, all of which were nitrogen poor having ratios of 7.2, 21 and 260 for each of the domains. All of my measurements are in agreement with domain 2. The 122/57 μm ratio is used to determine the ratio of ionisation states in Nitrogen. Singly ionised Nitrogen is the dominant species with an N^+/N^{2+} ratio of between 2.3 and 5.3.

2.1.2 Velocity Structure

The velocity structure and expansion of supernova remnants can be investigated using the doppler red and blue shifts of atomic line emissions

$$v = \frac{\Delta\lambda}{\lambda} c \quad (2.2)$$

where v is the velocity, λ is the rest wavelength of the observed line and $\Delta\lambda$ is the difference between the observed and rest wavelengths of this line and c is the speed of light. As supernova remnants are expanding both towards and away from us, the line profile is double peaked around the rest wavelength. As infrared lines are not obscured by dust in the supernova remnant we are able to use the far infrared fine structure lines to observe both blue (towards us) and red (away from us) components of these lines. As optical lines may be obscured by dust in the remnant red and blue shifted lines suffer different extinction therefore does not give us a complete picture. Not all lines are double peaked as the material in the supernova remnant is not homogenous, so some regions only contain either the red- or blue-shifted component.

Figure 2.3 shows the 25 spaxels PACS-IFU of the Crab Nebula (see Table 2.1) plotted in velocity space. The 88 μm [O III] line is in black, the 63 μm [O I] line is in red and the 158 μm [C II] line is in green. A table of fluxes and velocities for each of these lines can be found in Appendix A.

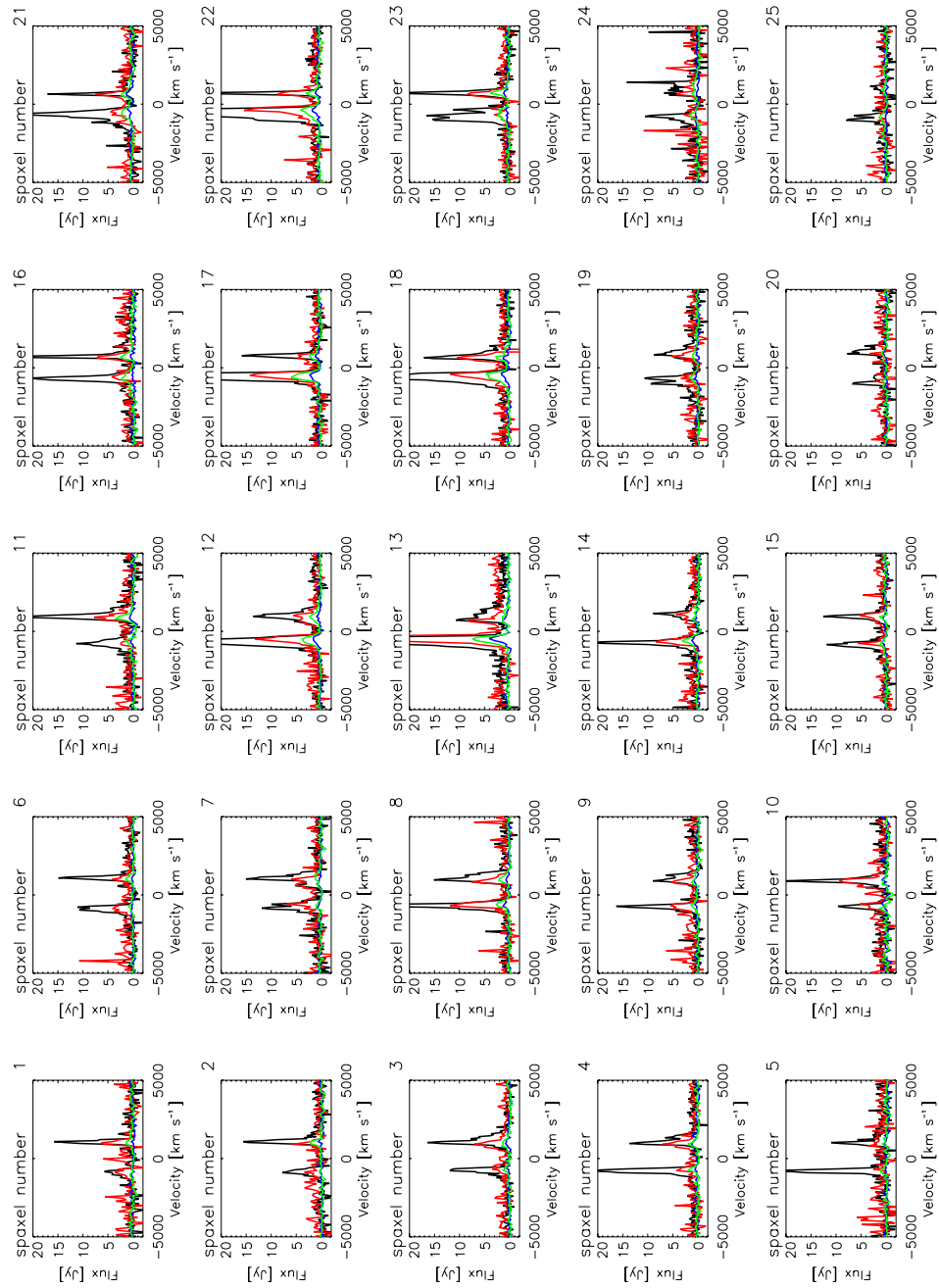


Figure 2.3. The 25 individual PACS spaxels plotted in velocity space. The $88 \mu\text{m} [\text{O III}]$ line is in black, the $63 \mu\text{m} [\text{O I}]$ line is in red and the $158 \mu\text{m} [\text{C II}]$ line is in green.

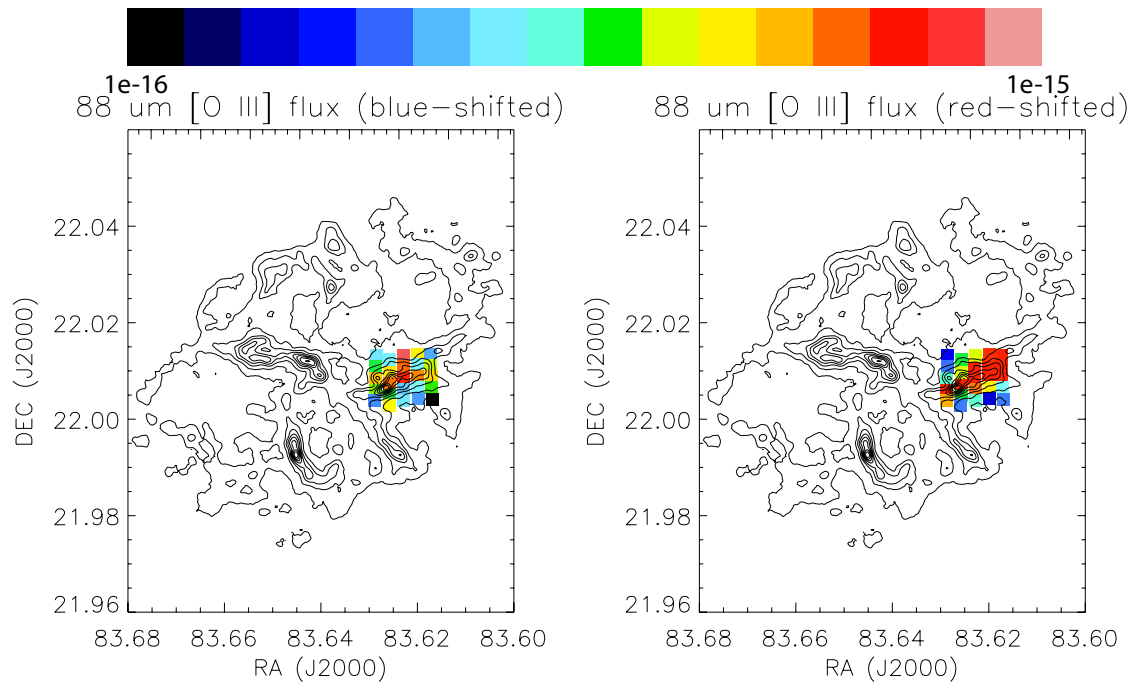


Figure 2.4. A brightness map of the blue and red shifted emission components of the $88 \mu\text{m}$ $[\text{O III}]$ line for each PACS-IFU spaxel, plotted over the PACS $70 \mu\text{m}$ map plotted as a contour plot.

Instrument	Date	Time	RA	DEC	TDT/ObsID	Time
SPIRE-FTS	2011-08-22	19:55:15	05h 34m 29.47s	$22^\circ 00' 31.48''$	1342204022	3476s

Table 2.3. Details of the *Herschel* SPIRE-FTS observation of the Crab Nebula.

Figures 2.4, 2.5 and 2.6 show the fluxes of the individual spaxels of the PACS-IFU observations of the central knot of the Crab Nebula plotted on $70 \mu\text{m}$ PACS contour plots. Whilst stronger in the regions where the $70 \mu\text{m}$ emission is brightest (and thus the dustiest region), the $88 \mu\text{m}$ $[\text{O III}]$ comes from all over the observed region. The $63 \mu\text{m}$ $[\text{O I}]$ and $158 \mu\text{m}$ $[\text{C II}]$ emissions are coincident only with the brightest dustiest regions of the observation.

2.2 The Crab Nebula with SPIRE-FTS

A single observation of the Crab Nebula was made using the *Herschel* SPIRE-FTS by the MESS collaboration. Figure 2.7 shows the positions of the SPIRE-FTS spectra of the Crab Nebula on a PACS $70 \mu\text{m}$ image, while Table 2.3 gives details of the observations.

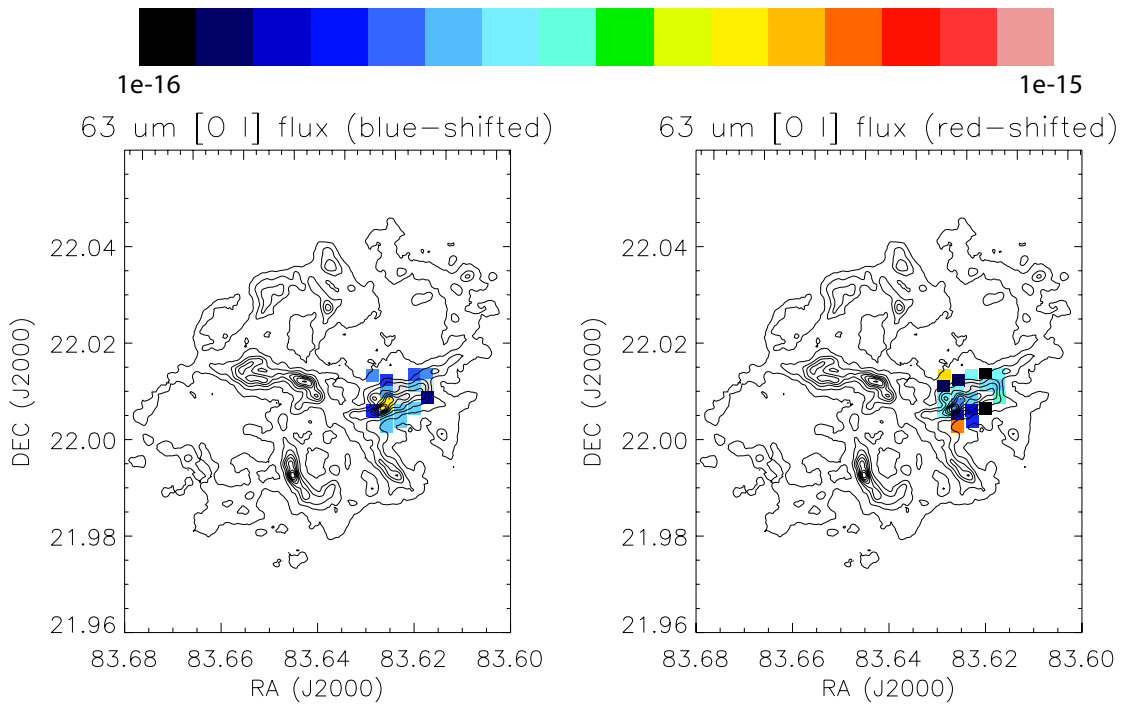


Figure 2.5. A brightness map of the blue and red shifted emission of the 63 μm $[\text{O I}]$ line for each PACS-IFU spaxel, plotted over the PACS 70 μm map plotted as a contour plot.

2.2.1 Unidentified Lines

The SPIRE-FTS spectra of the Crab Nebula were largely free of emission. None of the carbon monoxide lines often observed in these wavelengths were detected. The only lines observed were red and blue shifted $J=2-1$, $F=5/2-3/1$ OH^+ line emission at 971.8038 GHz, observed in the overlap region between the SSW and SLW spectra, plus two previously unidentified lines, one at 618 GHz in the SLW spectra, and one at 1235 GHz in the SSW spectra. Unusually for unidentified lines, it is the strongest line in the spectra, examples of which is shown in Figures 2.8 (SLW) and 2.9 (SSW). Figure 2.7 shows positions of the SPIRE-FTS spectra of the Crab Nebula are taken on a PACS 70 μm image. The SSW detectors are shown in green while the SLW detectors are shown in white. The positions with crosses are those in which an unidentified line has been detected. The bright knots in the 70 μm image are from the dust emission, showing that these unidentified lines are mostly coincident with the dust.

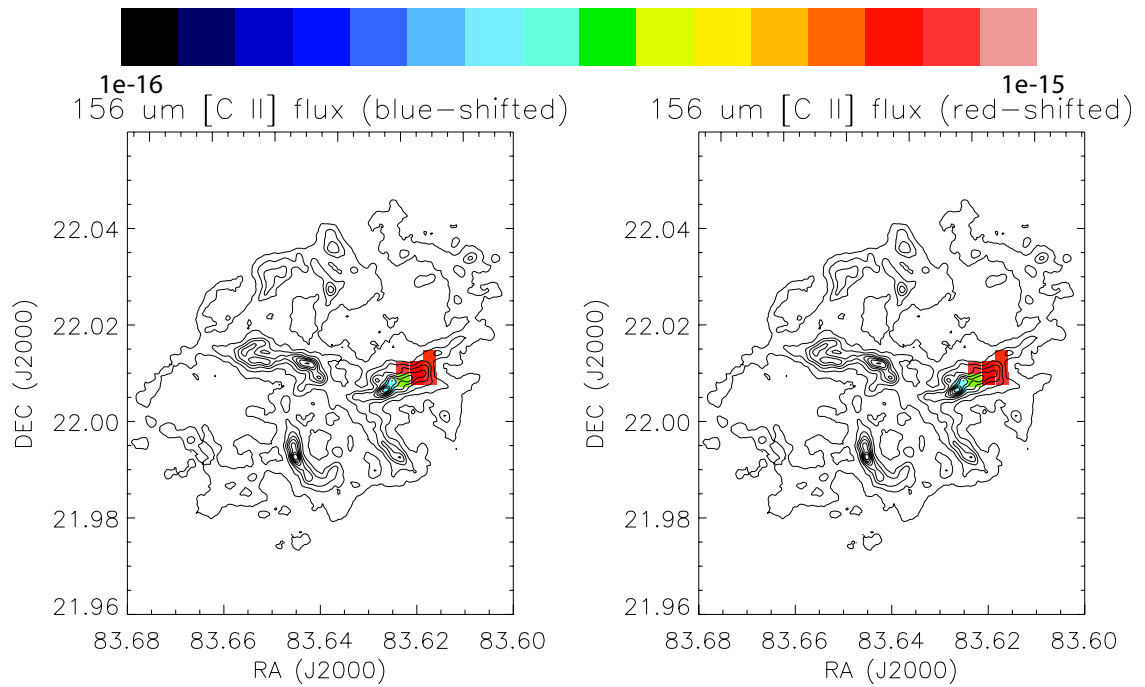


Figure 2.6. A brightness map of the blue and red shifted emission of the 158 μm [C II] line for each PACS-IFU spaxel, plotted over the PACS 70 μm map plotted as a contour plot. Note the scale is an order of magnitude less than the plots for the [O I] and [O III] maps.

2.2.2 Identifying the Line

The knots and filaments in the Crab Nebula exhibit a wide range of expansion velocities (Hester 2008). To determine a rest frequency for the unidentified line emission, velocity measurements of the OH⁺ line were taken for each of the spectra. These ranged between -603 and 1037 km s⁻¹, consistent with the wide range of velocities exhibited by the knots in the Crab. In the four SLW spectra in which the 618 GHz and OH⁺ lines are both present a rest frequency of 617.554 ± 0.209 GHz was determined for the unidentified line. In the five SSW spectra in which the 1235 GHz line and the OH⁺ line are present a mean rest frequency of 1234.768 ± 0.643 GHz was determined.

The ratio of these two frequencies gives a value of 1.9995 ± 0.0012 , a 2:1 ratio most likely imply the J=1-0 and J=2-1 transitions of a molecule containing two atoms. After an extensive search of the Cologne Molecular Database for Spectroscopy (Muller et al. 2005), the only candidate was discovered to be the 36-Argon Hydride cat-ion, $^{36}\text{ArH}^+$ (Barlow et al. 2013). This is the first detection of a molecule containing a noble gas in space. A search in the PACS-IFU spectra of the Crab Nebula (Section 2.2.6) failed to find higher

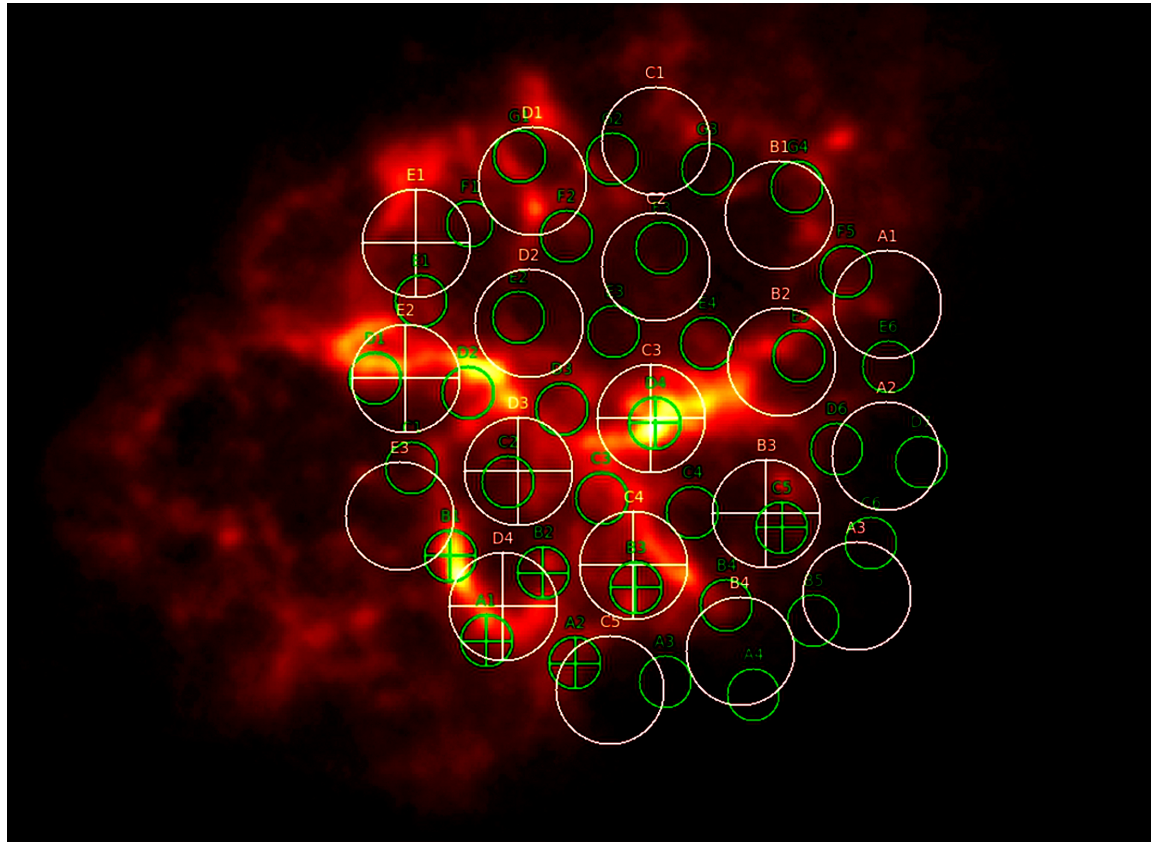


Figure 2.7. The SPIRE-FTS detectors for the Crab Nebula observations shown on a $70 \mu\text{m}$ PACS broadband image. Green circles are the SSW detectors, white circles are the SLW detectors. Circles with a cross denote the detectors in which the unidentified lines were observed.

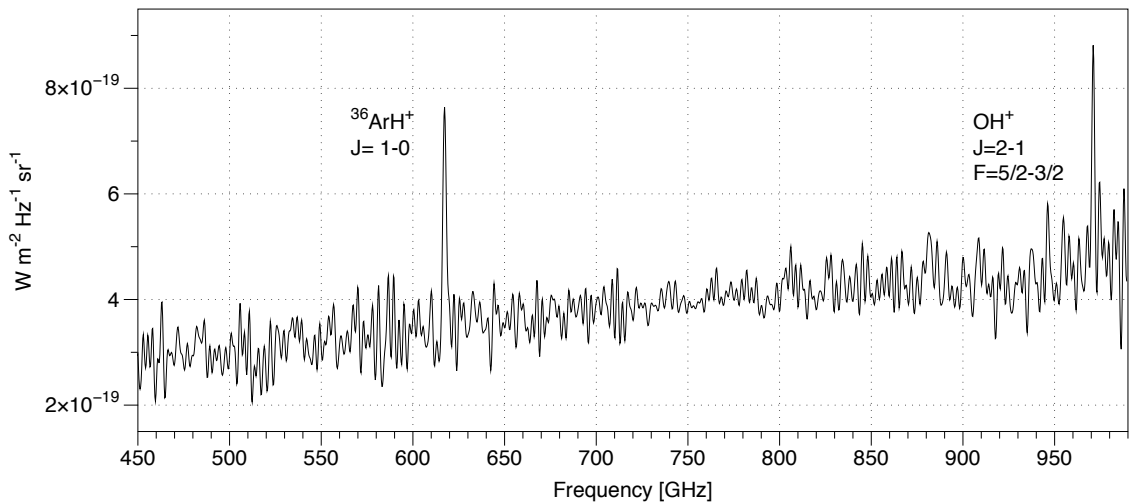


Figure 2.8. SLW D4 spectrum showing one of the initially unidentified lines at 618 GHz.

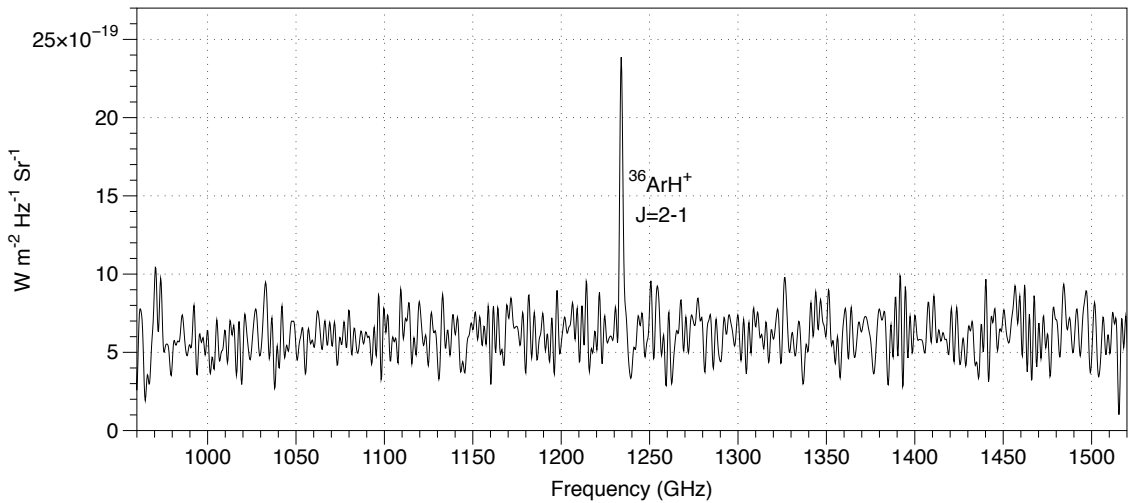


Figure 2.9. SSW B1 spectrum showing one of the initially unidentified lines at 1235 GHz.

J rotational transitions of ArH^+ , or any other noble gas hydride ions, such as the much searched for HeH^+ far infrared lines (Liu et al. 1997; Moorhead et al. 1988).

2.2.3 ArH⁺ Line Fluxes

Table 2.4 shows the observed surface brightness and velocities in each of the *Herschel* SPIRE-FTS detectors in which the $J = 1-0$ 617.525 GHz (SLW) and $J = 2-1$ 1234.603 GHz (SSW) $^{36}\text{ArH}^+$ lines are observed. Detectors which are spatially coincident with one another is SLW and SSW are listed next to each other.

2.2.4 Formation and Destruction Mechanisms for ArH⁺

Argon is a noble gas; it has a full outer shell of electrons and in its atomic state is highly unreactive. When ionised it is as reactive as any other species without a full outer shell of electrons. The Crab Nebula is predominantly gas that has been ionised by synchrotron radiation from the pulsar wind Hester (2008). It also contains a large number of clumps of very cold, neutral H₂ (Loh et al. 2011) (Figure 2.10 shows the location of all the Loh et al. (2011) H₂ knots on the *Herschel* PACS 70 μm image). There will be transition zones between these two regions where partially ionised argon can react with molecular hydrogen to form ArH⁺.



SLW Detector	Radial Velocity km s ⁻¹	Surface Brightness 10 ⁻¹⁰ W m ⁻¹ Sr ⁻¹	SSW Detector	Radial Velocity km s ⁻¹	Surface Brightness 10 ⁻¹⁰ W m ⁻¹ Sr ⁻¹
B3	+317 ± 67	2.23 ± 0.41	C5	-1354 ± 26	8.2 ± 1.2
C3	+933 ± 33	4.63 ± 0.40	D4	+743 ± 26	11.7 ± 1.6
C4	-58 ± 50	8.65 ± 0.55	B3	-101 ± 20	17.5 ± 1.4
D3	+826 ± 32	3.13 ± 0.34			
D3	-709 ± 42	2.30 ± 0.34	A1	-51 ± 52	13.9 ± 2.0
D4	+101 ± 27	0.89 ± 0.52	B2	-572 ± 25	10.8 ± 1.7
			B1	+140 ± 34	38.4 ± 1.6
			A2	+61 ± 28	10.1 ± 1.4
E1	+278 ± 46	5.69 ± 0.62			
E2	-594 ± 37	4.25 ± 0.46			

Table 2.4. SPIRE-FTS radial velocity and line surface brightness measurements for the J = 1-0 and 2-1 rotational lines of $^{36}\text{ArH}^+$ from the Crab Nebula. The table is laid out so that SLW and SSW detectors that correspond to one another spatially are next to each other.

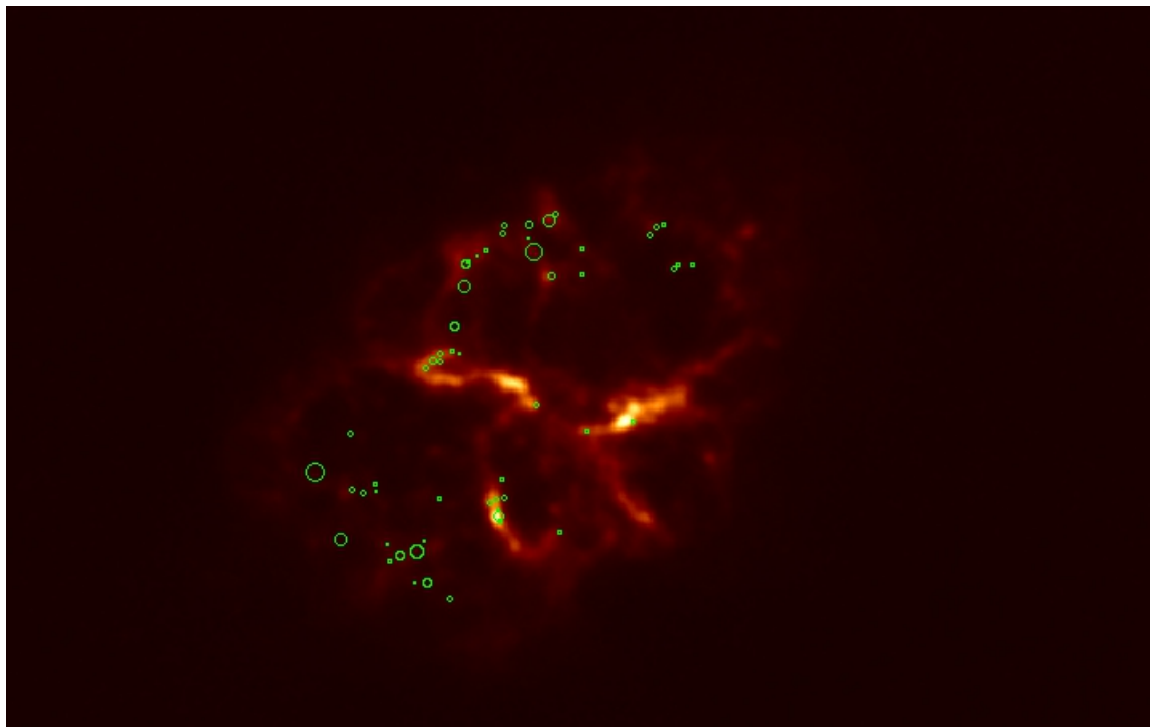


Figure 2.10. A *Herschel* PACS 70 μm image with the size and locations of the Loh et al. (2011) H_2 knots shown as green circles.

This is an endothermic reaction that releases 1.49 eV of energy (Roach & Kuntz 1970). This is because the ionisation potential of atomic argon is less than the ionisation potential of hydrogen and the dissociation energy of H_2 . This makes the charge exchange between the two very unlikely meaning that the formation of ArH^+ is the favoured reaction.

Another formation pathway which can occur in similar regions is the interaction between neutral argon and H_3^+



ArH^+ has unusually small rates for photodissociation and dissociative recombination ($\text{ArH}^+ + \text{e} \rightarrow \text{Ar} + \text{H}$) (Roueff et al. 2014). This means it is more stable than most molecules in the ISM and more likely to survive than other noble gas-containing molecules such as HeH^+ and NeH^+ .

2.2.5 Argon Nucleosynthesis

On earth the most abundant isotope of argon is ^{40}Ar (99.6%) with only 0.34% of it being the observed isotope ^{36}Ar . The ^{40}Ar is not a product of supernova or stellar nucleosynthesis, but a product of electron capture or positron emission from ^{40}K in rocks



^{40}K also decays to ^{40}Ca via β -decay.

^{36}Ar is the product of a chain of α capture reactions in supernovae and the cores of highly evolved stars (Arnett 1996). Starting with ^{12}C (which itself is formed in the triple- α process, where 3 helium nuclei fuse forming a resonant state of carbon), multiple reactions between nuclei and α particles fuse to form heavier nuclei.



In the cores of stars this process takes place before the silicon-silicon fusing stage and can continue on to ^{56}Ni before core collapse occurs. In core collapse supernovae this process can continue as far as ^{208}Pb . When ^{208}Pb captures another α particle, it becomes ^{212}Po , which has a half life of 299 nanoseconds to α -decay back to ^{208}Pb .

In general it is not possible to determine isotope ratios for atomic species via optical astronomical spectroscopy as the difference in wavelength between lines of different atomic transitions are unresolvable astronomically, so using molecular rotational spectroscopy of different isotopes provides a way to investigate nucleosynthesis.

2.2.6 The search for ArH⁺ with PACS

The next line in the rotation ladder of $^{36}\text{ArH}^+$ is the J=3-2 line which has a wavelength of $161.98\ \mu\text{m}$. This is in the wavelength range of the PACS-IFU. Figure 2.11 shows the PACS spaxels with the spectral region covering the J=3-2 rotational line of $^{36}\text{ArH}^+$.

There are no line detections above the noise in the spectra, however we can use the noise levels to set an upper limit on line detections. Taking a standard deviation of the signal per resolution element and multiplying by the number of bins per resolution element we find that a 3σ upper limit for the flux density of the J=3-2 $^{36}\text{ArH}^+$ to be $7.7 \times 10^{-18}\ \text{Wm}^{-2}$.

2.2.7 Temperature

The PACS-IFU observations are coincident with the SPIRE-FTS SLW-C3 and SSW-D4 detectors. This means we have two points and can construct a rotation diagram to estimate the temperature of the molecule as discussed in Section 1.11. Figure 2.12 shows the rotation diagram for these observations from the slope, the rotation temperature of the $^{36}\text{ArH}^+$ is $T_{rot} = 24 \pm 8\ \text{K}$. The uncertainty in the temperature is determined from the uncertainty in the slope fitting.

2.3 Follow-up with IRTF CSHELL AND VLT-CRIRES

Complementary observations using the NASA-IRTF CSHELL for H₂ 2.122 μm line emission and ArH⁺ and HeH⁺ near infrared spectroscopy using VLT-CRIRES have been made to follow up this discovery.

2.3.1 IRTF CSHELL observations of H₂ 2.122 μm line.

Loh et al. (2011) carried out a low resolution spectroscopic imaging survey of the Crab Nebula at 2.122 micron to map the regions with molecular hydrogen (H₂). Surveying two thirds of the visible nebula, they were able to identify 55 H₂ knots, sitting in the strongly associated with compact regions of low-ionisation gas. In Loh et al. (2012) present follow up observations with higher spectral resolution observations of some of these knots, but still not high enough to accurately resolve the widths of these lines. Measuring these line widths and velocities will give an idea as to the line widths of ArH⁺ lines in similar

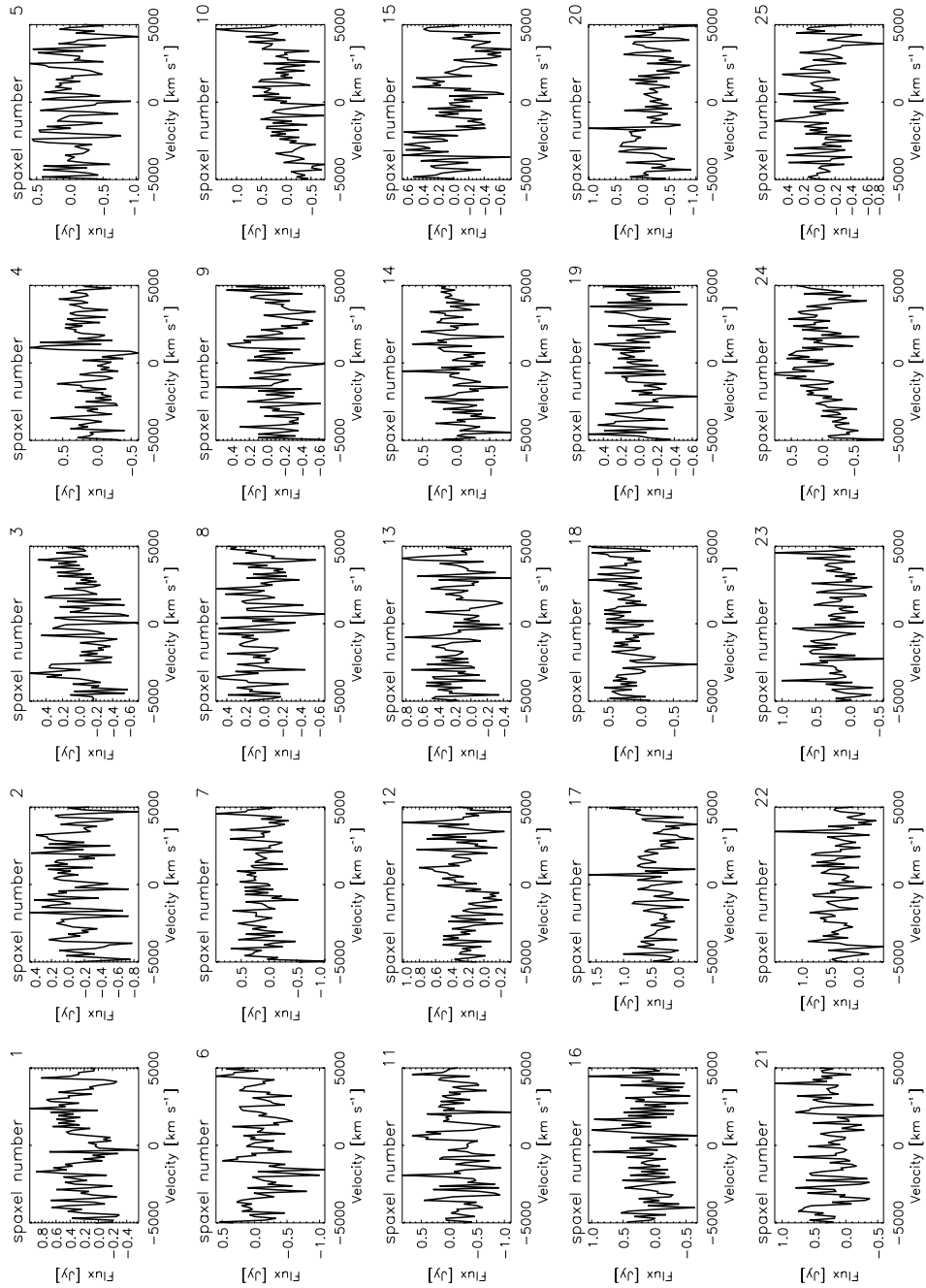


Figure 2.11. PACS-IFU observations of the region of the J=3-2 161.98 μm ${}^{36}\text{ArH}^+$ line.

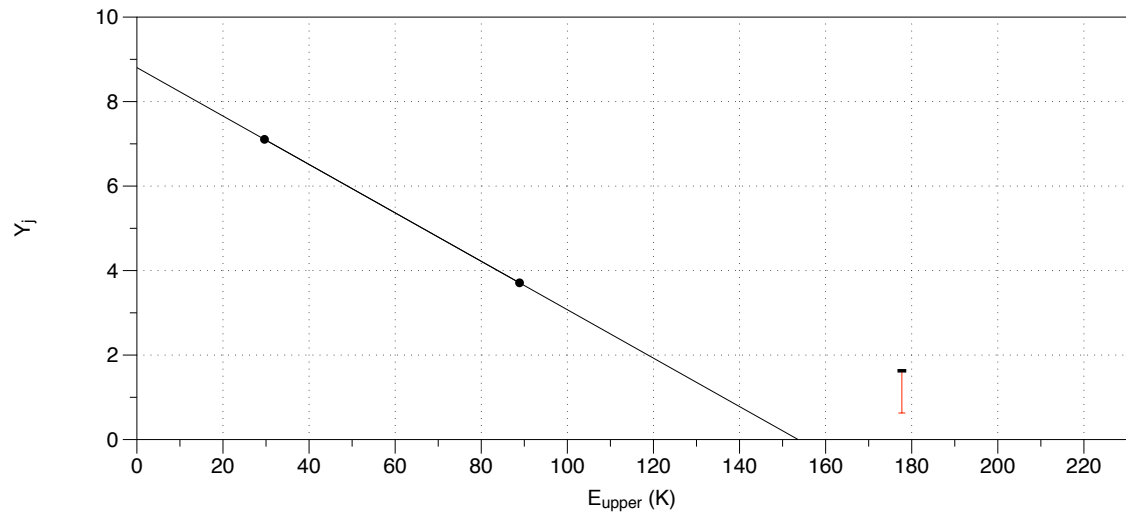


Figure 2.12. The rotation diagram used to determine the temperature of $^{36}\text{ArH}^+$ in the SLW-C3 SSW D4 and PACS-IFU observations

wavelengths range which will be useful in their identification.

The NASA IRTF is a 3 metre telescope on Mauna Kea in Hawaii, optimised for observations in the infrared. One of its instruments, CSHELL is a 1-5.5 μm echelle spectrograph with a resolving power of up to 30,000. This wavelength range contains the first ro-vibrational 1-0 S(1) line of H_2 at 2.122 μm . It has high enough resolution to get the line width data needed to more accurately place upper limits on the line fluxes of the ArH^+ and HeH^+ lines in the VLT-CRIRES spectra later in this chapter.

2.3.2 Observations of H_2 knots

Observations of knots 1 and 2 from Loh et al. (2011) were made using the CSHELL on the IRTF on 17th of November 2014. As CSHELL slit is 30" long, it can be used to observe both knots at the same time. The observation is made up of 120 exposures of 50 seconds each, half of which are on source, half of which are off the nebula. Argon and Krypton lamp lines are used for wavelength calibration and an observation of star HD 1791 was taken for flux calibration. These observations were made by me at the telescope.

2.3.3 CSHELL Data Reduction

The data were coadded by taking each pair of on and off source exposures and subtracting one from the other. This removes the sky lines and other line of sight artefacts. Each of the frames is then run through the same algorithm described in Section 2.4.2 to remove glitches such as those caused by cosmic rays. Each of these frames is then added together, and the cosmic ray algorithm is run again on each flux bin for extra cleaning. Figure 2.13 shows the position and spectral information from the observations after de-gltching, co-adding and cosmic ray removal. The two knots are clearly visible in the upper right quadrant of the observation.

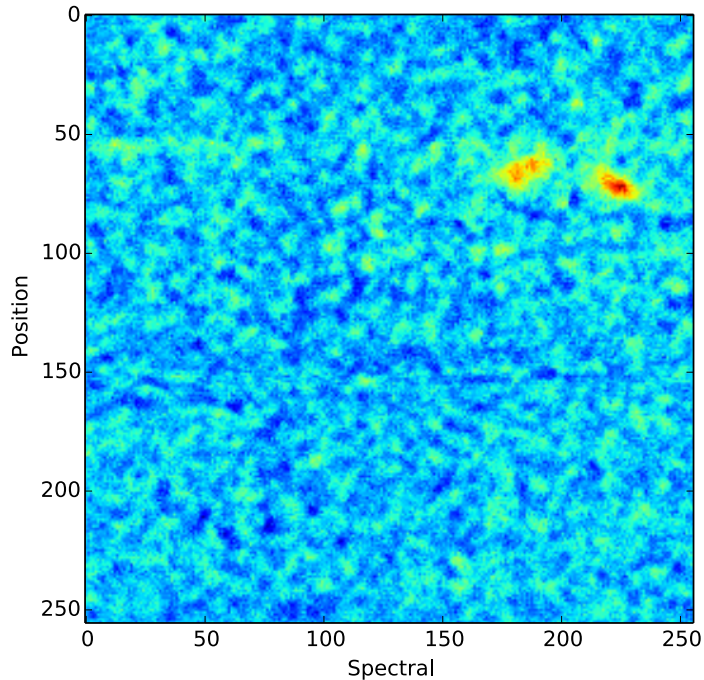


Figure 2.13. The CSHELL spectral image - position vs wavelength plot for Loh et al. (2011) knots 1 and 2 taken by the IRTF.

IRTF data sometimes needs to be offset by an angle to compensate for the slit position. To find out if this needed to be done, we look at the observation of HD 1791. Figure 2.14 shows the position vs spectral plot of the HD 1791 observation after it had undergone the same reduction process as the observation of the Crab knots.

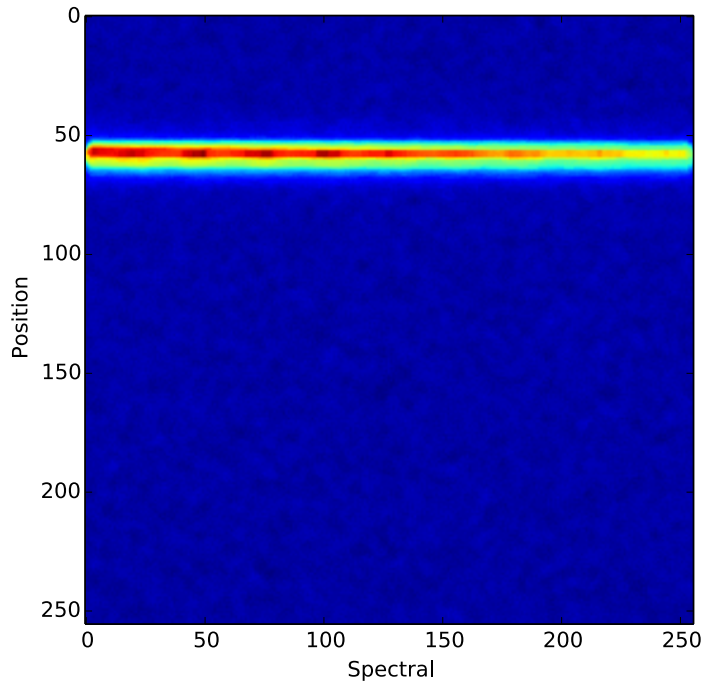


Figure 2.14. The position wavelength plot star HD 1791

IRTF spectra are sometimes rotated. This needs to be compensated for. By taking cuts at each end of the spectrum and fitting a gaussian to compare where the continuum centroid is at each end of the spectrum we can see if a rotation correction needs to be applied to my data. Figure 2.15 shows these cuts with the short wavelength end shown in blue and the long wavelength end of the spectrum shown in green. Fitting a Gaussian to these, the centres are at pixels 57.45 and 58.06 respectively, so no offset needed to be applied.

To extract the final spectrum, all the position rows in which the two knots are observed are added together. Wavelength calibration is then carried out based on the Ar and Kr lamp lines and the wavelength is translated in to velocity space. Figure 2.16 shows the extracted spectrum of the two knots.

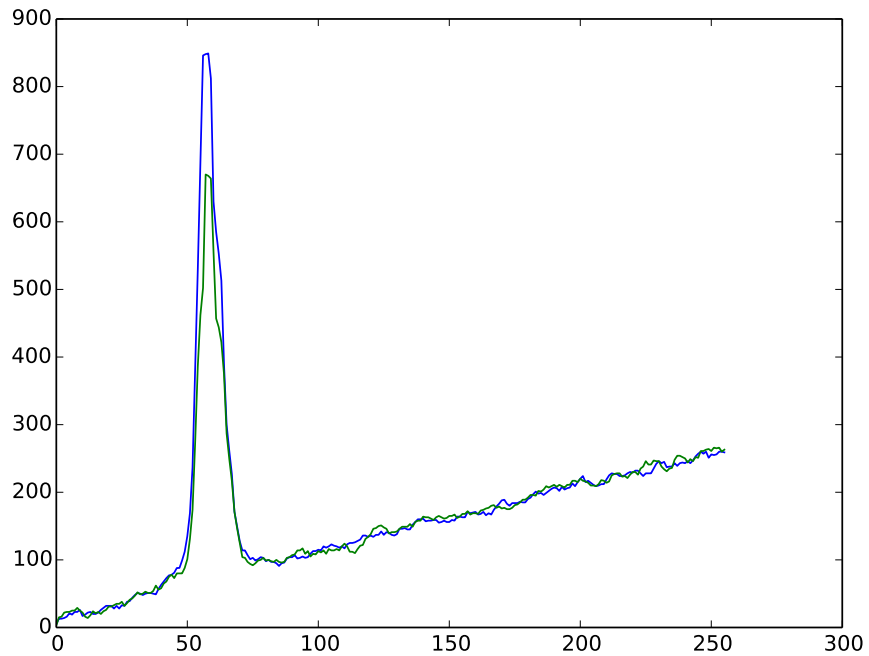


Figure 2.15. The cuts made perpendicular to the spectral direction for the observation of HD 1791 to investigate the need for rotational correction in the angle of the observations of the Crab knots. The cut through the short wavelength end shown in blue and the cut through the long wavelength end of the spectrum shown in green.

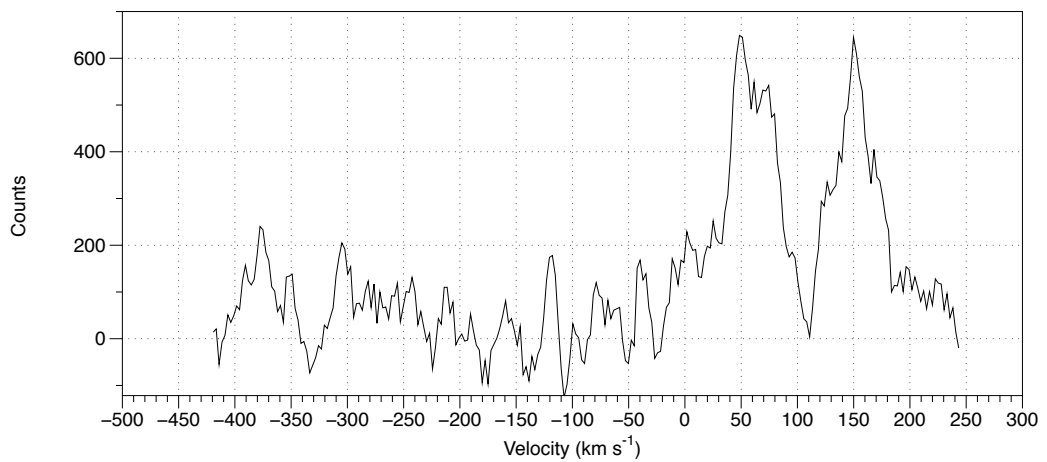


Figure 2.16. The extracted spectrum for Loh et al. (2011) knots 1 and 2 of the Crab Nebula in radial velocity units of km s^{-1} .

2.3.4 H₂ Line Width Results

The spectrum of knots 1 and 2 can be fitted with gaussians to estimate the full width half maximum (FWHM) of the lines. The lower velocity knot has two peaks, so should be fitted with 2 Gaussians. Figure 2.17 shows the spectrum fitted with one gaussian, with the results shown in Table 2.5. The fit for using three gaussians on the shorter wavelength knot are shown in Figure 2.18, with the results in Table 2.6.

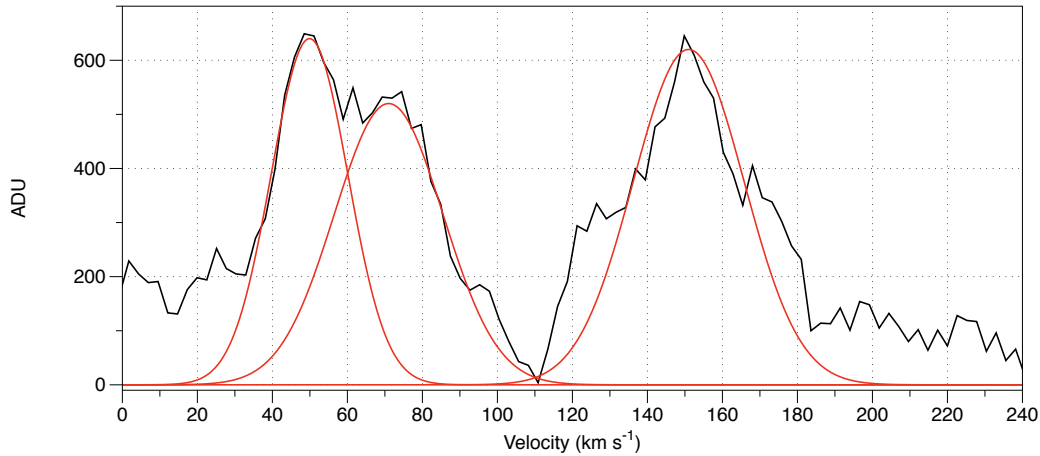


Figure 2.17. The extracted spectrum of the Loh et al. (2011) knots 1 and 2 of the Crab Nebula in velocity units with the gaussians fitted to determine the central velocity and line width using two gaussians for one knot and one for the other. There is no baseline as the central region between the two knots goes to zero.

Centre km s ⁻¹	Centre Err km s ⁻¹	FWHM km s ⁻¹	FWHM Err km s ⁻¹
58.6	0.8	51.2	2.2
150.2	0.8	44.6	2.0

Table 2.5. The velocity and line widths of the Loh et al. (2011) knots 1 and 2 in the Crab Nebula, by fitting one gaussian to each line as shown in 2.17.

2.4 VLT-CRIRES observations of ArH⁺ and HeH⁺

Due to the current lack of a sensitive far infrared observatory since the end of the *Herschel* mission; immediate follow up of the detection using these lines was not possible (although an ALMA proposal (PI:Swinyard) has been accepted to investigate the ratio of ³⁶Ar to

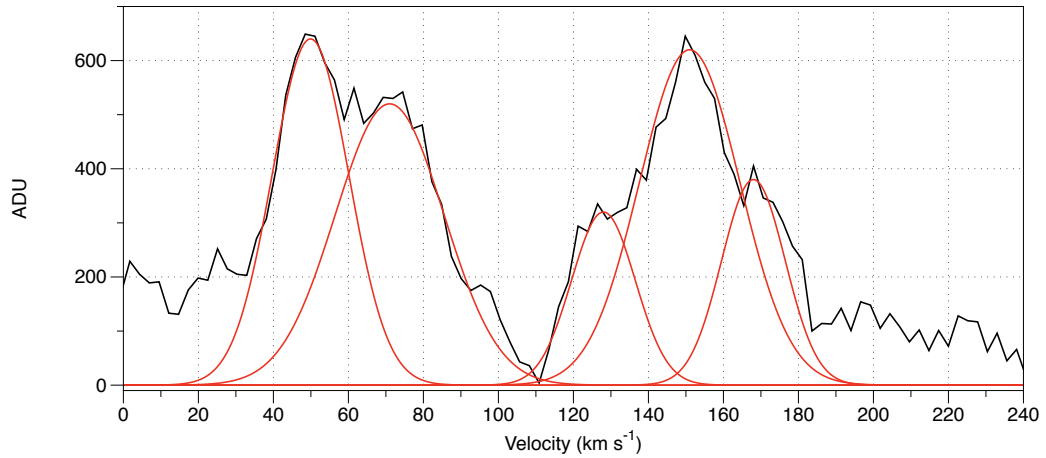


Figure 2.18. The extracted spectrum of the Loh et al. (2011) knots 1 and 2 of the Crab Nebula in velocity units with the gaussians fitted to determine the central velocity and line width using two gaussians to the slower/shorter wavelength knot and three gaussian to the faster/longer wavelength knot. There is no baseline as the central region between the two knots goes to zero

Centre km s ⁻¹	Centre Err km s ⁻¹	FWHM km s ⁻¹	FWHM Err km s ⁻¹
51.7	0.6	28.7	1.9
71.1	0.5	29.6	1.3
125.8	0.8	14.4	2.3
152.0	0.9	36.9	2.3
169.4	0.9	20.1	2.0

Table 2.6. The velocity and line widths of the Loh et al. (2011) knots 1 and 2 in the Crab Nebula, by fitting two gaussians to the slower/shorter wavelength knot and 3 gaussians to the faster/longer wavelength knot as shown in Figure 2.18.

^{38}Ar). However there are also several ro-vibrational lines of ArH^+ (Cueto et al. 2014), as well as several HeH^+ lines in the near infrared.

HeH^+ has been hypothesised to be the first molecule to form in the early universe (Lepp et al. 2002); however it has up to now never been detected in space (Persson et al. 2010). Given the conditions to form ArH^+ are similar to those required to form HeH^+ and that there is a high helium abundance in the Crab Nebula it is suggested that it might also be present in similar reasons to ArH^+ . Previous searches have been based around it's hypothesised formation in planetary nebulae (Roberge & Dalgarno 1982), which have also

not been successful (Liu et al. 1997; Moorhead et al. 1988).

During certain times of the year, the Crab Nebula is observable from telescopes in the southern hemisphere. The European Southern Observatorys (ESO) Very Large Telescope (VLT) CRIRES (CRyogenic InfraRed Echelle Spectrograph) instrument is a very high resolution spectrograph covering the near infrared wavelengths from 0.95-5.2 μm with a resolving power of up to 100,000, a slit width of 0.2" or 0.4" and a length of 40". 4 hours of Directors Discretionary Time (DDT) were granted for these observations. I was heavily involved in the planning, application and execution of these observations.

2.4.1 The VLT-CRIRES Observations

Assuming that $^{36}\text{ArH}^+$ is coincident with the regions of H_2 we took spectra of the brightest H_2 knot in the nebula, knot 1 of Loh et al. (2011), which is also coincident with the strongest detections of $^{36}\text{ArH}^+$ (shown in Figure 2.19, the magenta circle shows the location of the Loh et al. (2011) knot 1 while the green circles show nearby detections of $^{36}\text{ArH}^+$ with SPIRE SLW and the blue circle shows the detections with SPIRE SSW).

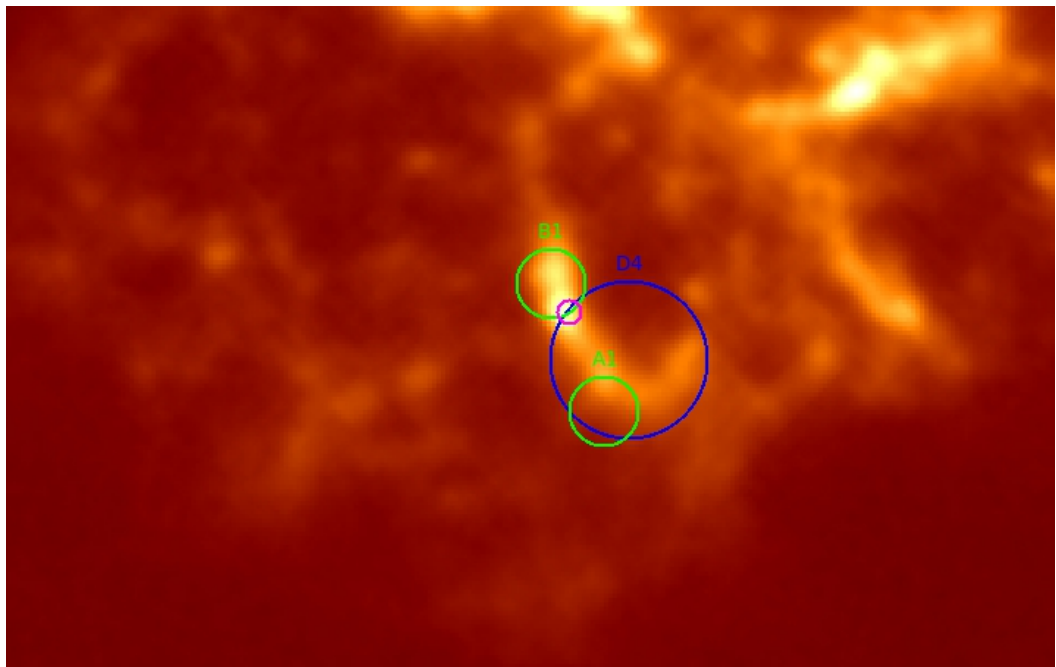


Figure 2.19. The location of the Loh et al. (2011) knot 1 (magenta circle) and nearby *Herschel* SPIRE-FTS detectors that detected $^{36}\text{ArH}^+$ (the two green circles are the SSW detectors, the blue circle is the SLW detector).

Figure 2.20 shows the finding chart for the knot. There is some ambiguity in its location, with the 2MASS 2^mm image and the information from Loh et al. (2011) (marked by a green circle) not agreeing. The slit of the spectrograph was positioned so as the knot would be observed whichever of the two was correct.

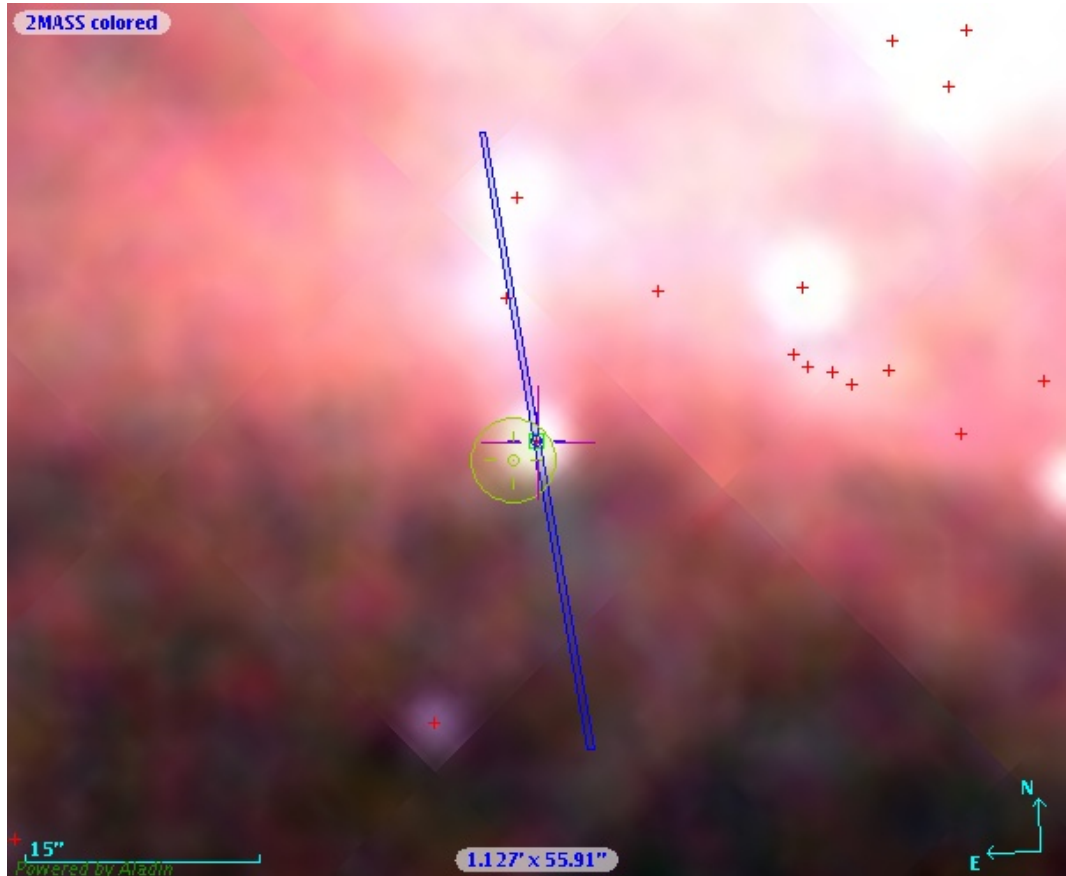


Figure 2.20. Finding chart for the VLT observations showing the slit position of the CRIRES spectrometer in blue on the 2MASS catalogue image of the Crab Nebula. The Loh et al. (2011) knot 1 position is shown as a green circle. the red crosses are the locations of objects in the 2MASS catalogue

The two strongest expected vibration-rotation lines of $^{36}\text{ArH}^+$ are at 3827.75 nm ($v=1-0$, $J=1-0$) and at 3799.99 nm ($v=1-0$, $J=2-1$) (Cueto et al. 2014). The measured radial velocities of both H₂ knot 1 in Loh et al. (2011) and from the $^{36}\text{ArH}^+$ observations in this region are both $+140 \text{ km s}^{-1}$. This would shift these lines to 3829.40 nm and 3801.63 nm respectively. One observation of 65 minutes was made to observe both these lines, 40 minutes of which was on the source. ι Tau was used as a telluric standard and for flux calibration it was adopted to have an effective temperature of 7500 K and a K-band

magnitude of +4.25.

In addition to searching for $^{36}\text{ArH}^+$ lines, we also targeted the R(0) and R(1) lines of HeH⁺. These lines have rest wavelengths of 3364.09 nm and 3302.10 nm respectively which would shift to 3365.66 nm and 3303.64 nm. These lines are free from atmospheric line contamination but are far enough apart that they need to be observed separately. Each line was observed for one hour and five minutes including all required overheads. The same telluric standard is used for corrections for the HeH⁺ lines as for the $^{36}\text{ArH}^+$ observations.

The observations were made in hour-long blocks. The HeH⁺ R(1) line observations were taken on the 3rd of February 2014 while the ArH⁺ and HeH⁺ R(0) line observations were made on the 11th of February 2014. Information on the Crab Nebula science observations can be found in Table 2.7.

Line	OB ID	Date	Exposure Time (s)	Air Mass
HeH ⁺ R(1)	1047046	2 / 3-Feb-2014	1950.000	1.549
ArH ⁺	1047031	10 / 11-Feb-2014	2400.000	1.454
HeH ⁺ R(0)	1047039	10 / 11-Feb-2014	2400.000	1.536

Table 2.7. Information about the VLT-CRIRES observations of the Crab Nebula ArH⁺ and HeH⁺.

Figure 2.21 shows all of the targeting images of these observations with the slit of the spectrograph over-plotted showing that they are all on target. The black line down the centre of the image is the position of the slit, the very bright region at the very centre of the slit is the bright knot.

2.4.2 CRIRES Data Reduction

The raw CRIRES spectra were first cleaned of cosmic rays. This was done using a median filtering technique, a process which involves replacing each pixel in the data file with the median of its neighbouring pixels. This removes any individual large spikes in a single pixel which will have been caused by a cosmic ray. The before and after processing image is shown in Figures 2.22 and 2.23. The vastly increased contrast in the image after processing is down to the cosmic ray hits being so much brighter than any of the actual

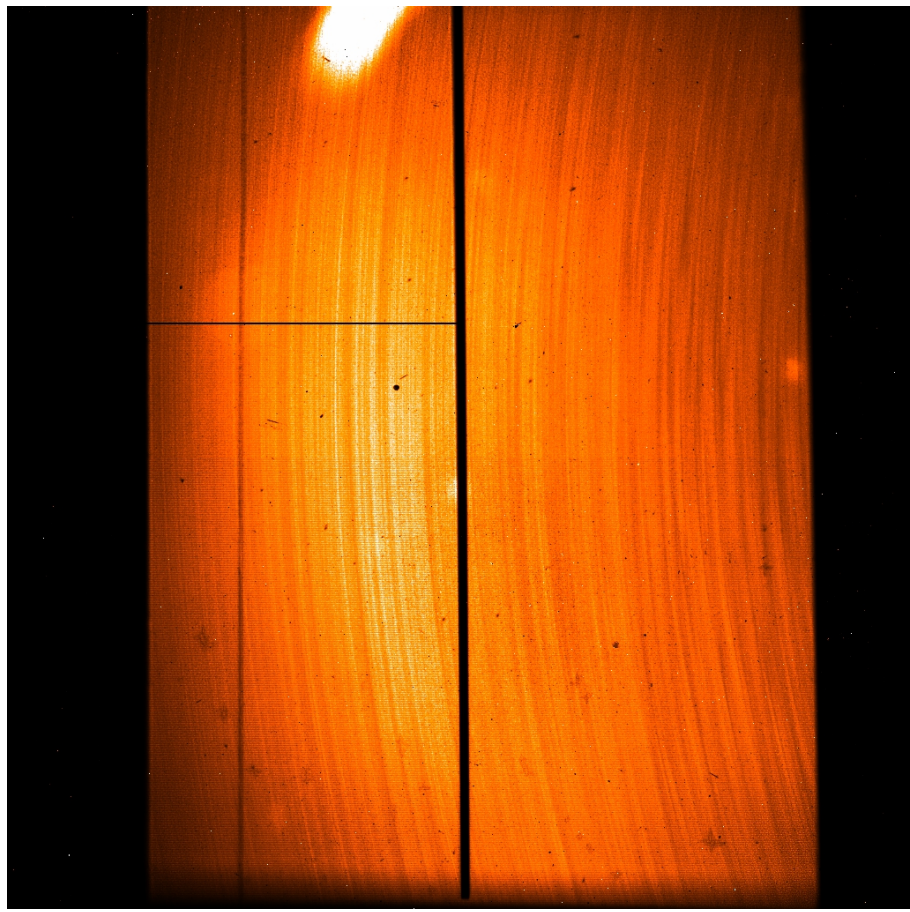


Figure 2.21. The targeting of the VLT showing the spectrograph slit over the central knots. The black line in the centre of the image is the slit, with the edges of the knot being region the bright which points at the side of the centre of the slit.

observational data.

The next step in the reduction of the data is to remove the emission contribution from the Earth's atmosphere. ESO provides an exposure time calculator tool (ETC) which provides very accurate models of the sky for a given observation angle, air mass and percentage of water vapour for the VLT. These sky lines can be used for both subtraction of the sky emission spectrum and wavelength calibration. Figure 2.24 shows the observed spectrum taken from the 8 central spatial pixels of the spectrograph (blue) and the sky model normalised to it (green), showing that the two do not line up exactly. The difference between them is also not constant across the detector array so the sky lines bracketing the region of interest are used to calibrate that region of the spectrum accurately.

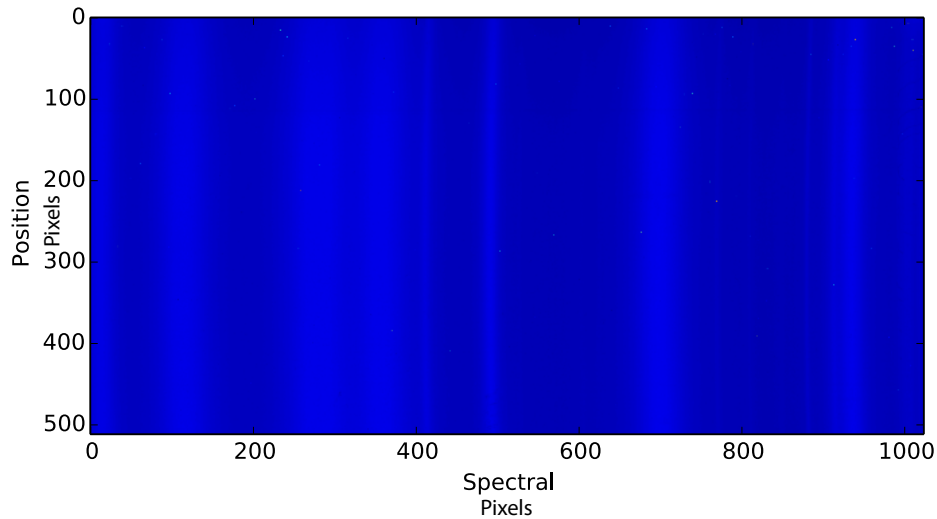


Figure 2.22. The raw spectral data from CRIRES observations of the Crab Nebula before any processing has taken place

The spectra are in units of counts of the analogue to digital converter (ADU) so need to be translated in to a flux unit. At the time that each observation was made an observation was also made of a star of known brightness and temperature which means that its flux distribution can be used to convert from detector counts to units of flux. In this case the star ι Tau is used. It is a A7V star with $T_{eff} = 7500$ K. It has an K-band magnitude of +4.25. The K-band wavelength is $2.19 \mu\text{m}$ and the zero magnitude point corresponds to $2.26 \times 10^{-8} \text{ W m}^{-2} \mu\text{m}^{-1}$. A blackbody spectrum was generated with this temperature and then normalised to the K-band flux. Figure 2.25 shows this normalised blackbody curve with the normalisation point shown as a green dot.

I then take the observed spectrum of ι Tau in ADU, which has been reduced in the same way as the Crab Nebula spectra, and divide it by this model flux distribution. This gives the Relative Spectral Response Function (RSRF) in $\text{ADU W}^{-1} \text{ m}^2 \mu\text{m}$. I can now use this to flux calibrate the Crab Nebula spectra. This is done by dividing the observed spectrum by the RSRF.

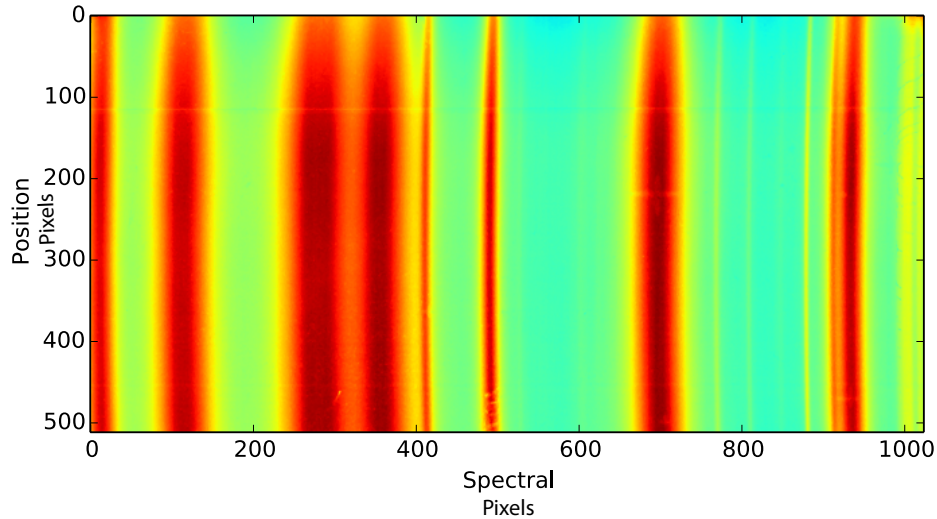


Figure 2.23. The spectral data from CRIRES observations of the Crab Nebula after they have been processed using a median filtering technique to remove cosmic rays from the data. The darker vertical bands correspond to the sky emission lines.

2.4.3 Results

Figures 2.26, 2.27, 2.29 and 2.28 show the regions of interest calibrated spectra for the central 8 spaxels of each observation. There is no clear detection of any of the lines we investigated, so we must put upper limits on the potentially observed fluxes based on the noise levels in the data.

Figures 2.31, 2.30, 2.32 and 2.33 show the regions of interest for calibrated spectra for the 8 of the 64 total spaxels of each observation for the 8 sets of 8 spaxels down the entire spectrograph. There are no clear detections of any of the lines we investigated. All the apparent features are coincident with sky features which have either not been fully subtracted or over compensated for.

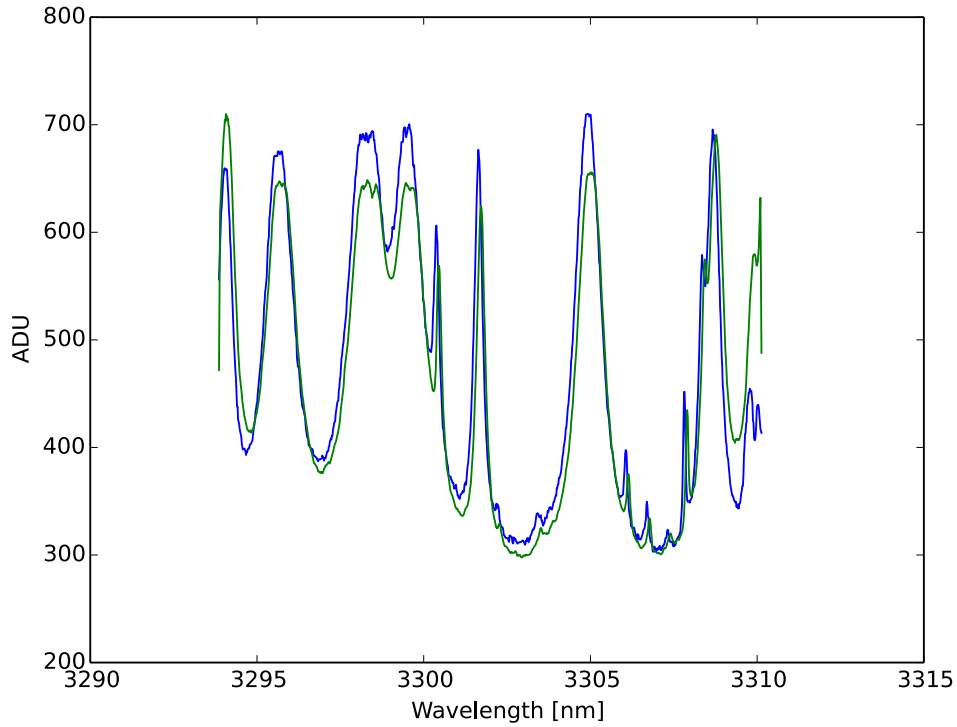


Figure 2.24. The spectrum of the observation of HeH^+ R(1) (blue) and model sky from the ETC (green).

2.4.4 CRIRES Line Flux Upper Limits

The resolving power of CRIRES with the 0.4 arcsec slit is 50000, so at 3302 nm the resolution element is 0.066 nm which is 4 spectral samples. I binned the data into 4 sample bins and take the standard deviation in each bin as representative of the noise on an integrated line. This noise can then be multiplied by the resolution to give the estimate of a 1-sigma detection limit. The H_2 emission in the region we are observing is known to lie between +90 and +145 km s^{-1} . The spectra are plotted in velocity and corrected for the motion of the earth and an upper limit is then fitted to this region of the spectrum. The spectra plotted in velocity space are shown in Figures 2.35, 2.34, 2.36 and 2.37. The values of the heliocentric correction and size of resolution element are shown in Table 2.8. The limits are shown in Table 2.9. The negative features (particularly in Figure 2.34) are residuals from the removal of telluric features and sky subtraction. The shaded regions correspond to the region of velocity interest, based on the measured line velocities of ArH^+

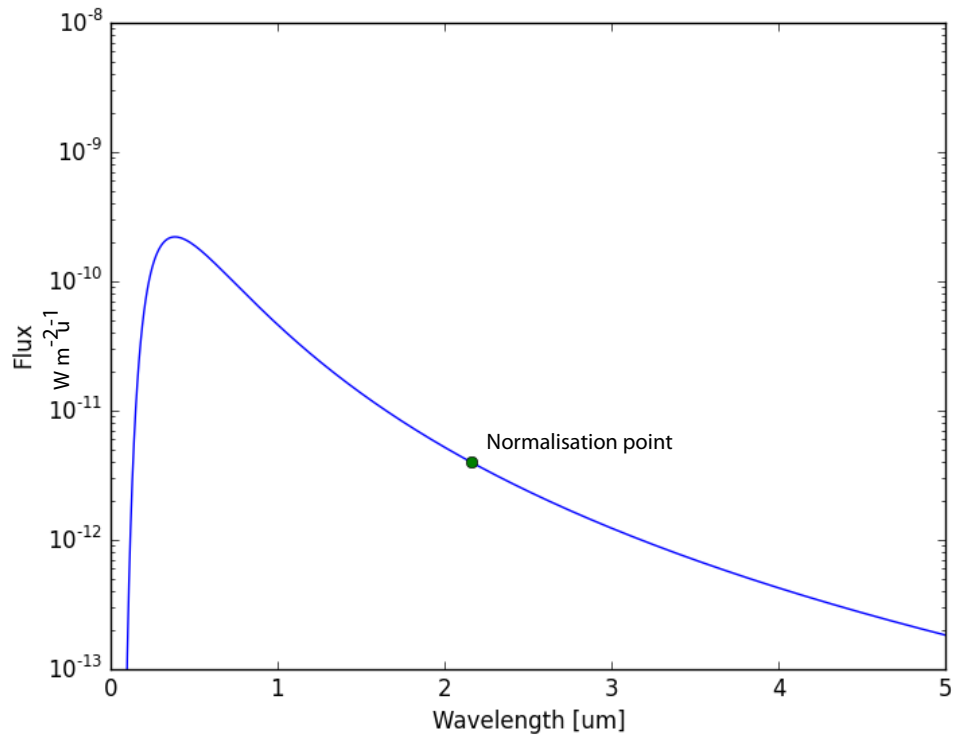


Figure 2.25. The modelled blackbody spectrum of ι Tau used for flux calibration.

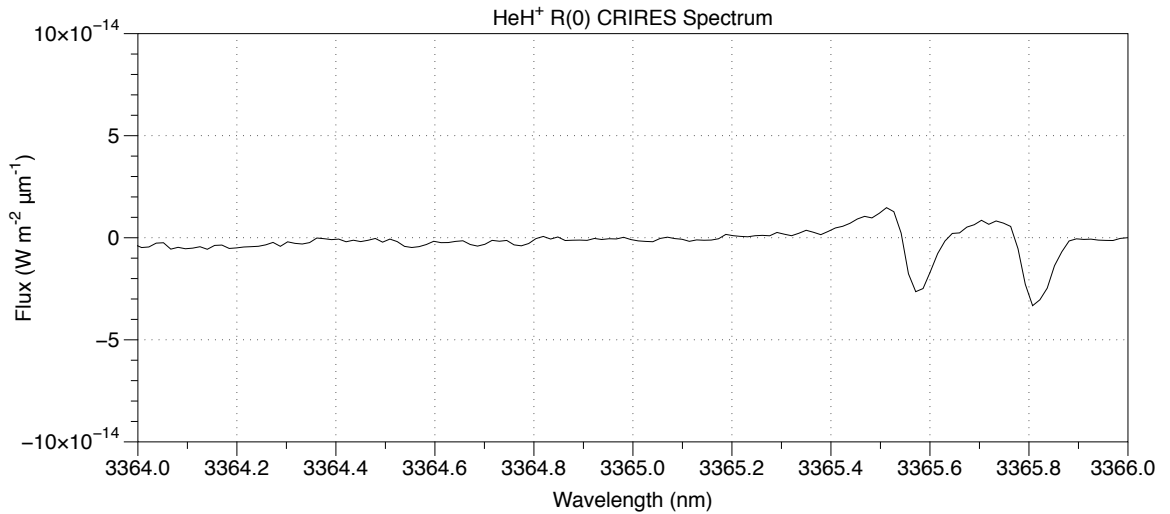


Figure 2.26. The spectrum of the region of the $\text{HeH}^+ \text{R}(0)$ 3364.09 nm line taken with VLT-CRIRES.

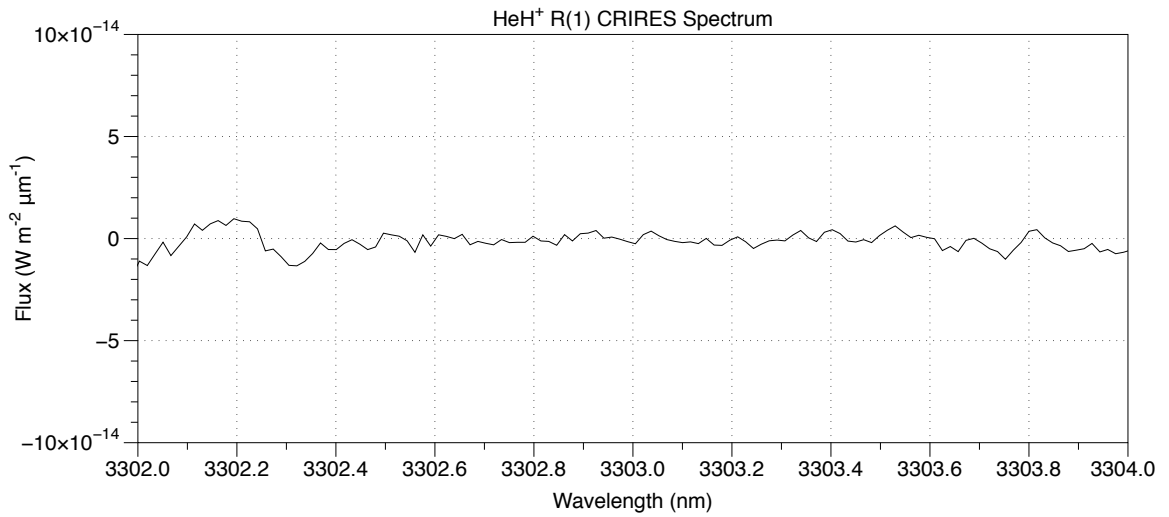


Figure 2.27. The spectrum of the region of the HeH^+ R(1) 3302.10 nm line taken with VLT-CRIRES.

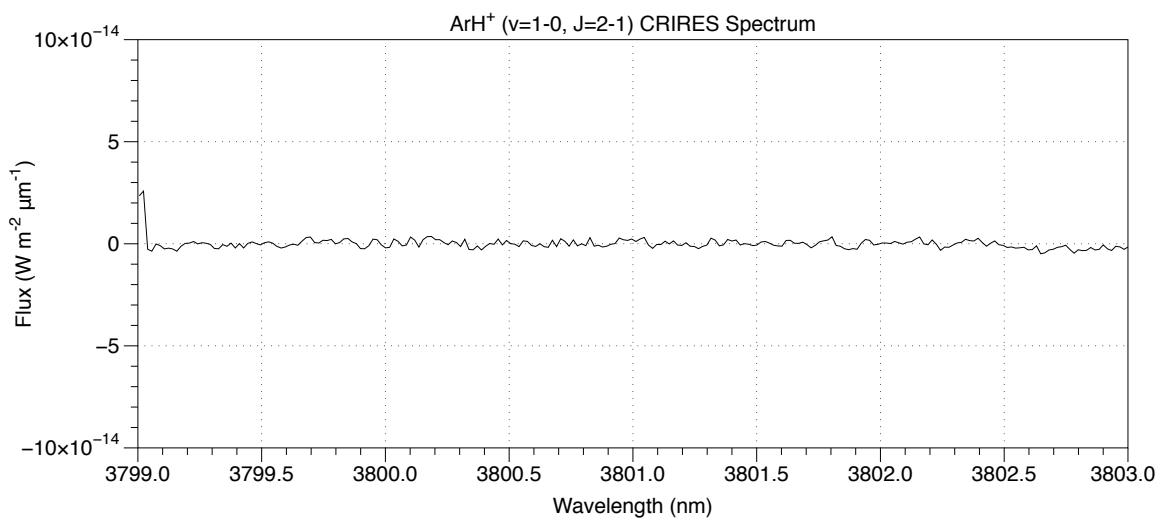


Figure 2.28. The spectrum of the region of the ArH^+ (v=1-0, J=2-1)) 3799.99 nm line taken with VLT-CRIRES.

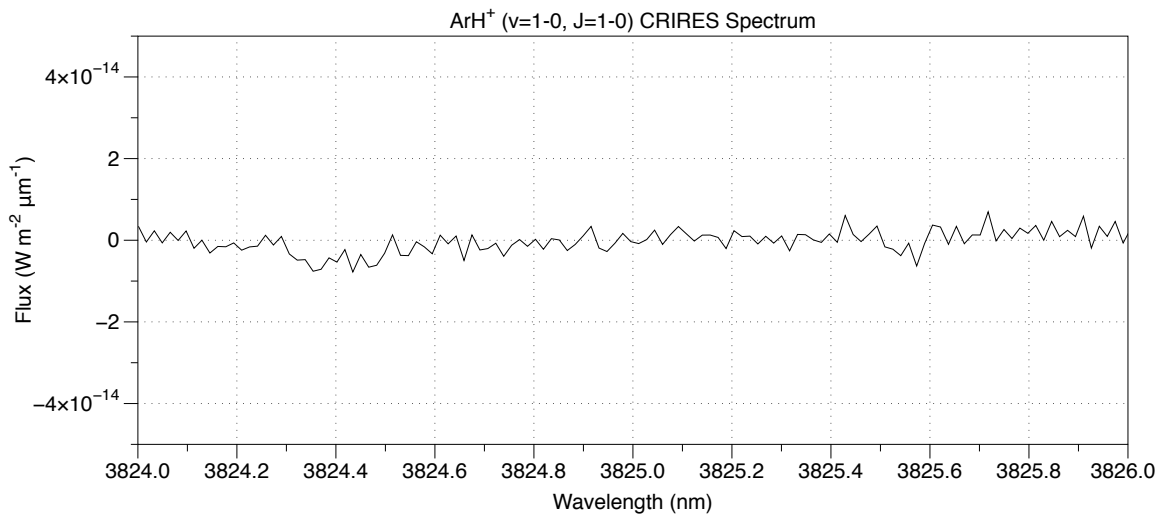


Figure 2.29. The spectrum of the region of the ArH^+ ($v=1-0$, $J=1-0$) 3827.75 nm line taken with VLT-CRIRES.

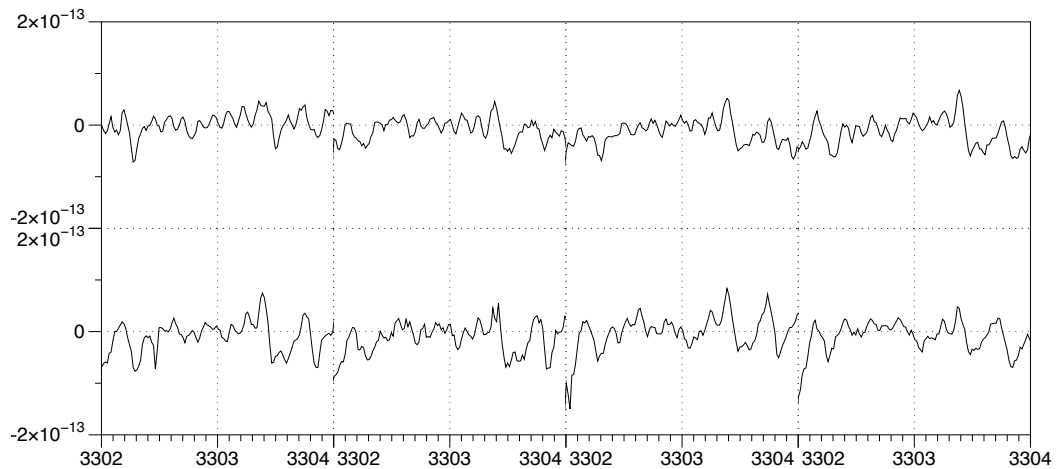


Figure 2.30. The 8 coadded spectra of the whole slit of the spectrograph in the region encompassing the HeH^+ R(1) 3302.10 nm line taken with VLT-CRIRES based on an assumed radial velocity of +140 km s⁻¹ for the knot (Barlow et al. 2013).

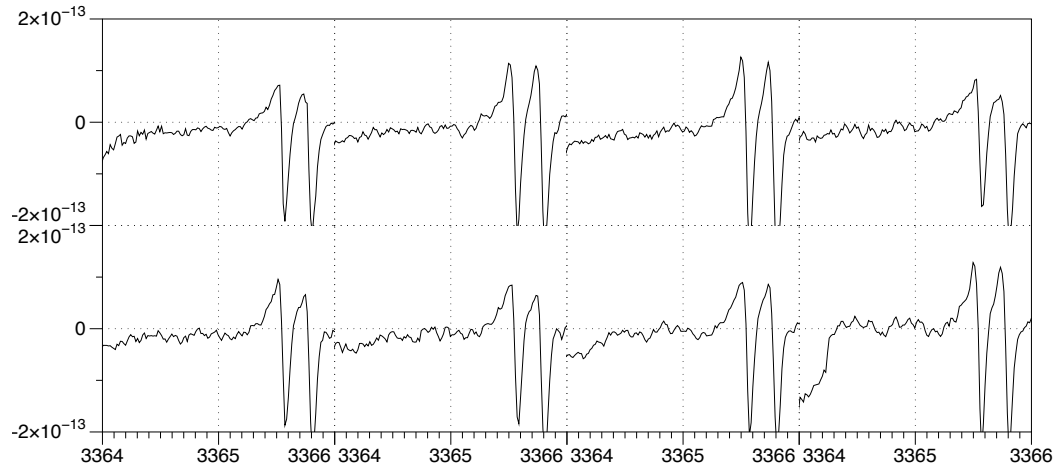


Figure 2.31. The 8 coadded spectra of the whole slit of the spectrograph in the region encompassing the HeH^+ $R(0)$ 3364.09 nm line taken with VLT-CRIRES based on an assumed radial velocity of $+140 \text{ km s}^{-1}$ for the knot (Barlow et al. 2013).

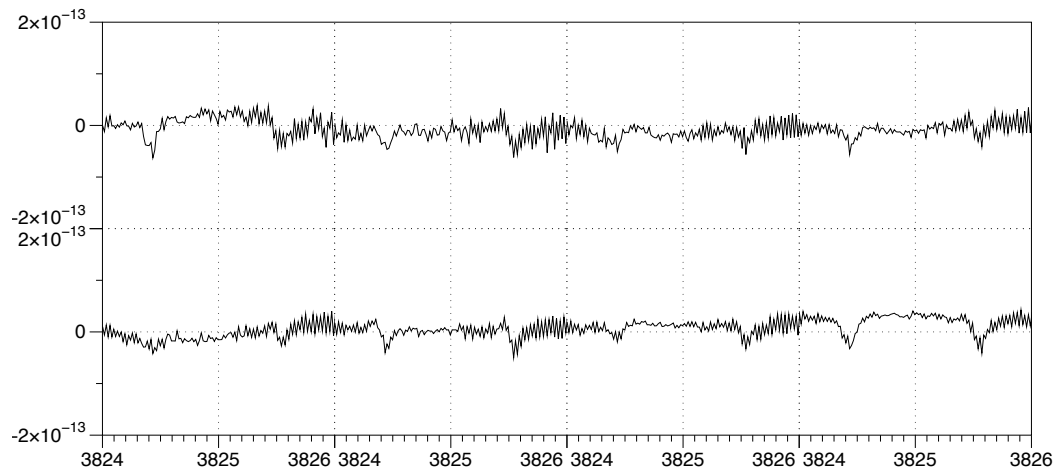


Figure 2.32. The 8 coadded spectra of the whole slit of the spectrograph in the region encompassing the ArH^+ ($v=1-0$, $J=1-0$) 3827.75 nm line taken with VLT-CRIRES based on an assumed radial velocity of $+140 \text{ km s}^{-1}$ for the knot (Barlow et al. 2013).

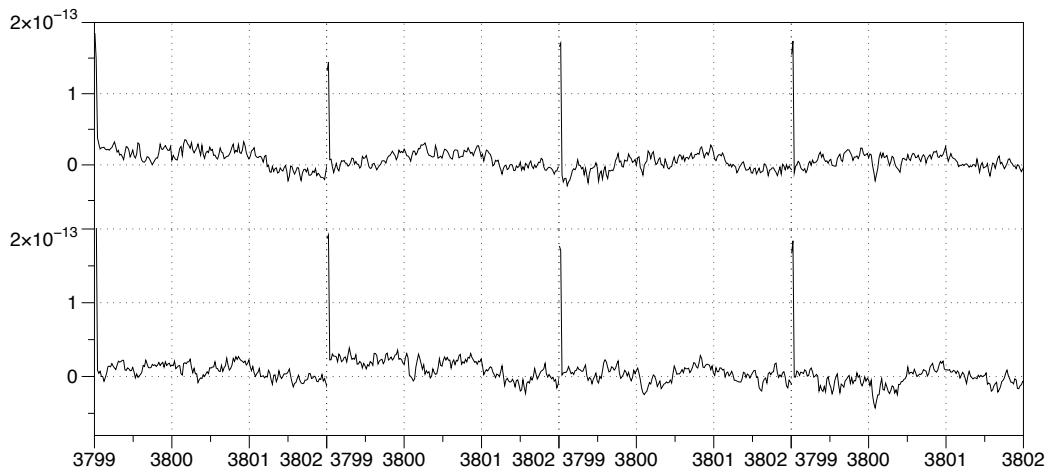


Figure 2.33. The 8 coadded spectra of the whole slit of the spectrograph in the region encompassing the ArH^+ ($v=1-0, J=2-1$) 3799.99 nm line taken with VLT-CRIRES based on an assumed radial velocity of $+140 \text{ km s}^{-1}$ for the knot (Barlow et al. 2013).

detections by *Herschel*.

Line	Wavelength (nm)	resolution element (nm)	Heliocentric Correction km s^{-1}
HeH^+ R(0)	3364.09	0.067 nm	-25.98
HeH^+ R(1)	3302.10	0.066 nm	-23.69
ArH^+ ($v=1-0, J=1-0$)	3827.75	0.076 nm	-26.12
ArH^+ ($v=1-0, J=2-1$)	3799.99	0.076 nm	-26.12

Table 2.8. The factors used in calculating the upper limits of detection in the CRIRES spectra. Heliocentric correction for motion of the earth taken from ESO Sky Calendar Tool <http://www.eso.org/sci/observing/tools/calendar/airmass.html>.

Having determined the line widths of the H_2 in the molecular knots, we can use them to determine the line widths of the ArH^+ and HeH^+ . Normally to do this we must take in to account the difference in mass between the very light H_2 molecule and the heavier ArH^+ and HeH^+ molecules. However, these line widths are far to broad to be purely thermal (as shown in Table 2.10) and must instead be attributed to local motion. Thus we take the FWHM of the H_2 lines to be the FWHM of the HeH^+ and ArH^+ as well.

The spectra are fitted with gaussians with the width of 10 km s^{-1} and 20 km s^{-1} ,

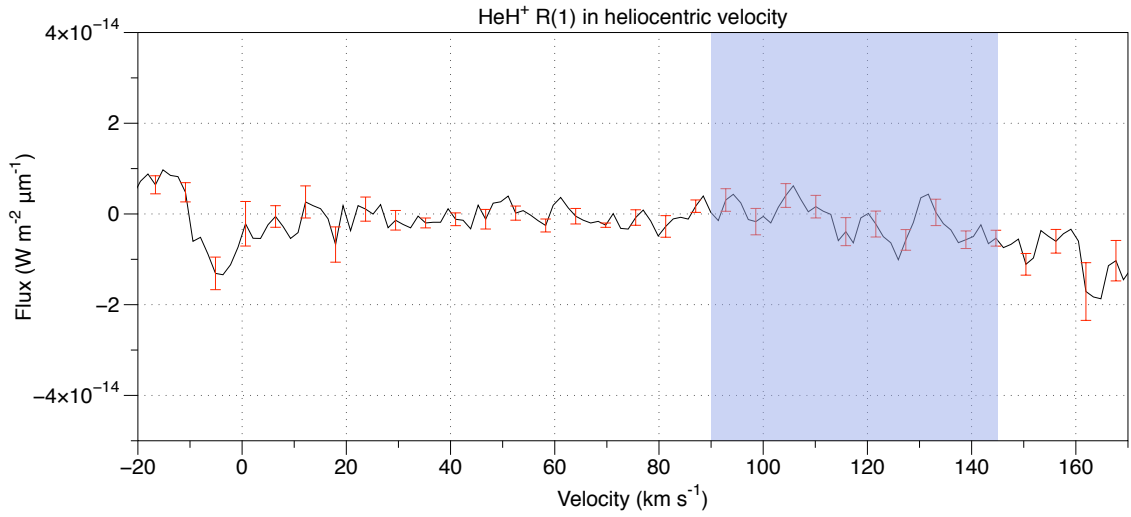


Figure 2.34. The spectrum of the region encompassing the HeH^+ R(1) 3302.10 nm line taken with VLT-CRIRES based on an assumed radial velocity of $+140 \text{ km s}^{-1}$ for the knot (Barlow et al. 2013). Negative features are due to sky subtractions.

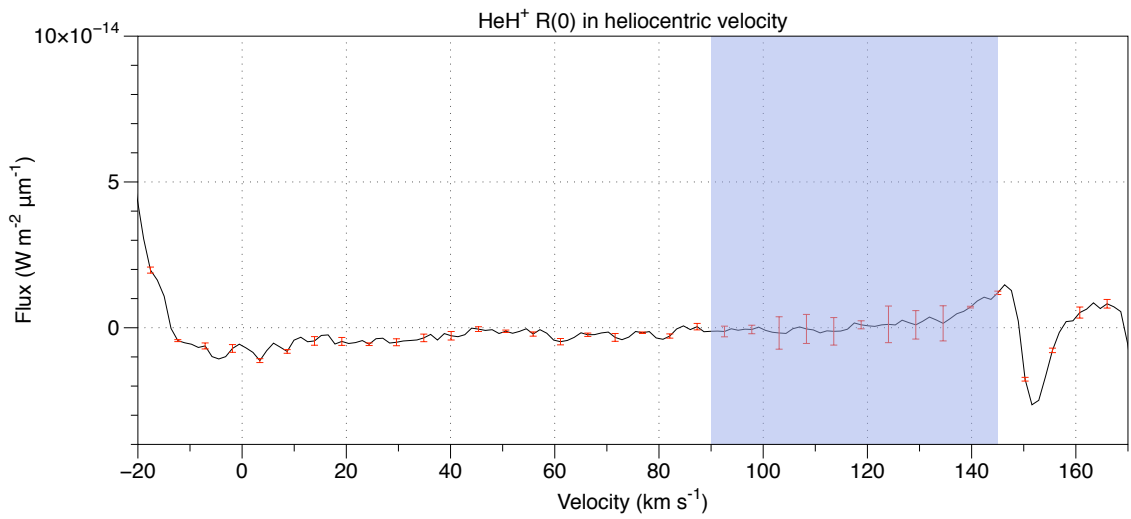


Figure 2.35. The spectrum of the region encompassing the HeH^+ R(0) 3364.09 nm line taken with VLT-CRIRES based on an assumed radial velocity of $+140 \text{ km s}^{-1}$ for the knot (Barlow et al. 2013).

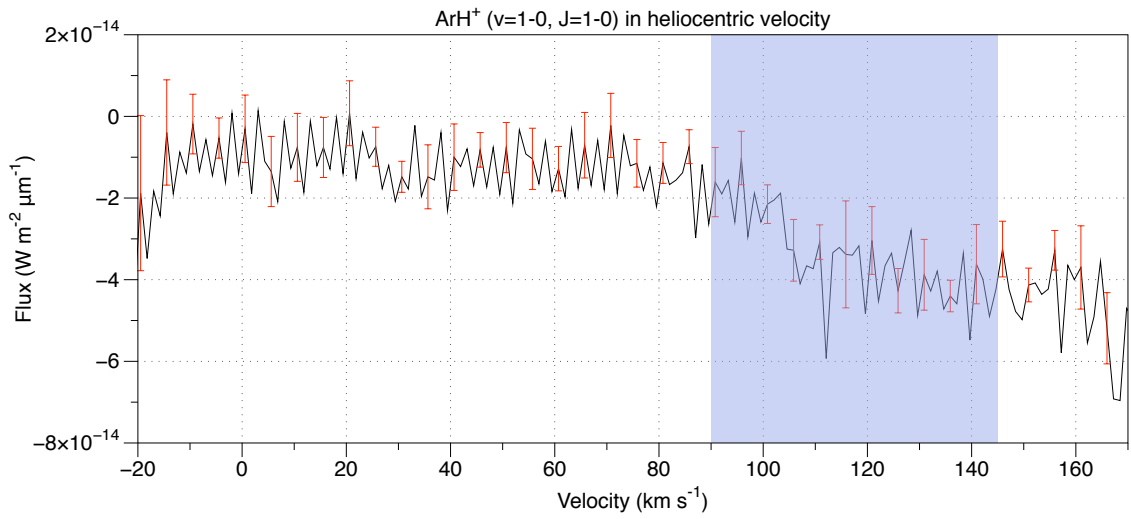


Figure 2.36. The spectrum of the region encompassing the ArH^+ ($v=1-0, J=1-0$) 3827.75 nm line taken with VLT-CRIRES based on an assumed radial velocity of $+140 \text{ km s}^{-1}$ for the knot (Barlow et al. 2013).

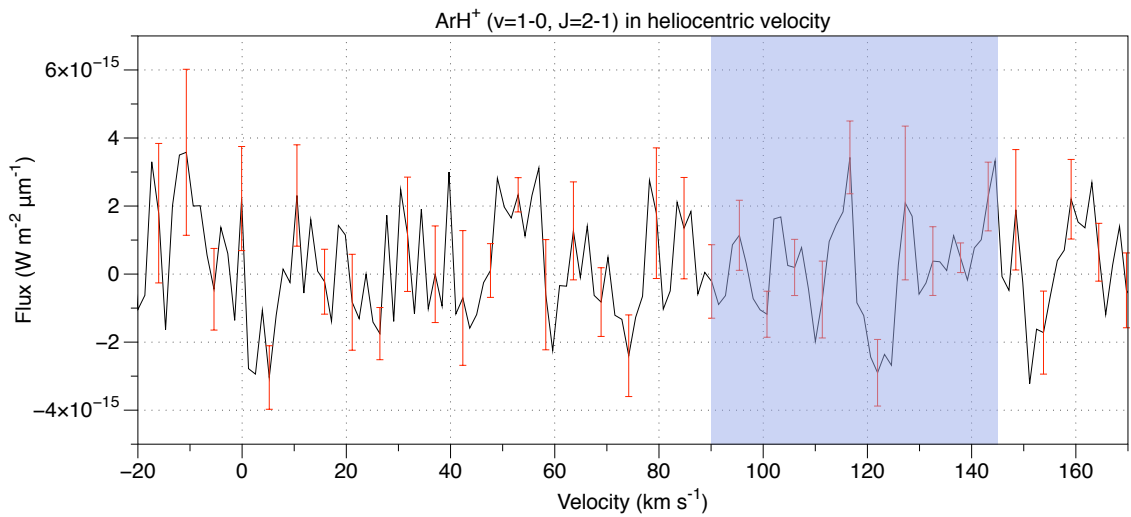


Figure 2.37. The spectrum of the region encompassing the ArH^+ ($v=1-0, J=2-1$) 3799.99 nm line taken with VLT-CRIRES based on an assumed radial velocity of $+140 \text{ km s}^{-1}$ for the knot (Barlow et al. 2013).

Line	Wavelength (nm)	3- σ Line Flux (6 km s ⁻¹ FWHM)
HeH ⁺ R(0)	3364.09	<1.3×10 ⁻¹³ W m ⁻²
HeH ⁺ R(1)	3302.10	<7.7×10 ⁻¹⁴ W m ⁻²
ArH ⁺ (v=1-0, J=1-0)	3827.75	<3.3×10 ⁻¹³ W m ⁻²
ArH ⁺ (v=1-0, J=2-1)	3799.99	<1.5×10 ⁻¹³ W m ⁻²

Table 2.9. The upper limits of detection of the HeH⁺ R(0), R(1) and ArH⁺ (v=1-0, J=1-0) and (v=1-0, J=2-1) lines with VLT-CRIRES

FWHM km s ⁻¹	Temperature K
51.1	320000
44.6	240000
36.9	18000
29.6	19000
20.1	15000
14.4	10000

Table 2.10. The temperature that the gas would be at if the line widths were purely from the thermal motion.

thus similar to the measured widths of the H₂ lines with the centre at the velocity of the observed ArH⁺ rotational lines. Figures 2.40 and 2.41 show the plots for the gaussians fitted for the ArH⁺ and Figures 2.38 and 2.39 show the plots of those fitted for HeH⁺.

Table 2.11 shows the upper limits on the detections of each line made by adding gaussians of width 10 and 20 km s⁻¹ similar to the observed widths of the H₂ knots observed by the IRTF until they are visible above the noise limit. These limits are comparable to those determined by the standard deviation of the noise in the VLT-CRIRES data.

This lack of a clear detection may mean several things. As the region with the ArH⁺ is may be below the required excitation temperature, these ro-vibrational states may not be excited. Alternatively it is possible we are investigating the wrong regions. Rather than the bright knots, the emission is in fact coming from the more diffuse regions. Further observations and modelling work will be required to determine which of these is the case.

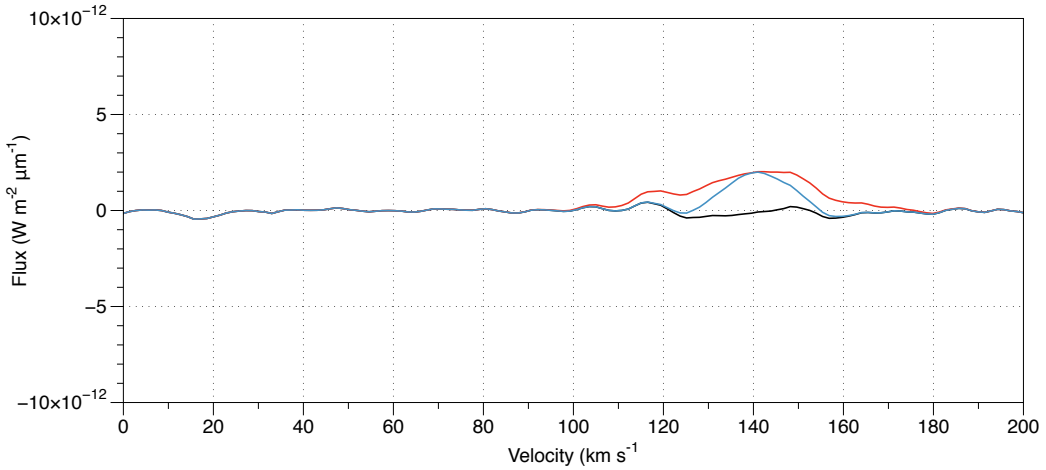


Figure 2.38. The coadded spectrum of the whole slit of the spectrograph in the region of the HeH^+ R(1) 3302.10 nm line taken with VLT-CRIRES with a gaussian of width of the H_2 as measured by the IRTF. The red line shows the observed spectrum with what a 3σ detection of a line of width 20 km s^{-2} would look like and the blue line shows the observed spectrum with what a 3σ detection of a line of width 10 km s^{-2} . The black line shows the actual observational data.

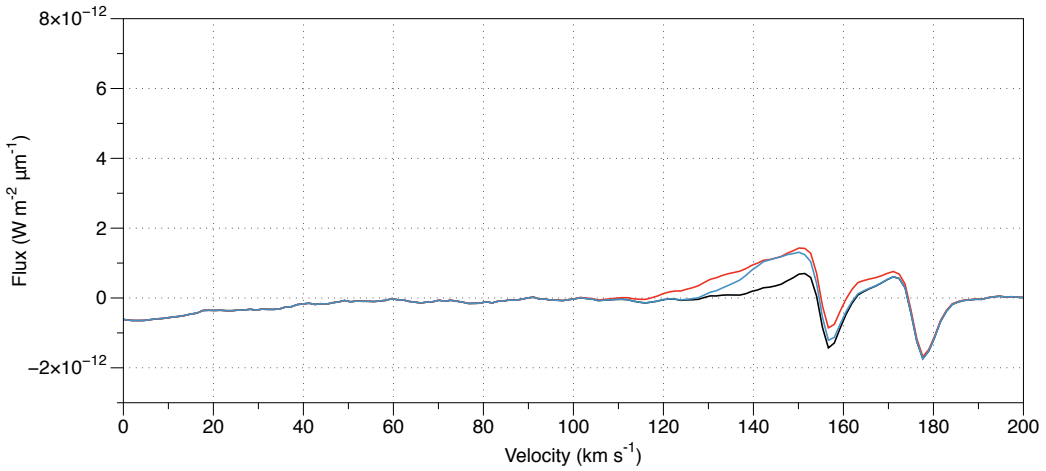


Figure 2.39. The coadded spectrum of the whole slit of the spectrograph in the region of the HeH^+ R(0) 3364.09 nm line taken with VLT-CRIRES with a gaussian of width of the H_2 as measured by the IRTF. The red line shows the observed spectrum with what a 3σ detection of a line of width 20 km s^{-2} would look like and the blue line shows the observed spectrum with what a 3σ detection of a line of width 10 km s^{-2} . The black line shows the actual observational data.

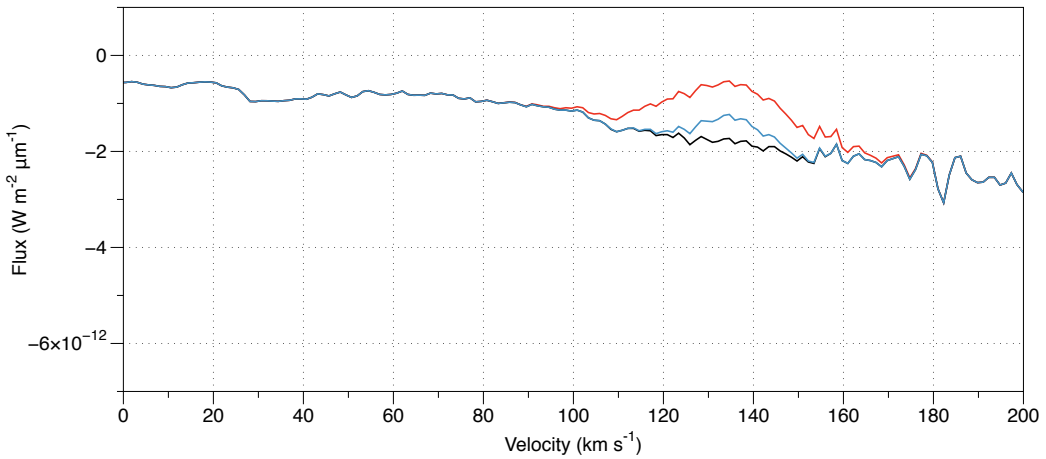


Figure 2.40. The coadded spectrum of the whole slit of the spectrograph in the region of the ArH^+ ($v=1-0$, $J=1-0$) 3827.75 nm line taken with VLT-CRIRES with a gaussian of width of the H_2 as measured by the IRTF. The red line shows the observed spectrum with what a 3σ detection of a line of width 20 km s^{-2} would look like and the blue line shows the observed spectrum with what a 3σ detection of a line of width 10 km s^{-2} . The black line shows the actual observational data.

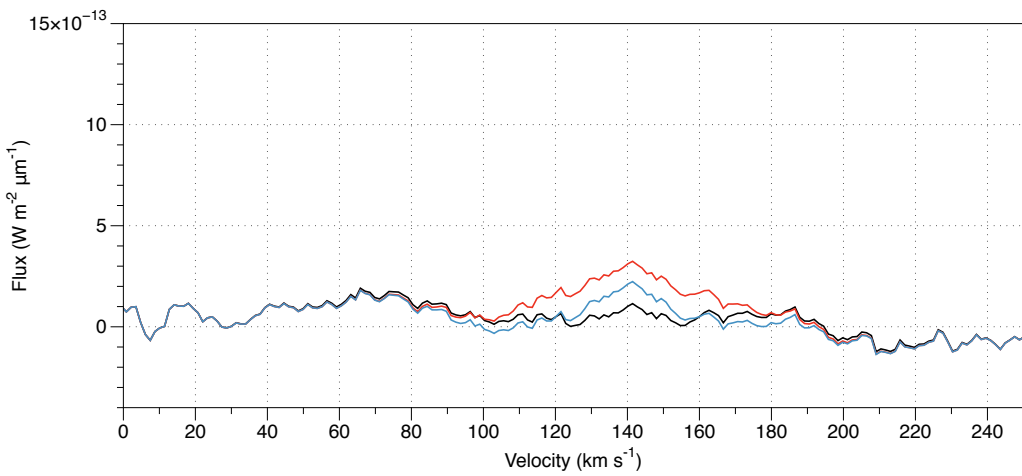


Figure 2.41. The coadded spectrum of the whole slit of the spectrograph in the region of the ArH^+ ($v=1-0$, $J=2-1$) 3799.99 nm line taken with VLT-CRIRES with a gaussian of width of the H_2 as measured by the IRTF. The red line shows the observed spectrum with what a 3σ detection of a line of width 20 km s^{-2} would look like and the blue line shows the observed spectrum with what a 3σ detection of a line of width 10 km s^{-2} . The black line shows the actual observational data.

Line	Wavelength nm	Detection Limit	Detection Limit	Detection Limit
		Width 10 km s ⁻² W m ⁻²	Width 20 km s ⁻² W m ⁻²	Noise W m ⁻²
HeH ⁺ R(0)	3364.09	<9.7×10 ⁻¹⁴	<1.6×10 ⁻¹³	<1.3×10 ⁻¹³
HeH ⁺ R(1)	3302.10	<9.8×10 ⁻¹⁴	<1.4×10 ⁻¹³	<7.7×10 ⁻¹⁴
ArH ⁺ (v=1-0, J=1-0)	3827.75	<9.9×10 ⁻¹⁴	v1.8×10 ⁻¹³	<3.3×10 ⁻¹³
ArH ⁺ (v=1-0, J=2-1)	3799.99	<1.02×10 ⁻¹³	<2.75 ×10 ⁻¹³	<1.5×10 ⁻¹³

Table 2.11. The upper limits of detection of the HeH⁺ R(0), R(1) and ArH⁺ (v=1-0, J=1-0) and (v=1-0, J=2-1) lines with VLT-CRIRES using the IRTF measured H₂ line widths. Also included are the upper limits based purely on the standard deviation of the noise in the CRIRES data

2.5 HeH⁺ line flux upper limits with PACS

The J=1-0 and J=2-1 HeH⁺ rotational lines at 149.25 μm and 74.83 μm are both within the wavelength range of PACS. Figures 2.43 and 2.43 show the individual PACS-IFU spaxels in velocity space for the two HeH⁺ lines using the standard deviation of the noise in each spaxel. Putting upper limits on these non detections we find 4.9 ×10⁻¹⁷ W m⁻² for the 1-0 line and 6.3 ×10⁻¹⁷ W m⁻² for the 2-1 line.

2.6 Conclusions

The Crab Nebula was observed with *Herschel* PACS-IFU and SPIRE-FTS. The PACS observations were used to investigate conditions such as electron density and temperature and ionic ratios in the nebula as well as the structure of its ionised and neutral regions.

The SPIRE-FTS spectra contained the first observations of a molecule containing a noble gas, ³⁶ArH⁺. This discovery was followed up by a search for near-infrared ro-vibrational lines of ³⁶ArH⁺ and HeH⁺ with the VLT and IRTF. These near infrared observations of knot 1 of Loh et al. (2011) in the Crab Nebula were obtained with CRIRES on the VLT and CSHELL on the IRTF. The CRIRES data were obtained to investigate the presence of the R(0) and R(1) ro-vibrational lines of ³⁶ArH⁺ and HeH⁺. The CSHELL data delivered high resolution line width measurements of the ro-vibrational 1-0 S(1) 2.122 μm line in H₂ which is used to accurately constrain the line widths of the ³⁶ArH⁺ and HeH⁺ lines. I have placed upper limits on the detections of the ionic noble gas hydride lines of 9.7×10⁻¹⁴ W m⁻² for the HeH⁺ R(0), 9.8×10⁻¹⁴ W m⁻² for the HeH⁺ R(1), 9.9×10⁻¹⁴ W m⁻² for

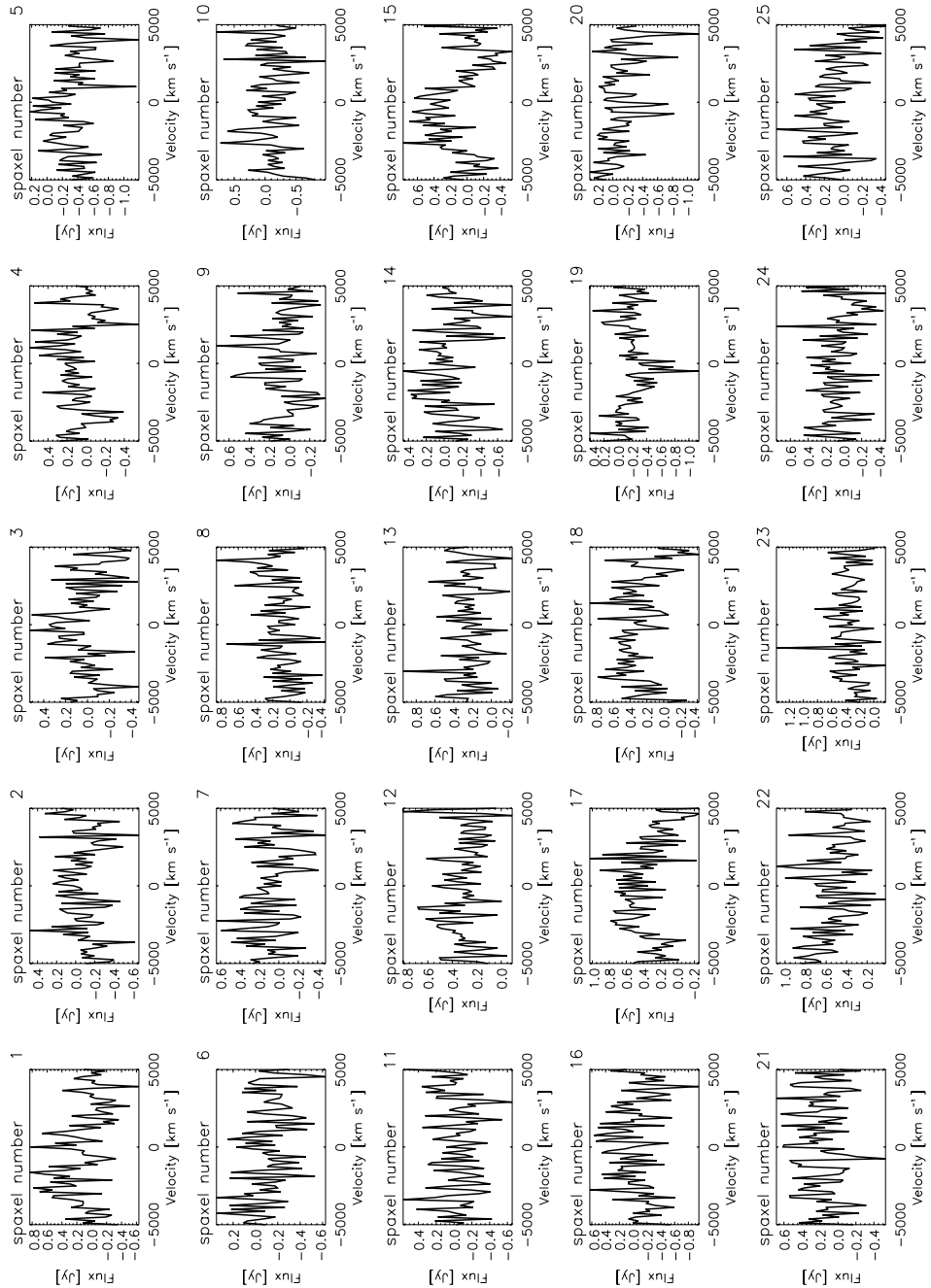


Figure 2.42. PACS-IFU observations of the region of the J=1-0 149.25 μm HeH⁺ line.

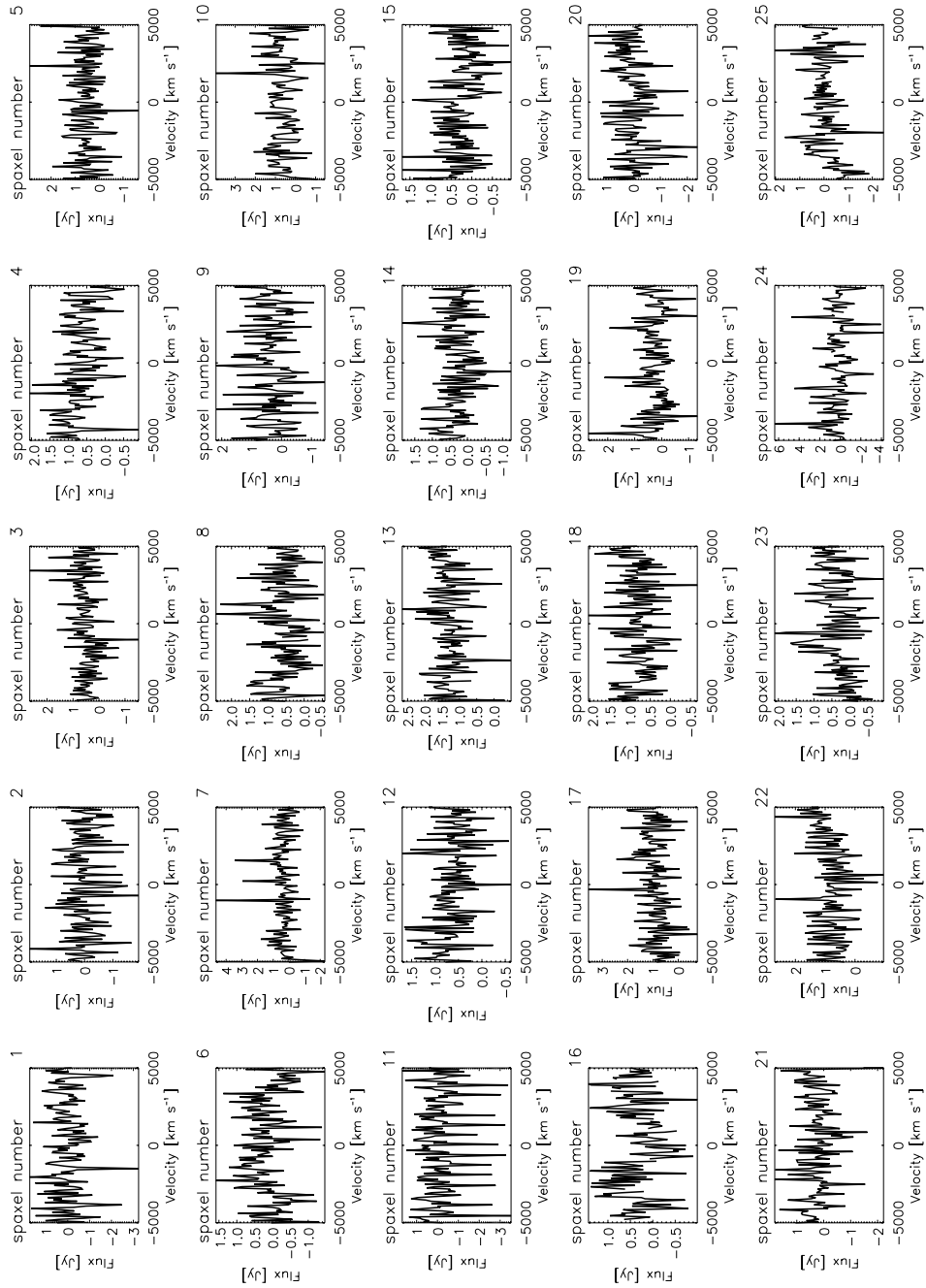


Figure 2.43. PACS-IFU observations of the region of the J=2-1 74.83 μm HeH⁺ line.

the ArH⁺ ($v=1\text{-}0$, $J=1\text{-}0$), and 1.02×10^{-13} W m⁻² for the ArH⁺ ($v=1\text{-}0$, $J=2\text{-}1$).

Despite its violent nature the Crab Nebula has a diverse structure and chemistry. This exotic chemistry, including the detection of a previously unobserved molecule, is opening new windows in astronomy as it can be used to investigate the abundances of other molecules. In addition to this can provide observational constraints on supernova nucleosynthesis models for the first time via the observations of different isotopologues. Future observations with ALMA will probe the ratios of $^{36}\text{Ar}/^{38}\text{Ar}$. ^{36}Ar is formed in an explosive α capture process, whereas ^{38}Ar is formed by a slow neutron capture process (the S-process).

This page was intentionally left blank

Chapter 3

Herschel Spectroscopy of Cassiopeia A

Star go poof! Star go boom!

Antonia Bevan

Cassiopeia A is a young oxygen rich supernova remnant (SNR). It is approximately 3.4 kpc away (Reed et al. 1995) and around 330 years old (Fesen et al. 2006). Cas A is one of the most-studied objects in the sky, having been observed in all wavelengths from radio waves through to γ -rays. Recent observations in the near infrared of light echoes from the original supernova event, due to absorption, re-emission and scattering by interstellar dust show that it is the remnant of a Type IIb supernova of intial mass of around $15 M_{\odot}$ (Krause et al. 2008). An investigation of the dust in the remnant including broadband *Herschel* PACS and SPIRE images was presented by Barlow et al. (2010). These images were corrected for line emission using ISO observations.

3.1 Cassiopeia A with PACS-IFU spectrometer

Spectra of Cas A were taken of nine different positions around the Cas A supernova remnant on January 1st 2011 using the PACS-IFU instrument. They focused on the reverse

shock and central regions. Their positions are shown in Figure 3.1 plotted on a $70\mu\text{m}$ image of Cas A. There is a strong foreground in the line of sight of Cas A so off-target positions used by the instrument's chopper to remove this emission are not shown as they're further away than the scale of the image allows. At each position two observations are made, one for the wavelength ranges $51\text{-}72\mu\text{m}$ and $102\text{-}146\mu\text{m}$ (Range Mode SED B2A + Short R1) and one for $70\text{-}105\mu\text{m}$ and $140\text{-}220\mu\text{m}$ (Range Mode SED B2B + Long R1). Data was reduced to level 2 using the standard PACS chopped large range scan and Spectral Energy Distribution (SED) pipeline in HIPE 8.0.1 (Ott 2010) using the PACS_CAL_32_0 calibration file. This is the level that allows science to be done on the data. The RA, DEC, and the time that the observation was made, the observation ID and the time on-source are shown in Table 3.1.

3.2 PACS Spectra

Figures 3.2 to 3.10 show the reduced spectra for PACS-IFU observations converted in to velocity with a central velocity of 45 km s^{-2} (Baade & Minkowski 1954). The $88\mu\text{m}$ [O III] line emission shown in black, the $63\mu\text{m}$ [O I] line emission shown in red and $158\mu\text{m}$ [C II] line emission shown in green.

3.2.1 Oxygen Fine Structure Lines

Cas A is an oxygen rich supernova remnant. There is [O III] $88\mu\text{m}$ line emission from most of the remnant. It is particularly strong in regions coinciding with the $70\mu\text{m}$ broadband emission. Figure 3.11 is the relative flux of the red shifted [O III] $88\mu\text{m}$ lines detected by PACS-IFU plotted over a contour plot of the PACS $70\mu\text{m}$ image. Figure 3.12 shows the relative flux of the blue shifted emissions of the [O III] $88\mu\text{m}$ detected by PACS-IFU plotted over a contour plot of the PACS $70\mu\text{m}$ image.

The observations with Spitzer by Rho et al. (2008) showed ionised gas to be present throughout the nebula. This is consistent with the PACS [O III] $88\mu\text{m}$ line emission. The only places where [O III] emission is weaker are the regions where ^{44}Ti emission has been observed with the NuSTAR hard X-ray telescope (Grefenstette et al. 2014). ^{44}Ti and oxygen are formed in different nucleosynthetic layers of a star, so this lack of coincidence

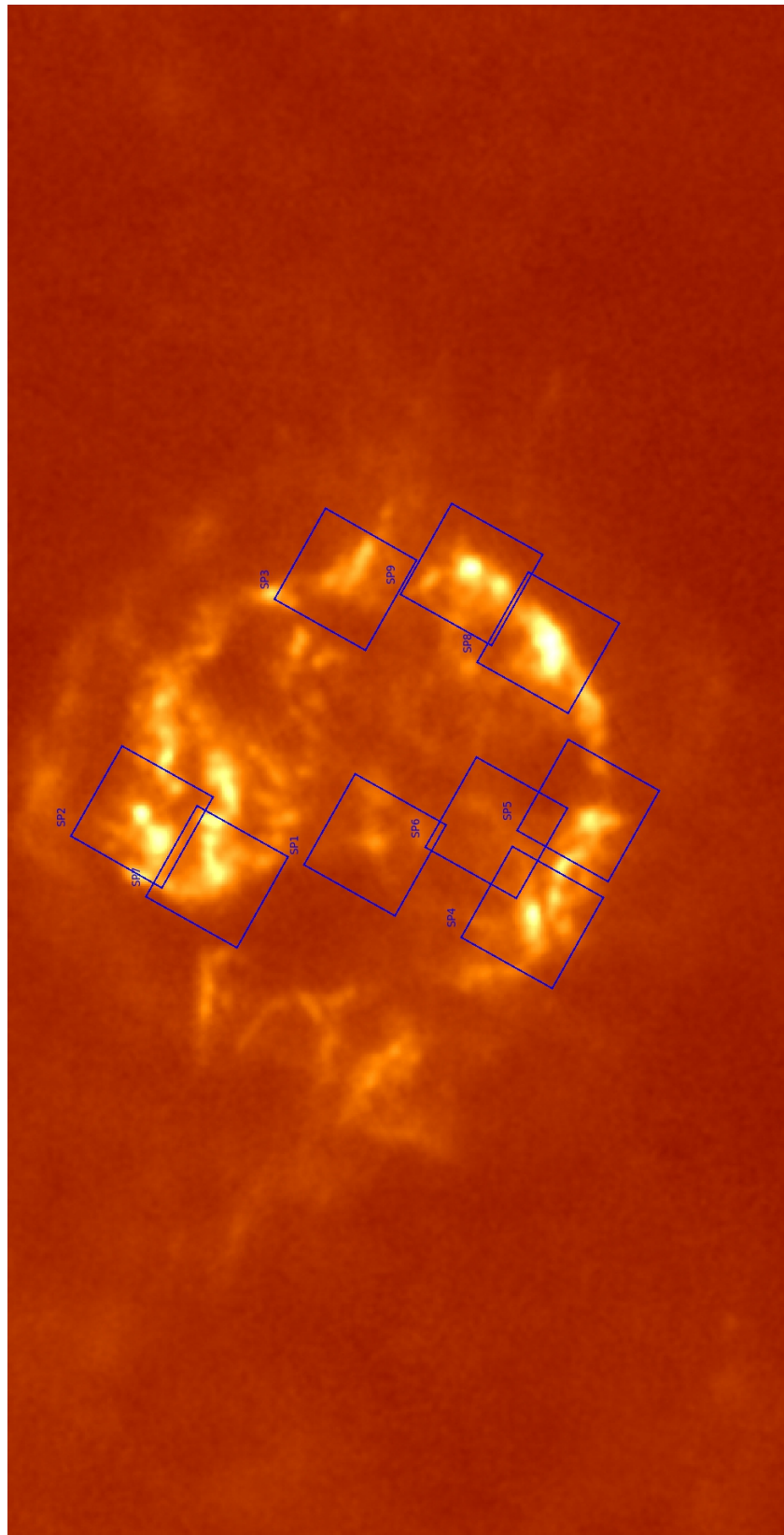


Figure 3.1. The positions of the observations of Cas A made with the *Herschel* PACS-IF,U plotted on a PACS 70 μ m image.

Object	Date	Time	RA (2000)	DEC (2000)	ObsID	Time on source
Cas A - SP1	2011-01-01	17:46:11	23h 23m 28.61s	58° 48' 59.17"	1342212249	2267
Cas A - SP1	2011-01-01	18:26:10	23h 23m 28.20ss	58° 49' 5.10"	1342212250	1139
Cas A - SP2	2011-01-01	19:48:25	23h 23m 24.94s	58° 51' 26.98"	1342212253	2267
Cas A - SP2	2011-01-01	20:28:24	23h 23m 24.50s	58° 51' 33.31"	1342212254	1139
Cas A - SP3	2011-01-01	21:50:39	23h 23m 12.76s	58° 49' 12.26"	1342212257	2267
Cas A - SP3	2011-01-01	22:30:38	23h 23m 13.19s	58° 49' 18.37"	1342212258	1139
Cas A - SP4	2011-01-01	15:43:57	23h 23m 32.82s	58° 47' 48.39"	1342212245	2267
Cas A - SP4	2011-01-01	16:23:56	23h 23m 32.41s	58° 47' 54.44"	1342212246	1139
Cas A - SP5	2011-01-01	18:47:18	23h 23m 27.40s	58° 47' 23.04"	1342212251	2267
Cas A - SP5	2011-01-01	19:27:17	23h 23m 26.99s	58° 47' 28.89"	1342212252	1139
Cas A - SP6	2011-01-01	14:42:50	23h 23m 40.49s	58° 48' 52.93"	1342212243	2267
Cas A - SP6	2011-01-01	15:22:49	23h 23m 39.61s	58° 49' 05.82"	1342212244	1139
Cas A - SP7	2011-01-01	16:45:04	23h 23m 30.45s	58° 50' 10.21"	1342212247	2267
Cas A - SP7	2011-01-01	17:25:03	23h 23m 30.03s	58° 50' 16.42"	1342212248	1139
Cas A - SP8	2011-01-01	20:49:32	23h 23m 16.84s	58° 47' 41.01"	1342212255	2267
Cas A - SP8	2011-01-01	21:29:31	23h 23m 16.43s	58° 47' 46.89"	1342212256	1139
Cas A - SP9	2011-01-01	22:51:46	23h 23m 12.87s	58° 48' 15.45"	1342212259	2267
Cas A - SP9	2011-01-01	23:31:45	23h 23m 12.46s	58° 48' 21.36"	1342212260	1139

Table 3.1. The positions of the PACS Spectroscopic observations of Cas A

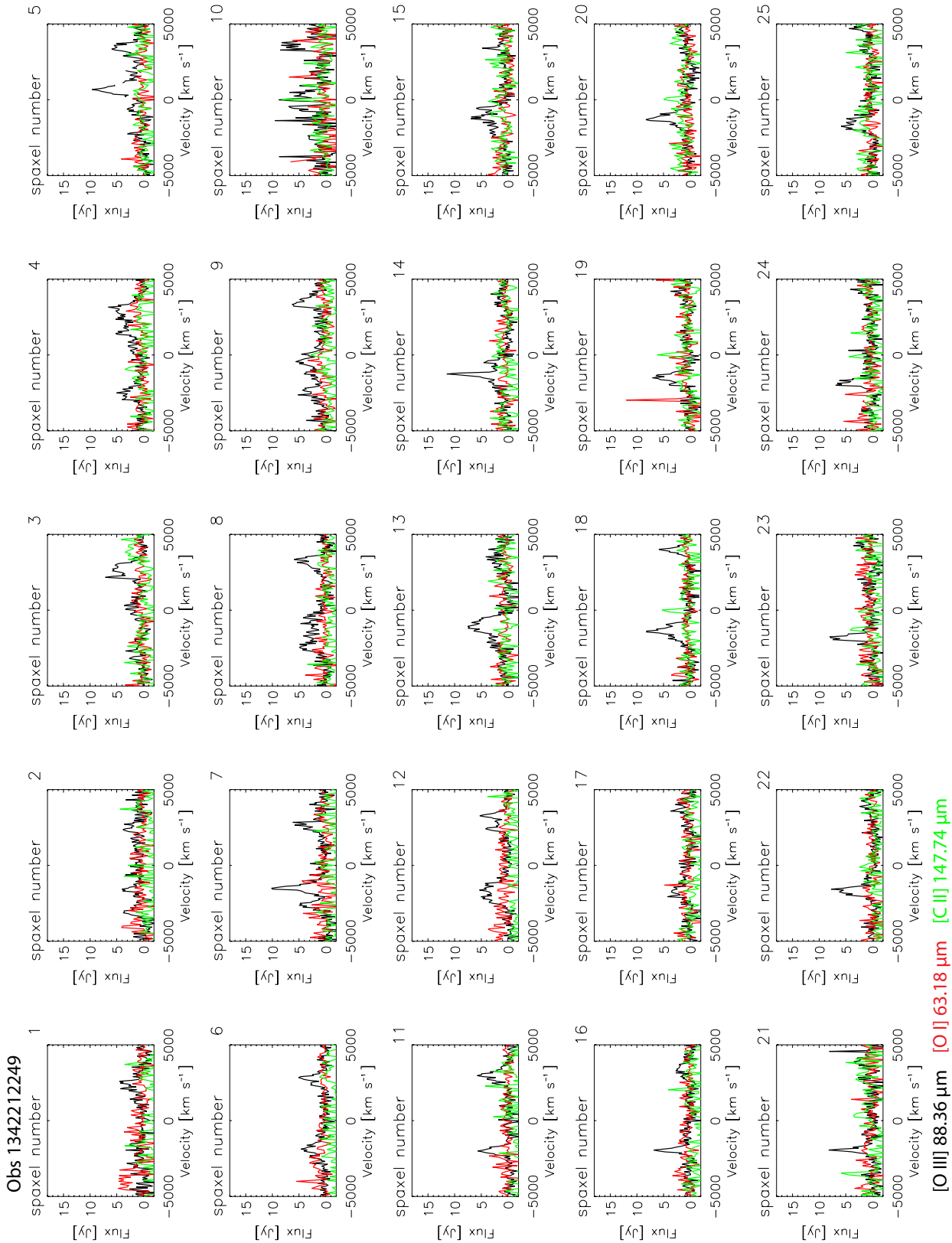


Figure 3.2. The 5x5 PACS-IFU observation SP1 of Cas A in velocity space. The black line shows the 88 μm [O III] line, the red line shows the 63 μm [O I] line and the green shows the 158 μm [C II] line.

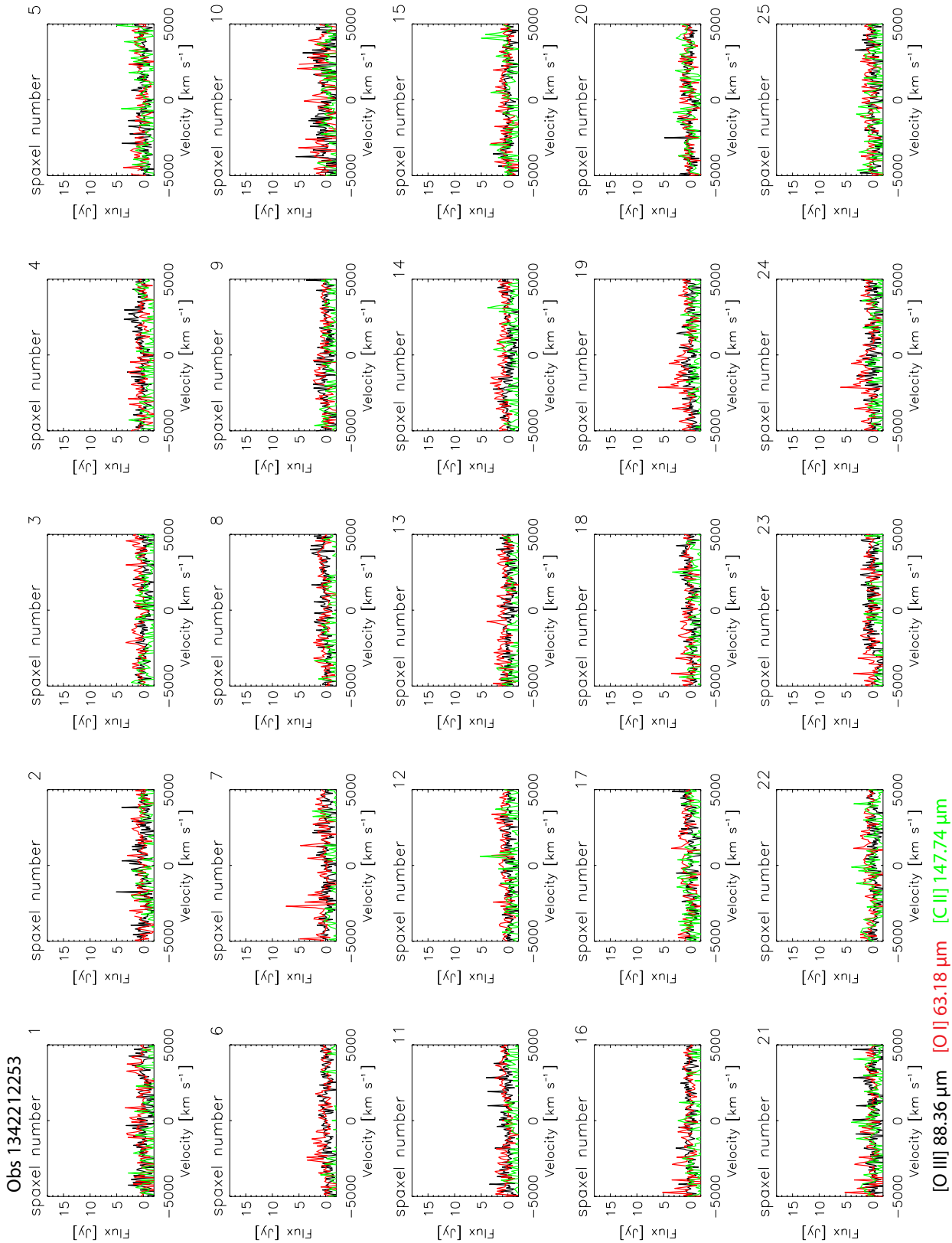


Figure 3.3. The 5x5 PACS-IFU observation SP2 of Cas A in velocity space. The black line shows the $88 \mu\text{m}$ [O III] line, the red line shows the $63 \mu\text{m}$ [O I] line and the green shows the $158 \mu\text{m}$ [C II] line.

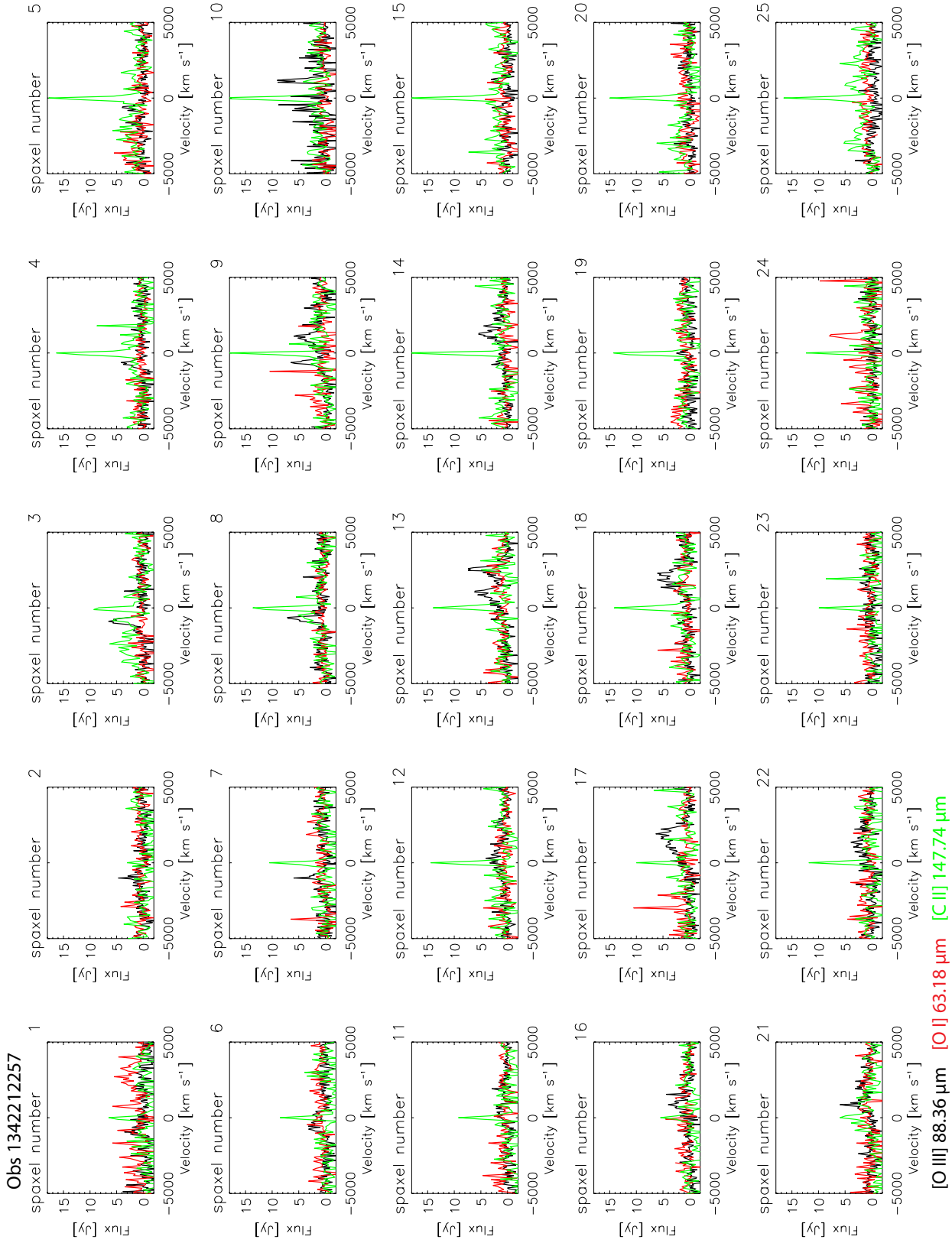


Figure 3.4. The 5x5 PACS-IFU observation SP3 of Cas A in velocity space. The black line shows the $88 \mu\text{m}$ [O III] line, the red line shows the $63 \mu\text{m}$ [O I] line and the green shows the $158 \mu\text{m}$ [C II] line.

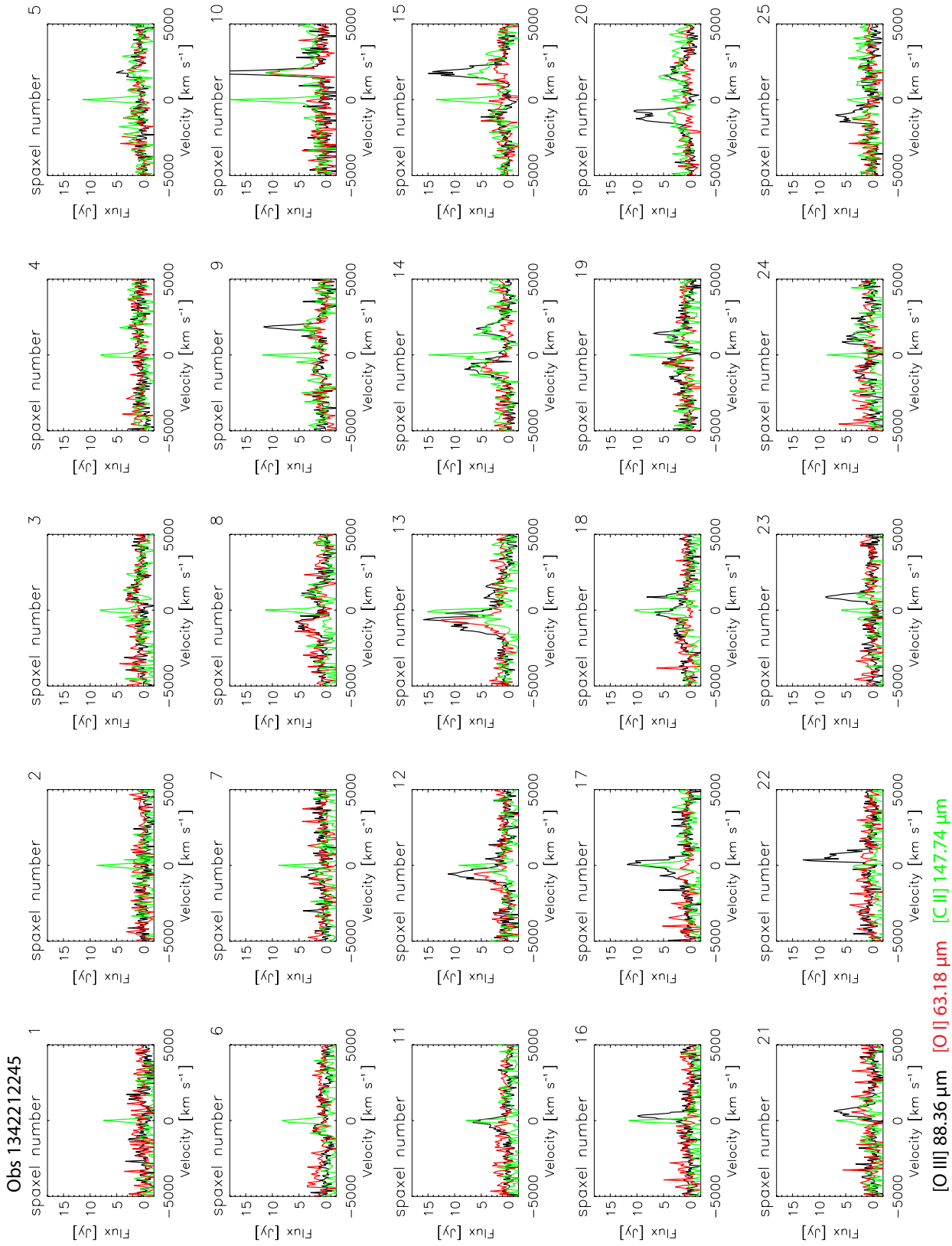


Figure 3.5. The 5x5 PACS-IFU observation SP4 of Cas A in velocity space. The black line shows the $88\ \mu\text{m}$ [O III] line, the red line shows the $63\ \mu\text{m}$ [O I] line and the green shows the $158\ \mu\text{m}$ [C II] line.

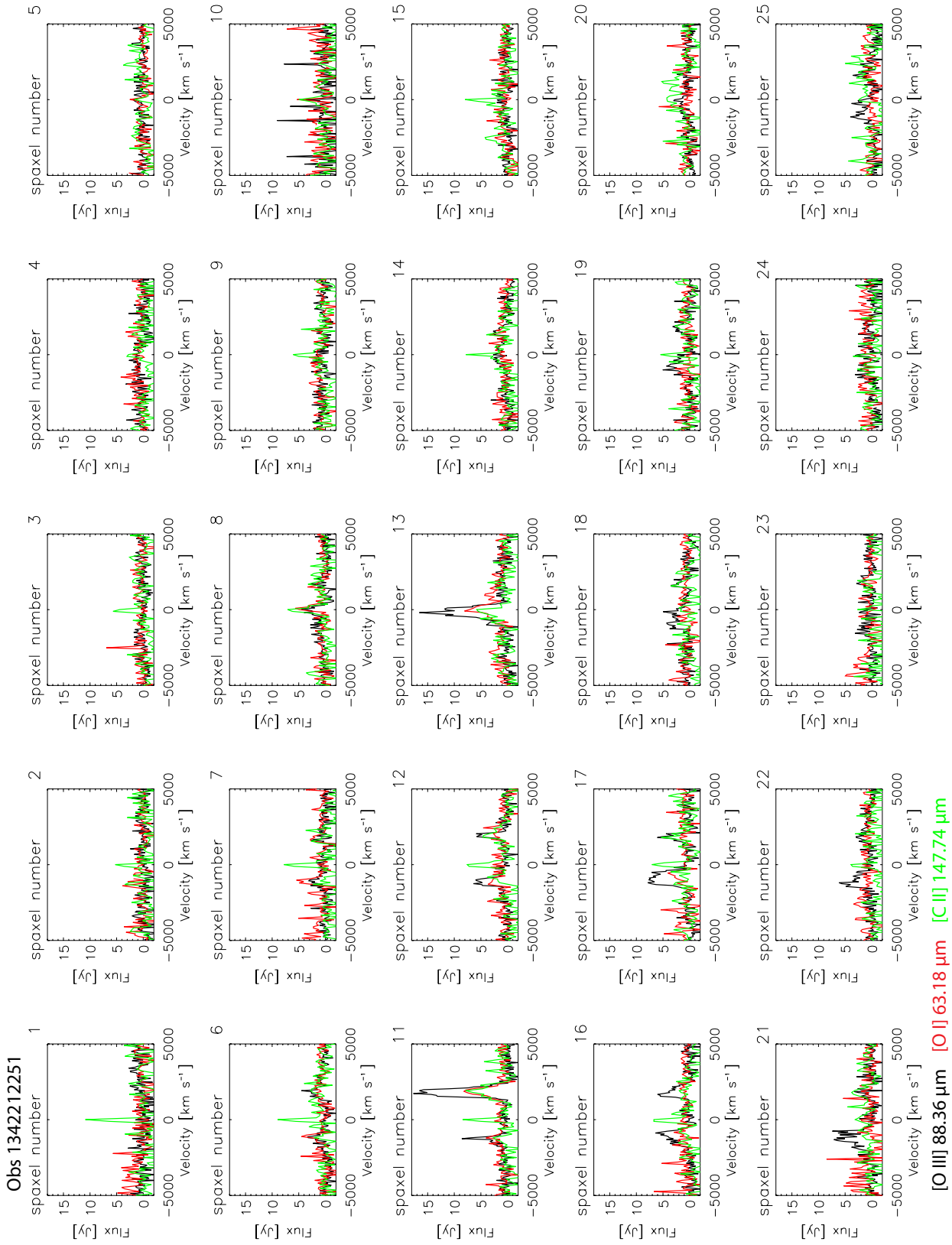


Figure 3.6. The 5x5 PACS-IFU observation SP5 of Cas A in velocity space. The black line shows the $88 \mu\text{m}$ [O III] line, the red line shows the $63 \mu\text{m}$ [O I] line and the green shows the $158 \mu\text{m}$ [C II] line.

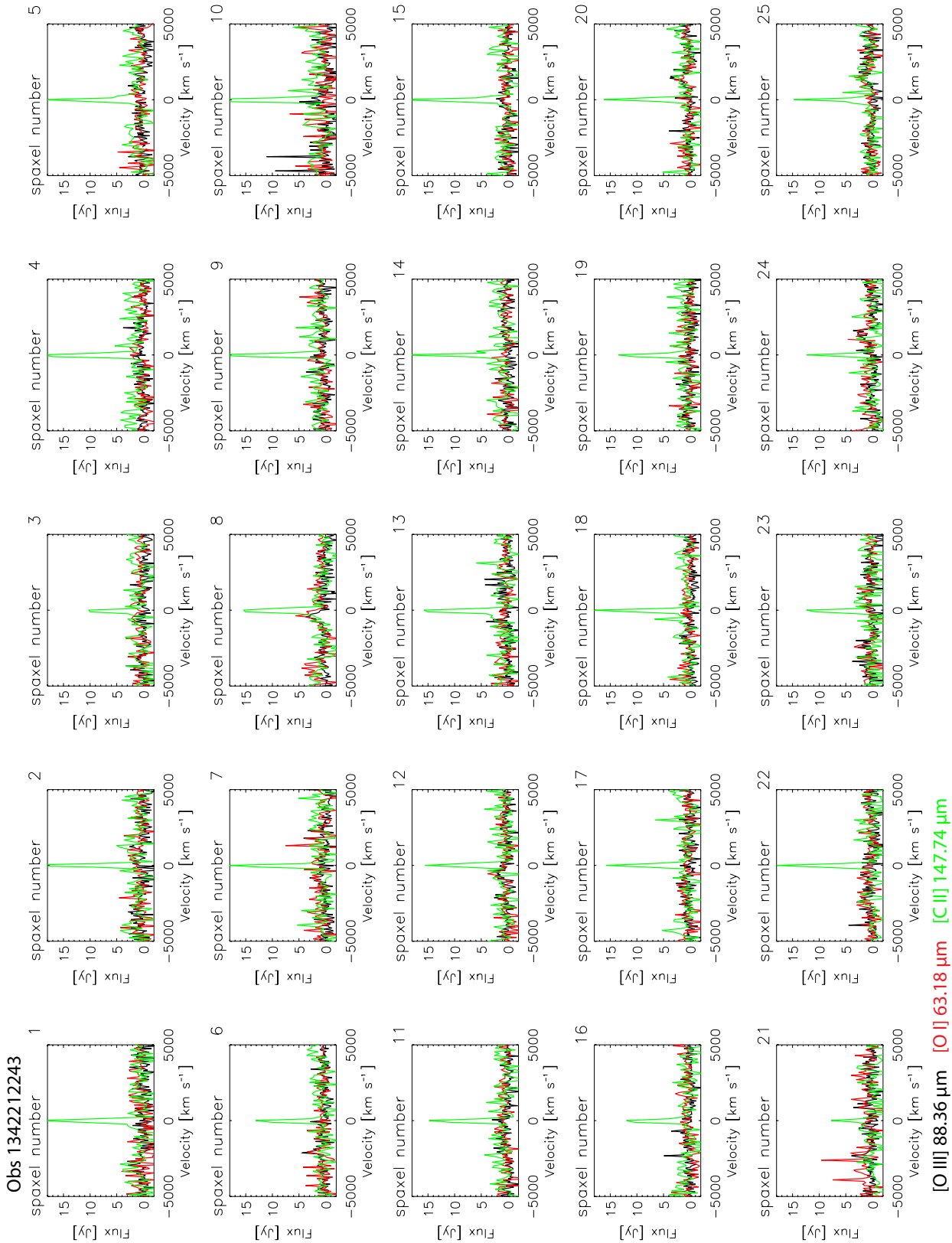


Figure 3.7. The 5x5 PACS-IFU observation SP6 of Cas A in velocity space. The black line shows the $88 \mu\text{m}$ $[\text{O III}]$ line, the red line shows the $63 \mu\text{m}$ $[\text{O I}]$ line and the green shows the $158 \mu\text{m}$ $[\text{C II}]$ line.

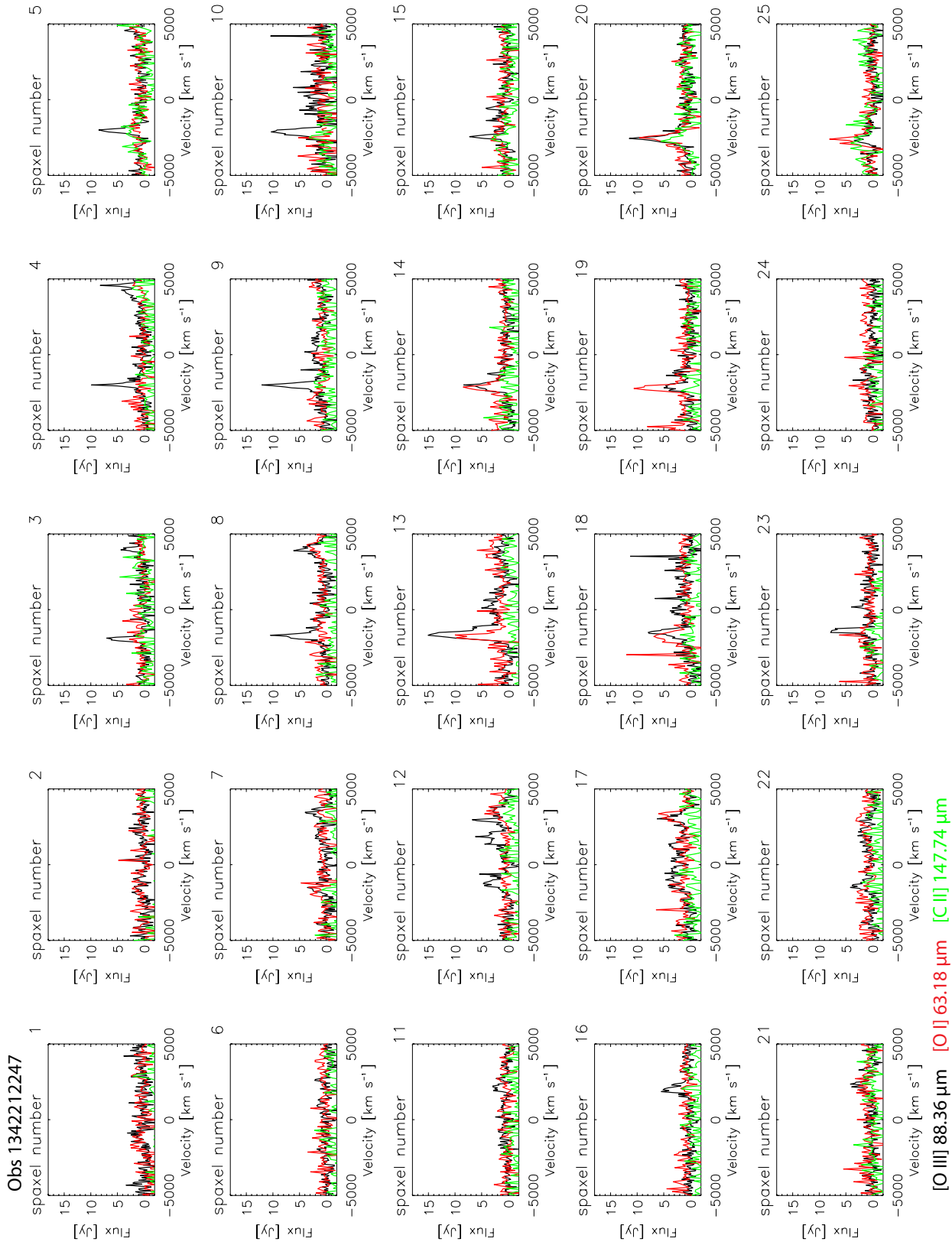


Figure 3.8. The 5x5 PACS-IFU observation SP7 of Cas A in velocity space. The black line shows the $88 \mu\text{m}$ [O III] line, the red line shows the $63 \mu\text{m}$ [O I] line and the green shows the $158 \mu\text{m}$ [C II] line.

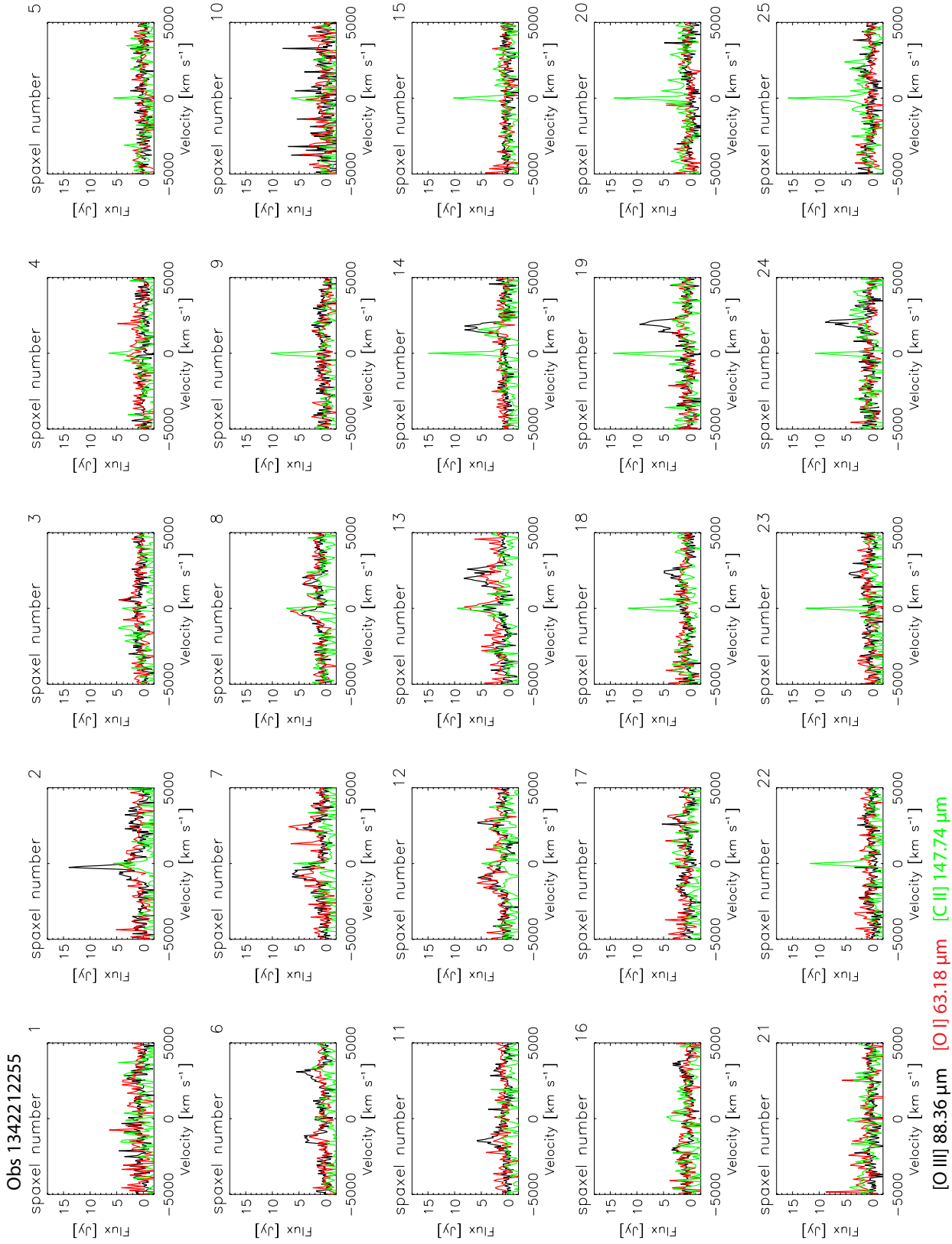


Figure 3.9. The 5x5 PACS-IFU observation SP8 of Cas A in velocity space. The black line shows the $88 \mu\text{m}$ [O III] line, the red line shows the $63 \mu\text{m}$ [O I] line and the green shows the $158 \mu\text{m}$ [C II] line.

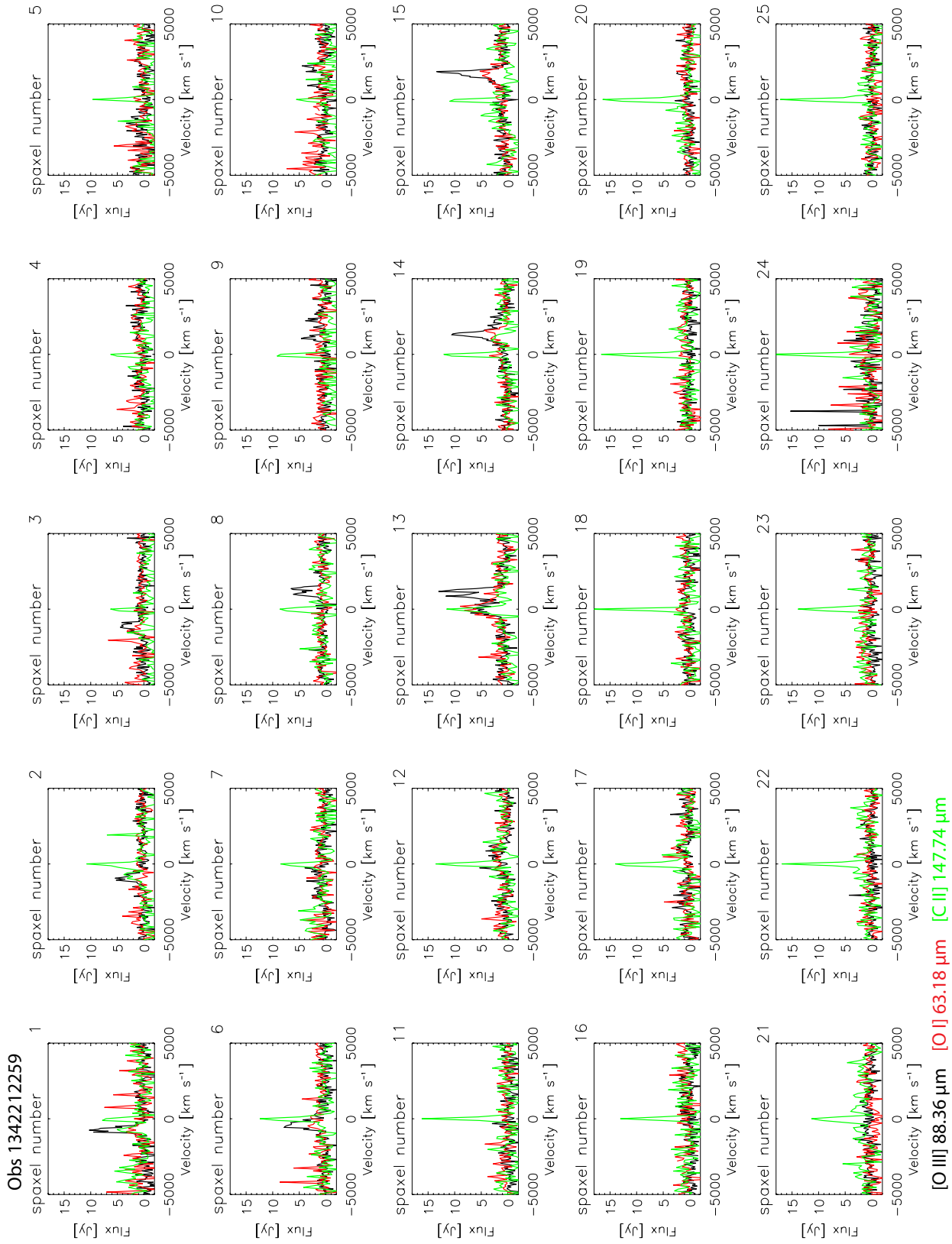


Figure 3.10. The 5x5 PACS-IFU observation SP9 of Cas A in velocity space. The black line shows the 88 μm [O III] line, the red line shows the 63 μm [O I] line and the green shows the 158 μm [C II] line.

between [O III] and ^{44}Ti is evidence of a lack of mixing between these layers. The emission is stronger in the "Bright ring" region of the remnant, this is the region that it illuminated by the reverse shock (Gotthelf et al. 2001).

The locations of the 63 μm [O I] line emission, as shown in Figures 3.13 (redshifted component) and 3.14 (blue shifted component) are much more strongly correlated with the regions of the 70 μm broadband emission. The 70 μm broadband emission traces mainly the dust in the supernova remnant. This dust provides shielding, both from shocks and ionising photons. This shielding along with higher densities reduces the degree of ionisation, enhancing [O I] emission from dusty regions.

Whilst some spaxels show 63 μm [O I] line emission, as shown in Figures 3.13 and 3.14, there is no 146 μm [O I] line emission detected anywhere in the nebula. Excitation to the $^3\text{P}_1$ level can give the 63 μm line while excitations to the $^3\text{P}_0$ level can give rise to the 146 μm and 63 μm lines (see Figure 3.15). In local thermodynamic equilibrium (LTE), statistical weights of the $^3\text{P}_2$, $^3\text{P}_1$ and $^3\text{P}_0$ levels are 5:3:1, so we would expect to see at least some emission from the $^3\text{P}_0$ to $^3\text{P}_1$ 146 μm transition. Strong [O I] 63 μm is usually an indicator of shocked material (Tielens 2005), and there are many strong shocks in Cas A (Sutherland & Dopita 1995), but models still predict some [O I] 146 μm (Dоценко & Суняев 2010). Optical thickness and self absorption in the 63 μm line (Liseau et al. 2006) can be used to explain when the situation is the other way around. These PACS-IFU observations showing a lack of [O I] 146 μm line emission are consistent with the ISO observations of Cas A (Swinyard, private communication).

3.2.2 Upper Limits to the [O I] 146 μm line flux

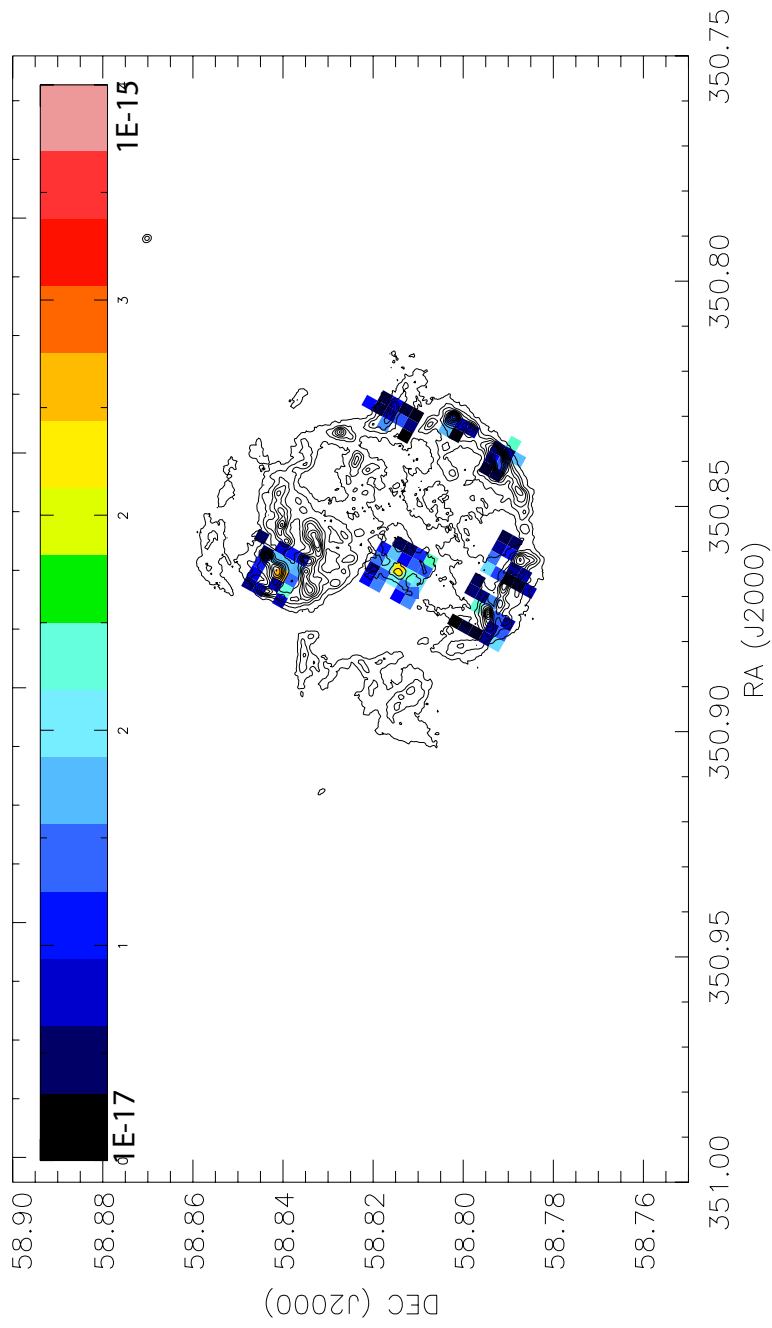


Figure 3.11. The relative flux of the red shifted emission of the [O III] 88 μ m in Cas A plotted over a contour map of the PACS 70 μ m image.

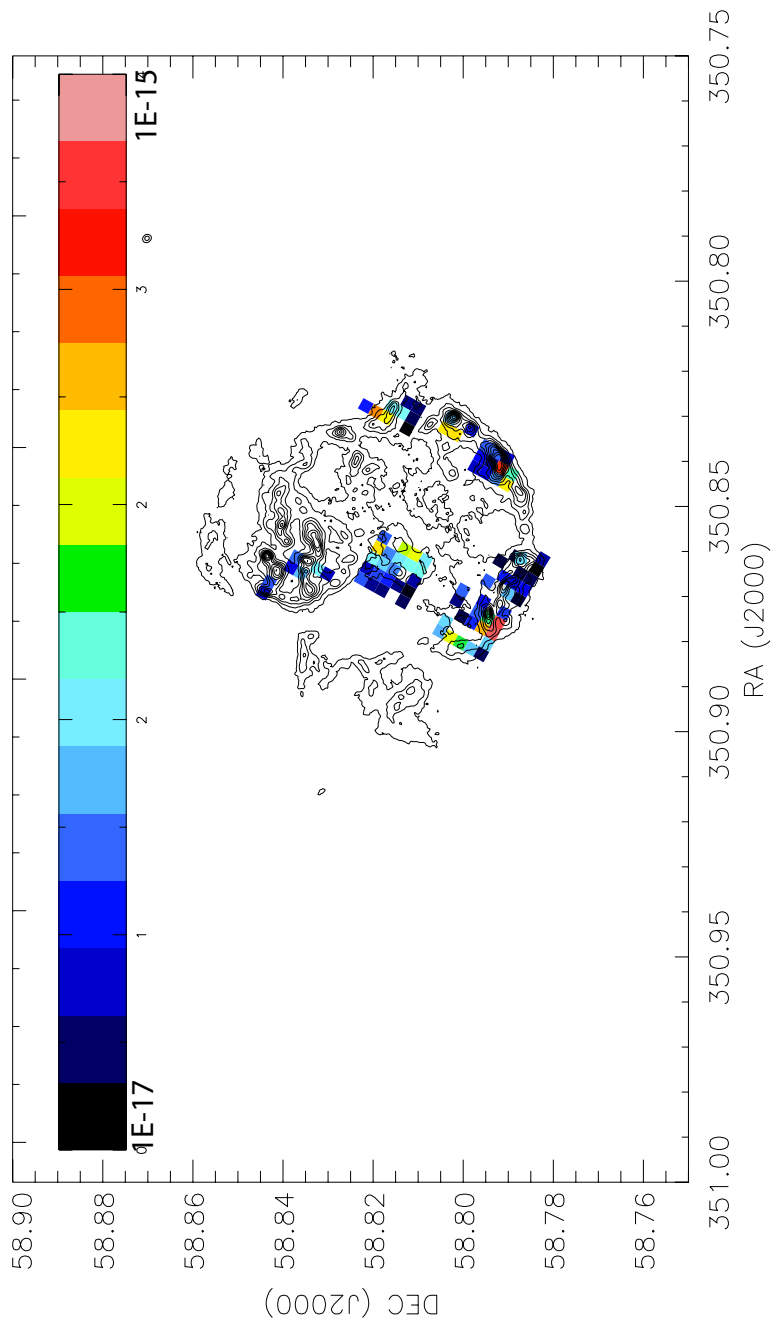


Figure 3.12. The relative flux of the blue shifted emission of the [O III] 88 μm in Cas A plotted over a contour map of the PACS 70 μm image.

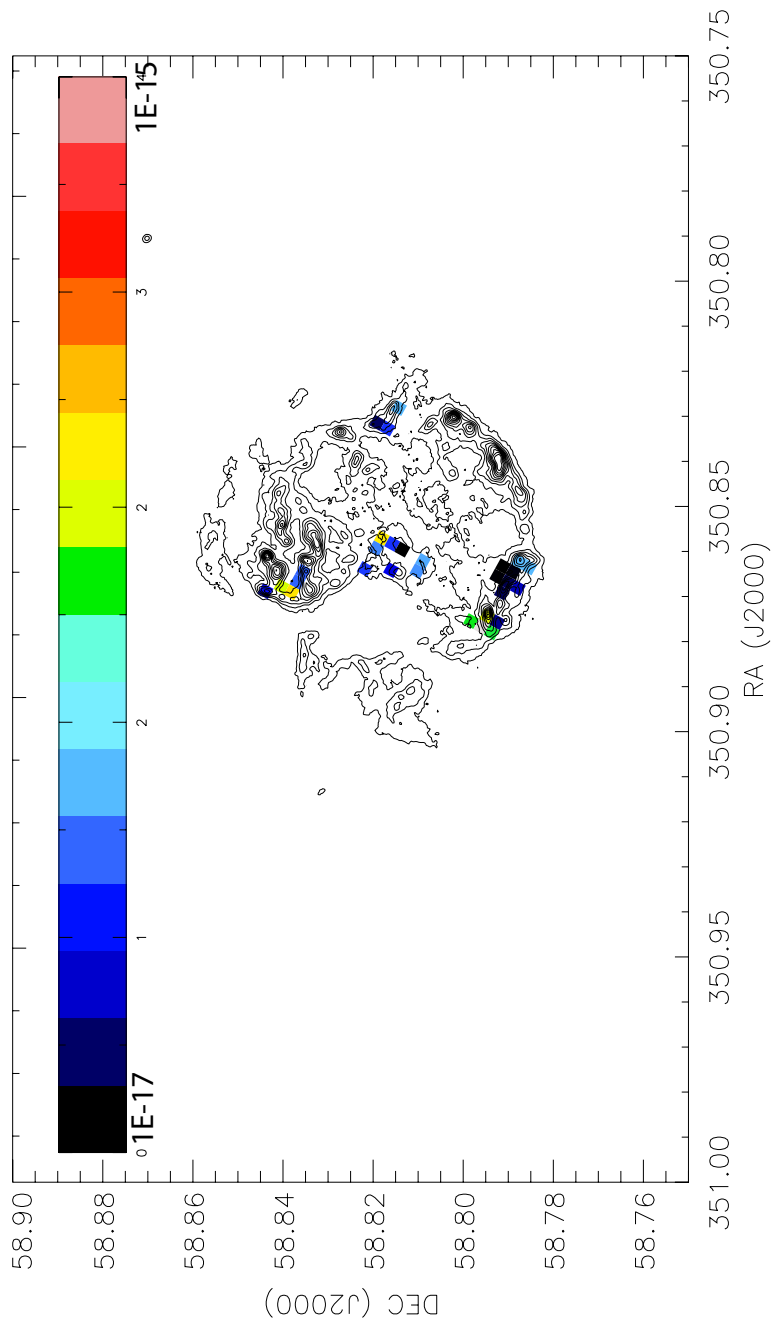


Figure 3.13. The relative flux of the red shifted emission of the [O I] 63 μm in Cas A plotted over a contour map of the PACS 70 μm image.

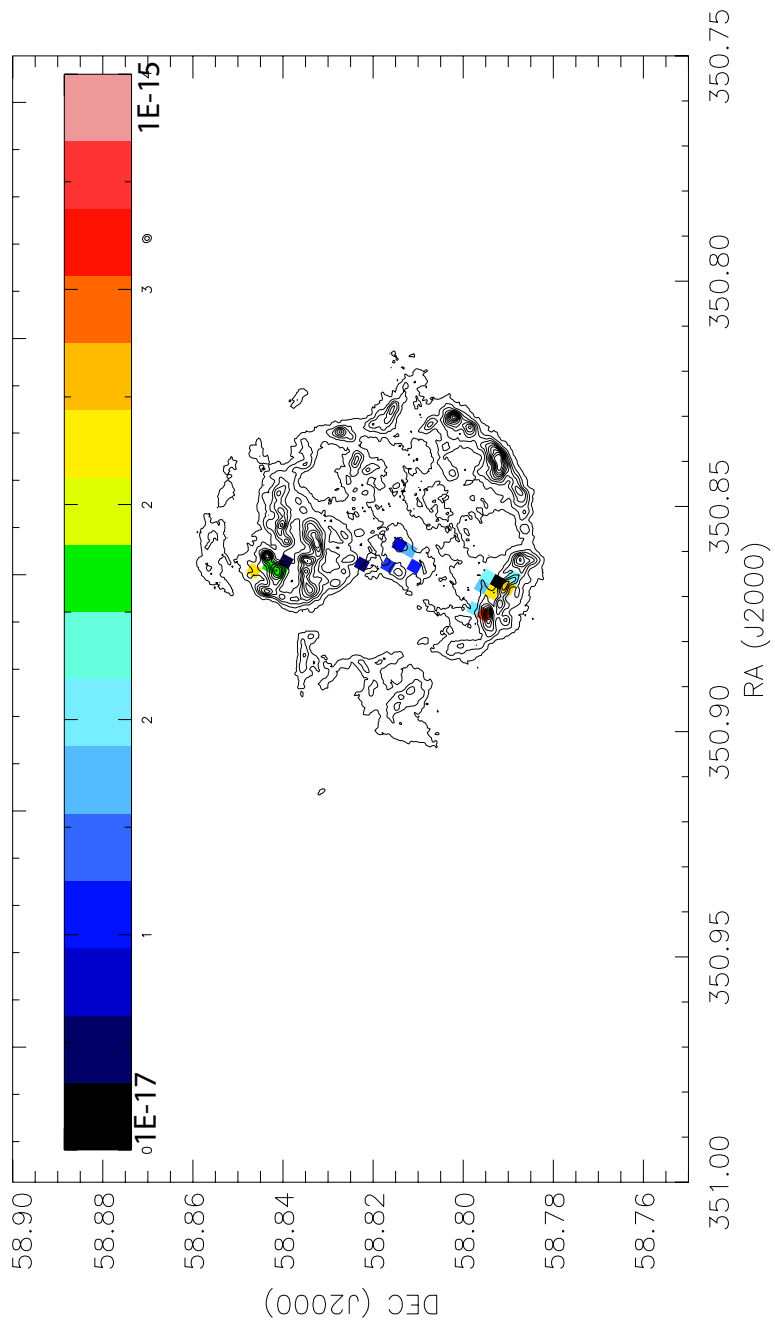


Figure 3.14. The relative flux of the blue shifted emission of the [O I] 63 μm in Cas A plotted over a contour map of the PACS 70 μm image.

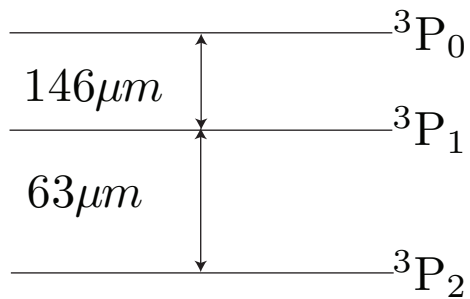


Figure 3.15. [O I] Fine-structure energy levels

The [O I] 146 μm line is not detected in the PACS spectra, so we fitted upper limits to its detection. Assuming that it will be moving at the same velocity and with the line width as the [O I] 63 μm line in the same spaxels, an upper limit was determined based on the noise in that spaxel to determine the strongest emission that would be present if the line was present. These flux limits were then used to calculate a temperature of the oxygen in the remnant via the statistical equilibrium using the multi-level code Equib (Adams et al. 1984) with collisional rate data from Launay & Roueff (1977) and transition probabilities taken from Baluja & Zeippen (1988). Figure 3.16 shows the range of temperatures and densities for one of the observed ratios (in this case the ratio of 42.1 which is calculated from the central pixel of observation SP8). The temperature upper limit is taken to be the value determined by the point at which the required density becomes very large. The results for these upper limits, ratios and temperatures are listed in Tables 3.2 for the red-shifted lines, and 3.3 for the blue-shifted lines.

The temperature upper limits range is determined to be between 100-1000 K depending on the ratio. Figure 3.17 shows a plot of the range of temperatures vs the I_{63}/I_{146} ratio. As the ratio gets lower, the temperature upper limit increases and the diagnostic becomes much less sensitive.

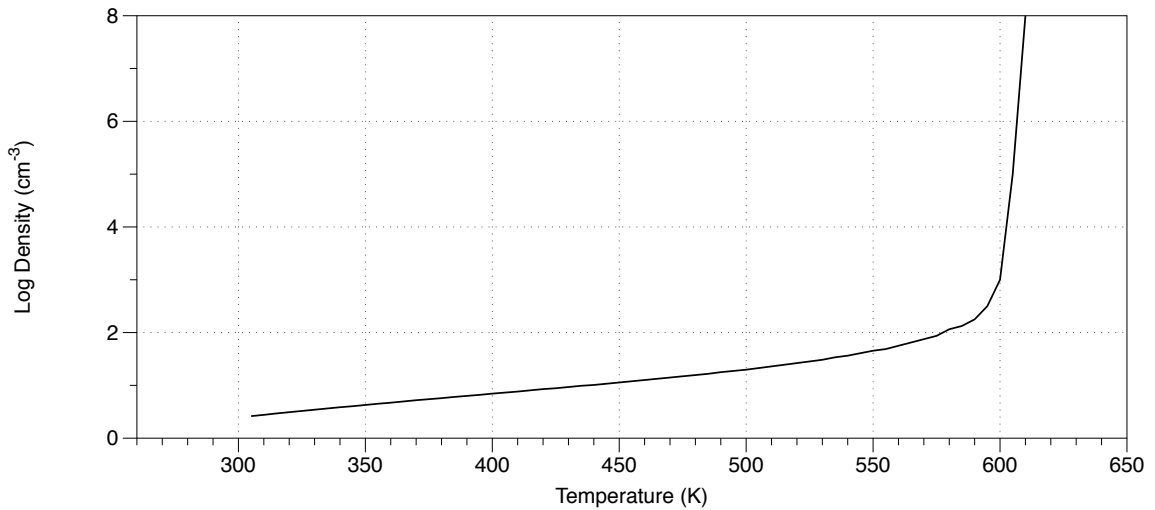


Figure 3.16. Temperature vs log density for the I_{63}/I_{146} ratio of 42.1 to illustrate the method for temperature determination.

RA	Dec	146 μm Upper Limit W m^{-2}	63 μm Flux W m^{-2}	I_{63}/I_{146}	Temperature K
350.8830042	58.81470525	<9.80E-18	2.50E-16	>25.5	<1080
350.8811421	58.81060735	<2.80E-18	2.10E-16	>75.0	<130
350.8714753	58.81447459	<7.89E-18	2.40E-16	>30.4	<1010
350.8624284	58.81765492	<7.88E-18	1.90E-16	>24.1	<1090
350.8968227	58.79279707	<3.92E-17	1.20E-15	>30.6	<1010
350.8986712	58.79093934	<2.01E-17	4.10E-16	>20.4	<1160
350.8644343	58.7899063	<1.20E-17	3.50E-16	>29.2	<1050
350.8664882	58.78777791	<3.40E-17	8.40E-16	>24.7	<1090
350.8906214	58.83448768	<9.55E-18	7.90E-16	>82.7	<115
350.8678496	58.83422957	<6.98E-18	2.30E-16	>32.9	<1070
350.8260403	58.79509426	<9.32E-18	3.50E-16	>37.6	<1000
350.8281279	58.79296599	<1.10E-17	3.70E-16	>33.6	<1000
350.8204221	58.79491939	<6.40E-18	2.30E-16	>35.9	<995
350.8224839	58.79279298	<5.10E-18	2.00E-16	>39.2	<885
350.8042412	58.80444108	<5.21E-18	3.40E-16	>65.2	<160
350.8082356	58.80020732	<8.90E-18	7.20E-16	>80.9	<120
350.8102679	58.79804986	<6.58E-18	4.90E-16	>74.5	<130
350.7991019	58.8036398	<3.07E-18	2.90E-16	>94.5	<90

Table 3.2. The upper limits on the red shifted component of the [O I] 146 μm emission [O I] 63 μm observed fluxes along with the lower limit on the ratio between them and the upper limit on observed temperature in the observations of Cas A by PACS-IFU

RA	Dec	146 μm Upper Limit W m $^{-2}$	63 μm Flux W m $^{-2}$	I ₆₃ /I ₁₄₆	Temperature K
350.8763588	58.82106041	<8.89E-18	6.30E-16	>70.9	<140
350.8785458	58.81913918	<7.97E-18	2.80E-16	>35.1	<670
350.8850601	58.8127964	<6.46E-18	3.70E-16	>57.3	<200
350.8726197	58.81907781	<8.73E-18	4.20E-16	>48.1	<320
350.8811421	58.81060735	<1.04E-17	4.60E-16	>44.2	<450
350.8714753	58.81447459	<8.38E-18	3.70E-16	>44.2	<455
350.8624284	58.81765492	<3.33E-18	2.40E-16	>72.1	<140
350.8946665	58.79497488	<9.90E-18	6.10E-16	>61.6	<180
350.8968227	58.79279707	<4.13E-17	1.03E-15	>24.9	<1090
350.8869759	58.79694464	<8.40E-18	5.40E-16	>64.3	<165
350.8890209	58.79481388	<5.02E-17	1.11E-15	>22.1	<1100
350.8911322	58.79265854	<8.90E-18	4.80E-16	>53.9	<235
350.8594759	58.78901977	<9.00E-18	5.90E-16	>65.6	<160
350.8615879	58.78684646	<8.11E-18	3.10E-16	>38.2	<1000
350.8635584	58.78470866	<9.03E-18	2.80E-16	>31.0	<1080
350.8571246	58.78561607	<6.07E-18	2.50E-16	>41.2	<590
350.8906214	58.83448768	<2.88E-18	1.90E-16	>66.0	<165
350.8790856	58.83426174	<2.12E-17	5.20E-16	>24.5	<1090
350.881202	58.83210713	<1.20E-17	6.34E-16	>52.8	<250
350.8720678	58.8355093	<1.54E-18	5.29E-17	>34.3	<1000
350.8761426	58.83119488	<9.01E-18	7.20E-16	>79.9	<120
350.8780442	58.8291443	<8.45E-18	6.00E-16	>71.0	<140
350.8678496	58.83422957	<9.99E-18	3.25E-16	>32.5	<1000
350.8697029	58.8321075	<7.12E-18	3.00E-16	>42.1	<585
350.8735146	58.82777344	<7.69E-18	5.90E-16	>76.7	<125
350.8260403	58.79509426	<8.78E-18	3.70E-16	>42.1	<585
350.8281279	58.79296599	<1.54E-17	4.60E-16	>29.9	<1050
350.8204221	58.79491939	<2.11E-17	6.60E-16	>31.3	<995
350.8224839	58.79279298	<1.32E-17	5.00E-16	>37.9	<990

Table 3.3. The upper limits on the blue shifted component of the [O I] 146 μm emission and [O I] 63 μm observed fluxes along with the lower limit on the ratio between them and the upper limit on observed temperature in the observations of Cas A by PACS-IFU

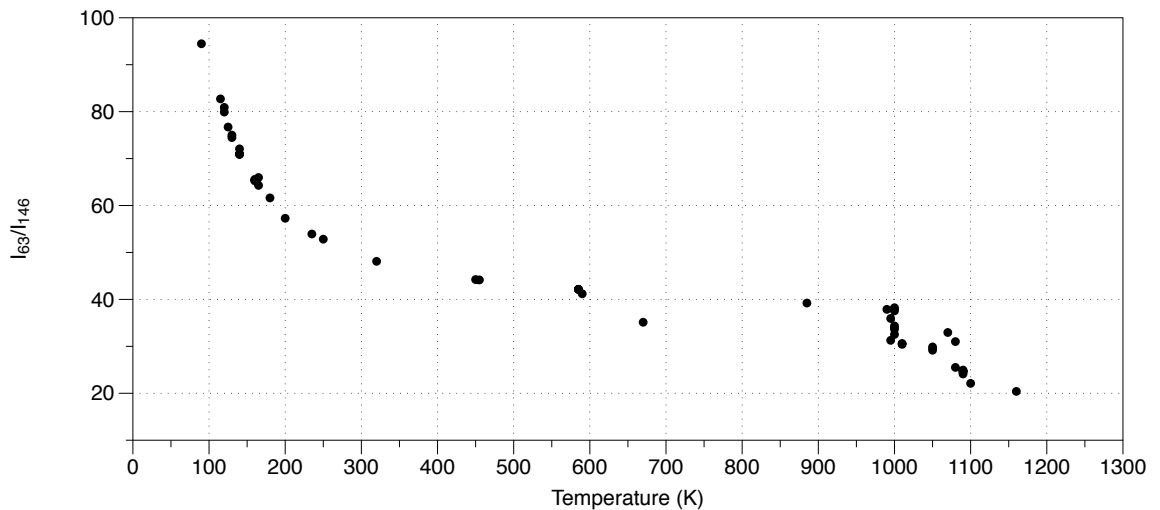


Figure 3.17. The temperature determined from the I_{63}/I_{146} ratio against that ratio to show the range of temperatures and the decrease in sensitivity as the ratio decreases.

3.2.3 The $158\ \mu\text{m}$ [C II] line

Although Cas A is vastly oxygen rich, we have also detected emission from the [C II] $158\ \mu\text{m}$ line. Whilst most of the observations of this line towards Cas A shows it to be narrow and slow-moving, and thus interstellar or circum-nebula in origin, we also for the first time detect some broad lines emission with similar velocities and line widths to the oxygen lines. Figure 3.18 (red) and 3.19 (blue) show the locations of both the red- and blue-shifted broad [C II] $158\ \mu\text{m}$ line emissions in Cas A.

Small amounts of carbon are predicted to be in the remnant by Docenko & Sunyaev (2010) due to the strong $6300\ \text{\AA}$ oxygen line, which they interpret as due to a charge exchange between carbon and oxygen. Although some of the carbon may be locked up in CO in neutral regions, some of it will be free as CO formation is a two way process particularly (meaning it can also be broken down in the its constituent carbon and oxygen) in high energy environments such as supernovae (Clayton et al. 1999) and in partially ionised regions. This is borne out by the [C II] $158\ \mu\text{m}$ line emission being coincident with the broadband $70\ \mu\text{m}$ emission. Dust shielding

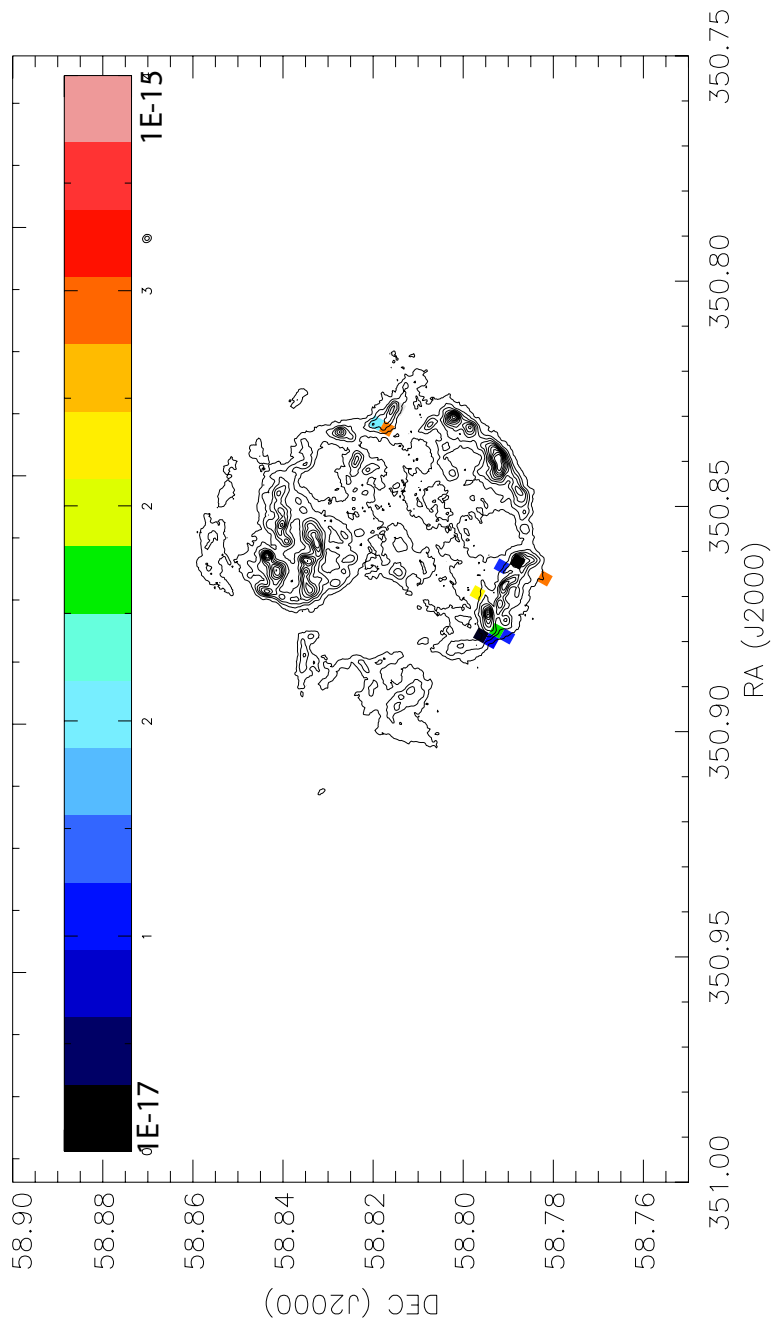


Figure 3.18. The relative flux of the red shifted emission of the [C II] 158 μm in Cas A plotted over a contour map of the PACS 70 μm image.

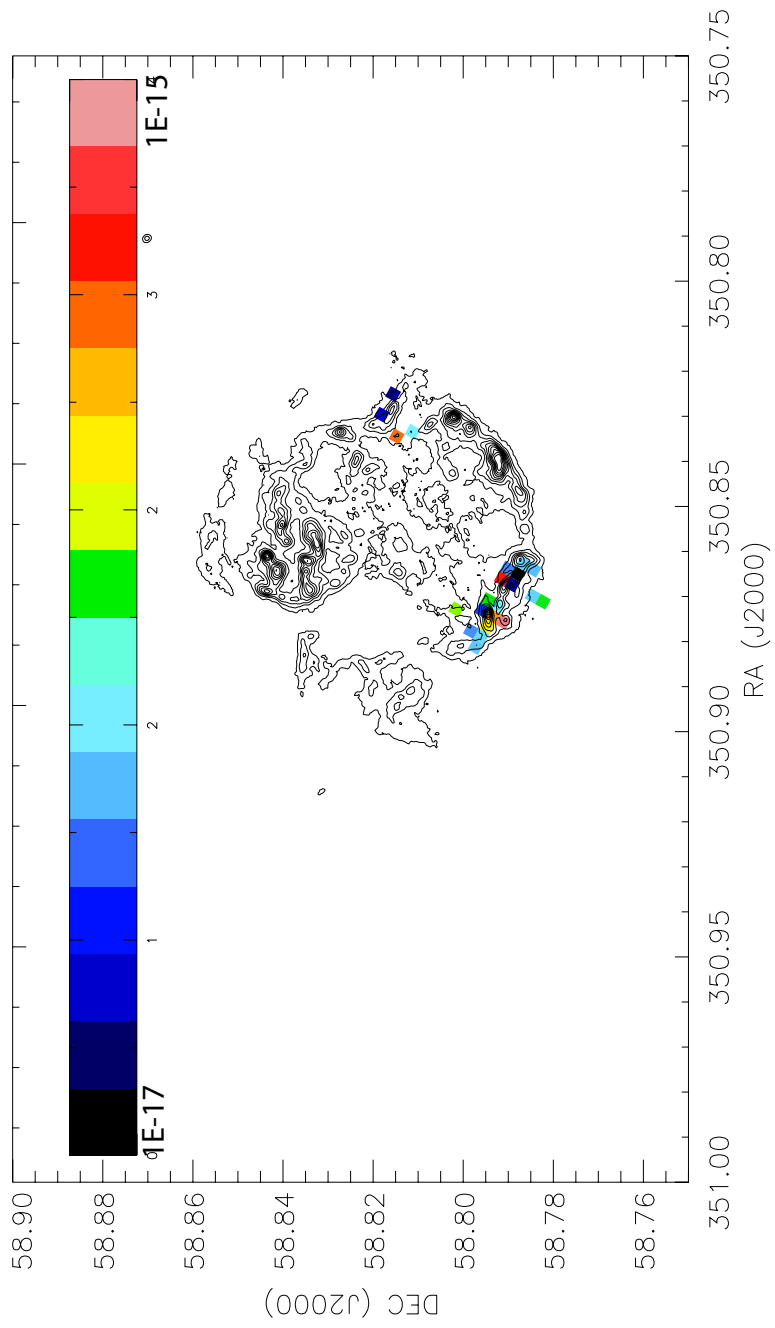


Figure 3.19. The relative flux of the blue shifted emission of the [C II] 158 μm in Cas A plotted over a contour map of the PACS 70 μm image.

3.3 Cas A with SPIRE-FTS

Near-Infrared line emission in the fundamental vibrational mode of carbon monoxide (CO) has been observed in Cas A using *Spitzer* (Rho et al. 2009). Both hot (2000 K) and cold (200 K) populations of highly rotationally excited CO have been observed with *Herschel*-PACS by Wallström et al. (2013).

The *Herschel* SPIRE-FTS spectrometer was used to observe 3 positions towards Cas A on the 23rd of August 2010. The positions of the SSW detectors for each of these observations are shown in Figure 3.20. Data were processed using HIPE version 11.0.1 (Ott 2010) using the standard pipeline. A polynomial was fitted to remove the continuum and then lines were fitted with a sinc function, used because this is the instrumental profile of a Fourier Transform Spectrometer such as SPIRE-FTS.

The majority of the SPIRE spectra contain narrow [C I] and J=5-4 and 4-3 CO lines which are interstellar or circum-nebula in origin. However, in two detector positions in the North of the remnant on the "bright ring", we observed several broad high-J CO lines. These were observed close to a structure related the structure where Wallström et al. (2013) have observed CO with *Herschel*-PACS, as shown in Figure 3.21 which shows the two SPIRE-FTS detectors which detected CO along with the position Wallström et al. (2013) PACS observation plotted on a 70 μm *Herschel* image. One of the SPIRE positions is coincident with the position Wallström et al. (2013) and Rho et al. (2009) detected broad CO emission, whilst the other is in a separate structure to the north of it. Figure 3.22 shows the spectrum of SSWC5 detector where the broad CO lines have been observed with the observed transitions labelled. The fluxes of these lines and the lines detected by the SSWC4 detector are listed in Table 3.4.

Figure 3.23 is a rotational excitation diagram for the broad CO lines observed with SPIRE-FTS detector SSWC4 using the technique described in section 1.11. The best fit parameters for this give a CO rotation temperature of $T_{ex} = 305 \pm 15$ K and assuming a knot size of 0.5" as adopted in previous investigations (Rho et al. 2009; Wallström et al. 2013) a column density of $N_{CO} = 8.7 \pm 0.5 \times 10^{16} \text{ cm}^{-2}$. These values are lower than those determined for the adjacent region by Wallström et al. (2013) of $T_{ex} = 560 \pm 20$ K

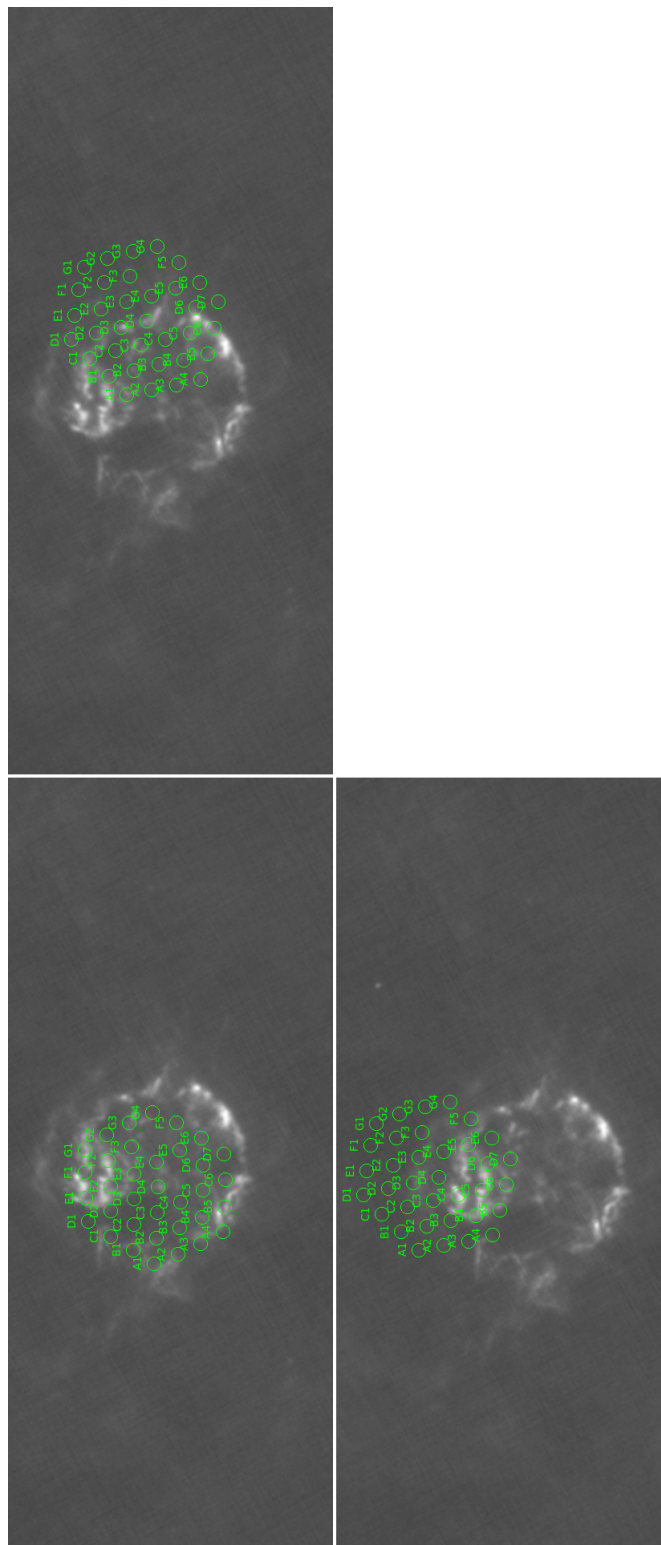


Figure 3.20. Positions of the SSW detectors of the three *Herschel* SPIRE-IFU on Cas A plotted on a $70 \mu\text{m}$ image. The "Central" observation is shown in top left, top right is the "North West" and bottom left is the "North" observation.

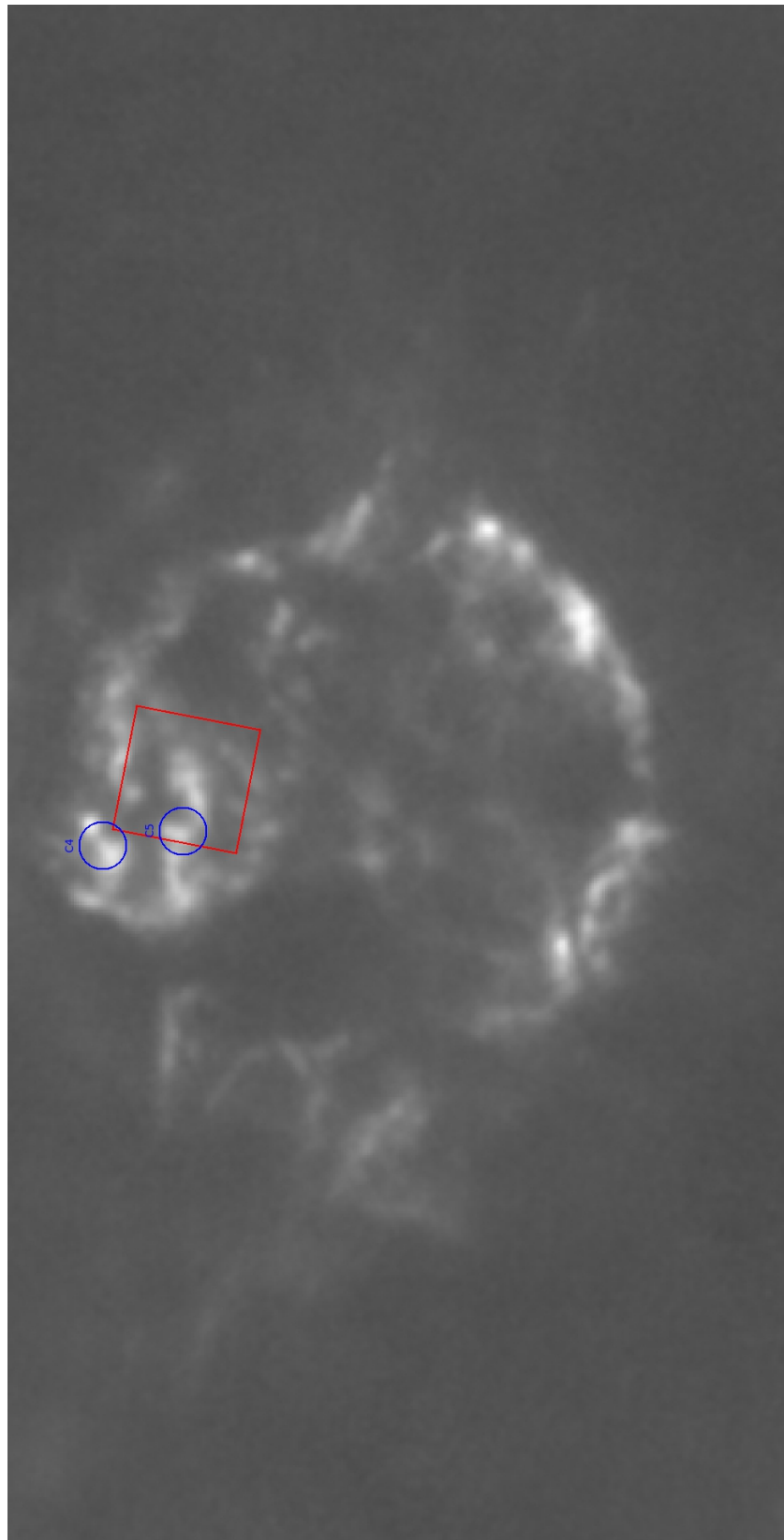


Figure 3.21. Blue circles show SPIRE SSWC4 and C5 in which CO was detected. Red square shows the locations of the PACS CO detections of Wallström et al. (2013) plotted on a $70\text{ }\mu\text{m}$ Herschel PACS image of the northern half of the remnant.

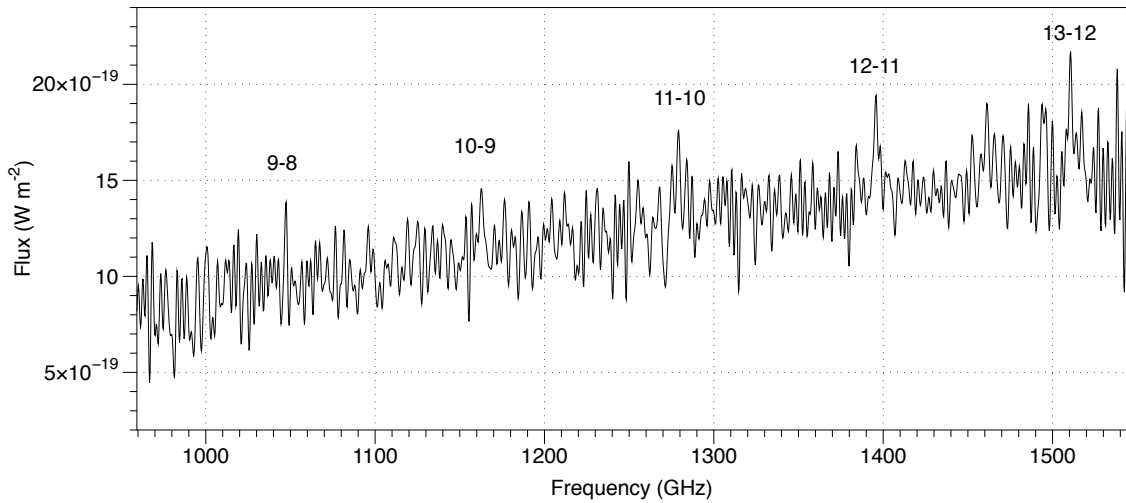


Figure 3.22. the observed spectrum of Cas A with detector SSWC5 of the Herschel SPIRE-FTS - lines from CO rotational transitions are labelled.

SSWC4			
CO J Transition	Flux W m ⁻²	Radial Velocity km s ⁻¹	FWHM km s ⁻¹
9-8	6.61×10^{-16}	-2987	661
10-9	8.63×10^{-16}	-2800	418
11-10	1.59×10^{-16}	-2659	599
12-11	1.53×10^{-16}	-2991	509
13-12	1.41×10^{-16}	-2715	700
SSWC5			
CO J Transition	Flux W m ⁻²	Radial Velocity km s ⁻¹	FWHM km s ⁻¹
9-8	1.59×10^{-16}	-3624	400
10-9	1.07×10^{-16}	-3302	491
11-10	1.82×10^{-16}	-3041	447
12-11	1.99×10^{-16}	-2805	601
13-12	2.51×10^{-16}	-3331	576

Table 3.4. The measured fluxes, radial velocity and FWHM of the CO rotation lines observed with *Herschel* SPIRE-FTS. $T_{ex} = 305 \pm 15$ K $N_{CO} = 8.7 \pm 0.5 \times 10^{16}$ cm⁻².

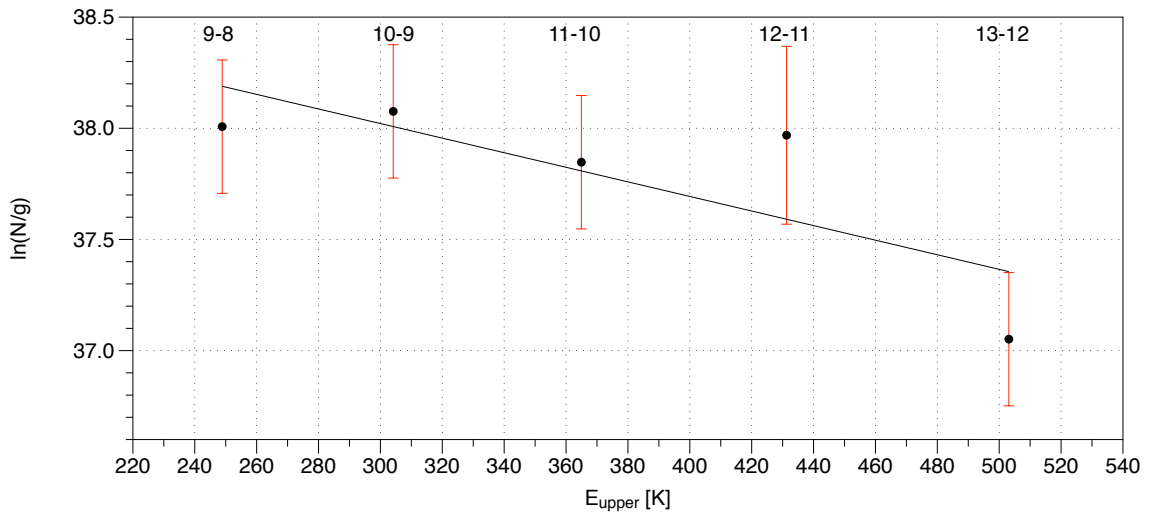


Figure 3.23. A CO rotation excitation to determine temperature and column density using Herschel SPIRE-FTS observations of Cas A-NW with detector SSW C4.

and $N_{CO} = 4.1 \pm 0.3 \times 10^{16} \text{ cm}^{-2}$.

Figure 3.24 is a rotation excitation population diagram of the CO observed with SPIRE-FTS detector SSWC5. This is the detector that is coincident with the Rho et al. (2008) and Wallström et al. (2013) observations of Cas A. The rotational temperature is determined to be $T_{ex} = 554 \pm 25 \text{ K}$ with a column density of $N_{CO} = 4.0 \pm 0.5 \times 10^{17} \text{ cm}^{-2}$ which is in very good agreement with the values determined by Wallström et al. (2013) from the higher J CO lines.

Figure 3.25 shows CO excitation diagram for the same set of observations and also includes the Wallström et al. (2013) observations. The best fit parameters for the temperature including the Wallström et al. (2013) observations is $T_{ex} = 540 \pm 25 \text{ K}$ with a column density of $N_{CO} = 4.3 \pm 0.5 \times 10^{17} \text{ cm}^{-2}$.

3.4 CO and [C II]

The regions of the nebula in which the broad, fast moving CO is detected and those in which the broad [C II] lines detected with PACS are observed are completely different as shown in Figure 3.26. In the region with the broad CO emission, the carbon may be locked up in the CO, while CO is yet to form or reform after shock interactions in the

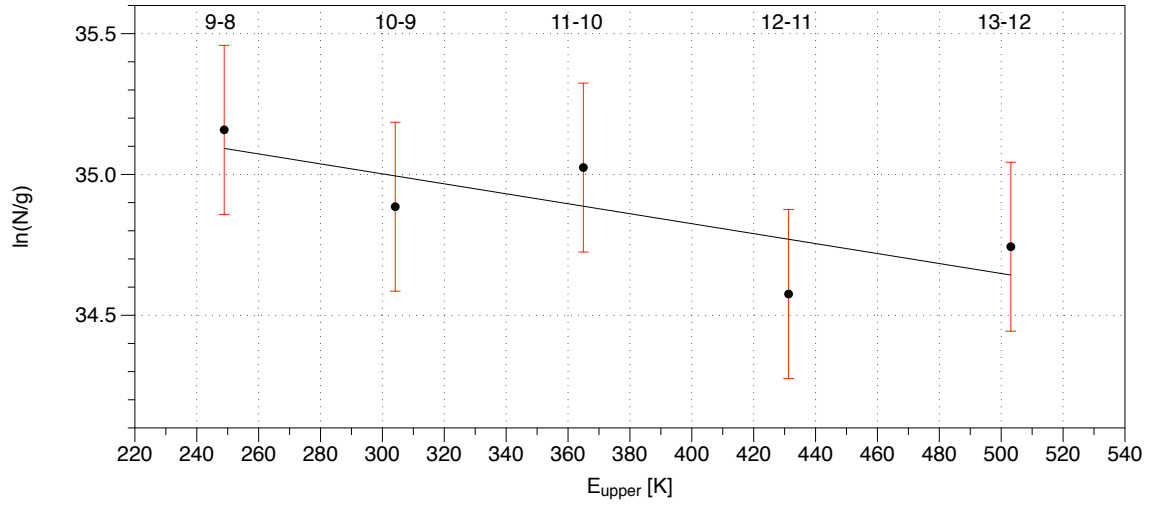


Figure 3.24. A CO rotation excitation to determine temperature and column density using Herschel SPIRE-FTS observations of Cas A-NW with detector SSW C5. $T_{\text{ex}} = 554 \pm 25$ K $N_{\text{CO}} = 4.0 \pm 0.5 \times 10^{17}$ cm $^{-2}$.

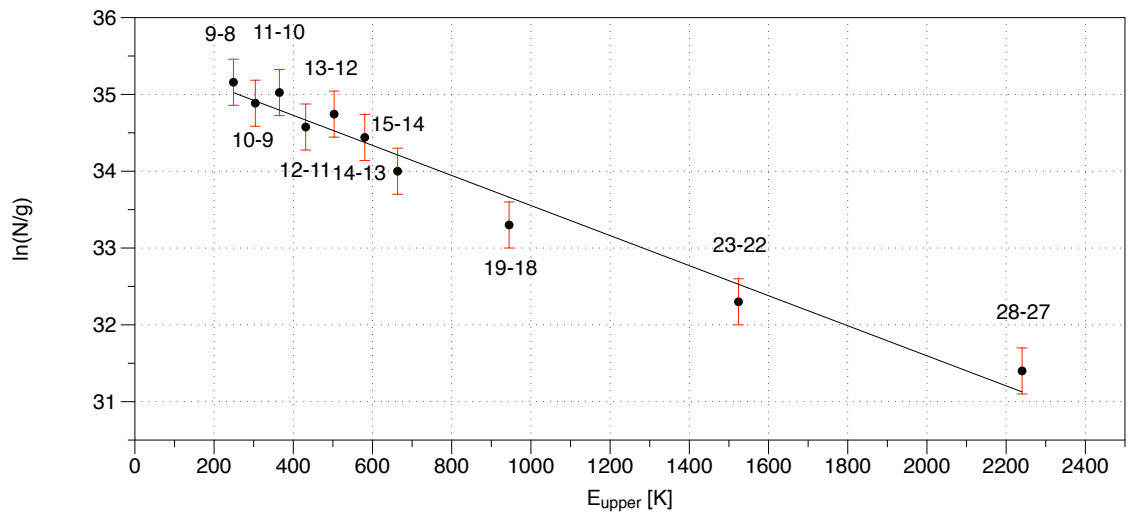


Figure 3.25. A CO rotation excitation to determine temperature and column density using Herschel SPIRE-FTS observations of Cas A-NW with detector SSW C5 and the *Herschel* PACS observations from Wallström et al. (2013). $T_{\text{ex}} = 540 \pm 25$ K $N_{\text{CO}} = 4.3 \pm 0.5 \times 10^{17}$ cm $^{-2}$.

regions when the broad [C II] line emission is observed. We did not detect any of the high J CO lines detected by Wallström et al. (2013) in the PACS spectra presented here. The Wallström et al. (2013) observations were done as line scans looking just in the region of the specific lines rather than being made over the entire wavelength range of the detectors. The Wallström et al. (2013) observations were also an order of magnitude longer on source than those presented here.

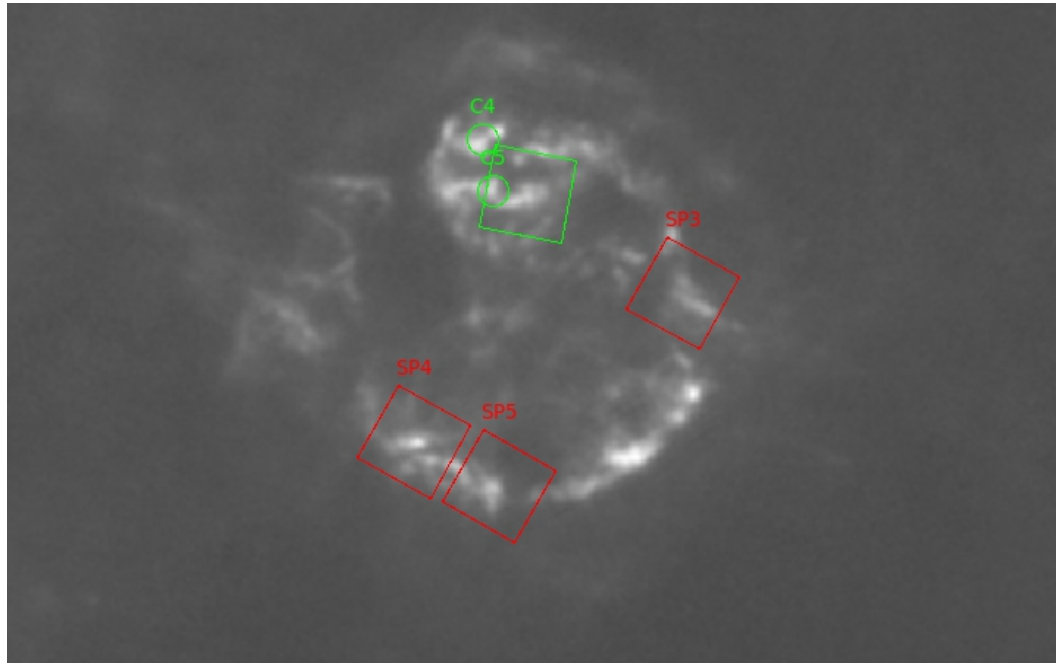


Figure 3.26. *Herschel* PACS 70 μm map of Cas A shows the regions with where broad CO emission has been detected shown in green and the regions where the broad [C II] lines have been observed shown in red.

3.5 Conclusions

Cassiopeia A was observed with the Herschel PACS and SPIRE Spectrometers. The fact that the shortward end of the PACS-IFU does not go short enough to reasonably measure the 52 μm [O III] line means that the electron density can not be estimated using the [O III] 52/88 μm diagnostic discussed in the previous chapter. Broad, high velocity emission from the 158 μm [C II] line was observed for the first time in Cas A in the south of the remnant, with PACS, while broad carbon monoxide emission has been observed with SPIRE, as well as by previous observers (Wallström et al. 2013; Rho et al. 2009) in the north of the remnant.

The broad $63 \mu\text{m}$ [O I] line is also observed, but $146 \mu\text{m}$ [O I] line emission is not, so upper limits were determined for its observation based on the velocity, and line width of the $63 \mu\text{m}$ [O I] line emissions. The observed lower limits to the ratio of $63 \mu\text{m}$ to $146 \mu\text{m}$ [O I] fluxes can not be explained using electron collision alone as to get the strength of $63 \mu\text{m}$ observed with the upper detection limit of the $146 \mu\text{m}$ [O I] line would require temperatures of 10^7 K using electrons as the collision partner, which is far too high for a the region of the remnant with neutral hydrogen and oxygen present. However, using neutral atomic hydrogen as an collision partner for the excitation, we find a range of temperatures from 100-1000 K which is consistent with the temperatures of 300-500 K determined from the CO rotation temperatures. Although Cas A is hydrogen poor, there are currently no data for oxygen-oxygen collisional excitation which might give a more realistic result. Table 3.5 gives a summary of the temperatures determined in the supernova remnant using the different measures.

Method	Lowest Temperature Measured	Highest Temperature Measured
Oxygen Line Ratio	120	1080
CO Rotation	305	554

Table 3.5. Temperatures measured in Cas A, using CO rotational temperatures and $63 \mu\text{m}$ [O I] line emission and upper limits placed on $146 \mu\text{m}$ [O I] line emission.

Emission the $88 \mu\text{m}$ [O III] is stronger in the regions when the $70 \mu\text{m}$ broadband emission is brightest (and thus the dustiest regions), however it is present in most of the remnant. The broad $63 \mu\text{m}$ [O I] and $158 \mu\text{m}$ [C II] emissions are coincident only with the brightest dustiest regions of the observations.

The analysis of the CO lines observed with SPIRE-FTS using rotation diagrams is consistent with previous observations by Wallström et al. (2013), giving a temperatures of 300-500 K and a column density $5 \times 10^{17} \text{ cm}^{-2}$. We could not perform a more detailed non LTE analysis using a code such as RADEX (van der Tak et al. 2007) as it assumes that the collision partner is hydrogen. Cas A is so oxygen rich that it, rather than hydrogen will be the collision partner and data does not yet exist for collisions between oxygen and

CO.

This page was intentionally left blank

Chapter 4

Dust in the Crab Nebula

You've got to make the dust before you can destroy it

Mike Barlow

Mid infrared dust mass estimates for the Crab Nebula using *Spitzer* found relatively small amounts of dust in the Crab Nebula supernova remnant. Temim et al. (2006) found $0.001\text{--}0.01 M_{\odot}$ of dust, which was later refined to an even lower $(1.2\text{--}12)\times 10^{-3} M_{\odot}$ using *Spitzer* IRS spectroscopy rather than relying purely on photometry (Temim et al. 2012).

These observations did not have far infrared information beyond $70 \mu\text{m}$, needed to accurately measure the total dust mass by constraining the mass of cold dust. Gomez et al. (2012) presented far infrared dust emission data from *Herschel*, along with observations from the *Planck* point source catalogue of the Crab Nebula between 350 and 1323 μm , the latter being used to more tightly constrain the synchrotron background than any previous measurements of dust mass. Using these data, along with data from *Spitzer* and WISE (Wide-field Infrared Survey Explorer), allowed Gomez et al. (2012) to make an estimate of the total dust mass in the remnant for the first time. They found between 0.1 and $0.3 M_{\odot}$ of dust, depending on the grain species assumed.

Earlier still, IRAS made observations between $12\text{--}100 \mu\text{m}$ (Marsden et al. 1984), with observed fluxes at $100 \mu\text{m}$ within 10% of those observed by *Herschel*. However, when esti-

mating the dust, a much larger synchrotron component was subtracted by Marsden et al. (1984) as it was not so tightly constrained at the time. This led to an estimated dust mass of $10^{-3} M_{\odot}$ for 80 K grains having a λ^{-1} emissivity or $0.03 M_{\odot}$ for 50 K grains having a λ^{-2} emissivity. Green et al. (2004) combined ISO 60 and 100 μm fluxes with 850 μm observations taken using the Submillimetre Common-User Bolometer Array (SCUBA) on the James Clerk Maxwell Telescope (JCMT). The ISO 60 and 100 μm observations were 1.5 and 1.7 times lower than the *Herschel* fluxes which may be attributable to calibration problems with the ISOPHOT instrument at that time and the data not being scientifically validated (Lemke et al. 1996). From these observations Green et al. (2004) determined the dust mass to be 0.01-0.07 M_{\odot} for the case of silicates and 0.003-0.02 M_{\odot} for the case of graphite dust. The Green et al. (2004) lower estimate comes from both the lower fluxes at 60 and 100 μm and the non-detection of an infrared excess, attributable to dust, the Crab Nebula at 170 μm where the observed flux limit was below the estimated synchrotron background.

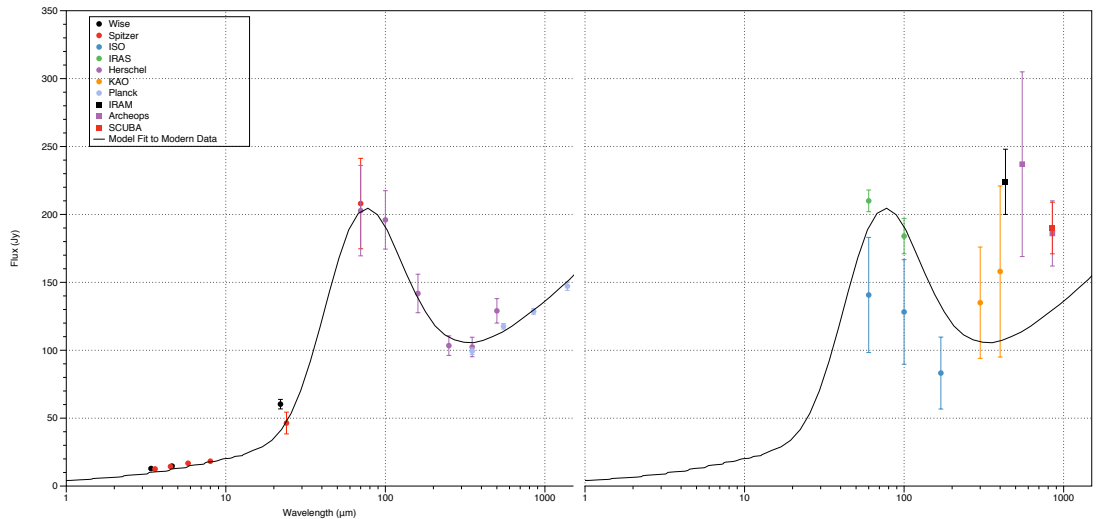


Figure 4.1. Left: Modern infrared observations of the Crab Nebula from *Spitzer* (red circles), *Herschel* (purple circles) and *Planck* (light blue circle) as used by Gomez et al. (2012) with modelled SED. Right: Archival/previous IR observations of the Crab Nebula taken from WISE (black circles), ISO (dark blue circles), IRAS (green circles), KAO (orange circles), IRAM (black square), Archeops (purple squares) and SCUBA (red square) also shown with a modelled fitted to the modern data for comparison.

Figure 4.1 shows a plot of the more recent data used by Gomez et al. (2012) on the

left, and a plot of all the previous fluxes on the right. This clearly illustrates where the large differences in the measured dust masses have come from. The higher *Herschel* flux measurements in the far infrared combined with the lower submm fluxes taken from the Planck Early Release Compact Source Catalogue, constraining the background couple to yield a much increased estimate for the amount of cold dust in the nebula, especially when compared to the much lower ISO dust flux and higher SCUBA, IRAM 30 m telescope, Kuiper Airborne Observatory (KAO) and Archeiops points constraining the synchrotron background at that time.

The Crab Nebula is rare amongst SNRs in not being collisionally ionized but is instead photoionized by synchrotron radiation from the pulsar wind nebula at the center of the remnant (Hester 2008). This means that it can be successfully modelled using 3D photo-ionization codes such as the MOCASSIN code (Ercolano et al. 2003, 2005, 2008) which allows for arbitrary gas and dust geometries and density distributions, diffuse radiation fields and multiple point input radiation sources with user-specified spectra, and multiple dust grain species having user-specified grain size distributions.

Dust absorbs light in the UV and optical regimes. This heats the dust which then causes it to emit light in the far infrared. This infrared emission leads to an excess over the continuum. By observing and fitting to this infrared excess it is possible to quantify the mass of dust in an object. At its simplest case, the can be done by fitting a modified black body curve to the emission and using the equation (Hildebrand 1983)

$$M_d = \frac{S_\nu D^2}{\kappa_\nu B(\nu, T)} \quad (4.1)$$

where S_ν is the flux density, D is the distance, κ_ν is the dust mass absorption coefficient and $B(\nu, T)$ is the Planck function. Different temperature grains can be considered by using multiple Planck functions, as done by Temim & Dwek (2013). This in turn can be considered analogous to different grain sizes as smaller grains emit less efficiently, and are thus warmer. Observational fits typically use two temperature components; one for warm dust and one for cold dust. Regardless of how many different temperature components are used, this method does not take into account how the dust is heated and assumes that each grain of the same size has the same temperature. This method also does not consider

the location of the dust, assuming it to be isotropically distributed. If the dust is contained within dense clumps, rather than smoothly distributed throughout the nebula then the dust on the outside of the clumps will absorb all the heating photons. This will mean that the dust further into the clumps is heated less and will emit at a colder temperature, which in turn means that a higher mass of dust will be needed to give the observed emitted flux. Figure 4.2 displays a composite Hubble Space Telescope and *Herschel* 70 μm image showing the dust emission closely aligned with the optical knots and filaments showing that dust is not homogeneously distributed throughout the nebula.

There are several different species of dust in the interstellar medium. The two main types are believed to be amorphous carbon and silicate grains (Mathis, Rumpl, & Nord-sieck 1977). For each of these species there are several sets of optical constants available, determined using different experimental techniques and theoretical models. Amorphous carbon is an umbrella term used for grains made of carbon and hydrocarbon chains. Silicate grains can be made up of several compounds containing silicon, magnesium, iron, and oxygen. They are more reflective in optical wavelengths than carbon grains thus absorb less there and so emit less. This means that typically more silicate dust is required to fit observed infrared excess continuum emission. Which species of dust dominates depends on the elemental abundances and chemistry in the region.

4.1 The Models

MOCASSIN (Ercolano et al. 2003, 2005, 2008) is a fully benchmarked and validated 3D photo-ionization and dust radiative transfer code. It allows for cartesian grid geometries for gas and dust, multiple or diffuse radiation sources with a given input spectrum, multiple dust grain species and a specified grain size distribution. With these parameters it self consistently solves the equations of radiative transfer to calculate the degree of ionisation, electron and dust grain temperatures in each cell as well as an overall spectral energy distribution (SED) of the whole region being modelled. The validation process involves comparisons with both benchmarks used by many radiative transfer codes and to analytical results each time the code is compiled. Using MOCASSIN 2.02.70 we have constructed models of the Crab Nebula to determine the mass of dust formed in its ejecta

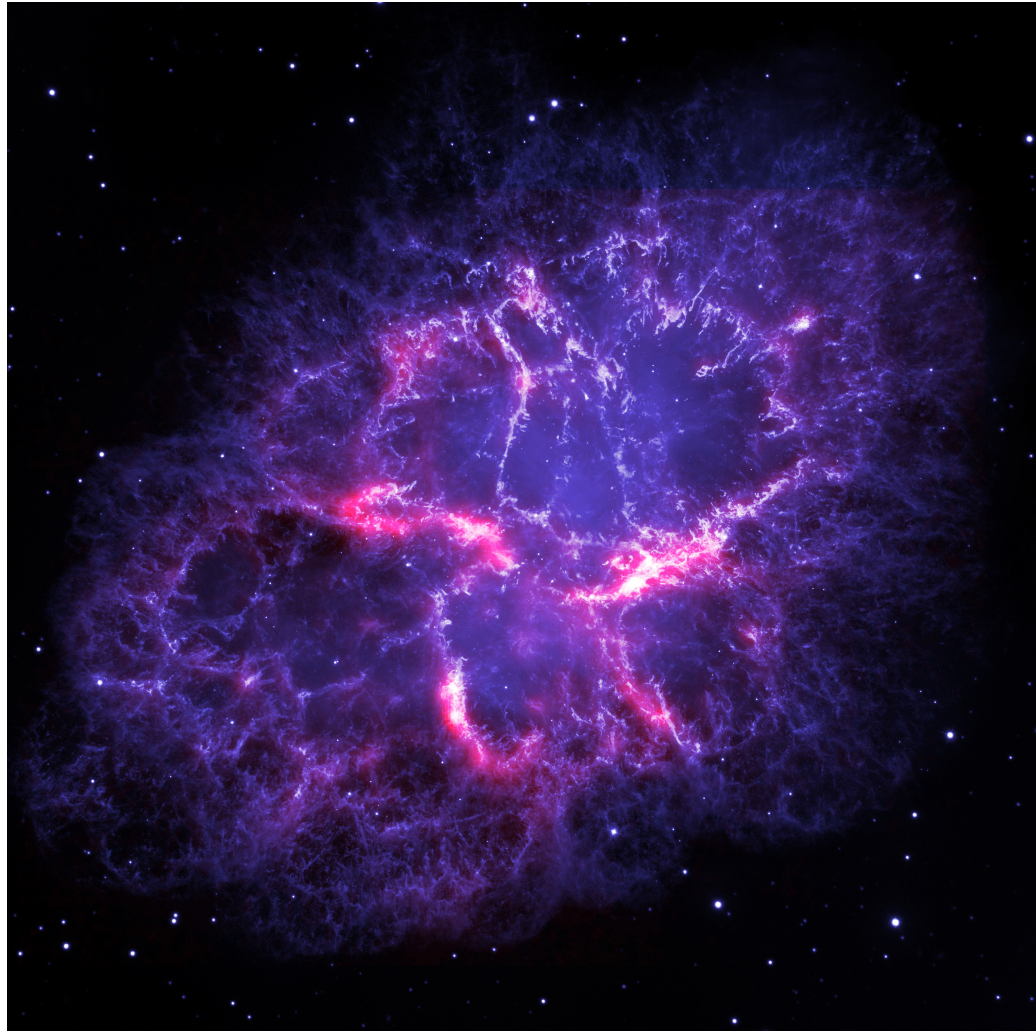


Figure 4.2. Composite image of the Crab Nebula, obtained by combining a *Hubble Space Telescope* optical emission line image (blue-white) with a *Herschel Space Observatory* 70- μm dust emission image (red), showing the emitting dust to be closely aligned with the optical knots and filaments. The image is 5.65 arcmin on a side; north is up and east is to the left. Credits: Oli Usher (UCL); *Herschel Space Observatory*, *Hubble Space Telescope*: ESA, NASA.

by fitting to the observed far infrared excess in the SED (Temim et al. 2006; Gomez et al. 2012; Planck Collaboration 2011) and optical line fluxes (Smith 2003).

4.1.1 Geometry and Spectrum

The general geometry adopted is an ellipsoid with a major axis of 4.0 pc and a minor axis of 2.9 pc (Hester 2008). The location of dust and gas within the nebula is open to slightly more debate with Čadež et al. (2004) placing most of the material in a spherical shell of radius 0.55 pc. Davidson & Fesen (1985) and Lawrence et al. (1995) have more similar geometries, assuming ellipsoids with inner diameters of 1.05×0.75 pc and 1.15×0.85 pc respectively. The pulsar wind nebula's synchrotron spectrum from 0.36 nm to 1 m that was used for the modelling was a digitized version of the spectrum plotted by Hester (2008). The level of the submillimeter part of the input spectrum needed to be lowered slightly in order to be consistent with recent *Planck* observations (Planck Collaboration 2011). Figure 4.3 shows this spectrum. The spectrum was scaled to have an integrated luminosity of 1.3×10^{38} erg s $^{-1}$ (Hester 2008). The angular extent of the synchrotron emission from the pulsar wind nebula appears to be a function of frequency, with the radio emission extending throughout the 4.0×2.9 pc ellipsoidal nebula (Hester 2008), while at X-ray wavelengths the PWN has a diameter of ~ 1 pc (Hester et al. 2002). It is a much smoother

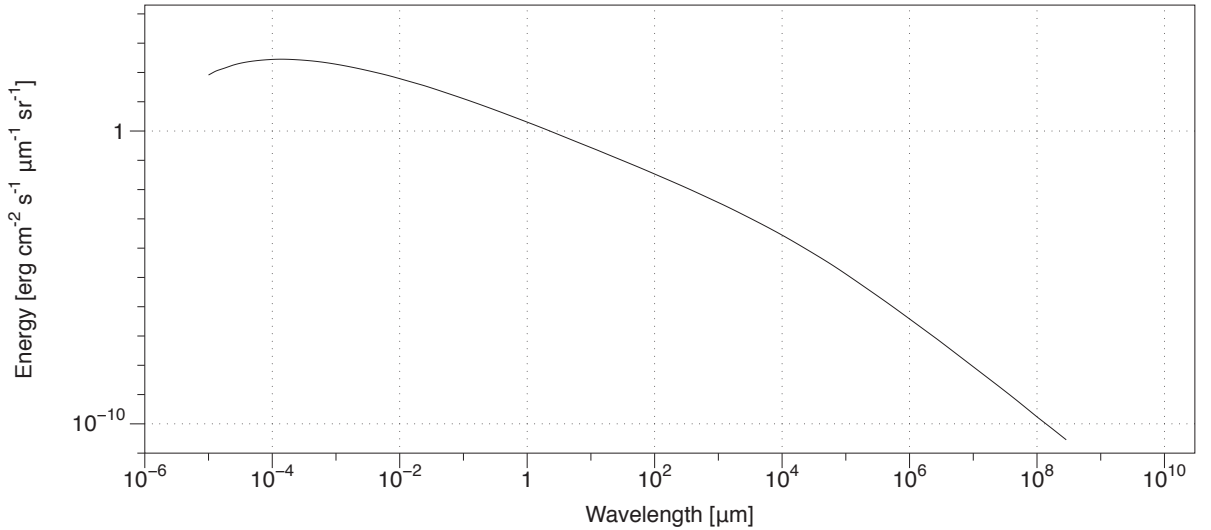


Figure 4.3. The input Spectrum used to heat the dust and ionise the gas, taken from Hester (2008) and adjusted for Planck Collaboration (2011) in the sub-mm.

Table 4.1. Continuum IR Fluxes from the Crab Nebula

Wavelength (μm)	Total Flux ¹ (Jy)	Uncertainty (Jy)	Dust Flux (Jy)	Instrument ²
3.6	12.6	0.22		<i>Spitzer</i>
4.5	14.4	0.26		<i>Spitzer</i>
5.8	16.8	0.10		<i>Spitzer</i>
8.0	18.3	0.13		<i>Spitzer</i>
24	46.4	8.0	17.2	<i>Spitzer</i>
70	202.4	20	156.8	<i>Herschel</i>
100	196.5	20	143.6	<i>Herschel</i>
160	141.8	15	77.5	<i>Herschel</i>
250	103.4	7.2	25.9	<i>Herschel</i>
350	102.4	7.2	13.2	<i>Herschel</i>
350	99.3	2.1	10.1	<i>Planck</i>
500	129.0	9.0		<i>Herschel</i>
550	117.7	2.1		<i>Planck</i>
850	128.6	3.1		<i>Planck</i>
1382	147.2	3.1		<i>Planck</i>

¹ The 24-, 70- and 100- μm fluxes have been corrected for line emission following Table 2 of Gomez et al. (2012).

² *Spitzer* data: Temim et al. (2006); *Herschel* data: Gomez et al. (2012); *Planck* data: Planck Collaboration (2011).

spectrum than the one used by many models use which are taken from the Davidson & Fesen (1985) parametrization. Davidson & Fesen (1985) fitted three power laws to different parts of the spectrum and missed out the ultraviolet region, where a large number of the ionizing photons are emitted. The adapted Hester (2008) spectrum is used to provide diffuse heating source with an integrated luminosity of 1.3×10^{38} erg s $^{-1}$ (Hester 2008). This photon source heats the dust radiatively rather than assuming a given temperature for each grain size or that all grains are the same temperature. Rather than using a point source, the photon packets are emitted from a diffuse source initially occupying the middle two thirds of the ellipsoid to better simulate the synchrotron emission from the pulsar wind nebula.

4.1.2 Spectral Energy Distribution

The model dust SEDs were fitted to the observed infrared and submm photometric fluxes, using observations made by *Spitzer* (Temim et al. 2006), *Herschel* (Gomez et al. 2012) and *Planck* (Planck Collaboration 2011), along with the mean synchrotron-subtracted *Spitzer*-IRS continuum spectrum of Temim & Dwek (2013), to better constrain the warm dust

emission. The 24-, 70- and 100- μm points have been corrected for line emission, using the line contribution factors listed in Table 2 of Gomez et al. (2012). The dust+synchrotron continuum fluxes are listed in Table 4.1, along with 24–350- μm dust continuum fluxes obtained by subtracting the synchrotron fluxes listed in Table 4 of Gomez et al. (2012). For a distance of 2 kpc (Trimble 1968), the total luminosity emitted by dust at infrared wavelengths is $1190 L_\odot$, corresponding to the absorption and re-radiation of 28% of the luminosity of the pulsar wind nebula emitted between 0.1 nm and 1.0 μm .

Fitting the models to the observations was done by assuming that the uncertainties of each of the observed fluxes were Gaussian, sampling randomly within this uncertainty range to generate 1000 versions of the SED. These were compared to the model SEDs and the set of parameters generating the lowest χ^2 value was taken to be the most likely.

4.1.3 Optical Lines

As well as aiming to fit the nebular infrared photometric fluxes due to dust emission, we also fitted the emission line fluxes from the ionized gas, principally the optical line fluxes measured for the entire nebula by Smith (2003), which we dereddened using $E(\text{B-V}) = 0.52$ (Miller 1973) and the Galactic reddening law of Howarth (1983). We assumed an intrinsic "Case B" $\text{H}\alpha/\text{H}\beta$ flux ratio of 2.85 in order to determine the [N II] 6584,6548 Å contribution to the dereddened combined $\text{H}\alpha + [\text{N II}]$ flux, and a "Case B" $\text{H}\gamma/\text{H}\beta$ flux ratio of 0.47 in order to determine the [O III] 4363 Å contribution to the dereddened $\text{H}\gamma + [\text{O III}]$ flux. To diagnose the abundances of carbon and argon, lines of which did not fall within the spectral coverage of Smith (2003), we fitted the [C I] 9824, 9850 Å lines and the [Ar III] 7136 Å line, using the dereddened line intensities relative to $\text{H}\beta$ measured by Rudy et al. (1994) for Knot 6 (FK 6) of Fesen & Kirshner (1982). We note that for FK 10 Rudy et al. (1994) measured [C I] and [Ar III] intensities relative to $\text{H}\beta$ that were 4.0 and 2.2 times higher, respectively, than for FK 6. We used their FK 6 relative line intensities because at shorter wavelengths the FK 6 relative line intensities of Henry et al. (1984) show a better match to those measured for the entire nebula by Smith (2003).

As initial nebular abundances, we used the Crab Nebula 'Domain 2' heavy element abundances from Table 2 of MacAlpine & Satterfield (2008). Adopting a distance of 2 kpc, we fitted the dereddened total $\text{H}\beta$ flux by varying the value of the density of hydrogen in

the smooth shell models, or within the clumps in the clumped shell models. The heavy element abundances were iteratively adjusted in order to match the observed line fluxes, including those sensitive to the nebular temperature.

4.1.4 Grain species and optical properties

The Crab Nebula is a carbon rich nebula (MacAlpine & Satterfield 2008) and there is no feature in its dust spectrum at 10 or 20 μm which would be caused by the Si-O bond vibrations in silicate grains so we focus on carbonaceous grain species. As well as fitting several sets of amorphous carbon dust optical properties and graphite we do fit one set of silicate optical constants. Silicates tend to require more dust than amorphous carbon grains as they are less absorbent at optical and UV wavelengths and thus reflect and scatter more than other species. Graphite dust being even darker than other carbon species, absorbs far more strongly at optical and UV wavelengths.

As well as investigating different species of dust, each species has multiple sets of optical constants. The optical constants are the real and imaginary parts of the refractive index.

$$\tilde{n}(\lambda) = n(\lambda) - ik(\lambda) \quad (4.2)$$

where n is the refractive index and k is the absorption index. These govern how much light at a given wavelength is absorbed and how much is scattered by a dust particle. There are several different sets of these constants available for different species of cosmic dust, based on sets of laboratory experiments to determine the wavelength dependent extinction coefficients of materials similar to those considered as constituents of dust. Earlier sets of amorphous carbon data were based on inconsistent sets of laboratory data (e.g. Rouleau & Martin (1991) using the data sets from Bussoletti et al. (1987)). The more recent sets of optical constants using self consistent data sets (e.g. Zubko et al. (1996) using data from Colangeli et al. (1995)) are likely to be more reliable. Most sets of optical constants also provide multiple sets of constants for cosmic dust analogues produced in different ways. Usually two methods are used: one involving electrical discharge through a carbon electrode in either H₂ or argon (ACH2 and ACAR) and another burning benzene samples

(BE). The optical constants determined from these different methods of preparing dust analogues also have very different optical properties. Optical properties used here are the ACAR and BE samples from Zubko et al. (1996) and those from Rouleau & Martin (1991) and Hanner (1988) for amorphous carbon and Draine & Lee (1984) for silicates and graphite.

The dust analogue used for determining these optical properties that is thought to be most like the dust formed in supernovae is the Zubko et al. (1996) BE sample. It is highly graphitic and formed in a more chemically reactive environment, closer to that of a supernova than the ACAR samples (Colangeli et al. 1995).

The ACAR and BE amorphous carbon optical constants of Zubko et al. (1996) have no data points for wavelengths shorter than 40 nm and 54 nm, respectively. Since a significant fraction of the Crab PWN luminosity is emitted shortwards of these wavelengths, we extended the BE and the ACAR optical constants down to shorter wavelengths using the 2.8 nm to 30 nm amorphous carbon optical constant measurements of Uspenskii et al. (2006), which are presented in Appendix C. Also listed there are n and k optical constants suitable for Zubko et al. (1996) BE and ACAR grains over the 0.35-54 nm wavelength range, obtained as described in the Appendix C. Figure 4.32 shows a comparison from 0.35 nm to 1000 μm between the absorption efficiencies of 0.1- μm radius amorphous carbon grains for the supplemented Zubko et al. (1996) BE and ACAR optical constants, as well as for the optical constants of Rouleau & Martin (1991). As the latter do not have any data points longwards of 300 μm , we extrapolated them to 1000 μm by fitting power laws to their n and k data points from 10-300 μm , since they change smoothly over this range.

For our modelling we adopted a mass density of 1.85 g cm^{-3} for amorphous carbon, 2.2 g cm^{-3} for graphite, and 3.3 g cm^{-3} for silicate.

As well as the models based on single grain species, a model using multiple grain species was run. The ratios of amorphous carbon to silicates used are based on the constraints imposed by the nucleosynthesis models, using the Zubko et al. (1996) BE amorphous carbon and Draine & Lee (1984) silicate optical properties.

4.1.5 Density distributions

13 separate dust and gas distributions are considered:

- I. smooth distributions where all gas and dust is isotropically distributed throughout the ellipsoid. The density $N_H = 775 \text{ cm}^{-3}$ is selected so the modelled H_β flux matches the observed flux. The geometry is shown in Figure 4.4.

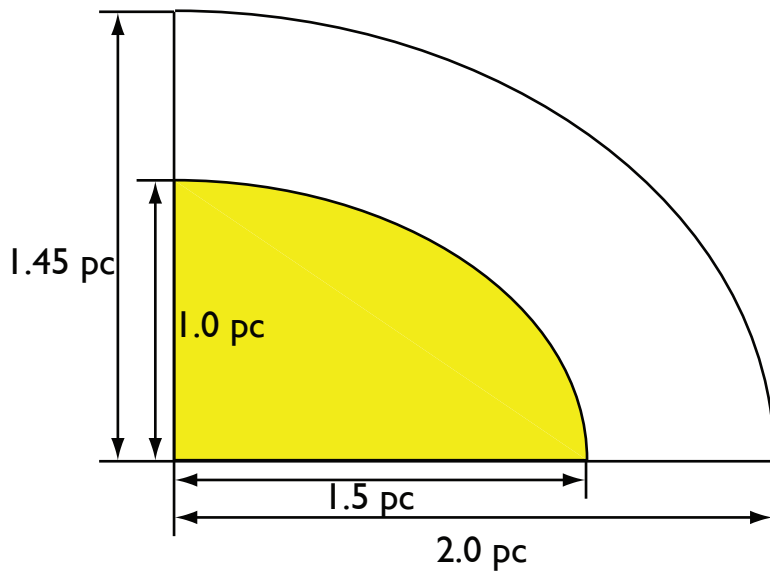


Figure 4.4. A cartoon schematic of geometry I

- II. a smooth shell distribution where all the gas and dust is isotropically distributed in a shell in the outer third of the ellipsoid. This means that all the gas and dust are outside the ionising source. A density of $N_H = 850 \text{ cm}^{-3}$ is selected so the total modelled H_β flux matches the observed H_β flux. The geometry is shown in Figure 4.5.
- III. a smooth shell distribution where the gas and dust are isotropically distributed in a shell of 0.5 pc thickness at a radius of $1.05 \times 0.7 \text{ pc}$, entirely inside the ionising radiation source in agreement with Davidson & Fesen (1985). A density of 850 cm^{-3} is selected to match total modelled H_β flux matches observed H_β flux

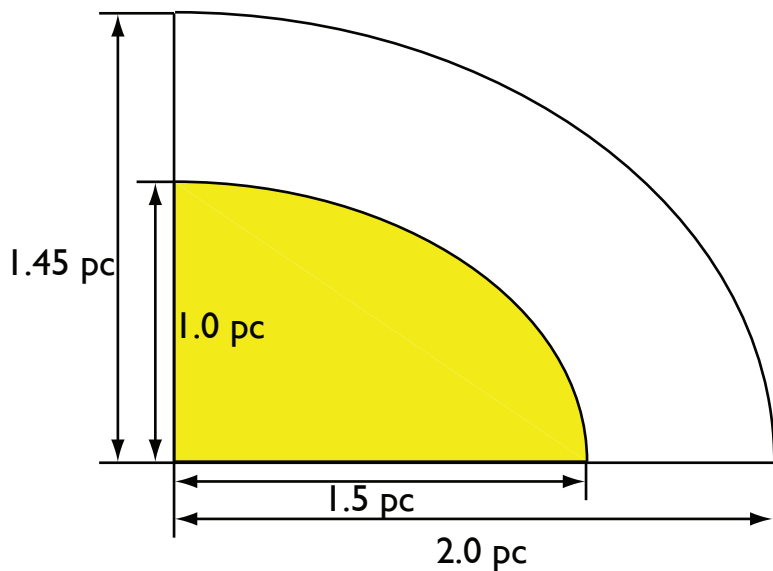


Figure 4.5. A cartoon schematic of geometry II

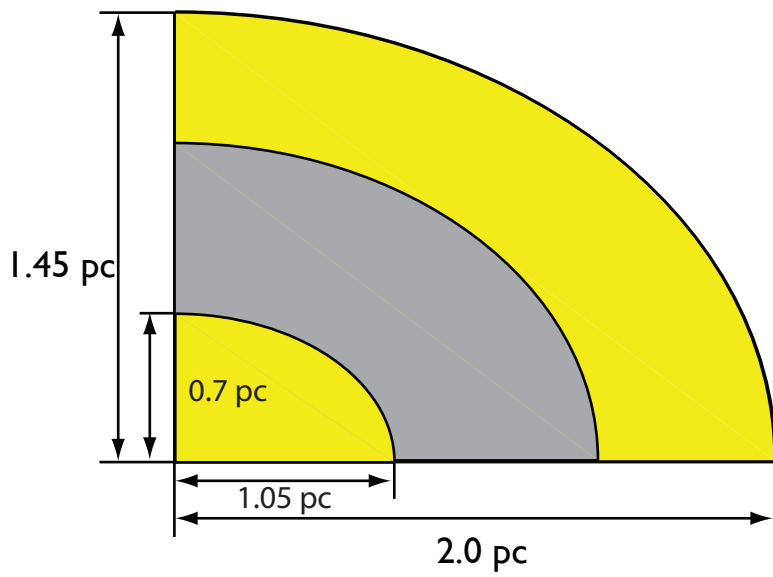


Figure 4.6. A cartoon schematic of geometry III

- IV. a smooth shell distribution where the gas and dust are isotropically distributed in all the way to the edge of the nebula starting at a radius of 1.05×0.7 pc, entirely inside the ionising radiation source in agreement with Davidson & Fesen (1985). A density of 550 cm^{-3} is selected to match total modelled H_β flux matches the observed H_β flux. This corresponds to Model II in Owen & Barlow (2015). A cartoon schematic of the geometry is shown in 4.7

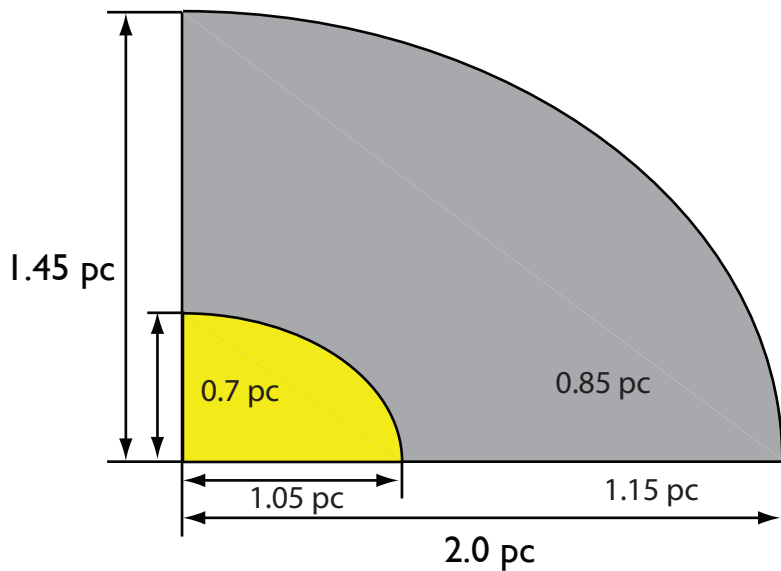


Figure 4.7. A cartoon schematic of geometry IV

- V. a smooth shell distribution where the gas and dust are isotropically distributed in all the way to the edge of the nebula starting at a radius of 1.15×0.85 pc, entirely inside the ionising radiation source in agreement with Lawrence et al. (1995). A density of 650 cm^{-3} is selected to match total modelled H_β flux matches the observed H_β flux. This corresponds to Model III in Owen & Barlow (2015). A cartoon schematic of the geometry is shown in 4.8.

- VI. a smooth shell distribution with the gas and dust in a shell 0.1 pc thick at a radius of 0.55 pc, entirely inside the ionising radiation field to match models used by Temim & Dwek (2013) and Čadež et al. (2004) observations. A density of 1400 cm^{-3} is selected to match total modelled H_β flux matches the observed H_β flux . A cartoon schematic of the geometry is shown in Figure 4.9.

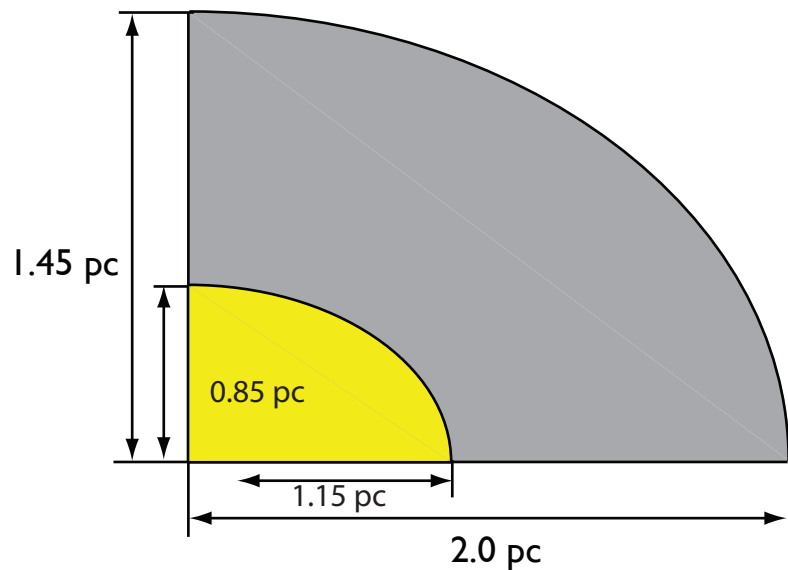


Figure 4.8. A cartoon schematic of geometry V

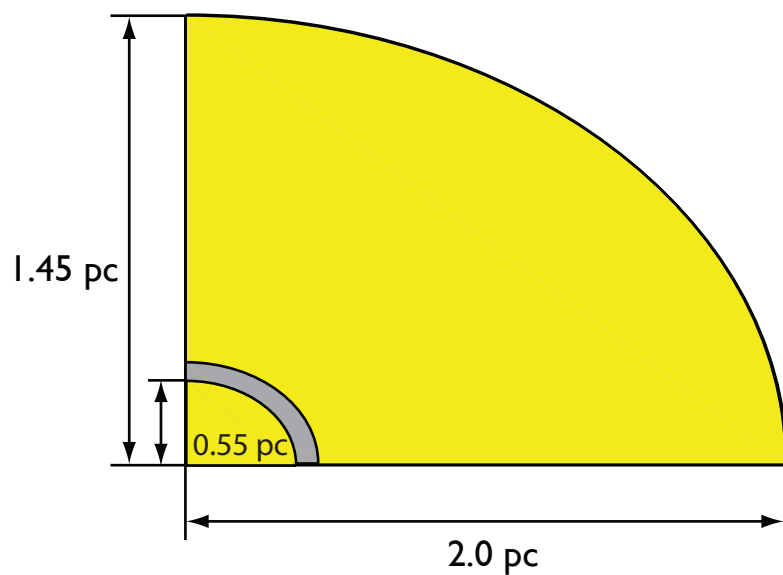


Figure 4.9. A cartoon schematic of geometry VI

VII. a clumped distribution with all the material outside the the ionising source. The degree of clumping is determined by fitting to the optical lines. A clump filling factor is found to be 0.1 with a density in the clumps of $N_H = 1400 \text{ cm}^{-3}$. With this clump filling factor and the geometry of the model, the clumps are 0.11-pc in diameter. The mass of dust and gas decreases linearly with radius. A schematic of this model is shown in Figure 4.10. The clumps are modelled using sub grids for finer variations in the density as in Ercolano et al. (2007). This corresponds to Model iv of Owen & Barlow (2015). A cartoon schematic of the geometry is shown in Figure 4.10.

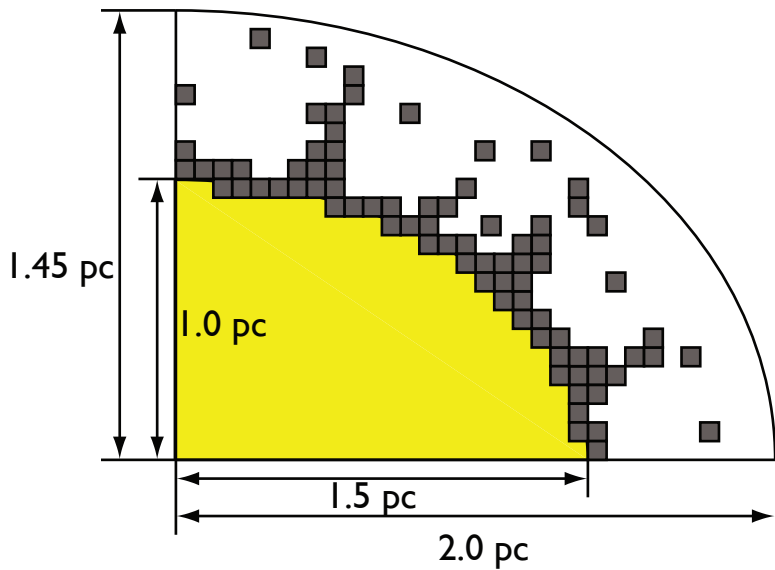


Figure 4.10. A cartoon schematic of geometry VII

VIII. a clumped distribution with all the material outside the ionising source. Also determined by matching the optical lines with a filling factor of 0.1 and a of $N_H = 1700 \text{ cm}^{-3}$. The clumps are 0.037-pc in diameter. The mass of dust and gas decreases linearly with radius. A schematic of the geometry of this model is shown in Figure 4.11.

IX. a clumped distribution with all of the material inside the ionising source, with a filling factor of 0.1 and density of $N_H = 1900 \text{ cm}^{-3}$ in the clumps. The inner semi-axes of the material is at $1.05 \times 0.75 \text{ pc}$ (Davidson & Fesen 1985) and decreases as r^{-2} . The clumps are 0.037-pc in radius. A cartoon schematic of the geometry this model is

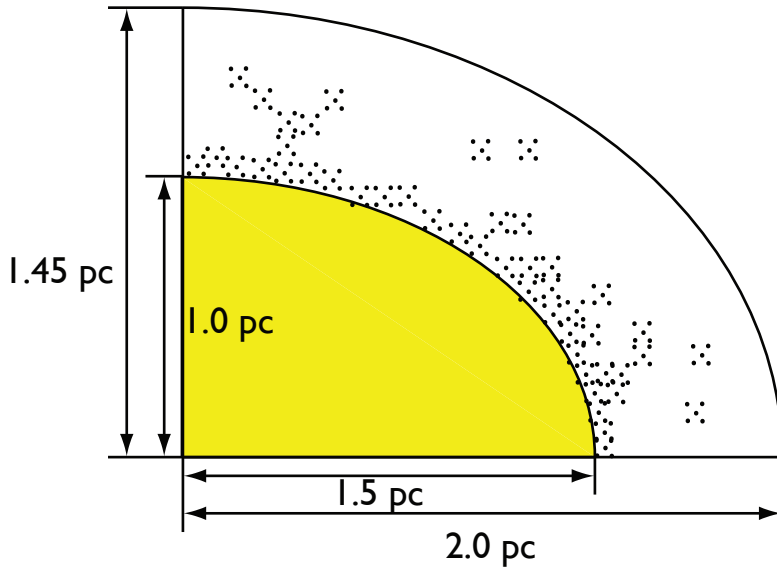


Figure 4.11. A cartoon schematic of geometry VIII

shown in Figure 4.12.

- X. a clumped distribution with all of the material inside the ionising source with a filling factor of 0.1 and density of 1900 in the clumps. The inner semi-axes of the material is at 1.15×0.85 pc (Lawrence et al. 1995) and decreases as r^{-2} . The clumps are 0.037-pc in radius. A cartoon schematic of the geometry of this model is shown in Figure 4.13. This corresponds to Model v in Owen & Barlow (2015).
- XI. a *smooth* shell distribution, with the gas and dust located at a radius of 0.55 pc in a 0.1 pc thick shell (i.e. both inner radii 1.1 pc in length), with the PWN diffuse field radiation field emitting uniformly from within the inner nebular radius of 1.1 pc. This shell geometry was argued for by Čadež et al. (2004) based on their multi-slit spectroscopy and was adopted by Temim & Dwek (2013) for their dust modelling. A shell hydrogen density of 1400 cm^{-3} was found to be needed to match the total (dereddened) H β flux from the nebula. A cartoon schematic of the geometry of this model is shown in Figure 4.14. This corresponds to model i in Owen & Barlow (2015).
- XII. a *clumped* shell distribution where the gas and dust clumps start at inner axes of 2.3×1.7 pc (Lawrence et al. 1995), and with an r^{-2} distribution of clumps that

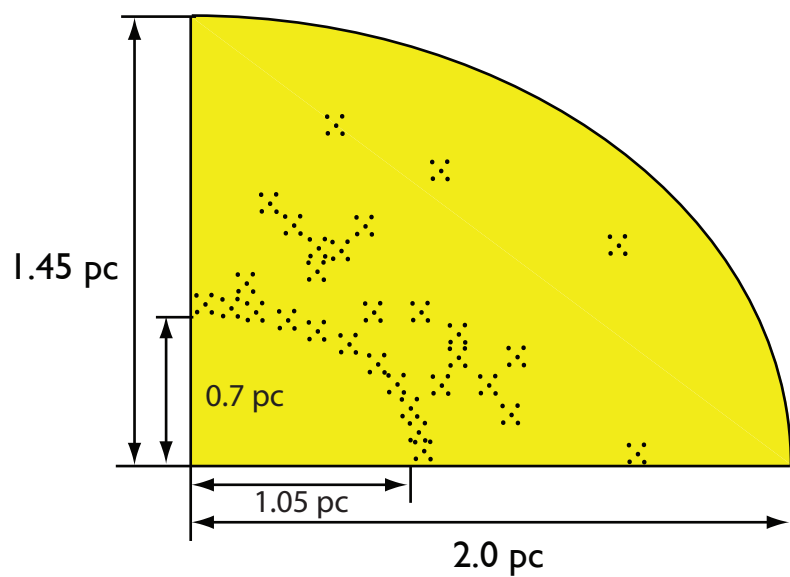


Figure 4.12. A cartoon schematic of geometry IX

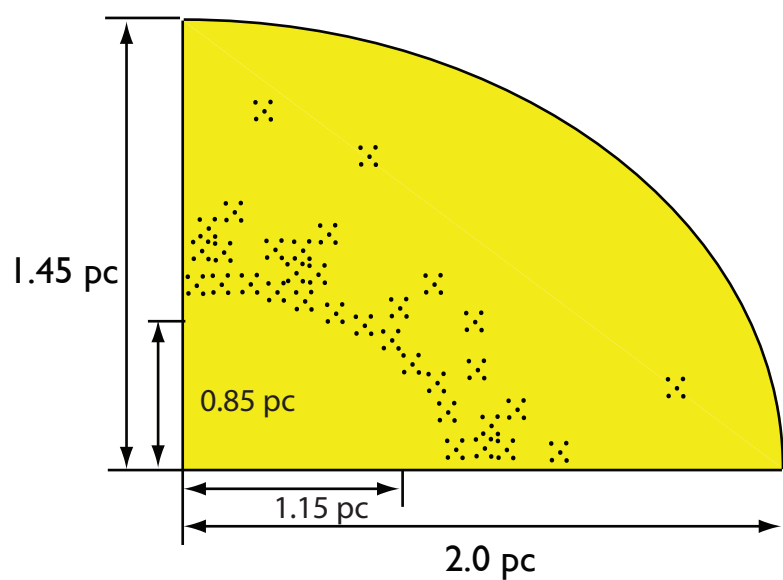


Figure 4.13. A cartoon schematic of geometry X

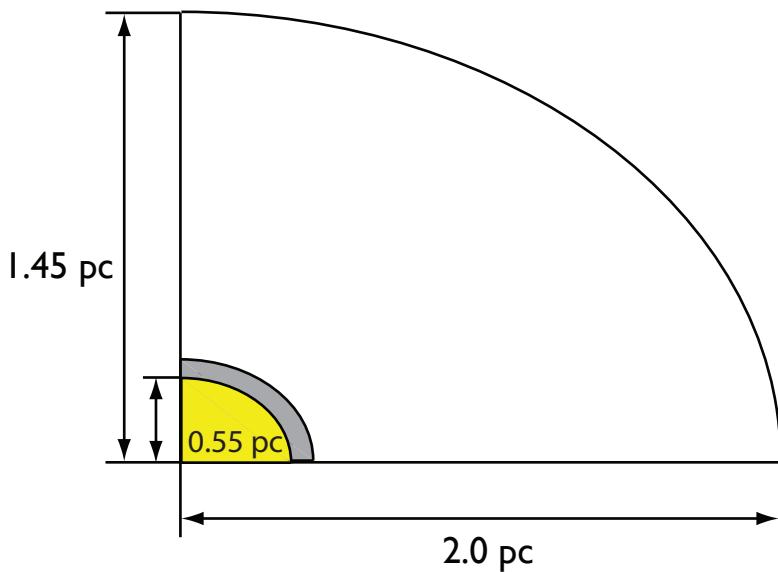


Figure 4.14. A cartoon schematic of geometry XI

extends to the 4.0×2.9 pc outer boundaries of the nebula, with a volume filling factor of 0.10. The PWN radiation field is a diffuse source emitting uniformly within a 1.1 pc diameter sphere at the centre of the nebula. For 0.037-pc radius clumps, a H-density of 1900 cm^{-3} within the clumps was found to match the total H β flux from the nebula. A cartoon schematic of the geometry of this model is shown in Figure 4.15. This corresponds to Model VI in Owen & Barlow (2015).

XIII. a *clumped* shell distribution where the gas and dust clumps start at inner axes of 1.1×1.5 pc (Davidson & Fesen 1985), and with an r^{-2} distribution of clumps that extends to the 4.0×2.9 pc outer boundaries of the nebula, with a volume filling factor of 0.10. The PWN radiation field is a diffuse source emitting uniformly within a 1.1 pc diameter sphere at the centre of the nebula. For 0.037-pc radius clumps, a H-density of 1900 cm^{-3} within the clumps was found to match the total H β flux from the nebula. A cartoon schematic of the geometry of this model is shown in Figure 4.16.

These density distributions are summarised in Table 4.2.

Some of these models are based on entirely on observational data, whilst others included were those used to develop the model and increase its complexity. My preferred

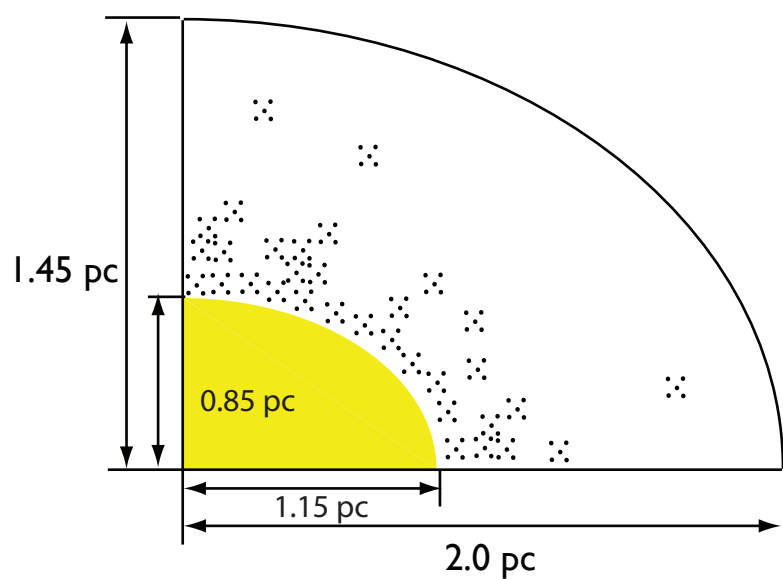


Figure 4.15. A cartoon schematic of geometry XII

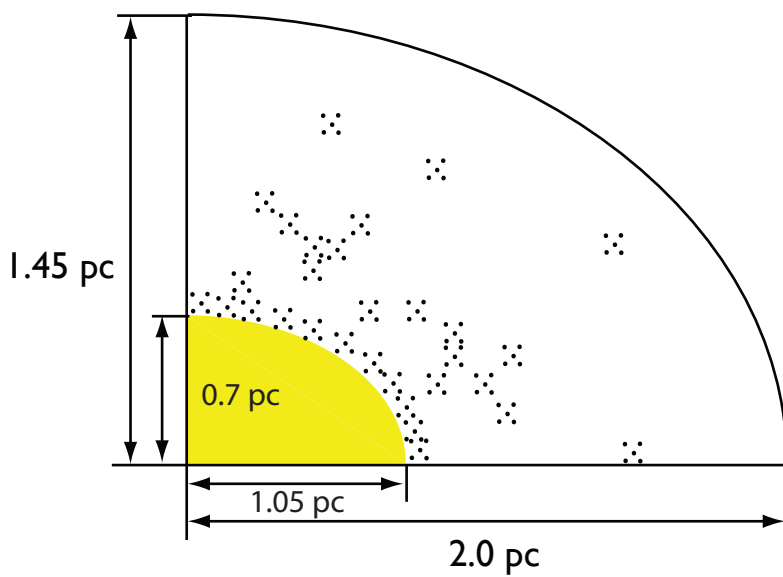


Figure 4.16. A cartoon schematic of geometry XIII

model (model XII) was selected as it is based on the most recent consistent observations of the Crab Nebula.

4.1.6 Nucleosynthesis

Another constraint on the mass of dust that is able to form in a supernova is the abundances of the constituent elements of the dust. The supernova nucleosynthesis models of Woosley & Weaver (1995) estimate a carbon mass of 0.11 M_\odot and an oxygen mass of 0.27 M_\odot for a supernova with a progenitor with a main sequence mass of 12 M_\odot . Previous studies by MacAlpine & Satterfield (2008) have shown that the Crab Nebula is carbon rich and oxygen poor in contrast to these nucleosynthesis models, so we take the total abundance of carbon and oxygen combined to be correct, but the ratio of the two to be incorrect. This would allow for a carbon mass of up to $0.11 \text{ M}_\odot + (12/16)\times 0.27 \text{ M}_\odot = 0.31 \text{ M}_\odot$.

The abundance of magnesium from the Woosley & Weaver (1995) models is 0.02 M_\odot , 0.06 M_\odot of Silicon and 0.03 M_\odot of Iron are predicted. Assuming these go in to MgSiO_3 and FeSiO_3 we get $0.02 + 0.02 + 3\times(16/28)\times 0.02 \text{ M}_\odot = 0.074 \text{ M}_\odot$ of MgSiO_3 and $0.03 + (28/56)\times 0.03 + 3\times(16/56)\times 0.03 \text{ M}_\odot = 0.071 \text{ M}_\odot$ of FeSiO_3 . This would imply upper limit of 0.15 M_\odot for silicate dust.

4.2 Results

4.2.1 Elemental Abundances and Ionisation

From Table 4.3 the total nebular gas mass required to match the observed line fluxes ranges from 15.5 M_\odot to 49 M_\odot for the smoothly distributed models, whereas for the clumped models the total gas mass is only 6.9 M_\odot to 7.0 M_\odot . The clumped model gas masses are consistent with the $8\text{-}10 \text{ M}_\odot$ mass estimated for the Crab Nebula's progenitor star (Smith (2013) and references therein), whereas the smooth models are clearly ruled out as the masses of gas required are at a minimum twice that of the mass of the progenitor star. Optical emission line images of the Crab Nebula (e.g. Figure 4.2) also clearly rule out a smooth distribution for the emitting gas. The elemental abundances relative to hydrogen to obtain these masses and match lines are listed in Table 4.4. The modelled and observed

	Model I	Model II	Model III	Model IV	Model V	Model VI
Density distribution	Smooth	Smooth	Smooth	Smooth	Smooth	Smooth
Total dimensions	4.0×2.9 pc					
Inner radii	0	3.0×2.0 pc	1.05×0.7 pc	2.1×1.4 pc	2.3×1.7 pc	1.1×1.1 pc
Shell thickness	4.0×2.9 pc	1.0×0.8 pc	0.5 pc	1.9×1.5 pc	1.7×1.2 pc	0.1 pc
H-density	775 cm ⁻³	850 cm ⁻³	850 cm ⁻³	775 cm ⁻³	775 cm ⁻³	1400 cm ⁻³
Radius of each clump	Inner Third	To Edge				
Radiation field	Inner Third	To Edge				
	Model VII	Model VIII	Model IX	Model X	Model XI	Model XII
Density distribution	Clumped	Clumped	Clumped	Clumped	Smooth	Clumped
Total dimensions	4.0×2.9 pc					
Inner radii	3.0×2.0 pc	3.0×2.0 pc	3.0×2.0 pc	2.3×1.7 pc	1.1×1.1 pc	2.3×1.7 pc
Shell thickness	1.0×0.8 pc	1.0×0.8 pc	1.0×0.8 pc	1.7×1.2 pc	0.1 pc	1.7×1.2 pc
H-density	1400 cm ⁻³	1700 cm ⁻³	1900 cm ⁻³	1900 cm ⁻³	1400 cm ⁻³	1900 cm ⁻³
Radius of each clump	0.11 pc	0.037 pc	0.037 pc	0.037 pc	To Edge	Central source
Radiation field	Central Source	Central Source	To Edge	To Edge	Central source	Central source
	Model XIII					
Density distribution	Clumped					
Total dimensions	4.0×2.9 pc					
Inner radii	3.0×2.0 pc					
Shell thickness	1.0×0.8 pc					
H-density	1900 cm ⁻³					
Radius of each clump	0.037 pc					
Radiation field	Central source					

Table 4.2. A summary of the density distributions of the different models.

fluxes for each of the models are listed in Tables 4.5 to 4.11.

Table 4.12 presents the global elemental ion fractions obtained from our clumped Model XII for the Crab Nebula (the ion fraction patterns are very similar for its smooth model equivalent, Model V). Most elements are found to have a neutral fraction of about 10%, with the exception of helium, whose neutral fraction is significantly higher, at 33%. A consequence of the high helium neutral fraction in the Crab is that standard abundance analyses based on recombination lines of H^+ , He^+ and He^{2+} will underestimate the true He/H ratios. We find a helium mass fraction of 85% (Table 4.3), in agreement with the 89% derived by MacAlpine & Satterfield (2008) from their photoionization modelling of spectra from many locations within the nebula. They also found that the majority of their locations (their ‘Domain 2’) had C/O ratios greater than unity, both by number and by mass. Our clumped models for the entire nebula are consistent with those results, yielding a C/O ratio of 1.65 by number. The mass ratio of C/(H+He) is enhanced by a factor 6.2 in the Crab Nebula relative to the solar abundances of Asplund et al. (2009), while the O/(H+He) mass ratio is enhanced by only a factor of 2.3. The corresponding mass ratios of neon, sulphur and argon for the Crab are enhanced by factors of 3.8, 4.9 and 3.1 relative to Solar, while nitrogen is depleted by a factor of 1.7.

C/O mass ratios exceeding unity are not currently predicted by any supernova nucleosynthesis models, for any mass of progenitor star. For the CCSN yields tabulated by Woosley & Weaver (1995), the ejecta C/O mass ratio did increase with decreasing progenitor mass but for the lowest mass cases that they treated ($11\text{--}12 M_\odot$) the predicted C/O mass ratio was 0.39, for the case of initial solar metallicity, and the predicted carbon yield was only $0.053 M_\odot$, i.e. lower than the Crab Nebula’s gas-phase carbon mass alone of $0.099 M_\odot$. In addition, their $11 M_\odot$ model predicted an ejecta He/H mass ratio of 0.67, versus the very much larger He/H mass ratio of 7.3 found here for the Crab Nebula. For the lowest progenitor mass model ($13 M_\odot$) of Thielemann et al. (1996), an even lower ejecta carbon mass and C/O mass ratio was predicted than for the Woosley & Weaver (1995) model of the same mass. The $13 M_\odot$ model of Nomoto et al. (2006) predicted a He/H mass ratio of 0.7 and a C/O mass ratio of 0.5, also too low compared to Crab Nebula ratios. The trend for predicted carbon yields to increase with decreasing progenitor mass suggests that it would be useful to calculate yields for CCSN progenitor masses down to

Smooth Models	Mass (M_{\odot})	I	II	III	IV	V	VI
		Mass (M_{\odot})	Mass (M_{\odot})				
Hydrogen	5.52	4.53	2.88	4.71	4.84	1.80	
Helium	41.98	34.43	21.89	34.86	36.80	13.18	
Carbon	0.62	0.51	0.32	0.58	0.54	0.21	
Nitrogen	0.012	0.010	0.006	0.016	0.010	0.006	
Oxygen	0.71	0.58	0.37	0.47	0.54	0.21	
Neon	4.97×10^{-2}	4.08×10^{-2}	2.59×10^{-2}	4.62×10^{-1}	4.36×10^{-2}	7.20×10^{-2}	
Sulphur	8.84×10^{-3}	7.25×10^{-3}	4.61×10^{-3}	6.03×10^{-3}	7.75×10^{-3}	2.30×10^{-2}	
Argon	1.19×10^{-3}	9.78×10^{-4}	6.22×10^{-4}	1.70×10^{-3}	8.72×10^{-3}	3.24×10^{-3}	
Total	48.9	40.1	25.5	41.1	42.8	15.5	

Clumped Models	Mass (M_{\odot})	VII	VIII	IX	X	XI	XII	XIII
		Mass (M_{\odot})	Mass (M_{\odot})					
Hydrogen	0.81	0.78	0.79	0.79	1.75	0.85	0.85	
Helium	5.95	5.71	5.85	5.85	12.82	6.27	6.27	
Carbon	0.09	0.09	0.10	0.10	0.20	0.10	0.10	
Nitrogen	2.85×10^{-3}	2.73×10^{-3}	2.77×10^{-3}	2.77×10^{-3}	6.13×10^{-3}	2.97×10^{-3}	2.97×10^{-3}	
Oxygen	9.37×10^{-2}	8.98×10^{-2}	7.84×10^{-2}	7.84×10^{-2}	2.02×10^{-1}	8.40×10^{-2}	8.40×10^{-2}	
Neon	3.25×10^{-2}	3.12×10^{-2}	7.75×10^{-2}	7.75×10^{-2}	7.00×10^{-2}	8.30×10^{-2}	8.30×10^{-2}	
Sulphur	1.04×10^{-2}	9.98×10^{-3}	1.01×10^{-3}	1.01×10^{-3}	2.24×10^{-2}	1.08×10^{-3}	1.08×10^{-3}	
Argon	1.46×10^{-3}	1.40×10^{-3}	2.85×10^{-4}	2.85×10^{-4}	3.15×10^{-3}	3.05×10^{-4}	3.05×10^{-4}	
Total	7.2	6.9	7	7	15.5	7.5	7.5	

Table 4.3. The masses of emitting gas phase elements in the Crab Nebula determined by the MOCASSIN models

	Smooth Models	Model I	Model II	Model III	Model IV	Model V	Model VI	
Hydrogen	1.00	1.00	1.00	1.00	1.00	1.00	1.00	
Helium	1.90	1.90	1.90	1.90	1.85	1.90	1.83	
Carbon	9.3×10^{-3}	9.3×10^{-3}	9.3×10^{-3}	1.02×10^{-2}	9.3×10^{-3}	9.7×10^{-3}	9.7×10^{-3}	
Nitrogen	1.5×10^{-4}	1.5×10^{-4}	1.5×10^{-4}	2.5×10^{-4}	1.5×10^{-4}	2.5×10^{-4}	2.5×10^{-4}	
Oxygen	8.0×10^{-3}	8.0×10^{-3}	8.0×10^{-3}	6.2×10^{-3}	7.0×10^{-3}	7.2×10^{-3}	7.2×10^{-3}	
Neon	4.5×10^{-4}	4.5×10^{-4}	4.5×10^{-4}	4.9×10^{-3}	4.5×10^{-4}	2.0×10^{-3}	2.0×10^{-3}	
Sulphur	5.0×10^{-5}	5.0×10^{-5}	5.0×10^{-5}	4.0×10^{-5}	5.0×10^{-5}	4.0×10^{-4}	5.0×10^{-5}	
Argon	6.0×10^{-6}	6.0×10^{-6}	6.0×10^{-6}	1.0×10^{-5}	5.0×10^{-5}	5.0×10^{-5}	5.0×10^{-5}	
	Clumpy Models	Model VII	Model VIII	Model IX	Model X	Model XI	Model XII	Model XIII
Hydrogen	1.00	1.00	1.00	1.00	1.00	1.00	1.00	1.00
Helium	1.83	1.83	1.85	1.85	1.83	1.85	1.85	1.85
Carbon	9.7×10^{-3}	9.7×10^{-3}	1.02×10^{-2}	1.02×10^{-2}	9.7×10^{-3}	1.02×10^{-2}	1.02×10^{-2}	1.02×10^{-2}
Nitrogen	2.5×10^{-4}	2.5×10^{-4}	2.5×10^{-4}	2.5×10^{-4}	2.5×10^{-4}	2.5×10^{-4}	2.5×10^{-4}	2.5×10^{-4}
Oxygen	7.2×10^{-3}	7.2×10^{-3}	6.2×10^{-3}	6.2×10^{-3}	7.2×10^{-3}	6.2×10^{-3}	6.2×10^{-3}	6.2×10^{-3}
Neon	2.0×10^{-3}	2.0×10^{-3}	4.9×10^{-3}	4.9×10^{-3}	2.0×10^{-3}	4.9×10^{-3}	4.9×10^{-3}	4.9×10^{-3}
Sulphur	4.0×10^{-4}	4.0×10^{-4}	4.0×10^{-5}	4.0×10^{-5}	4.0×10^{-4}	4.0×10^{-5}	4.0×10^{-5}	4.0×10^{-5}
Argon	5.0×10^{-5}	5.0×10^{-5}	1.0×10^{-5}	1.0×10^{-5}	5.0×10^{-5}	1.0×10^{-5}	1.0×10^{-5}	1.0×10^{-5}

Table 4.4. Derived elemental abundances of emitting gas in the Crab Nebula relative to hydrogen

Species	Wavelength [Å]	Observed Flux	Modelled Flux	Obs/Model	Modelled Flux	Obs/Model
		Model I	Model II		Model I	Model II
H_{β}	4861	6.64×10^{-11}	6.32×10^{-11}	1.05	7.74×10^{-11}	0.86
[O II]	3726+3729	18.11	20.10	0.90	19.40	0.93
[Ne III]	3869	4.65	3.79	1.23	4.12	1.13
[S II]	4069+4076	0.37	0.32	1.16	0.35	1.06
[O III]	4363	0.57	0.54	1.06	0.59	0.97
He I	4471	0.37	0.43	0.86	0.43	0.86
He II	4686	0.78	0.79	0.99	0.86	0.91
H_{β}	4861	1.00	1.00	1.00	1.00	1.00
[O III]	5007	11.92	9.57	1.25	9.57	1.25
[N I]	5198+5200	0.13	0.14	0.93	0.14	0.93
[N II]	5755	0.09	0.09	1.08	0.08	1.16
[O I]+[S III]	6300,6363+6312	1.23	1.63	0.75	1.33	0.92
Ha	6563	2.85	2.92	0.98	2.90	0.98
[N II]	6548+6584	6.87	6.38	1.08	6.31	1.09
[S II]	6717+6731	4.31	3.98	1.08	4.16	1.04
[Ar III]	7136	0.34	0.33	1.03	0.34	1.00
[C I]	9824+9850	0.36	0.66	0.55	0.88	0.41

Table 4.5. Observed and modelled absolute H_{β} fluxes. Observed and modelled line strengths are relative to H_{β} . All observed lines are taken from Smith (2003), except for [C I] 9824+9850 from Rudy et al. (1994), [Ar III] 7136+7751 from Davidson & Fesen (1985) and [Ar III] 89911 from Temim et al. (2012).

Species	Wavelength [Å]	Observed Flux	Modelled Flux	Obs/Model	Modelled Flux	Obs/Model
		Model III	Model IV			
H_{β}	4861	6.64×10^{-11}	6.32×10^{-11}	1.05	7.74×10^{-11}	0.86
[O II]	3726+3729	18.11	20.00	0.91	20.02	0.90
[Ne III]	3869	4.65	3.99	1.17	4.03	1.15
[S II]	4069+4076	0.37	0.29	1.28	0.33	1.14
[O III]	4363	0.57	0.52	1.10	0.55	1.04
He I	4471	0.37	0.41	0.90	0.51	0.73
He II	4686	0.78	0.88	0.89	0.96	0.81
H_{β}	4861	1.00	1.00	1.00	1.00	1.00
[O III]	5007	11.92	10.03	1.19	10.08	1.18
[N I]	5198+5200	0.13	0.14	0.93	0.20	0.66
[N II]	5755	0.09	0.07	1.33	0.12	0.75
[O I]+[S III]	6300,6363+6312	1.23	1.33	0.92	1.35	0.91
Ha	6563	2.85	2.93	0.97	2.96	0.96
[N II]	6548+6584	6.87	6.37	1.08	6.37	1.08
[S II]	6717+6731	4.31	3.93	1.10	3.97	1.09
[Ar III]	7136	0.34	0.33	1.03	0.33	1.03
[C I]	9824+9850	0.36	0.66	0.55	0.66	0.55

Table 4.6. Observed and modelled absolute H_{β} fluxes. Observed and modelled line strengths are relative to H_{β} . All observed lines are taken from Smith (2003), except for [C I] 9824+9850 from Rudy et al. (1994), [Ar III] 7136+7751 from Davidson & Fesen (1985) and [Ar III] 89911 from Temim et al. (2012).

Species	Wavelength [Å]	Observed Flux	Modelled Flux	Obs/Model	Modelled Flux	Obs/Model
		Model V	Model VI		Model VI	
H_{β}	4861	6.64×10^{-11}	6.32×10^{-11}	1.05	7.74×10^{-11}	0.86
[O II]	3726+3729	18.11	20.09	0.90	20.16	0.90
[Ne III]	3869	4.65	4.06	1.14	4.10	1.13
[S II]	4069+4076	0.37	0.39	0.96	0.41	0.90
[O III]	4363	0.57	0.55	1.04	0.63	0.91
He I	4471	0.37	0.42	0.89	0.51	0.72
He II	4686	0.78	0.92	0.85	0.92	0.85
H_{β}	4861	1.00	1.00	1.00	1.00	1.00
[O III]	5007	11.92	10.11	1.18	10.12	1.18
[N I]	5198+5200	0.13	0.15	0.85	0.21	0.62
[N II]	5755	0.09	0.10	0.96	0.13	0.74
[O I]+[S III]	6300,6363+6312	1.23	1.35	0.91	1.36	0.91
Ha	6563	2.85	2.94	0.97	2.99	0.95
[N II]	6548+6584	6.87	6.40	1.07	6.42	1.07
[S II]	6717+6731	4.31	3.99	1.08	4.01	1.08
[Ar III]	7136	0.34	0.33	1.03	0.41	0.83
[C I]	9824+9850	0.36	0.66	0.55	0.28	1.29

Table 4.7. Observed and modelled absolute H_{β} fluxes. Observed and modelled line strengths are relative to H_{β} . All observed lines are taken from Smith (2003), except for [C I] 9824+9850 from Rudy et al. (1994), [Ar III] 7136+7751 from Davidson & Fesen (1985) and [Ar III] 89911 from Temim et al. (2012).

Species	Wavelength [Å]	Observed Flux	Modelled Flux	Obs/Model	Modelled Flux	Obs/Model
			Model VII		Model VIII	
H_{β}	4861	6.64×10^{-11}	6.32×10^{-11}	1.05	7.74×10^{-11}	0.86
[O II]	3726+3729	18.11	20.11	0.90	20.18	0.90
[Ne III]	3869	4.65	4.16	1.12	4.22	1.10
[S II]	4069+4076	0.37	0.49	0.76	0.54	0.69
[O III]	4363	0.57	0.57	1.00	0.60	0.95
He I	4471	0.37	0.48	0.76	0.53	0.69
He II	4686	0.78	0.94	0.83	1.03	0.76
H_{β}	4861	1.00	1.00	1.00	1.00	1.00
[O III]	5007	11.92	10.15	1.17	10.17	1.17
[N I]	5198+5200	0.13	0.19	0.68	0.23	0.57
[N II]	5755	0.09	0.17	0.55	0.19	0.48
[O I]+[S III]	6300,6363+6312	1.23	1.40	0.88	1.44	0.86
Ha	6563	2.85	2.98	0.96	3.03	0.94
[N II]	6548+6584	6.87	6.43	1.07	6.52	1.05
[S II]	6717+6731	4.31	4.06	1.06	4.14	1.04
[Ar III]	7136	0.34	0.33	1.03	0.41	0.83
[C I]	9824+9850	0.36	0.66	0.55	0.28	1.29

Table 4.8. Observed and modelled absolute H_{β} fluxes. Observed and modelled line strengths relative are to H_{β} . All observed lines are taken from Smith (2003), except for [C I] 9824+9850 from Rudy et al. (1994), [Ar III] 7136+7751 from Davidson & Fesen (1985) and [Ar III] 89911 from Temim et al. (2012).

Species	Wavelength [Å]	Observed Flux	Modelled Flux	Obs/Model	Modelled Flux	Obs/Model
		Model IX	Model IX	Model X	Model X	Model X
H_{β}	4861	6.64×10^{-11}	6.32×10^{-11}	1.05	7.74×10^{-11}	0.86
[O II]	3726+3729	18.11	20.12	0.90	20.18	0.90
[Ne III]	3869	4.65	4.21	1.10	4.27	1.09
[S II]	4069+4076	0.37	0.49	0.75	0.56	0.66
[O III]	4363	0.57	0.61	0.94	0.68	0.84
He I	4471	0.37	0.52	0.71	0.60	0.62
He II	4686	0.78	1.02	0.77	1.03	0.76
H_{β}	4861	1.00	1.00	1.00	1.00	1.00
[O III]	5007	11.92	10.19	1.17	10.22	1.17
[N I]	5198+5200	0.13	0.20	0.67	0.24	0.55
[N II]	5755	0.09	0.20	0.46	0.20	0.45
[O I]+[S III]	6300,6363+6312	1.23	1.47	0.84	1.53	0.80
Ha	6563	2.85	3.05	0.94	3.09	0.92
[N II]	6548+6584	6.87	6.47	1.06	6.49	1.06
[S II]	6717+6731	4.31	4.15	1.04	4.17	1.03
[Ar III]	7136	0.34	0.33	1.03	0.41	0.83
[C I]	9824+9850	0.36	0.66	0.55	0.28	1.29

Table 4.9. Observed and modelled absolute H_{β} fluxes. Observed and modelled line strengths are relative to H_{β} . All observed lines are taken from Smith (2003), except for [C I] 9824+9850 from Rudy et al. (1994), [Ar III] 7136+7751 from Davidson & Fesen (1985) and [Ar III] 89911 from Temim et al. (2012).

Species	Wavelength [Å]	Observed Flux	Modelled Flux	Obs/Model	Modelled Flux	Obs/Model
		Model XI	Model XII		Model XII	
H_{β}	4861	6.64×10^{-11}	6.32×10^{-11}	1.05	7.74×10^{-11}	0.86
[O II]	3726+3729	18.11	20.17	0.90	20.23	0.90
[Ne III]	3869	4.65	4.28	1.09	4.30	1.08
[S II]	4069+4076	0.37	0.54	0.69	0.59	0.63
[O III]	4363	0.57	0.69	0.82	0.71	0.80
He I	4471	0.37	0.58	0.63	0.66	0.56
He II	4686	0.78	1.10	0.71	1.16	0.67
H_{β}	4861	1.00	1.00	1.00	1.00	1.00
[O III]	5007	11.92	10.27	1.16	10.32	1.16
[N I]	5198+5200	0.13	0.20	0.66	0.21	0.61
[N II]	5755	0.09	0.29	0.33	0.35	0.27
[O I]+[S III]	6300,6363+6312	1.23	1.51	0.82	1.59	0.77
Ha	6563	2.85	3.07	0.93	3.17	0.90
[N II]	6548+6584	6.87	6.50	1.06	6.54	1.05
[S II]	6717+6731	4.31	4.15	1.04	4.17	1.03
[Ar III]	7136	0.34	0.33	1.03	0.41	0.83
[C I]	9824+9850	0.36	0.66	0.55	0.28	1.29

Table 4.10. Observed and modelled absolute H_{β} fluxes. Observed and modelled line strengths are relative to H_{β} . All observed lines are taken from Smith (2003), except for [C I] 9824+9850 from Rudy et al. (1994), [Ar III] 7136+7751 from Davidson & Fesen (1985) and [Ar III] 89911 from Temim et al. (2012).

Species	Wavelength [Å]	Observed Flux	Modelled Flux	Obs/Model
			Model XIII	
H β	4861	6.64×10 ⁻¹¹	7.74×10 ⁻¹¹	0.86
[O II]	3726+3729	18.11	20.22	0.90
[Ne III]	3869	4.65	4.33	1.07
[S II]	4069+4076	0.37	0.58	0.64
[O III]	4363	0.57	0.78	0.73
He I	4471	0.37	0.63	0.59
He II	4686	0.78	1.14	0.68
H β	4861	1.00	1.00	1.00
[O III]	5007	11.92	10.29	1.16
[N I]	5198+5200	0.13	0.30	0.44
[N II]	5755	0.09	0.35	0.26
[O I]+[S III]	6300,6363+6312	1.23	1.59	0.77
H α	6563	2.85	3.14	0.91
[N II]	6548+6584	6.87	6.50	1.06
[S II]	6717+6731	4.31	4.22	1.02
[Ar III]	7136	0.34	0.33	1.03
[C I]	9824+9850	0.36	0.66	0.55

Table 4.11. Observed and modelled absolute H β fluxes. Observed and modelled line strengths are relative to H β . All observed lines are taken from Smith (2003), except for [C I] 9824+9850 from Rudy et al. (1994), [Ar III] 7136+7751 from Davidson & Fesen (1985) and [Ar III] 89911 from Temim et al. (2012).

	Neutral	1^+	2^+	3^+	4^+	5^+
Hydrogen	0.130	0.870				
Helium	0.332	0.630	3.77×10^{-2}			
Carbon	1.01×10^{-2}	0.730	0.248	2.08×10^{-2}	2.01×10^{-6}	1.04×10^{-10}
Nitrogen	1.04×10^{-2}	0.708	0.237	5.39×10^{-3}	1.17×10^{-6}	2.34×10^{-9}
Oxygen	0.144	0.721	0.107	2.75×10^{-3}	1.05×10^{-6}	7.37×10^{-8}
Neon	0.114	0.772	0.113	3.72×10^{-4}	4.10×10^{-6}	9.93×10^{-9}
Sulphur	0.198	0.449	0.299	6.95×10^{-3}	3.34×10^{-5}	5.66×10^{-8}
Argon	2.31×10^{-5}	0.116	0.702	0.178	2.31×10^{-3}	4.25×10^{-5}

Table 4.12. Global ionisation fractions of elements in model x.

$8 M_{\odot}$. However, we conclude that since no existing CCSN yield predictions match the case of the Crab Nebula, they therefore do not provide useful constraints on the total masses of heavy elements that could be in the gas phase or tied up within dust grains in the Crab Nebula.

From an empirical analysis, Fesen et al. (1997) estimated a total gas mass of $4.6 \pm 1.8 M_{\odot}$ for the Crab Nebula, of which $1.5 M_{\odot}$ was estimated to be in neutral filaments. From our clumped photoionization model we find a total gas mass $7.0 \pm 0.5 M_{\odot}$, of which $2.1 \pm 0.2 M_{\odot}$ is neutral. Fesen et al. (1997) used an observed total $H\beta$ flux of $1.78 \pm 0.20 \times 10^{-11} \text{ ergs cm}^{-2} \text{ s}^{-1}$, from MacAlpine & Uomoto (1991), versus the value of $1.38 \pm 0.07 \times 10^{-11} \text{ ergs cm}^{-2} \text{ s}^{-1}$ from Smith (2003) used here. Kirshner (1974) measured a total $H\beta$ flux of $1.30 \pm 0.40 \times 10^{-11} \text{ ergs cm}^{-2} \text{ s}^{-1}$, while Davidson (1987) estimated $1.16 \pm 0.12 \times 10^{-11} \text{ ergs cm}^{-2} \text{ s}^{-1}$. We adopt a factor of 1.15 uncertainty in the total $H\beta$ flux, which corresponds to a factor of $1.15^{1/2} = 1.07$ uncertainty in the total nebular gas mass of $7.0 \pm 0.5 M_{\odot}$. The photoionization models described above included the dust grain components that are described in the next Section. However, running the models without dust made an insignificant difference to the emission line fits, i.e. dust does not compete significantly for the photons that determine the global gas-phase ionization balance and line emission from the nebula. By contrast, for a model run without gas, the dust emission was a factor of 1.17 lower than for the gas+dust model, indicating that absorption of nebular gaseous emission lines makes a significant contribution to the dust luminosity.

Argon and ArH⁺

As discussed in Chapter 2, Barlow et al. (2013) discovered the noble gas molecular ion $^{36}\text{ArH}^+$ in the Crab Nebula, via the detection of its J=1-0 and 2-1 rotational emission lines in *Herschel*-SPIRE FTS spectra. We therefore included argon in our photoionization modelling of the nebula. As noted above, for Knot FK 6, typical of the nebula as a whole, argon's mass fraction was found to be enhanced by a factor of three relative to solar. However, [Ar III] relative line intensities at Knot FK 10, where ArH⁺ emission is strongest, are a factor of two higher than at FK 6, suggesting a larger enhancement of the argon abundance there. Following the detection of ArH⁺ emission in the Crab Nebula, Schilke et al. (2014) were able to use a previously unidentified interstellar absorption feature, now identified as due to ground-state absorption by the J=1-0 rotational line of ArH⁺, to diagnose the physical conditions in the absorbing interstellar clouds. They concluded that the formation reaction $\text{H}_2 + \text{Ar}^+ \rightarrow \text{H} + \text{ArH}^+$ must take place in regions where hydrogen is overwhelmingly in the form of neutral atoms. This is relevant to the Crab Nebula, since photoionization models predict the existence of significant zones of atomic hydrogen (see Table 4.12 and Richardson et al. (2013)). Richardson et al. (2013) concluded from their models that the Crab Nebula knots from which H₂ line emission had been detected were almost entirely atomic. The likelihood that ArH⁺ also forms and emits in these regions should be investigated with further modelling.

4.2.2 Dust Masses

I. Smooth Model.

The dust best fits for Model 1 to the observed SED of the Crab Nebula are shown in Figure 4.17, with the parameters used to achieve these fits shown in Table 4.13. The results using the Zubko AC optical constants, as used by Gomez et al. (2012) are in good agreement with the empirically determined dust mass. The dust mass determined for the silicates is further from the empirically determined mean mass but still within the measured uncertainty which could be as high as 0.5 M_\odot .

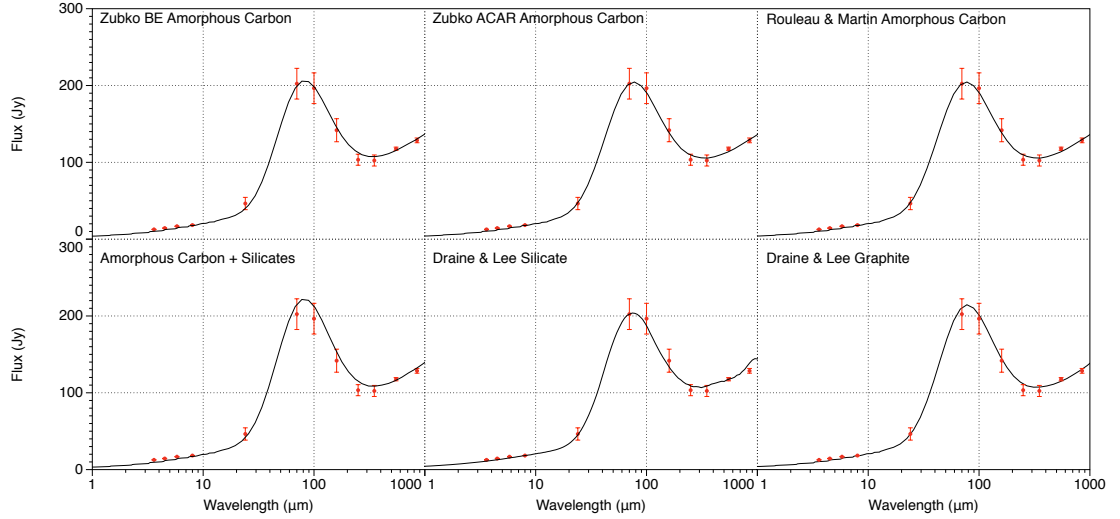


Figure 4.17. Best fit models plotted with observed SEDs for the six different sets of optical constants using a smooth isotropic density distribution with a density of 775 cm^{-3} (Model I).

Optical Constants	a_{min}	a_{max}	α	M_{dust}	χ^2
Zubko AC	$0.005 \mu\text{m}$	$1.0 \mu\text{m}$	2.9 ± 0.1	$0.30 M_\odot$	3.12
Zubko BE	$0.005 \mu\text{m}$	$0.7 \mu\text{m}$	2.9 ± 0.1	$0.14 M_\odot$	3.97
Hanner	$0.01 \mu\text{m}$	$1.0 \mu\text{m}$	2.9 ± 0.1	$0.30 M_\odot$	4.01
Rouleau & Martin AC	$0.01 \mu\text{m}$	$1.0 \mu\text{m}$	3.0 ± 0.1	$0.08 M_\odot$	10.0
Mixed Model	$0.01 \mu\text{m}$	$0.9 \mu\text{m}$	3.0 ± 0.1	$0.18 M_\odot$	3.33
				$0.08 M_\odot$ Zubko BE $0.1 M_\odot$ DL silicates	
Draine & Lee Silicate	$0.001 \mu\text{m}$	$1.0 \mu\text{m}$	3.5 ± 0.1	$0.46 M_\odot$	2.99
Draine & Lee Graphite	$0.001 \mu\text{m}$	$0.25 \mu\text{m}$	3.0 ± 0.1	$0.09 M_\odot$	4.01

Table 4.13. The results for model I, the smooth isotropic density distribution.

II. Smooth Shell Model.

The best fits for Model II to the observed SED of the Crab Nebula are shown in Figure 4.18 with parameters used to achieve these fits shown in Table 4.14. The dust and gas are smoothly distributed in the outer third of the nebula with a hydrogen number density of 850 cm^{-3} . The dust masses determined are slightly less than those measured using a smooth density distribution with material throughout the nebula. As with model I, the dust masses obtained using the same optical constants used by Gomez et al. (2012) are in agreement with their empirical fit.

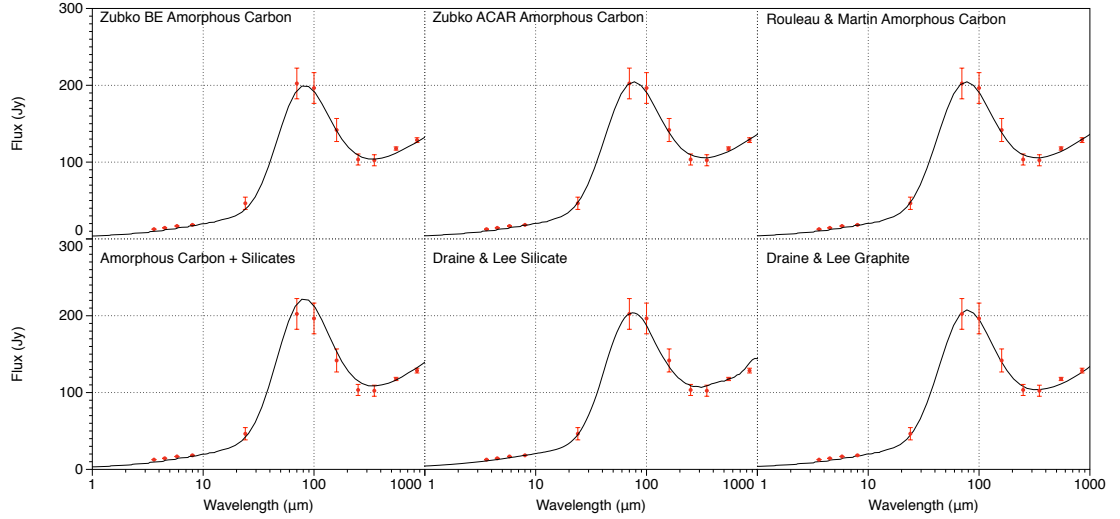


Figure 4.18. Best fit models plotted with observed SEDs for the six different sets of optical constants using a smooth isotropic density distribution in a shell in the outer third of the nebula with a density of 850 cm^{-3} outside the diffuse radiation source (Model II)

Optical Constants	a_{min}	a_{max}	α	M_{dust}	χ^2
Zubko AC	$0.07 \mu\text{m}$	$1.0 \mu\text{m}$	2.9 ± 0.1	$0.27 M_\odot$	9.9
Zubko BE	$0.07 \mu\text{m}$	$0.2 \mu\text{m}$	2.9 ± 0.1	$0.11 M_\odot$	9.7
Rouleau & Martin AC	$0.07 \mu\text{m}$	$1.0 \mu\text{m}$	3.0 ± 0.1	$0.08 M_\odot$	12.1
Mixed Model	$0.01 \mu\text{m}$	$1.0 \mu\text{m}$	3.0 ± 0.1	$0.25 \pm 0.05 M_\odot$ $0.13 M_\odot$ Zubko BE $0.12 M_\odot$ DL silicates	5.23
Draine & Lee Silicate	$0.07 \mu\text{m}$	$1.0 \mu\text{m}$	3.5 ± 0.1	$0.40 M_\odot$	11.3
Draine & Lee Graphite	$0.001 \mu\text{m}$	$0.25 \mu\text{m}$	3.0 ± 0.1	$0.08 M_\odot$	11.0

Table 4.14. The results for model II. the smooth isotropic density distribution with outer diameters of $4.0 \times 2.9 \text{ pc}$ and inner diameters of $3.0 \times 2.0 \text{ pc}$ outside the radiation source.

III. Geometry from Davidson & Fesen (1985) with dust and gas in a shell 0.5 pc thick.

Figure 4.19 shows the best fit for Model III to the observed SED for the smooth isotropic density distribution in a shell 0.5 pc thick and inner axes of 2.1×1.4 pc entirely inside the diffuse radiation source. This model is based on observations presented in Davidson & Fesen (1985). The shell thickness is taken as an intermediate value as the values given in the paper span a range of 0.3-07 pc averaging at 0.5 pc with a hydrogen number density of 850 cm^{-3} . The dust masses, shown in table 4.15, are required to fit the SED with this geometry are lower, although still very close to those measured by Gomez et al. (2012).

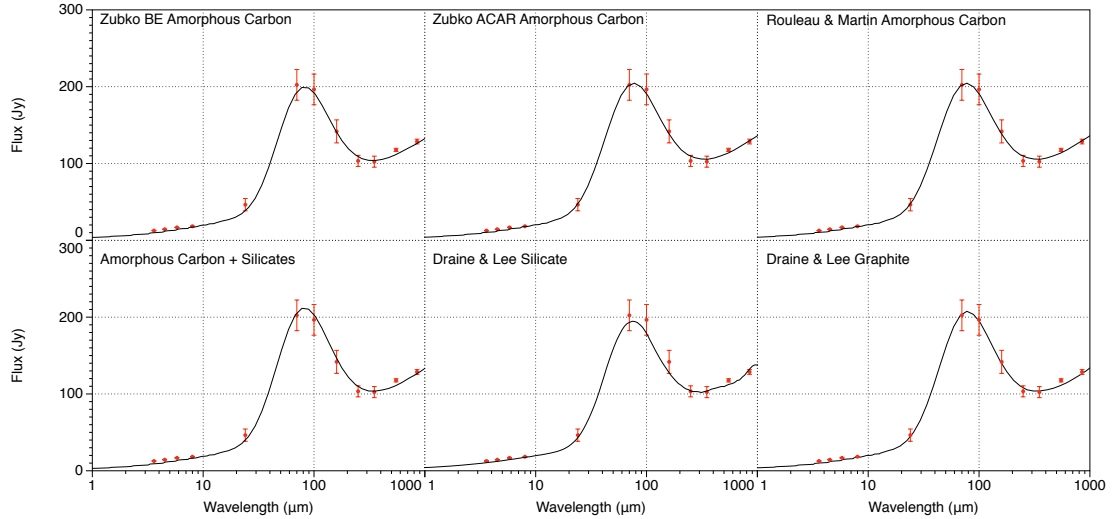


Figure 4.19. Best fit Models plotted with observed SEDs for the six different sets of optical constants using a smooth isotropic density distribution in a shell 0.5 pc thick and a inner diameters of 2.1×1.4 pc entirely inside the diffuse radiation source (Model III).

Optical Constants	a_{min}	a_{max}	α	M_{dust}	χ^2
Zubko et al. ACAR	0.01 μm	0.7 μm	2.9 ± 0.1	$0.12 \pm 0.03 M_\odot$	5.22
Zubko et al. BE	0.005 μm	0.5 μm	2.8 ± 0.1	$0.09 \pm 0.02 M_\odot$	5.97
Rouleau & Martin AC1	0.01 μm	0.7 μm	3.0 ± 0.1	$0.05 \pm 0.01 M_\odot$	4.89
Mixed Model	0.01 μm	0.8 μm	3.0 ± 0.1	$0.14 \pm 0.02 M_\odot$ 0.05 M_\odot Zubko BE 0.09 M_\odot DL silicates	6.01
Draine & Lee Silicate	0.001 μm	0.9 μm	3.5 ± 0.1	$0.32 \pm 0.06 M_\odot$	5.14
Draine & Lee Graphite	0.001 μm	0.25 μm	2.9 ± 0.1	$0.06 \pm 0.01 M_\odot$	6.66

Table 4.15. The results for model III. the smooth isotropic density distribution in a shell 0.5 pc thick and a inner axes of 2.1×1.4 pc entirely inside the diffuse radiation source.

IV. Geometry from Davidson & Fesen (1985) with dust and gas distributed from the inner radius to the edge of the nebula.

Figure 4.20 shows the best fit to observed SEDs for the smooth isotropic density distribution in a shell with inner axes of 2.1×1.4 pc and outer edge of the nebula at 4.0×2.9 pc, with the radiation field filling the whole nebula out to the same radii following geometry from Davidson & Fesen (1985) and a hydrogen number density of 775 cm^{-3} . The masses of dust required, listed in Table 4.16, are larger than that needed for the geometry with a thinner shell.

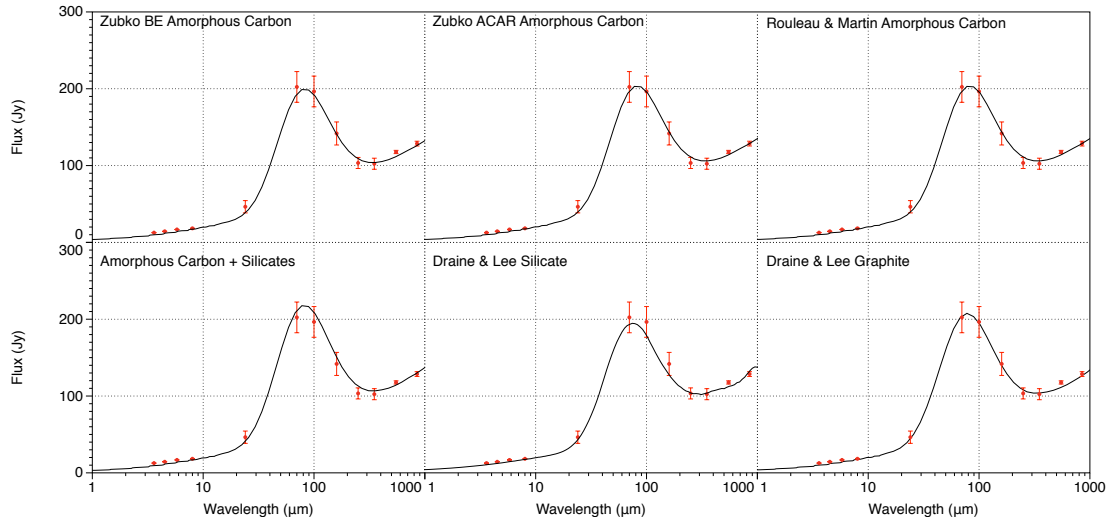


Figure 4.20. Best fit models plotted with observed SEDs for the six different sets of optical constants using a smooth isotropic density distribution in a shell all the way to the edge of the nebula and a inner diameters of 2.1×1.4 pc entirely inside the diffuse axes source (Model IV).

Optical Constants	a_{min}	a_{max}	α	M_{dust}	χ^2
Zubko et al. ACAR	0.01 μm	1.0 μm	2.9 ± 0.1	$0.18 M_\odot$	9.9
Zubko et al BE	0.01 μm	0.2 μm	2.9 ± 0.1	$0.14 M_\odot$	9.7
Rouleau & Martin AC1	0.01 μm	1.0 μm	3.0 ± 0.1	$0.08 M_\odot$	12.1
Mixed Model	0.01 μm	0.8 μm	3.0 ± 0.1	$0.21 \pm 0.02 M_\odot$ $0.05 M_\odot$ Zubko BE $0.09 M_\odot$ DL silicates	6.01
Draine & Lee Silicate	0.01 μm	1.0 μm	3.5 ± 0.1	$0.48 M_\odot$	11.3
Draine & Lee Graphite	0.001 μm	0.25 μm	3.0 ± 0.1	$0.09 M_\odot$	11.0

Table 4.16. The results for Model iv. the smooth isotropic density distribution with outer diameters of 4.0×2.9 pc and inner axes of 2.1×1.4 pc entirely inside the diffuse radiation source.

V. Geometry from Lawrence et al. (1995) with dust and gas distributed from the inner radius to the edge of the nebula.

The best first for Model v to the observed SED for a smooth model with inner diameters of 2.3×1.7 pc entirely inside the diffuse radiation source based on observations by Lawrence et al. (1995) and a hydrogen number density of 675 cm^{-3} are shown in Figure 4.21, with corresponding fitted parameters in Table 4.17.

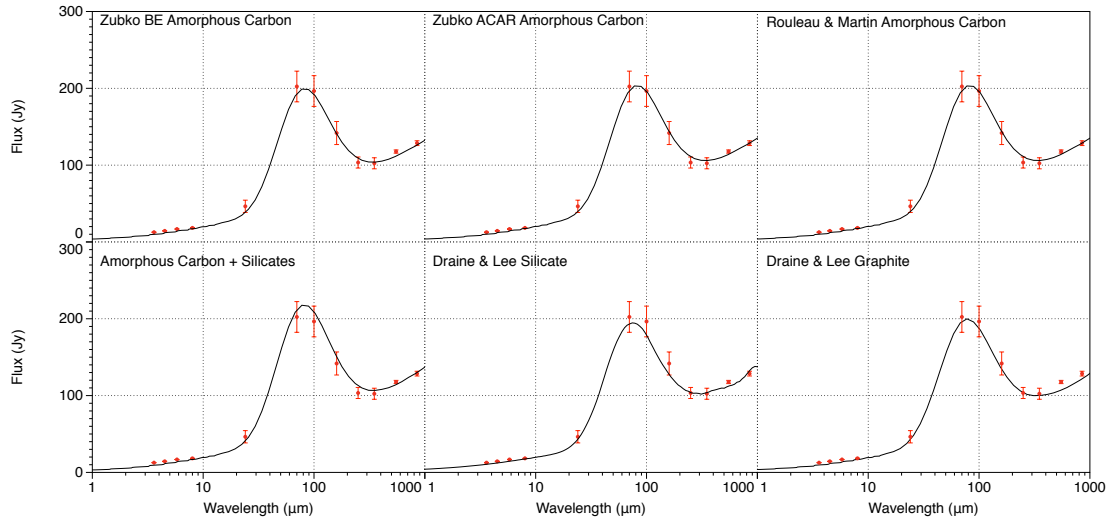


Figure 4.21. Best fit models plotted with observed SEDs for the six different sets of optical constants using a smooth isotropic density distribution in a shell all the way to the edge of the nebula and a inner axes of 2.3×1.7 pc entirely inside the diffuse radiation source (Model v).

Optical Constants	a_{min}	a_{max}	α	M_{dust}	χ^2
Zubko et al. ACAR	0.01 μm	0.7 μm	2.9 ± 0.1	$0.14 \pm 0.04 M_\odot$	5.22
Zubko et al. BE	0.005 μm	0.5 μm	2.8 ± 0.1	$0.11 \pm 0.02 M_\odot$	5.97
Rouleau & Martin AC1	0.01 μm	0.7 μm	3.0 ± 0.1	$0.06 \pm 0.01 M_\odot$	4.89
Mixed Model	0.01 μm	0.8 μm	3.0 ± 0.1	$0.16 \pm 0.02 M_\odot$	6.01
				$0.05 M_\odot$ Zubko BE	
				$0.09 M_\odot$ DL silicates	
Draine & Lee Silicate	0.001 μm	0.9 μm	3.5 ± 0.1	$0.37 \pm 0.06 M_\odot$	5.14
Draine & Lee Graphite	0.001 μm	0.25 μm	2.9 ± 0.1	$0.07 \pm 0.01 M_\odot$	6.66

Table 4.17. The results for model v. the smooth isotropic density distribution with outer diameters of 4.0×2.9 pc and inner axes of 2.13×1.7 pc entirely inside the diffuse radiation source.

VI. Geometry from Čadež et al. (2004) with dust and gas in a shell 0.1 pc thick.

The best fits for the clumpy model with the inner radius of 0.55 pc in a 0.1 pc thick shell with a diffuse radiation source going from the centre to the edge of the nebula with the dust and gas entirely bathed in the radiation source and a hydrogen number density of 1400 cm^{-3} . The best fits to the observed SED are shown in Figure 4.22 with parameters used to achieve these fits listed in Table 4.18.

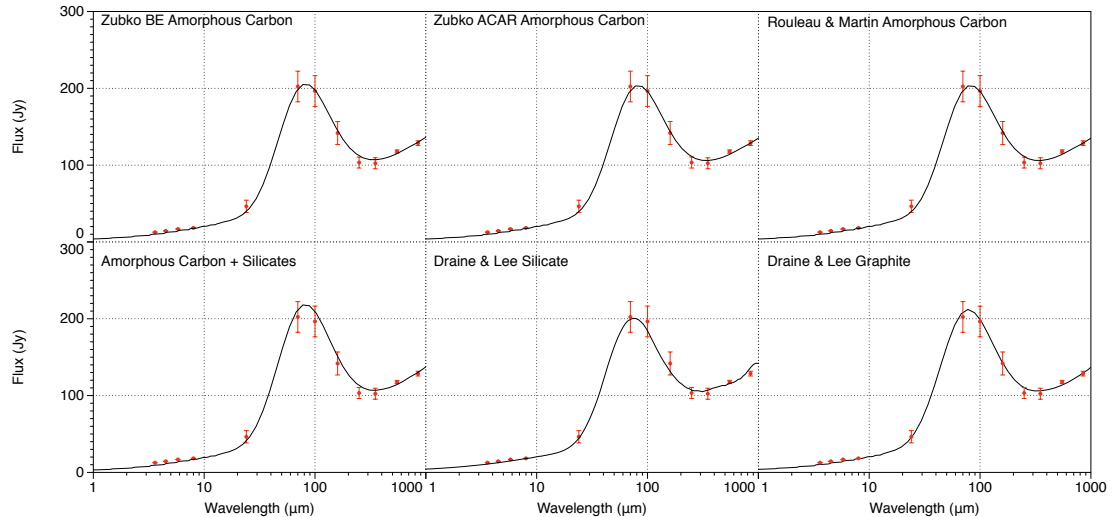


Figure 4.22. Best fit models plotted with observed SEDs for the six different sets of optical constants using a smooth isotropic density distribution in a shell 0.1 pc thick and a inner diameter of 1.1 pc entirely inside the diffuse radiation source (Model vi).

Optical Constants	a_{min}	a_{max}	α	M_{dust}	χ^2
Zubko et al. ACAR	0.005 μm	0.7 μm	2.7 ± 0.1	$0.10 \pm 0.02 M_\odot$	6.08
Zubko et al. BE	0.005 μm	0.5 μm	2.7 ± 0.1	$0.08 \pm 0.01 M_\odot$	5.99
Rouleau & Martin AC1	0.01 μm	0.8 μm	2.9 ± 0.1	$0.05 \pm 0.01 M_\odot$	4.98
Mixed Model	0.01 μm	1.0 μm	3.0 ± 0.1	$0.12 \pm 0.02 M_\odot$	5.23
				$0.04 M_\odot$ Zubko BE	
				$0.08 M_\odot$ DL silicates	
Draine & Lee Silicate	0.01 μm	0.9 μm	3.5 ± 0.1	$0.26 \pm 0.04 M_\odot$	5.44
Draine & Lee Graphite	0.001 μm	0.25 μm	2.8 ± 0.1	$0.6 \pm 0.01 M_\odot$	6.03

Table 4.18. The results for Model VI. the smooth isotropic density distribution in a shell 0.1 pc thick and a diameter of 1.1 pc entirely inside the diffuse radiation source..

VII. Clumpy Model - Clumps with radius 0.111 pc outside of the radiation field

The best fits for model VII to the observed SED for the model with all the material in the clumps with a filling factor of 0.1 and a hydrogen number density of 1400 cm^{-3} are shown in Figure 4.23 with parameters used to achieve these fits shown in Table 4.19. There is a factor of 2-3 increase in the mass of the dust determined using the clumpy models depending on the set of optical constants used. The clumps are outside the radiation field and start at inner axes of 3.0×2.0 pc and decrease with an r^{-2} dependence.

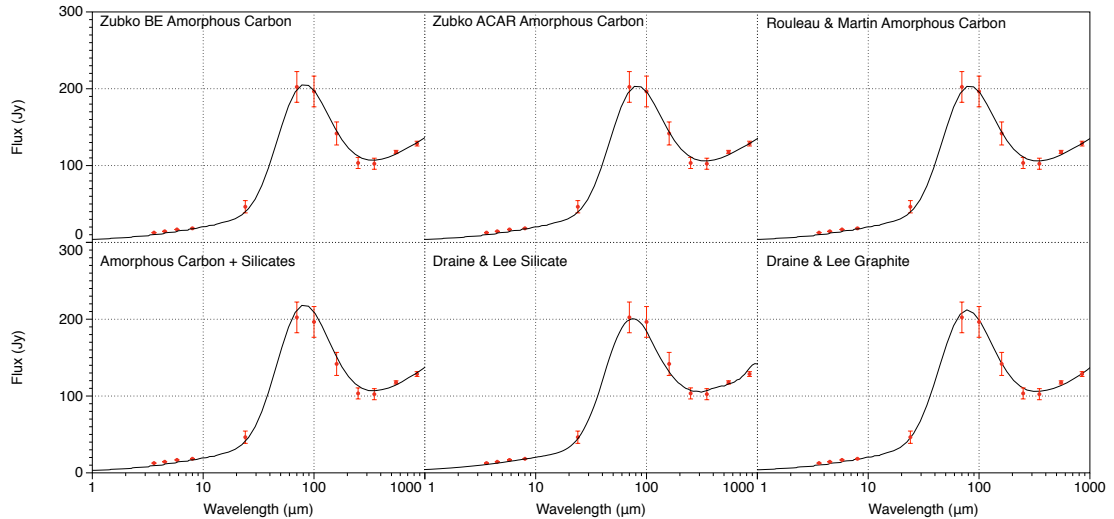


Figure 4.23. Best fit dust models plotted with the observed SEDs for six different sets of optical constants using a density distribution when all of the matter is in clumps with radius 0.111 pc and a density of 1400 cm^{-3} (Model VII).

Optical Constants	a_{min}	a_{max}	α	M_{dust}	χ^2
Zubko AC	0.07 μm	1.0 μm	2.9 ± 0.1	$0.4 M_\odot$	11.3
Zubko BE	0.07 μm	0.2 μm	2.9 ± 0.1	$0.3 M_\odot$	11.5
Hanner	0.07 μm	1.0 μm	2.9 ± 0.1	$0.38 M_\odot$	13.1
Rouleau & Martin AC	0.07 μm	1.0 μm	3.0 ± 0.1	$0.24 M_\odot$	14.3
Mixed Model	0.07 μm	1.0 μm	3.0 ± 0.1	$0.40 M_\odot$	10.0
				$0.25 M_\odot$ Zubko BE	
				$0.15 M_\odot$ DL silicates	
Draine & Lee Silicate	0.07 μm	1.0 μm	3.5 ± 0.1	$1.5 M_\odot$	14.4
Draine & Lee Graphite	0.001 μm	0.25 μm	3.0 ± 0.1	$0.40 M_\odot$	13.2

Table 4.19. The results for model VII. A clumpy geometry with clumps starting at radii of 3.0×2.0 pc decreasing with r^{-2} entirely outside the radiation source. The clumps have a of radius 0.111 pc with a density of 1400 cm^{-3} .

VIII. Clumpy Model - Clumps with radius 0.037 pc outside of the radiation field.

The best fits to the observed SED for the model with all the material in the clumps with a volume filling factor of 0.1 and a hydrogen number density of 1900 cm^{-3} , clump radius of 0.037 pc are shown in Figure 4.24, with the parameters used to achieve these fits shown in Table 4.20. The clumps are outside the radiation source emission region and start at inner axes of of 1.5×1.0 pc and hydrogen number density decreases with an r^{-2} dependence.

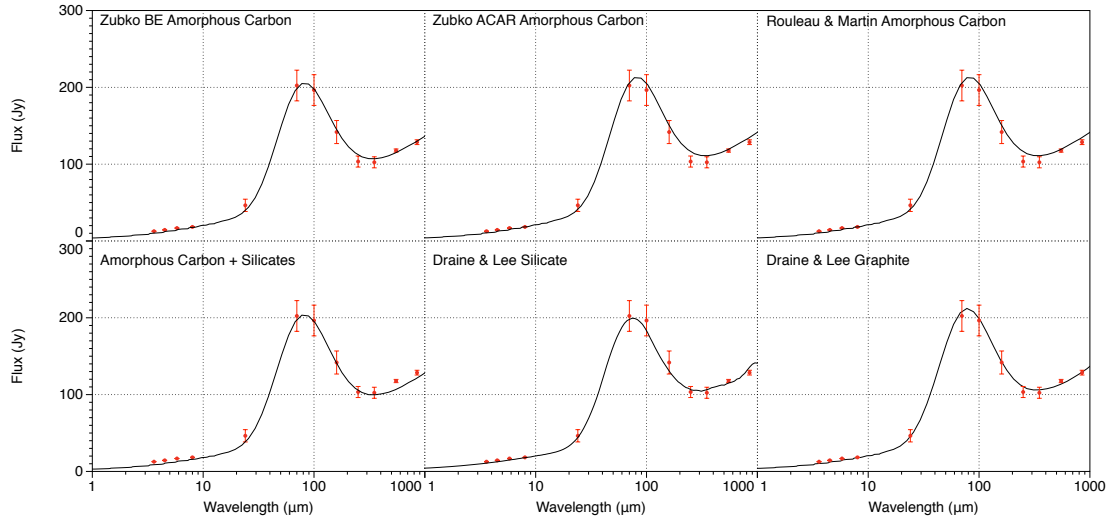


Figure 4.24. Best fit dust models plotted with observed SEDs for the six different sets of optical constants using a density distribution when all of the matter is in clumps of radius 0.037 pc with a H number density of 1900 cm^{-3} (Model VIII).

Optical Constants	a_{min}	a_{max}	α	M_{dust}	χ^2
Zubko AC	0.07 μm	1.0 μm	2.9 ± 0.1	$0.68 M_\odot$	11.2
Zubko BE	0.07 μm	0.2 μm	2.9 ± 0.1	$0.50 M_\odot$	10.9
Mixed Model	0.01 μm	1.0 μm	3.0 ± 0.1	$0.25 \pm 0.05 M_\odot$ $0.13 M_\odot$ Zubko BE $0.12 M_\odot$ DL silicates	5.23
Rouleau & Martin AC	0.07 μm	1.0 μm	3.0 ± 0.1	$0.44 M_\odot$	13.7
Draine & Lee Silicate	0.07 μm	1.0 μm	3.5 ± 0.1	$2.0 M_\odot$	12.1
Draine & Lee Graphite	0.001 μm	0.25 μm	3.0 ± 0.1	$0.47 M_\odot$	12.2

Table 4.20. The results for Model VIII. A clumpy geometry with clumps starting at radii of 3.0×2.0 pc decreasing with r^{-2} entirely outside the radiation source. The clumps have a of radius 0.037 pc with a H number density of 1900 cm^{-3} .

IX. Clumpy model with Davidson & Fesen (1985) geometry.

The best fits to the SED for the clumpy model with the inner semi-axes of 1.05×0.7 pc with a H number density decreasing with an r^{-2} dependence with all the clumps inside the radiation field are shown in Figure 4.25 with the parameters used to achieve these fits shown in Table 4.21. The clumps have a hydrogen number density of 1900 cm^{-3} , and a clump radius of 0.037 pc. The clump density decreases outwards with a an r^{-2} dependence.

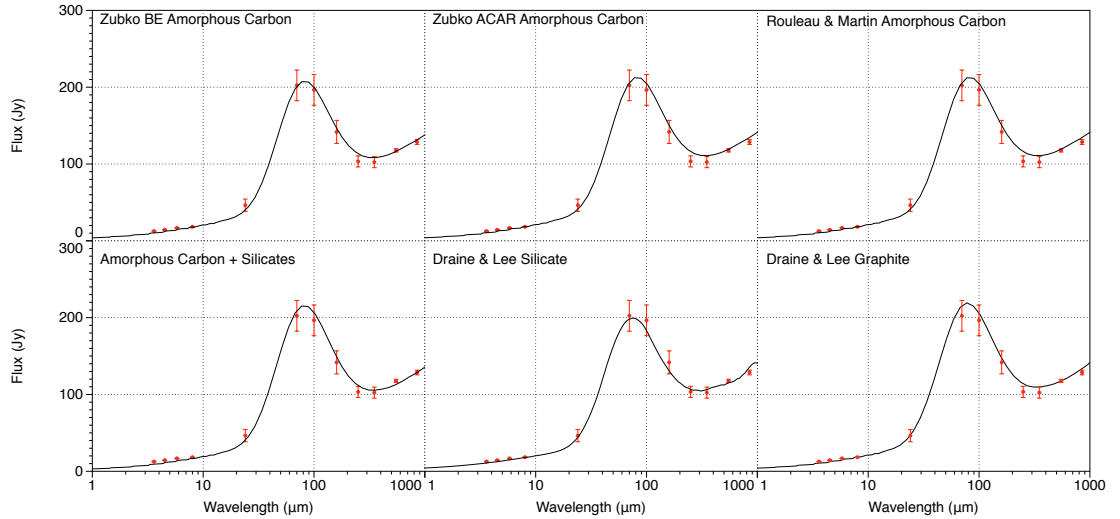


Figure 4.25. Best fit dust models plotted with observed SEDs for the six different sets of optical constants using a density distribution when all of the matter is in clumps of radius 0.037 pc with a H number density of 1900 cm^{-3} (Model IX).

The dust mass determined with the Zubko et al. (1996) BE grain optical properties

used by Gomez et al. (2012) is almost twice that of the mass determined empirically. The mass determined using Draine & Lee (1984) silicate optical properties is three times higher than the dust mass Gomez et al. (2012) empirically determined.

Optical Constants	a_{min}	a_{max}	α	M_{dust}	χ^2
Zubko et al. ACAR	0.005 μm	0.7 μm	2.7 ± 0.1	$0.25 \pm 0.04 M_\odot$	6.08
Zubko et al. BE	0.005 μm	0.5 μm	2.7 ± 0.1	$0.18 \pm 0.03 M_\odot$	5.99
Rouleau & Martin AC1	0.01 μm	0.8 μm	2.9 ± 0.1	$0.15 \pm 0.03 M_\odot$	4.98
Mixed Model	0.01 μm	1.0 μm	3.0 ± 0.1	$0.25 \pm 0.05 M_\odot$	5.23
				0.13 M_\odot Zubko BE	
				0.12 M_\odot DL silicates	
Draine & Lee Silicate	0.01 μm	0.9 μm	3.5 ± 0.1	$0.98 \pm 0.19 M_\odot$	5.44
Draine & Lee Graphite	0.001 μm	0.25 μm	2.8 ± 0.1	$0.17 \pm 0.03 M_\odot$	6.03

Table 4.21. The results for model IX. A clumpy geometry with clumps starting at radii of 2.1×1.4 pc decreasing with r^{-2} entirely inside the radiation source (Model IX).

X. Clumpy model with Lawrence et al. (1995) geometry.

The best fits to the SED for the clumpy model with the inner semi-axes of 1.15×0.85 pc and a clump number density decreasing with an r^{-2} dependence, with all the clumps inside the radiation source shown in Figure 4.26, with the parameters used to achieve these fits listed in Table 4.22. The clumps have a hydrogen number density of 1900 cm^{-3} , and a clump radius of 0.037 pc.

Optical Constants	a_{min}	a_{max}	α	M_{dust}	χ^2
Zubko et al. ACAR	0.005 μm	0.7 μm	2.7 ± 0.1	$0.25 \pm 0.04 M_\odot$	5.12
Zubko et al. BE	0.005 μm	0.5 μm	2.7 ± 0.1	$0.18 \pm 0.03 M_\odot$	6.97
Rouleau & Martin AC1	0.01 μm	0.8 μm	2.9 ± 0.1	$0.15 \pm 0.03 M_\odot$	5.00
Mixed Model	0.01 μm	1.0 μm	3.0 ± 0.1	$0.25 \pm 0.05 M_\odot$	4.98
				0.13 M_\odot Zubko BE	
				0.12 M_\odot DL silicates	
Draine & Lee Silicate	0.01 μm	0.9 μm	3.5 ± 0.1	$0.98 \pm 0.19 M_\odot$	5.11
Draine & Lee Graphite	0.001 μm	0.25 μm	2.8 ± 0.1	$0.17 \pm 0.03 M_\odot$	6.03

Table 4.22. The results for model X. A clumpy geometry with clumps starting at radii of 2.3×1.7 pc decreasing with r^{-2} entirely inside the radiation source.

Dust masses derived for the different clumped geometries in models IX and X are identical. This is unsurprising as the models both use the same volume filling factor and have the same number of clumps. Each clump is embedded in the heating

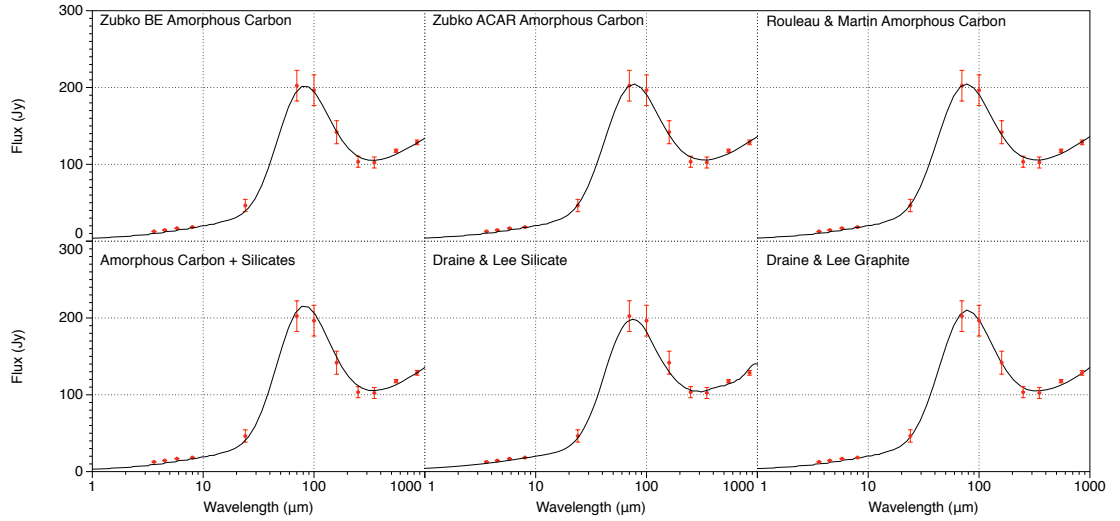


Figure 4.26. Best fit models plotted with observed SEDs for the six different sets of optical constants using a density distribution when all of the matter is in clumps of radius 0.037 pc with a density of 1900 cm^{-3} . (model x)

radiation source so they are heated from all around in the same way, which leads to the identical dust masses.

XI. Model with Čadež et al. (2004) geometry with the dust entirely outside the radiation source.

The best fits to the SED for the clumpy model with the inner radius of 0.55 pc in a 0.1 pc thick shell with a diffuse radiation source going up to the inner radius of the dust shell are shown in Figure 4.27 with the parameters used to achieve these fits shown in Table 4.23. This model is analogous to that used by Temim & Dwek (2013).

XII. Clumpy model with Lawrence et al. (1995) geometry with the dust entirely outside the radiation source.

The best fits to the observed SED are shown in Figure 4.28. The model is the clumpy model with the inner semi-axes of 1.15×0.85 pc and the number of clumps decreasing with an r^{-2} dependence with a diffuse radiation source going up to the inner radius of the dust shell. The parameters used to achieve these fits are shown in Table 4.24. The clumps have a hydrogen number density of 1900 cm^{-3} , and a radius of 0.037 pc.

XIII. Clumpy model with Davidson & Fesen (1985) geometry entirely outside the radiation

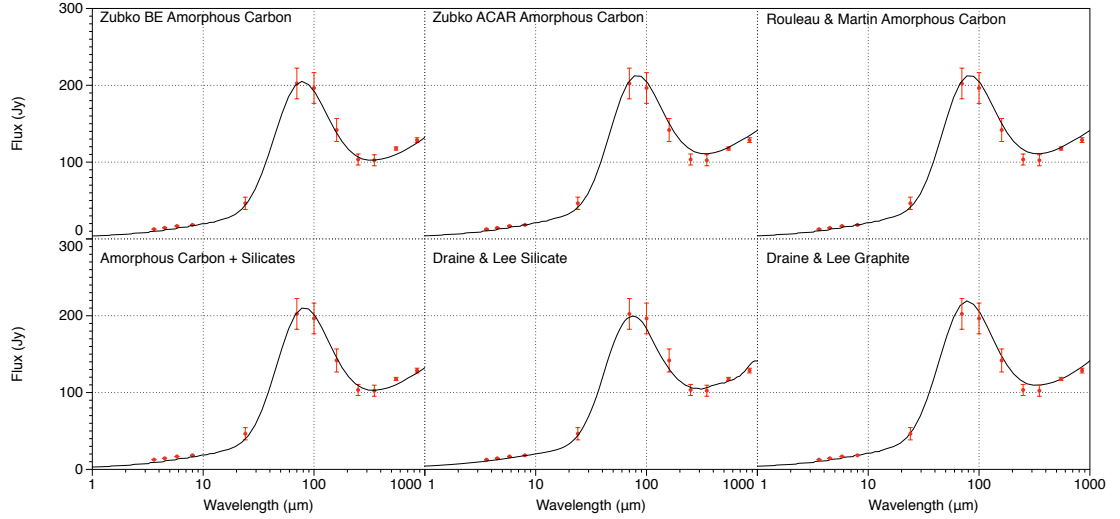


Figure 4.27. Best fit models plotted with the observed SEDs for the six different sets of optical constants using a density distribution starting at radius 0.55 pc in a 0.1 pc thick shell with a diffuse source going up to the inner radius of the dust shell (Model xi).

Optical Constants	a_{min}	a_{max}	α	M_{dust}	χ^2
Zubko et al. ACAR	0.005 μm	0.7 μm	2.7 ± 0.1	$0.25 \pm 0.04 M_\odot$	5.12
Zubko et al. BE	0.005 μm	0.5 μm	2.7 ± 0.1	$0.18 \pm 0.03 M_\odot$	6.97
Rouleau & Martin AC1	0.01 μm	0.8 μm	2.9 ± 0.1	$0.15 \pm 0.03 M_\odot$	5.00
Mixed Model	0.01 μm	1.0 μm	3.0 ± 0.1	$0.25 \pm 0.05 M_\odot$ 0.13 M_\odot Zubko BE 0.12 M_\odot DL silicates	4.98
Draine & Lee Silicate	0.01 μm	0.9 μm	3.5 ± 0.1	$0.98 \pm 0.19 M_\odot$	5.11
Draine & Lee Graphite	0.001 μm	0.25 μm	2.8 ± 0.1	$0.17 \pm 0.03 M_\odot$	6.03

Table 4.23. The results for Model xi. A geometry with clumps starting at radius 0.55 pc in a 0.1 pc thick shell with a diffuse source going up to the inner radius of the dust shell.

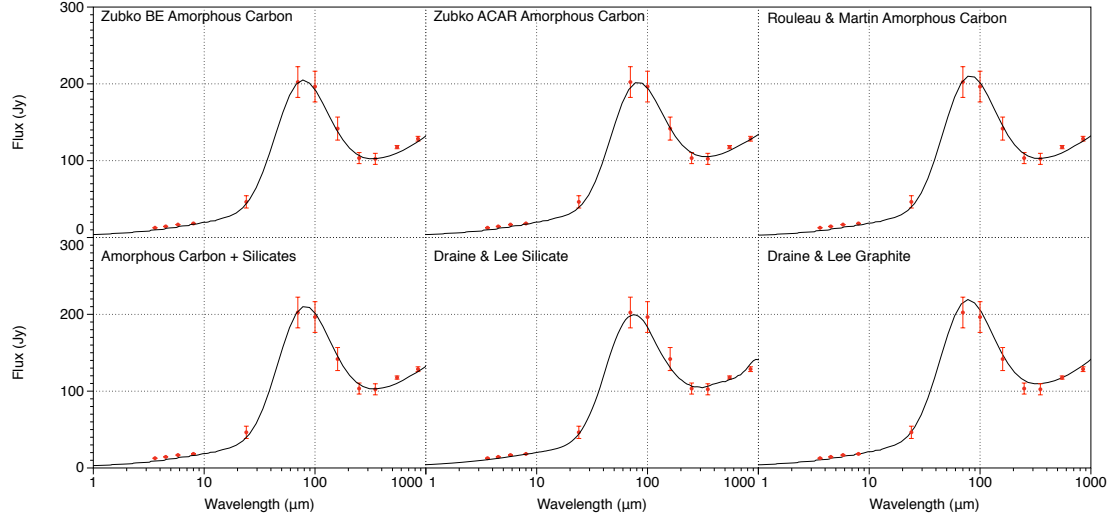


Figure 4.28. Best fit dust models plotted with observed SEDs for the six different sets of optical constants using a density distribution when all of the matter is in clumps of radius 0.037 pc with a H number density of 1900 cm^{-3} with a diffuse radiation source going up to the inner radius of the dust shell (Model XII).

Optical Constants	a_{min}	a_{max}	α	M_{dust}	χ^2
Zubko et al. ACAR	$0.005 \mu\text{m}$	$0.7 \mu\text{m}$	2.7 ± 0.1	$0.25 \pm 0.04 M_\odot$	5.12
Zubko et al. BE	$0.005 \mu\text{m}$	$0.5 \mu\text{m}$	2.7 ± 0.1	$0.18 \pm 0.03 M_\odot$	6.97
Rouleau & Martin AC1	$0.01 \mu\text{m}$	$0.8 \mu\text{m}$	2.9 ± 0.1	$0.15 \pm 0.03 M_\odot$	5.00
Mixed Model	$0.01 \mu\text{m}$	$1.0 \mu\text{m}$	3.0 ± 0.1	$0.25 \pm 0.05 M_\odot$ $0.13 M_\odot$ Zubko BE $0.12 M_\odot$ DL silicates	4.98
Draine & Lee Silicate	$0.01 \mu\text{m}$	$0.9 \mu\text{m}$	3.5 ± 0.1	$0.98 \pm 0.19 M_\odot$	5.11
Draine & Lee Graphite	$0.001 \mu\text{m}$	$0.25 \mu\text{m}$	2.8 ± 0.1	$0.17 \pm 0.03 M_\odot$	6.03

Table 4.24. The results for Model XII. A clumpy geometry with clumps starting at radii of $2.3 \times 1.7 \text{ pc}$ decreasing with r^{-2} with a diffuse radiation source going up to the inner radius of the dust shell.

source.

The best fits to the observed SED for the clumpy model with the inner semi-axes of 1.05×0.7 pc with the H number density decreasing with an r^{-2} dependence and a diffuse radiation field going up to the inner radius of the dust shell are shown in Figure 4.29. Parameters used to achieve these fits are shown in Table 4.25. The clumps have a hydrogen number density of 1900 cm^{-3} , and a radius of 0.037 pc.

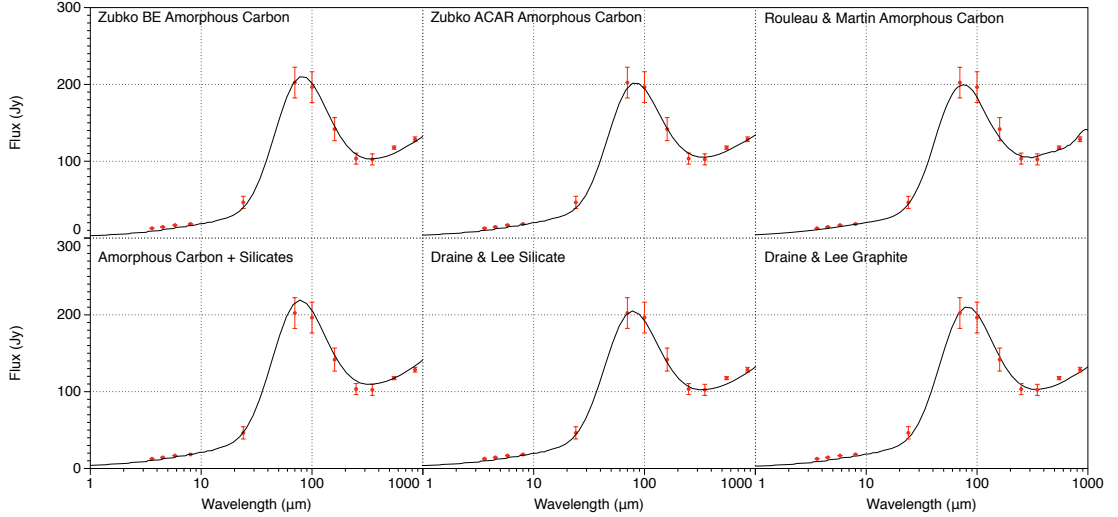


Figure 4.29. Best fit models plotted with observed SEDs for the six different sets of optical constants using a density distribution when all of the matter is in clumps of radius 0.037 pc with a density of 1900 cm^{-3} (Model XIII).

Optical Constants	a_{min}	a_{max}	α	M_{dust}	χ^2
Zubko et al. ACAR	$0.005 \mu\text{m}$	$0.7 \mu\text{m}$	2.7 ± 0.1	$0.25 \pm 0.04 M_\odot$	5.12
Zubko et al. BE	$0.005 \mu\text{m}$	$0.5 \mu\text{m}$	2.7 ± 0.1	$0.18 \pm 0.03 M_\odot$	6.97
Rouleau & Martin AC1	$0.01 \mu\text{m}$	$0.8 \mu\text{m}$	2.9 ± 0.1	$0.15 \pm 0.03 M_\odot$	5.00
Mixed Model	$0.01 \mu\text{m}$	$1.0 \mu\text{m}$	3.0 ± 0.1	$0.25 \pm 0.05 M_\odot$ $0.13 M_\odot$ Zubko BE $0.12 M_\odot$ DL silicates	4.98
Draine & Lee Silicate	$0.01 \mu\text{m}$	$0.9 \mu\text{m}$	3.5 ± 0.1	$0.98 \pm 0.19 M_\odot$	5.11
Draine & Lee Graphite	$0.001 \mu\text{m}$	$0.25 \mu\text{m}$	2.8 ± 0.1	$0.17 \pm 0.03 M_\odot$	6.03

Table 4.25. The results for Model XIII. A clumpy geometry with clumps starting at radii of 2.1×1.4 pc decreasing with r^{-2} with a diffuse radiation source going up to the inner radius of the dust shell.

4.3 Discussion

4.3.1 The importance of using both gas and dust

All models contained both gas and dust. Figure 4.30 shows model XII's synchrotron-subtracted SED and an SED with the same dust mass and density distribution, but no gas. This shows that heating of the dust by line emission plays an important role in the Crab Nebula. Calculating the integrated flux from the two different models, the dust plus gas model gives an IR dust emission flux of $9.58 \times 10^{-3} \text{ W m}^{-2}$, while the dust only model has an IR flux of $8.26 \times 10^{-3} \text{ W m}^{-2}$, which is 16% less than the gas and dust model. This difference in heating is also mirrored in the UV SEDs of the models, shown in Figure 4.31.

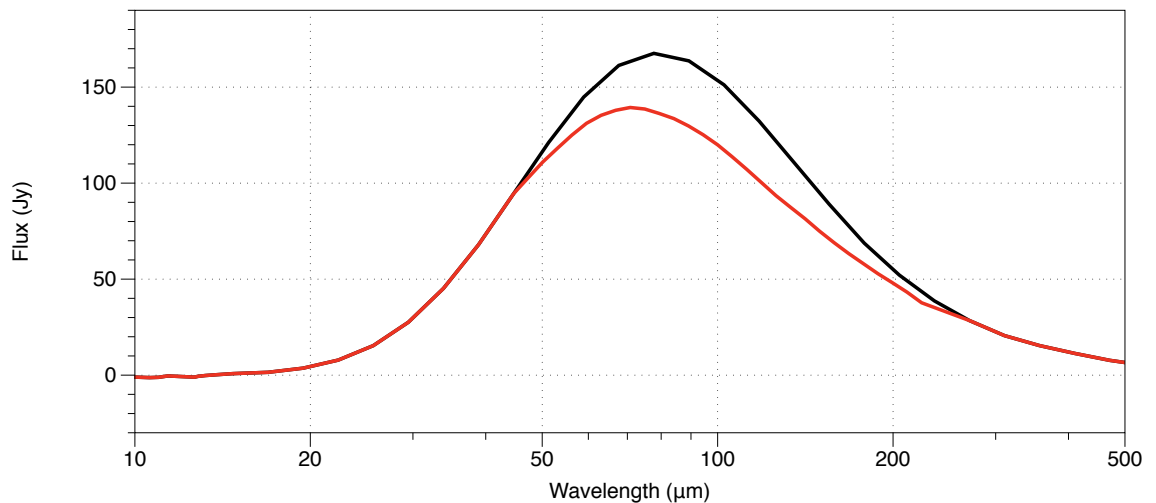


Figure 4.30. Synchrotron-subtracted infrared SEDs of the best fit dust mass for the gas and dust model (black line) and for a model with the same parameters with no gas, just dust (red line) Model XII.

4.3.2 Clumping

The dust masses for the models with smooth density distributions (models I to VI) both agree within the uncertainties with the empirically determined dust mass of Gomez et al. (2012) for the same adopted assumptions about grain properties.

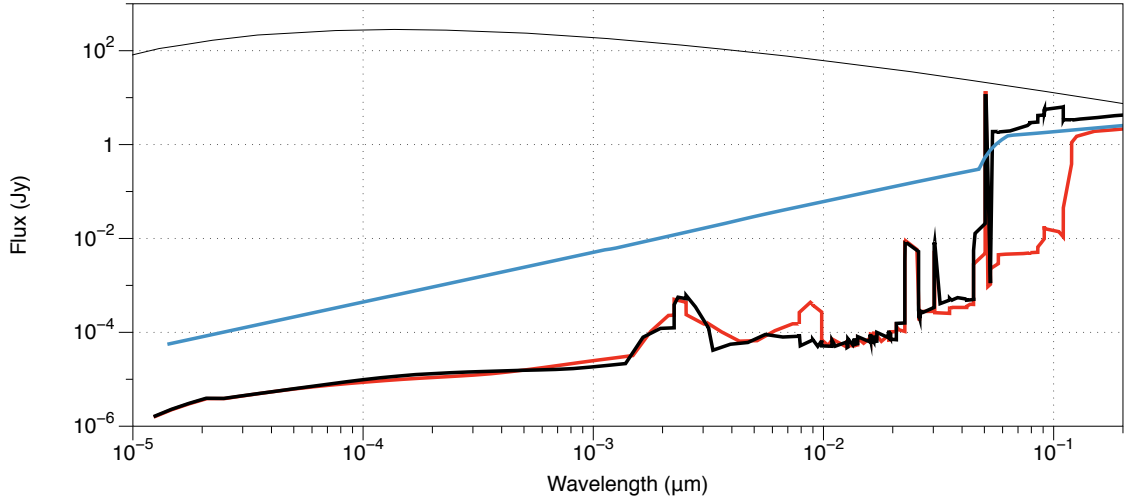


Figure 4.31. The ultraviolet SED for models with gas and dust (black), gas only (red) and dust only (blue) for Model XII

Using *Spitzer* spectra Temim et al. (2012) found the majority of the warm dust in the Crab Nebula to be in the clumpy filamentary structures. This is also supported by the synchrotron subtracted maps of Gomez et al. (2012) that show both the warm and cold dust to be concentrated in the filaments of the nebula. Using clumped density distributions to simulate the filamentary structure of the Crab Nebula increases the mass of dust required to fit the observed SED by a factor of between two and three, depending on the optical constants used. This increase is due to self-shielding in the dense regions of the clumps.

4.3.3 Optical Properties

The choice of optical properties has a large effect on the dust mass estimate. The optical constants of refractive (n) and absorption (k) indices can be used to calculate $Q_{\text{abs}}(\lambda)$, a factor showing how much light is absorbed by a grain at a given wavelength relative to its geometric cross section, using Mie scattering theory (Mie 1908). Figure 4.32 shows $Q_{\text{abs}}(\lambda)$ calculated for each of the amorphous carbon optical constants used, for a dust grain radius of $0.1 \mu\text{m}$.

Inspection of the absorption efficiencies plotted in Figure 4.32 shows significant differences between the supplemented Zubko et al. (1996) BE and ACAR efficiencies and

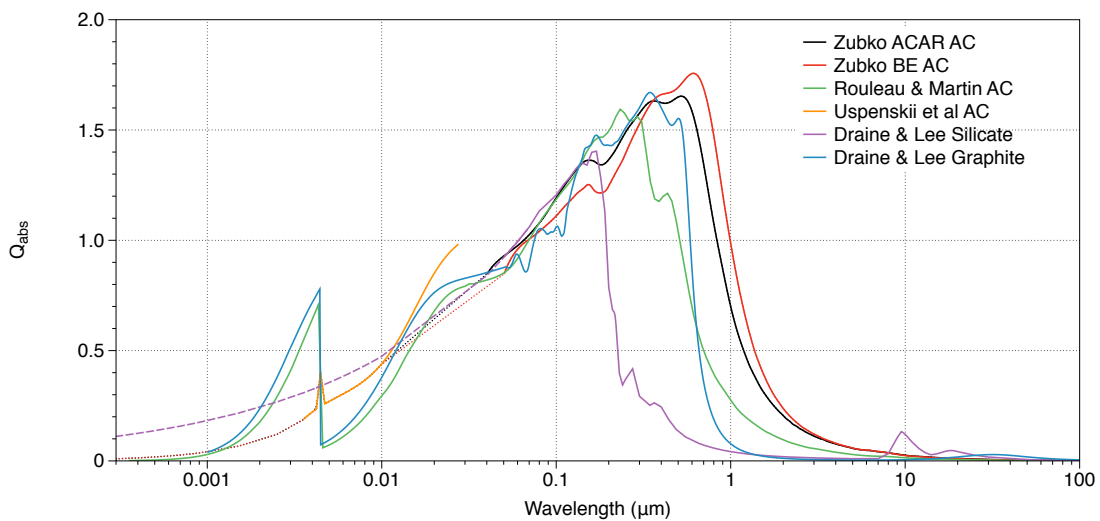


Figure 4.32. $Q_{\text{abs}}(\lambda)$ against Wavelength for amorphous carbon grain optical constants and a grain size of 0.1 μm .

those of Rouleau & Martin (1991), especially at wavelengths below 20 nm and longwards of 310 nm. For wavelengths below 100 nm we prefer the supplemented BE and ACAR data, since we extended these below 30 nm by using experimental optical constants for amorphous carbon measured by Uspenskii et al. (2006). In particular, the Uspenskii et al. (2006) data show a much smaller discontinuity at the carbon atom K-edge at 282 eV (4.4 nm) than the data of Rouleau & Martin (1991). Since K-shell edges correspond to the ejection by photons of inner shell electrons from atoms, the vast majority of the photon energy does not go into grain heating but into raising the K-shell electron out of its potential well. Therefore for grain heating calculations, the inclusion of K-shell absorption peaks will significantly overestimate the amount of grain heating that results.

The silicate K-edge varies depending on the species of silicate, but all are around 6 Å (Li et al. 1995), which is shorter than the shortest wavelengths used in these models.

For wavelengths longwards of 310 nm, the ‘AC1’ amorphous carbon optical constants presented by Rouleau & Martin (1991) made use of laboratory measurements of extinction efficiencies published by Bussoletti et al. (1987). The latter group subsequently obtained new laboratory measurements of mass extinction coefficients for different types of amorphous carbon particles (Colangeli et al. 1995). They noted that their new data agreed with the measurements of Koike et al. (1980) for similar particles but not with their own

(Bussoletti et al. 1987) earlier measurements. The newer data of Colangeli et al. (1995) were used to produce the amorphous carbon optical constants presented by Zubko et al. (1996), and overall we consider these, and their extensions here to shorter wavelengths, to provide the most reliable data available for amorphous carbon.

4.3.4 Grain Size Distribution

With the models run with standard MRN grain size distributions (Mathis, Rumpl, & Nordsieck 1977) ($\alpha = 3.5$, $a_{min} = 0.005 \mu\text{m}$ $a_{max} = 0.25 \mu\text{m}$ for graphite), there is a significant excess around $24 \mu\text{m}$. This implies that there is too much warm dust in the model. To better fit this, a_{min} , the minimum grain radius, was increased to remove smaller, warmer dust grains. The dust mass must be increased slightly to compensate for this.

The peak of the far infrared dust emission is also at a shorter wavelength than observed. This is addressed by increasing a_{max} , the maximum grain radius, making the dust population colder and therefore with its peak at a longer wavelength.

For MRN grain size distributions, the number of grains of a given radius is proportional to a power law

$$n(a) \propto a^{-\alpha} \quad (4.3)$$

with the mass being proportional to the grain volume

$$m(a) \propto a^3 \quad (4.4)$$

and the grain cross section:

$$\sigma(a) \propto a^2 \quad (4.5)$$

If $\alpha = 3.5$ as in the standard MRN size distribution, the total distribution of mass of dust

grains will be

$$\begin{aligned} \Sigma m(a) &\propto \int_{a_{min}}^{a_{max}} a^3 a^{-\alpha} da \\ &\propto \int_{a_{min}}^{a_{max}} a^3 a^{-3.5} da \propto \int_{a_{min}}^{a_{max}} a^{-0.5} da \propto a^{0.5} \end{aligned} \quad (4.6)$$

while the grain surface area:

$$\begin{aligned} \Sigma \sigma(a) &\propto \int_{a_{min}}^{a_{max}} a^2 a^{-\alpha} da \\ &\propto \int_{a_{min}}^{a_{max}} a^2 a^{-3.5} da \propto \int_{a_{min}}^{a_{max}} a^{-1.5} da \propto a^{-0.5} \end{aligned} \quad (4.7)$$

Most of the mass is in the larger grains whilst most of the surface area is in the smaller grains. Smaller grains will be hotter than larger grains, so to fit the data better one may vary the maximum and minimum grain sizes. However with $\alpha = 2.9$, as found for the best fitting Crab Nebula models.

$$\begin{aligned} \Sigma m(a) &\propto \int_{a_{min}}^{a_{max}} a^3 a^{-\alpha} da \\ &\propto \int_{a_{min}}^{a_{max}} a^3 a^{-2.9} da \propto \int_{a_{min}}^{a_{max}} a^{0.1} da \propto a^{1.1} \end{aligned} \quad (4.8)$$

while for surface area

$$\begin{aligned} \Sigma \sigma(a) &\propto \int_{a_{min}}^{a_{max}} a^2 a^{-\alpha} da \\ &\propto \int_{a_{min}}^{a_{max}} a^2 a^{-2.9} da \propto \int_{a_{min}}^{a_{max}} a^{-2.1} da \propto a^{-1.1} \end{aligned} \quad (4.9)$$

meaning there is more mass in the larger colder grains, but with the surface area still being dominated by the smaller grains. This makes sense given the dramatic increase in the derived dust mass when colder dust is observed with *Herschel* as opposed to when just the warmer dust as observed with *Spitzer*.

Figure 4.33 shows the effect of varying α on the fitted SED. The black line is shows the best fit of Model x using the Zubko et al. (1996) BE amorphous carbon dust and a slope of $\alpha = 2.9$. A higher value of α of 3.1 (green line) moves the peak of the distribution to shorter wavelengths whilst a lower α of 2.7 (blue line) moves the peak to a longer wavelength. The lower the value of α the more biased the distribution is towards larger grains,

which are colder and thus emit at longer wavelengths. Larger colder grains also require a greater mass than smaller, warmer grains to get the same amount of flux at a given wavelength. As a result of this, as α decreases the modelled flux at longer wavelengths will decrease for the same mass of dust.

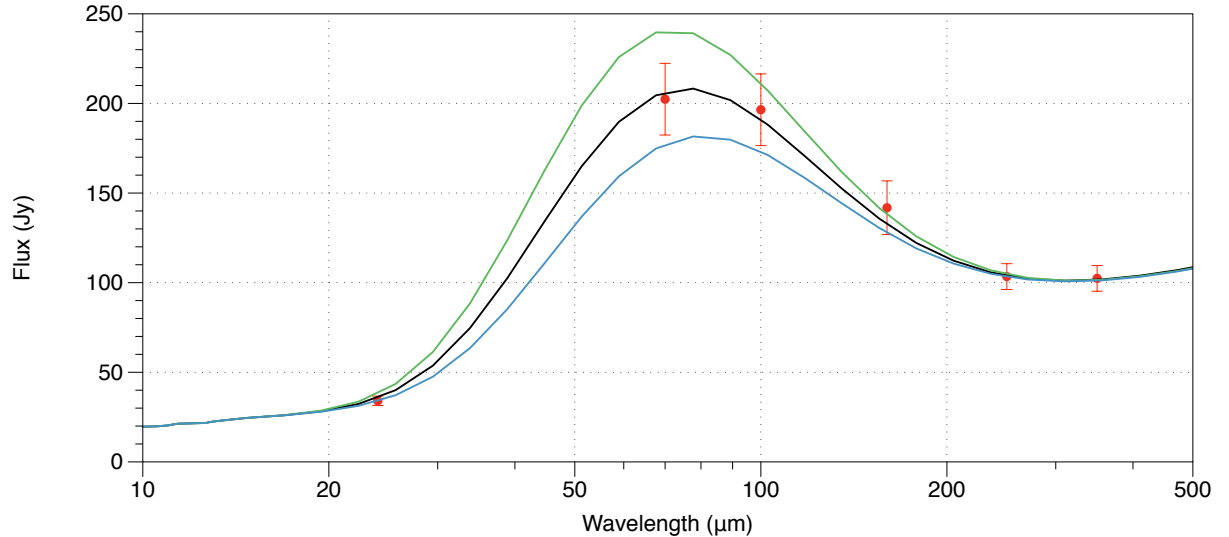


Figure 4.33. the effect on the SED of varying the power law slope α . The black line shows the best fit Model x with Zubko et al. (1996) BE dust properties. The green line is the same parameters but with $\alpha = 3.1$ and the blue line has the same parameters but $\alpha = 2.7$.

Figure 4.34 shows the effect of changing the upper limit of the grain size distribution using Model x with Zubko et al. (1996) BE amorphous carbon grain optical properties. The black line shows the best fit parameters, whilst the green line has a maximum grain radius of $1.5 \mu\text{m}$ and the blue line has a maximum grain radius of $0.5 \mu\text{m}$. Whilst the peak flux is in approximately the same place, the flux in the far infrared varies a lot. Larger dust grains are colder and thus require more mass to emit the same flux which is why there is less flux for the larger maximum grain size. Because there is a large mass of cold, large dust grains in the Crab Nebula, the maximum grain size has a big effect on the determination of the overall mass of dust.

Figure 4.35 is a plot to show the effect of changing the lower limit of the grain size distribution using Model x with the Zubko et al. (1996) BE amorphous carbon optical

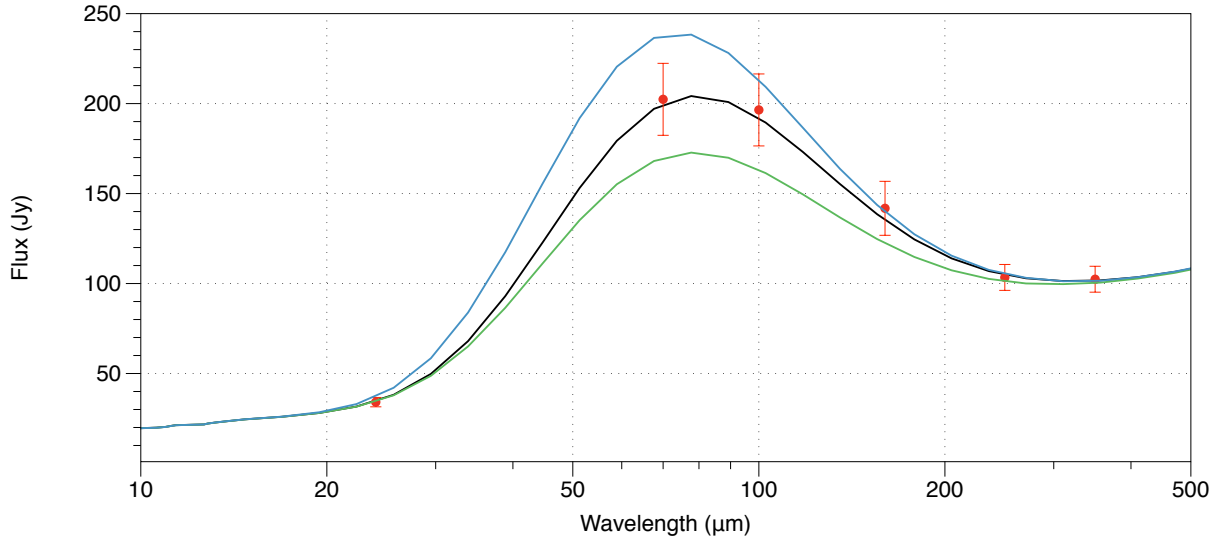


Figure 4.34. the effect of varying the maximum grain size, a_{max} on the fitted SED. The black line gives the best fits for Model x using Zubko et al. (1996) BE amorphous carbon, the green line uses the same parameters but has an a_{max} of $1.5 \mu\text{m}$ and the blue line has a maximum grain radius of $0.5 \mu\text{m}$.

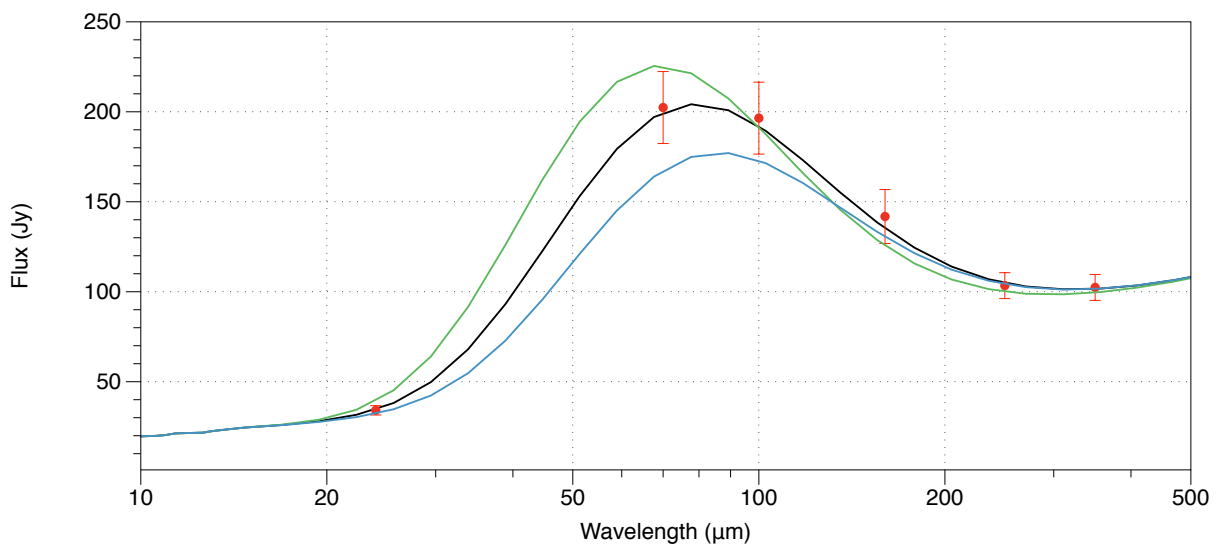


Figure 4.35. the effect of varying the minimum grain size, a_{min} on the fitted SED. The black line gives the best fits for Model x using Zubko et al. (1996) BE amorphous carbon, the green line uses the same parameters but has an a_{min} of $0.0001 \mu\text{m}$ and the blue line has a maximum grain radius of $0.01 \mu\text{m}$.

properties. The black line shows the best fit parameters, the green line shows a model with an a_{min} of $0.0001 \mu\text{m}$ and the blue line shows a model with an a_{min} of $0.01 \mu\text{m}$. As there is very little warm dust in the Crab Nebula, this is a very weak effect which over two orders of magnitude of variation in a_{min} shows only a very little difference in fitting the warm dust component, although it does have an effect on fitting the cooler dust component due to the large skewing effect such a large change in the minimum grain radius has on the power law grain size distribution.

There is a degeneracy between the maximum grain radius and the slope of the power law. It is possible to get similarly good fits to the results presented here using a higher α and a_{max} . However, to do so requires an unphysically large mass of dust to do so. Using Model x and the Zubko et al. (1996) BE amorphous carbon optical properties, $0.71 M_\odot$ of dust is required to fit the observed SED. This mass of dust is unphysical as it would require far more carbon that could plausibly be produced in the supernova and its progenitor. There is also a degeneracy with the power-law slope and the minimum grain radius as well, but the effect of the minimum grain radius is so small that this becomes negligible.

4.3.5 Continuous Distribution of Ellipsoids

The shapes of grains can have an effect on their optical properties. An alternative treatment for the scattering and absorption of light by particles is to use a continuous distribution of ellipsoids (CDE) (Bohren & Huffman 1983). Where Mie scattering theory assumes all grains are spherical, CDE takes a distribution of ellipsoids from needles to disks to spheres to attempt to take into account the likely non spherical nature of dust grains. This can have a significant effect on the mass of dust, requiring 20% less dust with Zubko BE amorphous carbon optical constants to fit the same observed far infrared flux (see Table 4.26 and Figure 4.36 for a set of results using CDE rather than Mie scattering using Model x). Given that this distribution considers everything from needles and discs to spheres, it is arguably less realistic than just assuming that the dust grains are spherical.

Optical Constants	a_{min}	a_{max}	α	M_{dust}	χ^2
Zubko et al. ACAR	0.005 μm	0.7 μm	2.7 ± 0.1	$0.20 \pm 0.04 M_\odot$	7.52
Zubko et al. BE	0.005 μm	0.5 μm	2.7 ± 0.1	$0.15 \pm 0.03 M_\odot$	9.69
Rouleau & Martin AC1	0.01 μm	0.8 μm	2.9 ± 0.1	$0.13 \pm 0.03 M_\odot$	7.50
Mixed Model	0.01 μm	1.0 μm	3.0 ± 0.1	$0.20 \pm 0.05 M_\odot$ $0.13 M_\odot$ Zubko BE $0.12 M_\odot$ DL silicates	4.89
Draine & Lee Silicate	0.01 μm	0.9 μm	3.5 ± 0.1	$0.85 \pm 0.19 M_\odot$	8.77
Draine & Lee Graphite	0.001 μm	0.25 μm	2.8 ± 0.1	$0.14 \pm 0.03 M_\odot$	7.13

Table 4.26. The results for Model x using a CDE scattering routine rather than a Mie scattering routine. A clumpy geometry with clumps starting at diameters of 2.3×1.7 pc with a clump number density decreasing with r^{-2} entirely inside the radiation source.

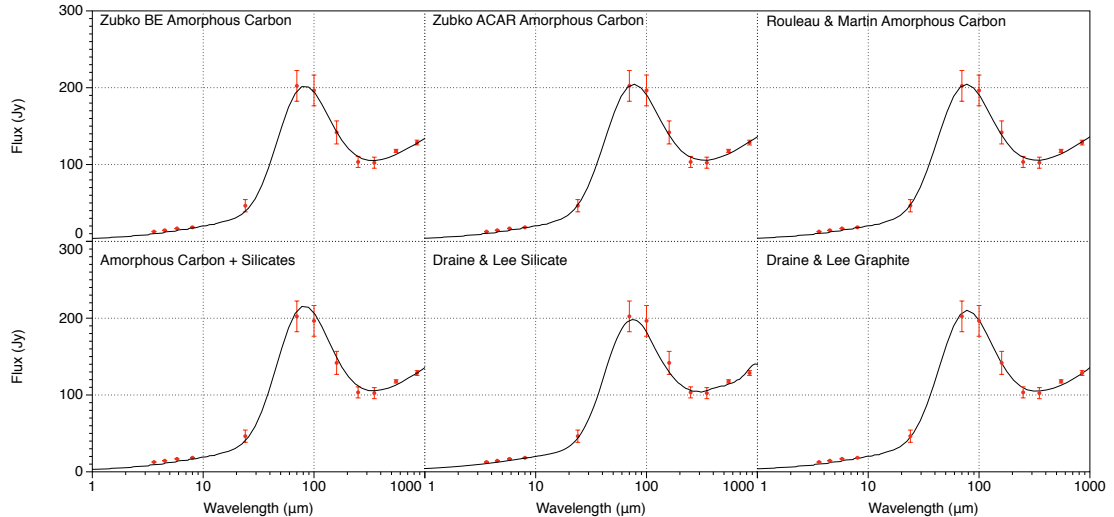


Figure 4.36. Best fit models plotted with the observed SED for the six different sets of optical constants using a density distribution where all of the matter is in clumps of radius 0.037 pc with a density of 1900 cm^{-3} using a continuous distribution of ellipsoids rather than modelling dust as a sphere using Mie scattering. (model x - with CDE)

4.3.6 Optical Depths of the Clumps

The optical depth of dust in a medium is given by

$$\tau(\lambda) = \int \kappa(\lambda) \rho dz \quad (4.10)$$

where κ is the mass absorption coefficient of the dust and ρ is the mass density of dust grains and z is the clump radius. The clump mass of gas and dust and the optical depth of each at τ_v are shown in Table 4.27 for the larger clumps of radius 0.11 pc, and Table 4.28 for the smaller clumps of radius 0.037 pc. The smaller clumps shown in 4.28 are in agreement with observed sizes and optical depths of clumps in the Crab Nebula (Sankrit et al. 1998).

Optical Properties	Gas Mass M_\odot	Dust Mass M_\odot	τ_v
Zubko ACAR	0.054	0.0029	3.11
Zubko BE	0.054	0.0023	4.29
Rouleau & Martin AC1	0.054	0.0018	3.61
Mixed Model	0.054	0.0031	3.57
Draine & Lee Silicate	0.054	0.012	2.84
Draine & Lee Graphite	0.054	0.0029	3.69

Table 4.27. The mass of dust, gas and the v-band optical depth of each clump from centre to surface for the models with the clumps outside the radiation field and a clump radius of 0.11 pc.

Optical Properties	Gas Mass M_\odot	Dust Mass M_\odot	τ_v
Zubko ACAR	0.024	8.6×10^{-4}	0.79
Zubko BE	0.024	6.3×10^{-4}	1.05
Rouleau & Martin AC1	0.024	5.2×10^{-4}	0.92
Mixed Model	0.024	8.6×10^{-4}	0.91
Draine & Lee Silicate	0.024	3.4×10^{-3}	0.72
Draine & Lee Graphite	0.024	5.9×10^{-4}	0.95

Table 4.28. The mass of dust, gas and the optical depth of each clump from centre to surface for the models with the clumps embedded in the radiation field with a clump radius of 0.037 pc.

4.3.7 Predicting Photometric Fluxes

As another way of validating the model, we use the modelled SEDs to predict the observed broadband photometric flux in each of the *Herschel* bands. This is done using the following relation

$$F = \frac{\int_0^\infty F(\lambda)S(\lambda)d\lambda}{\int_0^\infty S(\lambda)d\lambda} \quad (4.11)$$

Where $F(\lambda)$ is the flux and $S(\lambda)$ is the filter profile for the wavelength band. This is then colour corrected to account for the difference between the effective wavelength for that flux and the nominal wavelength of the filter. The predicted fluxes are shown, along with observed fluxes and colour corrections for the smooth and clumpy models using the Zubko et al. (1996) BE sample in Table 4.29.

Wavelength (μm)	Observed Flux (Jy)	Uncertainty	Smooth (Jy)	Correction	Clumpy (Jy)	Correction
24	46.4	8.0	40.6	1.02	41.2	1.011
70	202.37	20	209.3	0.981	193.3	1.010
100	196.48	20	196.3	0.994	200.1	0.982
160	141.8	15	134.6	1.025	148.0	1.020
250	103.4	7.2	102.6	1.006	114.0	0.996
350	102.4	7.2	100.5	1.003	106.3	1.009
500	129	9.0	108.9	1.008	111.0	1.020

Table 4.29. Observed and predicted photometric fluxes for the *Herschel* wave bands and their colour correction factors for Model XII.

The predicted fluxes are in good agreement with those observed, with the exception of the $500\ \mu m$ band. This difference is caused by the model also being fitted to the lower flux and better signal to noise of the *Planck* $550\ \mu m$ band.

4.4 Alternative Dust Mass Estimates

4.4.1 The Temim and Dwek 2013 Estimate

Temim & Dwek (2013) took a different approach to determining a mass of dust in the Crab Nebula. They did this by balancing an equation for the rate of grain heating with an equation for the radiative cooling of each grain. Repeating for a number of different

grain sizes they built up a flux distribution. This technique assumes that all the dust is in the same location, in this particular case at 0.55 pc from a central point heating source. As a result the dust is heated considerably more than if it were distributed throughout the nebula or treated by a full radiative transfer technique with the dust in a thin shell at that distance (as in Model XI). This increased heating leads to increased emission and thus a lower estimate of the dust mass. As previously discussed in section 4.3.2, the dust in the Crab Nebula is contained in filamentary structures so will not be uniformly heated. This difference in heating is illustrated in Figure 4.37 which shows the grain temperature versus radius from Temim & Dwek (2013), and the average grain temperature at 0.55 pc from the centre of the nebula taken from Model XI using the same Rouleau & Martin (1991) amorphous carbon optical constants as a comparison.

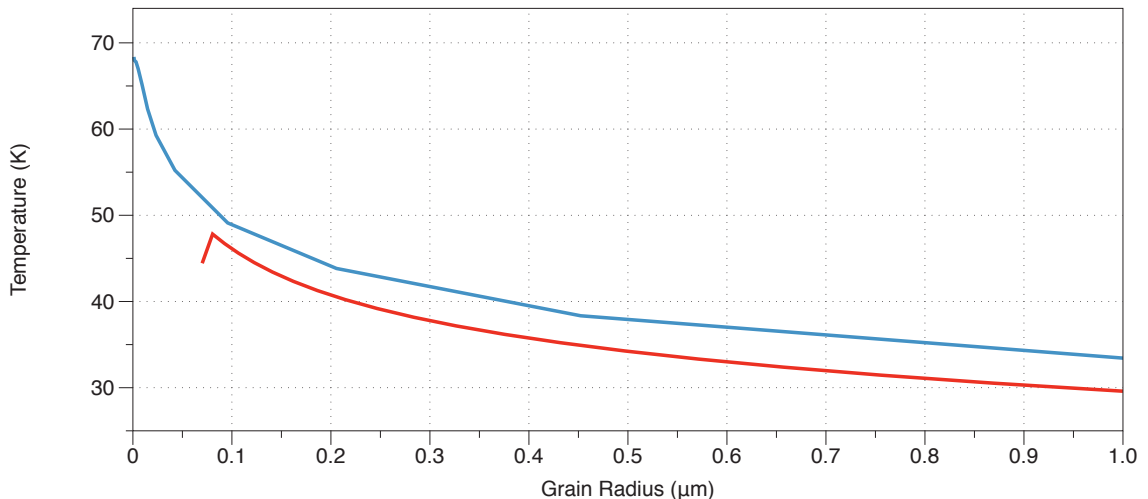


Figure 4.37. The dust temperature with grain size for Model XI using Rouleau & Martin (1991) amorphous carbon optical constants at 0.55 pc (red) and Temim & Dwek (2013) (blue) both of which use the Čadež et al. (2004) geometry as their basis.

4.4.2 Empirical Dust Masses

As the choice of optical constants seems to play a major role in the estimated dust mass, investigating the effect it has on the more often used empirical estimations of dust mass is useful. Calculating κ , the dust mass absorption coefficient for a single grain size of 0.1 μm using a Mie scattering routine and using a single temperature Planck function fit to the SED of the Crab Nebula, we can use equation 4.1 to investigate the effect that the

different sets of optical properties for amorphous carbon species have in this case. The results are shown in Table 4.30.

Optical properties	Dust Mass (M_{\odot})
Zubko AC	0.13
Zubko BE	0.09
Hanner	0.12
Rouleau & Martin	0.08

Table 4.30. Amorphous carbon dust masses in the Crab Nebula calculated empirically using equation 4.1.

As the empirical dust determinations only use the optical constants in the IR region where they are much more similar, the differences in dust mass calculated using this method are far less pronounced than they are when considering realistic heating and cooling of the dust using the entire wavelength range.

4.5 Conclusions

We have constructed a series of radiative transfer models to investigate and accurately determine the mass of dust formed in the ejecta of the supernova that has formed the Crab Nebula. Determining the mass of dust in the Crab Nebula using radiative transfer modelling gives higher dust masses than by fitting a simple two component black body to the spectral energy distribution (Gomez et al. 2012) and gives a mass of $0.1 M_{\odot}$ of amorphous carbon dust. The smooth model dust masses are in good agreement with those determined by empirical fitting to the SED. When clumped dust density distributions are used, the dust mass is determined to be 2-3 times higher depending on the optical properties chosen with $0.18-0.3 M_{\odot}$ of dust. This is summarised in Table 4.31 which shows the results for all the models with the Zubko et al. (1996) BE amorphous carbon grain optical properties and also the Zubko et al. (1996) ACAR results, and Table 4.32 which shows the results for Model XII for all sets of optical properties used.

For the dust formed in the Crab Nebula, the Zubko et al. (1996) BE amorphous carbon optical properties are our favoured choice. The BE sample is formed by burning a benzene sample in air, this gives a chemically rich highly graphitic amorphous carbon sample,

Model	Zubko et al. (1996) BE				Zubko et al. (1996) ACAR			
	a_{min}	a_{max}	α	dust mass	a_{min}	a_{max}	α	dust mass
	μm	μm		M_\odot	μm	μm		M_\odot
Smooth Models								
I	0.005	0.7	2.9 ± 0.1	0.14	0.005	1.0	2.9 ± 0.1	0.30
II	0.07	0.2	2.9 ± 0.1	0.11	0.07	1.0	2.9 ± 0.1	0.27
III	0.005	0.5	2.8 ± 0.1	0.09	0.01	0.7	2.9 ± 0.1	0.12
VI	0.01	0.2	2.9 ± 0.1	0.14	0.01	1.0	2.9 ± 0.1	0.18
V	0.005	0.5	2.8 ± 0.1	0.11	0.01	0.7	2.9 ± 0.1	0.14
VI	0.005	0.5	2.7 ± 0.1	0.08	0.005	0.7	2.7 ± 0.1	0.10
Clumped Models								
VII	0.07	0.2	2.9 ± 0.1	0.3	0.07	1.0	2.9 ± 0.1	0.40
VIII	0.07	0.2	2.9 ± 0.1	0.5	0.07	1.0	2.9 ± 0.1	0.68
IX	0.005	0.5	2.7 ± 0.1	0.18	0.005	0.7	2.7 ± 0.1	0.25
X	0.005	0.5	2.7 ± 0.1	0.18	0.005	0.7	2.7 ± 0.1	0.25
XI	0.005	0.5	2.7 ± 0.1	0.18	0.005	0.7	2.7 ± 0.1	0.25
XII	0.005	0.5	2.7 ± 0.1	0.18	0.005	0.7	2.7 ± 0.1	0.25
XIII	0.005	0.5	2.7 ± 0.1	0.18	0.005	0.7	2.7 ± 0.1	0.25

Table 4.31. The dust mass results for all of the models with the Zubko et al. (1996) BE amorphous carbon optical properties, the numbers in bold are the values for Model XII, the preferred model.

Optical Constants	a_{min}	a_{max}	α	M_{dust}	χ^2
Zubko et al. ACAR	0.005 μm	0.7 μm	2.7 ± 0.1	$0.25 \pm 0.04 M_\odot$	5.12
Zubko et al. BE	0.005 μm	0.5 μm	2.7 ± 0.1	$0.18 \pm 0.03 M_\odot$	6.97
Rouleau & Martin AC1	0.01 μm	0.8 μm	2.9 ± 0.1	$0.15 \pm 0.03 M_\odot$	5.00
Mixed Model	0.01 μm	1.0 μm	3.0 ± 0.1	$0.25 \pm 0.05 M_\odot$	4.98
				0.13 M_\odot Zubko BE	
				0.12 M_\odot DL silicates	
Draine & Lee Silicate	0.01 μm	0.9 μm	3.5 ± 0.1	$0.98 \pm 0.19 M_\odot$	5.11
Draine & Lee Graphite	0.001 μm	0.25 μm	2.8 ± 0.1	$0.17 \pm 0.03 M_\odot$	6.03

Table 4.32. The results for model XII. A clumpy geometry with clumps starting at radii of 2.3×1.7 pc decreasing with r^{-2} with a diffuse radiation source going up to the inner radius of the dust shell.

thought to be the most similar to supernova dust composition. Clumped Model XII with Zubko et al. (1996) BE amorphous carbon grains, the gas and dust masses in each clump were respectively $6.08 \times 10^{-3} M_{\odot}$ and $1.68 \times 10^{-4} M_{\odot}$, for a gas to dust mass ratio of 36, The V-band dust optical depth from the edge to the centre of each clump was $\tau_V = 1.12$. Following the detection by Woltjer & Veron-Cetty (1987) of absorption attributable to dust at the position of a bright [O III] filament in the Crab Nebula, Fesen & Blair (1990) measured angular diameters ranging from 0.9 to 4.8 arcsec for 24 ‘dark spots’ in the Crab Nebula. For comparison, the 0.037-pc radius clumps adopted for our clumped models would have an angular radius of 3.8 arcsec at a distance of 2 kpc which is in reasonable agreement with HST observations presented by Sankrit et al. (1998). The distribution of dust adopted is the gas distribution of Lawrence et al. (1995) which are the most recent reliable observations. For these reasons it is our favoured model.

How the dust is heated has a bigger impact on the mass of dust than its distribution within the nebula. When the dust is placed within the diffuse radiation field, the models with smooth distributions have dust masses that agree within the uncertainties, although systematically increasing with the volume of the nebula filled by gas and dust. When clumps are embedded in the radiation source, the mass of dust required to fit the SEDs is independent of where the dust is located and is entirely down to how it is heated. The size of the clumps also plays a role in the mass of dust required to fit observations, with smaller clumps requiring less dust than larger ones, although the size is constrained by other observations.

The choice of optical constants used for a grain species to determine the mass of dust is important. Different samples of carbon prepared in different ways have very different extinction curves which in turn means very different masses of dust are required to fit a given SED. There is a factor of 2-3 difference in the mass of dust between models that are otherwise identical but have different sets of optical constants for amorphous carbon. Not all of these optical constants are of equal quality and as discussed we prefer the amorphous carbon optical constants compiled by Zubko et al. (1996) supplemented by those of Uspenskii et al. (2006) at short wavelengths.

In reality the dust composition in the Crab Nebula is likely to be a mixture of many

different grain types so the true value for the dust mass will lie somewhere within the limits presented here. This is a large amount of dust leading a dust to gas mass ratio significantly higher than the interstellar medium. This means that dust condensation has been very efficient in the supernova remnant. Core collapse supernovae and their remnants may therefore provide enough dust to provide the observed dust masses in high redshift galaxies and make up the deficit in the dust budgets of local metal poor galaxies.

This page was intentionally left blank

Chapter 5

Conclusions and Future Work

If you can avoid using supernovae in your research, do!

Saul Perlmutter

This thesis presents a collection of work investigating Galactic core collapse supernova remnants in the far infrared. The work is based on observations made using the *Herschel* Space Observatory's PACS and SPIRE instruments, supplemented by other observatories across other wavelengths in order to investigate the physical conditions in supernovae and their effect on dust and molecule formation and destruction.

5.1 The Crab Nebula

The discovery of $^{36}\text{ArH}^+$ is a significant one that has opened up a new area of study in astrochemistry. It has been suggested as a better tracer of interstellar regions of atomic hydrogen than those currently used (Schilke et al. 2014). This discovery in the Crab Nebula will be followed up with ALMA observations. This should resolve the lines giving us much more accurate information about the conditions under which it exists and has formed. These observations should also be sensitive enough to see any $^{38}\text{ArH}^+$ present. ^{36}Ar is formed by the s-process of neutron capture whereas ^{36}Ar is formed by explosive α capture. This ratio of $^{36}\text{Ar}/^{38}\text{Ar}$ will be the first observational constraint on the ratio

between S-process and α capture process in supernovae.

We have constructed a series of radiative transfer models to determine the mass of dust present in the Crab Nebula. In the preferred models the gas and dust are located in clumps within an ellipsoidal diffuse synchrotron radiation source, powered by the pulsar wind nebula. The models are insensitive to the inner axis diameters from which the clump distributions extend.

Models with a smooth distribution of material require $0.10\text{--}0.27 M_{\odot}$ of Zubko et al. (1996) BE or ACAR amorphous carbon, respectively, or $0.35\text{--}0.48 M_{\odot}$ of Draine & Lee (1984) silicates, to fit the infrared and submillimeter SED defined by the *Herschel* and *Spitzer* observations of the nebula. This compares with the $0.12 \pm 0.02 M_{\odot}$ of Zubko BE amorphous carbon, or the $0.24^{+0.32}_{-0.08} M_{\odot}$ of Weingartner & Draine (2001) silicate dust, derived by Gomez et al. (2012) from two-component blackbody fits modified by the mass absorption coefficients for those materials.

Our smooth distribution models required implausibly large nebular gas masses of $16\text{--}49 M_{\odot}$ to fit the integrated optical line fluxes measured by Smith (2003) for the Crab Nebula, much larger than the $8\text{--}10 M_{\odot}$ initial mass usually estimated for the progenitor star, whereas our clumped models for the gas and dust, more consistent with the filamentary appearance of the nebula, required only $7.0 \pm 0.5 M_{\odot}$ of gas to match the integrated nebular emission line fluxes. The clumped model infrared SED fits, which are therefore preferred over those from the smooth models, required either $0.18 M_{\odot}$ (BE) or $0.25 M_{\odot}$ (ACAR) of Zubko amorphous carbon, $0.98 \pm 0.19 M_{\odot}$ of Draine & Lee silicate, or, for mixed chemistry dust, $0.11\text{--}0.21 \pm 0.04 M_{\odot}$ of Zubko BE amorphous carbon plus $0.4\text{--}0.6 \pm 0.03 M_{\odot}$ of silicates. Since our photoionization modelling yielded an overall gas-phase C/O ratio of 1.65 by number for the Crab Nebula, the clumped model dust masses obtained using just amorphous carbon, or amorphous carbon plus silicates, are favoured over silicate-only models. The total nebular mass (gas plus dust) is estimated to be $7.2 \pm 0.5 M_{\odot}$. The Crab Nebula's gas to dust mass ratio of 28–40 (depending on the exact grain type) is about 5–7 times lower than for the general ISM. As discussed in the Introduction, CCSN ejecta dust masses of $0.1 M_{\odot}$ or more, a constraint satisfied by the Crab Nebula, Cas A and SN 1987A, can potentially make a significant contribution to the dust budgets of galaxies.

Our best fit power-law grain size distributions, $n(a) \propto a^{-\alpha}$, had $\alpha \sim 3$, so that the majority of the dust mass resides in the largest particles, with $a_{max} = 0.5\text{-}1.0 \mu\text{m}$. Larger particles better withstand destruction by shock sputtering, for which the rate of reduction of grain radius, da/dt , is independent of the grain radius a , so that the smallest particles disappear first. The preponderance of larger particles in the Crab Nebula's dust, and the fact that they are in clumps, can help their longer-term survival when they eventually encounter the interstellar medium (Nozawa et al. 2007).

There is some debate about the fluxes from the *Planck* compact source catalogue. There are some significant differences between the ones used here, which were taken from the Early Release Catalogue and the now available full release catalogue. To investigate these differences, our preferred model geometry and grain optical constants (model XII with Zubko BE amorphous carbon) were run in a model using the "Gaussian" fluxes from the full catalogue. Figure ?? shows the best fitted SED using these fluxes. The results for the dust fitting parameters is shown in 5.1.

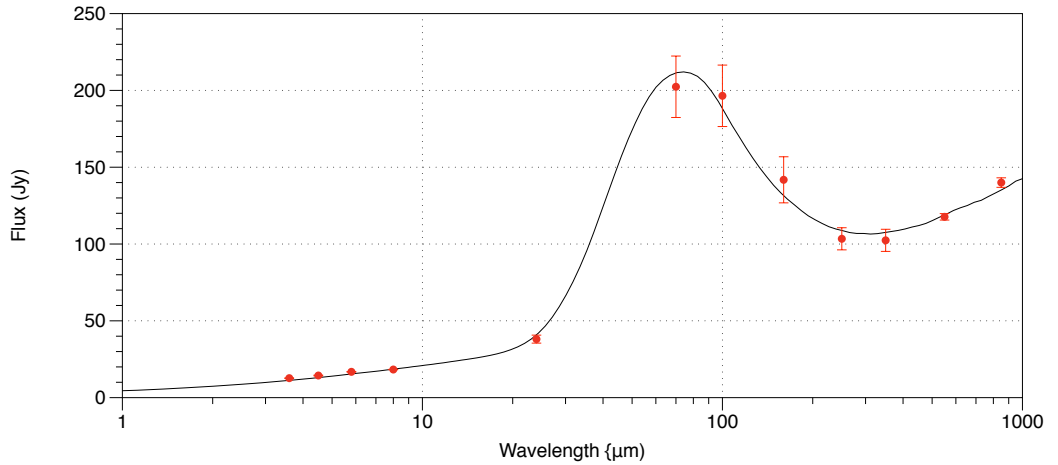


Figure 5.1. The results for Model XII. A clumpy geometry with clumps starting at radii of $2.3 \times 1.7 \text{ pc}$ decreasing with r^{-2} with a diffuse radiation source going up to the inner radius of the dust shell using the *Planck* "Gaussian" fitted Full Release Compact Source Catalogue fluxes.

The dust mass with the new fluxes $0.14 \pm 0.04 M_\odot$ is around 80% that of the dust mass required for the earlier results, although the two results are still within measured uncertainty of one another, so further investigation may be required. There are also slight

Planck Catalogue	a_{min}	a_{max}	α	M_{dust}	χ^2
Early Release "Flux"	0.005 μm	0.5 μm	2.7 ± 0.1	$0.18 \pm 0.03 M_{\odot}$	6.97
Full Release "Gaussian"	0.005 μm	0.7 μm	2.8 ± 0.1	$0.14 \pm 0.04 M_{\odot}$	10.3

Table 5.1. The results for Model XII using the Zubko BE amorphous carbon optical constants to compare the differences between different available *Planck* fluxes.

differences in the grain size parameters, but these are also within the uncertainties of previous results.

A mass of 8-13 M_{\odot} has previously been estimated for the Crab Nebula progenitor star (Hester 2008; Smith 2013). The fact that earlier nebular mass estimates have fallen well short of this mass range had been used as one of the arguments that faster moving material must exist beyond the main nebular boundaries (see e.g. Hester 2008). Arguments against that conclusion have however been presented by Smith (2013). The total nebular mass of $(7.2 \pm 0.5) M_{\odot}$ derived here, combined with a pulsar mass of at least $1.4 M_{\odot}$, implies a total mass of at least $8.6 M_{\odot}$, removing a nebular mass deficit as an argument for the existence of additional material beyond the visible boundaries of the Crab Nebula.

5.2 Cassiopeia A

Cassiopeia A was observed with the Herschel PACS and SPIRE Spectrometers. The fact that the shortward end of the PACS-IFU does not go short enough to accurately measure the $52 \mu\text{m}$ [O III] line means that the electron density cannot be estimated using the [O III] 52/88 μm diagnostic. The [O I] emission is anomalous ; there is no observed $146 \mu\text{m}$ line emission, despite the presence of strong $63 \mu\text{m}$ line emission. Limits to the detection of the $146 \mu\text{m}$ line based on the width of the $63 \mu\text{m}$ line emission have been determined. With electrons as a collision partner for the excitation the temperatures required for the line ratios determined using the observed $63 \mu\text{m}$ line emission and the determined upper limits placed on the $146 \mu\text{m}$ line emission, the temperatures determined are unphysically high being in the region of 2×10^7 K. Using neutral atomic hydrogen as the collision partner for the [O I] temperature the upper limits are within the range of 100-1000 K, which is in consistent with the temperature range determined using CO population analysis. Data for collisions between oxygen atoms is currently not available. Oxygen-oxygen collisions are likely given that regions of Cas A consist of as much as 90% oxygen by mass (Chevalier

& Kirshner 1978).

Broad 158 μm [C II] line emission has been observed in the Cas A remnant for the first time. The emission in the south of the remnant has line widths and velocities comparable to those of the observed [O III] emission in the same regions.

Emission from the 88 μm [O III] line is strongest in the regions when the 70 μm broad band emission is brightest (and thus the dustiest regions), however it originates from all over the observed regions. The broad 63 μm [O I] and 158 μm [C II] emissions are coincident only with the brightest dustiest 70 μm regions.

Carbon monoxide was not observed with the PACS observations presented here. It was however observed with PACS by Wallström et al. (2013) who used a much longer integration time in the region they observed as well as targeting the specific lines rather than making observations across the whole PACS-IFU wavelength range. Fast moving, broad CO was also observed using SPIRE. These data were analysed using rotational excitation diagrams to diagnose excitation temperature and column densities for CO. Analysis both with and without the data from Wallström et al. (2013) determined the temperature to be in the range 200-500 K, and a column density of 9×10^{16} - 4.3×10^{17} cm^{-2} . Cassiopeia A is predominantly shock ionised rather than photoionised (Docenko & Sunyaev 2010). This makes modelling far more difficult as both types of excitation have to be taken into account. In addition to this, Cas A is oxygen rich to the point where there may not be hydrogen, meaning that some of the regularly used methods cannot be applied. New modelling schemes will be required to create realistic models of Cas A to determine its composition and dust mass.

5.3 Other future work

My modelling of dust in the Crab Nebula along with other work (e.g. Gall et al. (2014); Wesson et al. (2015)) have shown that much better fits to supernova dust emission data can be made using non standard grain size distributions. Chemical kinetic dust formation models also predict non standard size distributions (Sarangi & Cherchneff 2013). This can be investigated via observations. The red-blue asymmetry displayed in optical emission

lines in supernovae can be used to build up information showing how the extinction by dust across the remnant varies with wavelength. This can then be used to determine a grain size distribution which will help to extend models such as the ones contained in this thesis.

When studying dust evolution in galaxies, most work starts with a standard size distribution for all dust regardless of how and where it is formed. This size distribution is usually assumed to be that of evolved galaxy dust, such as the standard MRN size distribution. Such models can be improved by using supernova determined size distributions as inputs to better understand the evolution of dust in galaxies.

Ultimately a picture is starting to emerge in which supernovae produce large amounts of dust in their remnants. Whether this dust ultimately survives to enrich the interstellar medium is a question that remains to be answered.

Appendix A

Appendix A

RA	Dec	Velocity	FWHM	Flux
83.62852218	22.01323803	-923	659	2.50E-16 ± 1.00E-17
83.62866621	22.01101197	-861	532	3.30E-16 ± 7.00E-18
83.62871147	22.00850666	-767	569	5.01E-16 ± 3.00E-17
83.62870622	22.00601326	-792	487	8.30E-16 ± 3.00E-17
83.62879153	22.00382905	-792	460	7.30E-16 ± 2.00E-17
83.62568949	22.01235416	-895	562	5.40E-16 ± 2.00E-17
83.62576296	22.0097284	-760	651	6.10E-16 ± 2.00E-17
83.62574985	22.00734111	-688	489	1.12E-15 ± 3.00E-17
83.6257573	22.0048935	-755	504	5.40E-16 ± 1.00E-17
83.62576837	22.00280341	-796	496	3.40E-16 ± 1.00E-17
83.62282148	22.01320358	-773	762	6.10E-16 ± 2.00E-17
83.62288508	22.01090502	-664	594	1.70E-15 ± 4.00E-17
83.62285993	22.00852548	-598	535	3.20E-15 ± 6.00E-17
83.62285583	22.00610845	-730	503	7.70E-16 ± 2.00E-17
83.62278817	22.00379783	-850	576	5.00E-16 ± 1.00E-17
83.61992343	22.01348996	-684	512	8.20E-16 ± 2.00E-17
83.61998262	22.01128774	-572	530	2.27E-15 ± 3.00E-17
83.6199592	22.00885683	-626	647	1.75E-15 ± 6.00E-17
83.61989292	22.00648624	-813	744	6.50E-16 ± 3.00E-17
83.619833	22.00421238	-876	608	2.30E-16 ± 2.00E-17
83.61733989	22.01346304	-678	666	1.23E-15 ± 6.00E-17
83.61725791	22.01114049	-561	694	2.52E-15 ± 1.00E-16
83.61713863	22.00881434	-757	802	1.20E-15 ± 7.00E-17
83.61709364	22.00654089	-841	666	4.70E-16 ± 2.00E-17
83.61690854	22.00405717	-893	614	3.40E-16 ± 1.00E-17

Table A.1. The red shifted component of the [O I] 63 μm emission in the Crab Nebula measured by PACS-IFU

RA	Dec	Velocity	FWHM	Flux
83.62852218	22.01323803	-955	456	6.90E-16 ± 9.00E-17
83.62866621	22.01101197	-881	532	1.60E-16 ± 1.00E-17
83.62871147	22.00850666	-562	735	4.50E-16 ± 1.00E-17
83.62870622	22.00601326	-790	1300	4.70E-16 ± 2.00E-17
83.62568949	22.01235416	-769	657	1.70E-16 ± 1.00E-17
83.62576296	22.0097284	-684	999	4.60E-16 ± 2.00E-17
83.62574985	22.00734111	-662	684	3.50E-16 ± 2.00E-17
83.6257573	22.0048935	-755	504	2.50E-16 ± 2.00E-17
83.62576837	22.00280341	-851	609	7.67E-16 ± 3.00E-17
83.62282148	22.01320358	-756	614	4.60E-16 ± 3.00E-17
83.62288508	22.01090502	-496	1024	6.55E-15 ± 1.00E-17
83.62285993	22.00852548	-522	638	4.10E-16 ± 4.00E-17
83.62285583	22.00610845	-463	641	2.52E-16 ± 2.00E-17
83.62278817	22.00379783	-578	588	2.80E-16 ± 2.00E-17
83.61992343	22.01348996	-722	704	4.10E-17 ± 2.00E-17
83.61998262	22.01128774	-572	530	4.30E-16 ± 2.00E-17
83.61989292	22.00648624	-813	744	1.00E-16 ± 3.00E-01
83.61733989	22.01346304	-599	874	4.70E-16 ± 3.00E-17
83.61725791	22.01114049	-445	920	4.00E-16 ± 2.00E-17
83.61713863	22.00881434	-599	778	5.00E-16 ± 3.00E-17

Table A.2. The blue shifted component of the [O I] 63 μm emission in the Crab Nebula measured by PACS-IFU

RA	Dec	Velocity	FWHM	Flux
83.62852218	22.01323803	1057	457	4.30E-16 ± 1.00E-17
83.62866621	22.01101197	1095	500	5.40E-16 ± 2.00E-17
83.62871147	22.00850666	1103	661	7.14E-16 ± 3.00E-17
83.62870622	22.00601326	1094	654	5.80E-16 ± 2.60E-17
83.62879153	22.00382905	1058	566	3.50E-16 ± 3.00E-17
83.62568949	22.01235416	1091	494	4.50E-16 ± 2.00E-17
83.62576296	22.0097284	1059	665	6.80E-16 ± 3.00E-17
83.62574985	22.00734111	1076	678	7.70E-16 ± 3.00E-17
83.6257573	22.0048935	1013	661	5.40E-16 ± 1.00E-17
83.62576837	22.00280341	911	512	6.40E-16 ± 1.00E-17
83.62282148	22.01320358	967	557	9.10E-16 ± 2.00E-17
83.62288508	22.01090502	965	735	7.80E-16 ± 2.00E-17
83.62285993	22.00852548	1020	1147	8.30E-16 ± 6.00E-17
83.62285583	22.00610845	1099	680	3.90E-16 ± 1.00E-17
83.62278817	22.00379783	950	518	4.30E-16 ± 1.00E-17
83.61992343	22.01348996	732	446	6.60E-16 ± 5.00E-17
83.61998262	22.01128774	780	486	4.60E-16 ± 2.00E-17
83.6199592	22.00885683	740	619	7.60E-16 ± 5.00E-17
83.61989292	22.00648624	916	746	4.60E-16 ± 2.00E-17
83.619833	22.00421238	1035	669	3.60E-16 ± 1.00E-17
83.61733989	22.01346304	674	470	3.70E-16 ± 2.00E-17
83.61725791	22.01114049	693	416	6.00E-16 ± 4.00E-17
83.61713863	22.00881434	717	475	7.00E-16 ± 2.00E-17
83.61709364	22.00654089	1069	912	5.60E-16 ± 5.00E-17
83.61690854	22.00405717	1082	501	9.30E-17 ± 1.00E-17

Table A.3. The red shifted component of the [O III] 88 μm emission in the Crab Nebula measured by PACS-IFU

RA	Dec	Velocity	FWHM	Flux
83.62852218	22.01323803	-923	659	2.50E-16 ± 1.00E-17
83.62866621	22.01101197	-861	532	3.30E-16 ± 7.00E-18
83.62871147	22.00850666	-767	569	5.01E-16 ± 3.00E-17
83.62870622	22.00601326	-792	487	8.30E-16 ± 3.00E-17
83.62879153	22.00382905	-792	460	7.30E-16 ± 2.00E-17
83.62568949	22.01235416	-895	562	5.40E-16 ± 2.00E-17
83.62576296	22.0097284	-760	651	6.10E-16 ± 2.00E-17
83.62574985	22.00734111	-688	489	1.12E-15 ± 3.00E-17
83.6257573	22.0048935	-755	504	5.40E-16 ± 1.00E-17
83.62576837	22.00280341	-796	496	3.40E-16 ± 1.00E-17
83.62282148	22.01320358	-773	762	6.10E-16 ± 2.00E-17
83.62288508	22.01090502	-664	594	1.70E-15 ± 4.00E-17
83.62285993	22.00852548	-598	535	3.20E-15 ± 6.00E-17
83.62285583	22.00610845	-730	503	7.70E-16 ± 2.00E-17
83.62278817	22.00379783	-850	576	5.00E-16 ± 1.00E-17
83.61992343	22.01348996	-684	512	8.20E-16 ± 2.00E-17
83.61998262	22.01128774	-572	530	2.27E-15 ± 3.00E-17
83.6199592	22.00885683	-626	647	1.75E-15 ± 6.00E-17
83.61989292	22.00648624	-813	744	6.50E-16 ± 3.00E-17
83.619833	22.00421238	-876	608	2.30E-16 ± 2.00E-17
83.61733989	22.01346304	-678	666	1.23E-15 ± 6.00E-17
83.61725791	22.01114049	-561	694	2.52E-15 ± 1.00E-16
83.61713863	22.00881434	-757	802	1.20E-15 ± 7.00E-17
83.61709364	22.00654089	-841	666	4.70E-16 ± 2.00E-17
83.61690854	22.00405717	-893	614	3.40E-16 ± 1.00E-17

Table A.4. The blue shifted component of the [O III] 88 μm emission in the Crab Nebula measured by PACS-IFU

RA	Dec	Velocity	FWHM	Flux
83.62574985	22.00734111	997	810	4.70E-17 ± 6.00E-18
83.62288508	22.01090502	1004	11187	8.90E-17 ± 4.00E-18
83.62285993	22.00852548	964	1112	5.80E-17 ± 3.00E-18
83.61998262	22.01128774	864	1130	8.50E-17 ± 4.00E-17
83.6199592	22.00885683	764	996	8.50E-17 ± 6.00E-18
83.61733989	22.01346304	702	1326	8.20E-17 ± 4.00E-18
83.61725791	22.01114049	764	1284	1.00E-16 ± 6.00E-18
83.61713863	22.00881434	769	927	8.90E-17 ± 5.00E-18

Table A.5. The red shifted component of the [C II] 158 μm emission in the Crab Nebula measured by PACS-IFU

RA	Dec	Velocity	FWHM	Flux
83.62574985	22.00734111	-663	911	6.63E-17 ± 3.00E-18
83.62288508	22.01090502	-602	911	1.39E-16 ± 3.00E-18
83.62285993	22.00852548	-548	823	2.22E-16 ± 8.00E-18
83.61998262	22.01128774	-566	881	1.97E-16 ± 5.00E-18
83.6199592	22.00885683	-575	950	1.78E-16 ± 4.00E-18
83.61733989	22.01346304	-614	869	9.20E-17 ± 5.00E-18
83.61725791	22.01114049	-528	861	1.70E-16 ± 4.00E-18
83.61713863	22.00881434	-683	1016	9.50E-17 ± 6.00E-18

Table A.6. The red shifted component of the [C II] 158 μm emission in the Crab Nebula measured by PACS-IFU

Appendix B

Appendix B

B.1 SP1

RA	Dec	Velocity	FWHM	Flux
350.8763587573	58.8210604144	-3988	1388	6.30E-16 ± 5.00E-17
350.8785458073	58.8191391838	-3624	1280	2.80E-16 ± 5.00E-17
350.8850600699	58.8127963966	-3188	2201	3.7E-16 ± 2.00E-17
350.8726196781	58.8190778149	-2646	1543	4.20E-16 ± 2.00E-17
350.8811420635	58.8106073526	-4370	969	4.60E-16 ± 1.00E-17
350.8714753377	58.8144745884	-2036	703	3.70E-16 ± 6.00E-17
350.8624284116	58.8176549156	-1187	1813	2.40E-16 ± 1.00E-17

Table B.1. The blue shifted component of the [O I] 63 μm emission in the SP1 observations of Cas A measured by PACS-IFU

RA	Dec	Velocity	FWHM	Flux
350.8830041766	58.8147052523	2848	2024	2.50E-16 ± 4.00E-017
350.8811420635	58.8106073526	1657	1375	2.10E-16 ± 1.00E-17
350.8714753377	58.8144745884	1074	1413	2.40E-16 ± 2.00E-17
350.8624284116	58.8176549156	1812	1244	1.90E-16 ± 2.00E-17

Table B.2. The red shifted component of the [O I] 63 μm emission in the SP1 observations of Cas A measured by PACS-IFU

RA	Dec	Velocity	FWHM	Flux
350.8763587573	58.8210604144	-2971	646	3.20E-016 ± 1.00E-017
350.8785458073	58.8191391838	-2728	1290	1.50E-016 ± 1.00E-017
350.8830041766	58.8147052523	-2355	644	3.50E-016 ± 1.00E-017
350.8726196781	58.8190778149	-2629	670	3.30E-016 ± 1.00E-017
350.8750456714	58.8167709739	-2318	1109	5.30E-016 ± 2.00E-017
350.8771236703	58.8146398673	-2529	1351	9.00E-016 ± 1.00E-016
350.8792872363	58.812463694	-2554	839	5.50E-016 ± 3.00E-017
350.8811420635	58.8106073526	-1977	703	9.00E-017 ± 8.00E-017
350.8673003148	58.8186234215	-1782	1384	2.20E-016 ± 1.00E-017
350.8694230882	58.8166038052	-1187	1579	6.10E-006 ± 4.00E-017
350.8714753377	58.8144745884	-1282	1619	1.04E-015 ± 6.00E-017
350.8735938572	58.8123208429	-1479	2089	7.60E-016 ± 6.00E-017
350.8755172641	58.8102349872	-1879	889	8.70E-016 ± 5.00E-017
350.8624284116	58.8176549156	-1808	870	2.20E-016 ± 1.00E-017
350.8644595806	58.8157192724	-1404	1138	2.90E-016 ± 3.00E-017
350.8665599515	58.8135451114	-1507	949	6.20E-016 ± 2.00E-017
350.8685386921	58.8114065225	-1248	1126	4.50E-016 ± 1.00E-017
350.8704423008	58.8093567199	-1895	748	5.70E-017 ± 1.00E-017
350.8583337102	58.8165401478	-1652	859	2.50E-016 ± 3.00E-017
350.8602457757	58.8144378199	-1771	797	3.90E-016 ± 2.00E-017
350.8621013114	58.8123165127	-1839	785	3.70E-016 ± 2.00E-017
350.8640287235	58.8102734529	-1583	955	3.60E-016 ± 1.00E-017
350.865917443	58.8079840044	-2512	1177	3.90E-016 ± 3.00E-017

Table B.3. The blue shifted component of the [O III] 88 μm emission in the SP1 observations of Cas A measured by PACS-IFU

B.2 SP3

RA	Dec	Velocity	FWHM	Flux
350.8785458073	58.8191391838	2620	1254	2.40E-016 ± 1.00E-017
350.8808206346	58.8169275996	2900	1271	7.00E-016 ± 3.00E-017
350.8830041766	58.8147052523	3335	1306	1.00E-015 ± 1.00E-016
350.8850600699	58.8127963966	2738	897	4.80E-016 ± 2.00E-017
350.8726196781	58.8190778149	2645	1224	3.00E-016 ± 1.00E-017
350.8750456714	58.8167709739	3127	948	3.60E-016 ± 1.20E-017
350.8771236703	58.8146398673	3485	1221	4.20E-016 ± 3.00E-017
350.8792872363	58.812463694	3611	968	5.20E-016 ± 2.00E-017
350.8811420635	58.8106073526	2948	914	5.40E-016 ± 3.00E-017
350.8673003148	58.8186234215	2947	1449	3.70E-016 ± 1.00E-017
350.8694230882	58.8166038052	3435	1625	5.20E-016 ± 8.00E-017
350.8714753377	58.8144745884	3719	1500	4.10E-016 ± 2.00E-017
350.8624284116	58.8176549156	3596	1068	2.00E-016 ± 2.00E-017
350.8644595806	58.8157192724	4020	3207	1.50E-016 ± 3.00E-017
350.8665599515	58.8135451114	4107	1103	2.80E-016 ± 1.00E-017
350.8685386921	58.8114065225	4499	666	1.90E-016 ± 2.00E-017
350.8583337102	58.8165401478	4008	786	2.40E-016 ± 2.00E-017
350.8602457757	58.8144378199	4382	993	1.00E-016 ± 1.00E-017

Table B.4. The red shifted component of the [O III] 88 μm emission in the SP1 observations of Cas A measured by PACS-IFU

RA	Dec	Velocity	FWHM	Flux
350.814987606	58.8162021106	995	950	6.50E-016 ± 3.00E-017
350.8168549018	58.8143490926	1169	452	4.00E-016 ± 1.00E-017
350.8071616039	58.8181990968	942	1095	6.10E-016 ± 4.00E-017
350.8092946018	58.8160491418	1159	500	7.40E-016 ± 5.00E-017
350.8112320019	58.8139667308	1129	374	1.79E-016 ± 5.00E-018
350.8001368762	58.8194313019	1495	1912	1.50E-015 ± 7.00E-017
350.8022518745	58.8172608934	1369	810	1.12E-015 ± 4.00E-017
350.7940049212	58.8202412936	842	626	4.34E-016 ± 2.00E-017

Table B.5. The red shifted component of the [O III] 88 μm emission in the SP3 observations of Cas A measured by PACS-IFU

RA	Dec	Velocity	FWHM	Flux
350.8120065904	58.8248046807	-985	500	1.60E-016 ± 3.00E-017
350.8142021845	58.8228883179	-904	592	3.90E-016 ± 3.00E-017
350.8164955674	58.8206775782	-684	460	4.90E-016 ± 4.00E-017
350.818694051	58.8184591207	-641	453	2.51E-016 ± 5.00E-018
350.8207741793	58.8165502378	-594	702	2.30E-016 ± 1.00E-017
350.8082755355	58.8228043033	-948	511	5.10E-016 ± 4.00E-017
350.8107170766	58.8205017979	-709	564	2.80E-016 ± 1.00E-017
350.8128094107	58.8183744099	-621	557	4.30E-016 ± 3.00E-017
350.814987606	58.8162021106	-600	566	4.00E-016 ± 3.00E-017
350.8168549018	58.8143490926	-428	1045	3.60E-016 ± 2.00E-017

Table B.6. The blue shifted component of the [O III] 88 μm emission in the SP3 observations of Cas A measured by PACS-IFU

RA	Dec	Velocity	FWHM	Flux
350.8128094107	58.8183744099	914	935	1.63E-016 ± 6.46E-001
350.8022518745	58.8172608934	1878	1421	1.00E-016 ± 2.50E-018
350.7940049212	58.8202412936	1186	716	1.53E-016 ± 1.00E-017
350.8016460967	58.8116986855	901	808	1.85E-016 ± 1.25E-017

Table B.7. The red shifted component of the [C II] 157 μm emission in the SP3 observations of Cas A measured by PACS-IFU

RA	Dec	Velocity	FWHM	Flux
350.8128094107	58.8183744099	-609	1016	1.30E-016 ± 6.00E-018
350.8001368762	58.8194313019	-922	956	1.63E-016 ± 4.08E-018
350.8022518745	58.8172608934	-1167	873	8.37E-017 ± 5.49E-018

Table B.8. The blue shifted component of the [C II] 157 μm emission in the SP3 observations of Cas A measured by PACS-IFU

B.3 SP4

RA	Dec	Velocity	FWHM	Flux
350.8939201758	58.8013959773	1587	1016	3.80E-016 ± 2.00E-017
350.8983678486	58.7972597937	1252	1642	2.60E-016 ± 3.00E-017
350.9025932041	58.7931253998	1836	1203	2.90E-016 ± 1.00E-017
350.8901776232	58.7994162188	1382	1064	1.10E-016 ± 1.00E-017
350.894666527	58.7949748759	1139	1266	3.30E-016 ± 2.00E-017
350.8968227127	58.7927970741	1775	1251	5.60E-016 ± 4.00E-017
350.8986712345	58.7909393377	2083	779	1.01E-015 ± 2.00E-017
350.8848599927	58.7989658594	887	1280	3.90E-016 ± 2.00E-017
350.8911321659	58.7926585358	1380	1514	4.30E-016 ± 1.00E-017
350.8930485793	58.7905712324	1754	1285	1.05E-015 ± 2.00E-017
350.8799881142	58.7980010509	1836	1288	4.20E-016 ± 1.00E-017
350.8820126715	58.7960638733	226	1359	1.00E-015 ± 1.00E-016
350.8841057123	58.7938881269	1290	1455	3.30E-016 ± 2.00E-017
350.8860772854	58.7917480454	1780	1399	4.40E-016 ± 3.00E-017
350.8879740138	58.7896968079	624	1132	4.50E-016 ± 2.00E-017
350.8758925836	58.7968893928	517	1351	4.10E-016 ± 2.00E-017
350.8777976336	58.7947856183	941	1094	6.60E-016 ± 3.00E-017
350.8796461261	58.7926629079	1393	1765	4.10E-016 ± 2.00E-017
350.8815666694	58.7906183913	1740	1572	3.80E-016 ± 3.00E-017

Table B.9. The red shifted component of the [O III] 88 μm emission in the SP4 observations of Cas A measured by PACS-IFU

B.4 SP5

RA	Dec	Velocity	FWHM	Flux
350.8939201758	58.8013959773	-1586	2176	3.50E-016 ± 3.00E-017
350.8901776232	58.7994162188	-360	1005	1.50E-016 ± 1.00E-017
350.8925957275	58.7971075478	-712	1488	2.10E-016 ± 6.00E-018
350.894666527	58.7949748759	-959	1645	5.30E-016 ± 2.00E-017
350.8869758637	58.7969446412	-530	1271	8.10E-016 ± 2.00E-017
350.8890209363	58.7948138774	-717	1679	1.77E-015 ± 5.00E-017
350.8911321659	58.7926585358	-859	1393	7.50E-016 ± 2.00E-017
350.8841057123	58.7938881269	-1405	1368	5.30E-016 ± 2.00E-017
350.8860772854	58.7917480454	-1670	1657	2.70E-016 ± 1.00E-017
350.8879740138	58.7896968079	-1115	1315	9.80E-016 ± 5.00E-017
350.8815666694	58.7906183913	-1210	1149	2.50E-016 ± 1.00E-017
350.8834478383	58.7883275168	-1109	1318	4.90E-016 ± 1.00E-017

Table B.10. The blue shifted component of the [O III] 88 μm emission in the SP4 observations of Cas A measured by PACS-IFU

RA	Dec	Velocity	FWHM	Flux
350.8968227127	58.7927970741	1602	1751	1.20E-15 ± 3.00E-17
350.8986712345	58.7909393377	1574	800	4.1E-16 ± 3.00E-16

Table B.11. The blue shifted component of the [O I] 63 μm emission in the SP4 observations of Cas A measured by PACS-IFU

RA	Dec	Velocity	FWHM	Flux
350.894666527	58.7949748759	-1026	1202	6.10E-16 ± 3.00E-17
350.8968227127	58.7927970741	-898	1403	1.03E-15 ± 3.00E-17
350.8869758637	58.7969446412	-741	1246	5.40E-16 ± 2.00E-17
350.8890209363	58.7948138774	-659	1624	1.11E-15 ± 3.00E-17
350.8911321659	58.7926585358	-791	1374	4.80E-16 ± 1.00E-17

Table B.12. The blue shifted component of the [O I] 63 μm emission in the SP4 observations of Cas A measured by PACS-IFU

RA	Dec	Velocity	FWHM	Flux
350.9005438729	58.7950358024	1377	737	5.42E-017 ± 1.11E-018
350.9025932041	58.7931253998	1850	1020	4.52E-017 ± 9.21E-019
350.8968227127	58.7927970741	1296	723	2.67E-017 ± 5.45E-019
350.8986712345	58.7909393377	1756	1234	7.43E-017 ± 1.52E-018
350.8848599927	58.7989658594	1863	777	9.42E-017 ± 1.92E-018
350.8869758637	58.7969446412	2019	873	5.69E-017 ± 1.16E-018
350.8930485793	58.7905712324	1692	1137	6.39E-017 ± 1.30E-018
350.8799881142	58.7980010509	1751	1177	1.01E-016 ± 2.06E-018
350.8860772854	58.7917480454	949	524	3.32E-017 ± 6.77E-019
350.8879740138	58.7896968079	1433	757	3.87E-017 ± 7.90E-019
350.8834478383	58.783275168	1120	766	3.74E-017 ± 7.62E-019

Table B.13. The red shifted component of the [C II] 157 μm emission in the SP4 observations of Cas A measured by PACS-IFU

RA	Dec	Velocity	FWHM	Flux
350.8939201758	58.8013959773	-1078	576	5.52E-017 ± 1.13E-018
350.8911321659	58.7926585358	-940	1368	4.61E-017 ± 9.40E-019
350.8930485793	58.7905712324	-1086	567	2.52E+014 ± 5.14E+012
350.8841057123	58.7938881269	-1123	512	3.72E-018 ± 7.59E-020
350.8860772854	58.7917480454	-849	612	1.61E-017 ± 3.28E-019

Table B.14. The blue shifted component of the [C II] 157 μm emission in the SP4 observations of Cas A measured by PACS-IFU

RA	Dec	Velocity	FWHM	Flux
350.8676247405	58.7923815851	1807	675	3.40E-016 ± 3.00E-017
350.8623101489	58.7919250597	1810	631	1.19E-015 ± 2.00E-017
350.8644343096	58.7899062966	1907	571	2.80E-016 ± 2.00E-017
350.8574434412	58.7909546022	1780	711	3.90E-016 ± 2.00E-017
350.8594759427	58.7890197747	1784	501	2.40E-016 ± 1.00E-017
350.8615779471	58.7868464578	1709	547	1.62E-016 ± 6.00E-018
350.8552672942	58.7877366342	1924	1069	2.90E-016 ± 2.00E-017

Table B.15. The red shifted component of the [O III] 88 μm emission in the SP5 observations of Cas A measured by PACS-IFU

RA	Dec	Velocity	FWHM	Flux
350.8676247405	58.7923815851	-1176	598	3.00E-016 ± 3.00E-017
350.8700523166	58.7900757196	-1059	716	3.10E-016 ± 2.00E-017
350.8623101489	58.7919250597	-1284	768	3.10E-016 ± 2.00E-017
350.8644343096	58.7899062966	-1114	786	4.03E-014 ± 8.00E-018
350.8574434412	58.7909546022	-1096	892	5.00E-016 ± 3.00E-017
350.8594759427	58.7890197747	-894	974	8.70E-016 ± 3.00E-017
350.853353556	58.7898381949	-1231	1110	6.70E-016 ± 3.00E-017
350.8552672942	58.7877366342	-1111	1025	4.50E-016 ± 2.00E-017
350.8571245719	58.7856160718	-1325	748	1.23E-015 ± 4.00E-017

Table B.16. The blue shifted component of the [O III] 88 μm emission in the SP5 observations of Cas A measured by PACS-IFU

RA	Dec	Velocity	FWHM	Flux
350.8644343096	58.7899062966	2243		3.50E-16 ± 2.00E-17
350.8664881628	58.7877779052	838	1870	8.40E-16 ± 2.00E-17

Table B.17. The blue shifted component of the [O I] 63 μm emission in the SP5 observations of Cas A measured by PACS-IFU

B.5 SP7

RA	Dec	Velocity	FWHM	Flux
350.8594759427	58.7890197747	-1281	751	5.90E-16 ± 3.00E-17
350.8615779471	58.7868464578	-1077	511	3.10E-16 ± 2.00E-17
350.8635583589	58.7847086645	-2715	1774	2.80E-16 ± 2.00E-17
350.8571245719	58.7856160718	-716	968	2.50E-16 ± 3.00E-17

Table B.18. The blue shifted component of the [O I] 63 μm emission in the SP5 observations of Cas A measured by PACS-IFU

RA	Dec	Velocity	FWHM	Flux
350.8700523166	58.7900757196	1977	1112	2.10E-016 ± 1.68E-017
350.8721319017	58.7879454493	1880	1156	1.90E-016 ± 1.52E-017
350.8623101489	58.7919250597	1848	973	1.80E-016 ± 1.44E-017
350.8644343096	58.7899062966	1999	1064	3.60E-017 ± 2.88E-018
350.8574434412	58.7909546022	1831	1050	4.69E-016 ± 3.75E-017
350.8594759427	58.7890197747	1872	909	9.10E-017 ± 7.28E-018
350.8635583589	58.7847086645	1888	777	2.10E-016 ± 1.68E-017
350.8654704362	58.7826877874	1157	1103	2.90E-016 ± 2.32E-017

Table B.19. The red shifted component of the [C II] 157 μm emission in the SP5 observations of Cas A measured by PACS-IFU

RA	Dec	Velocity	FWHM	Flux
350.8644343096	58.7899062966	-937	405	9.10E-017 ± 8.03E-018
350.8705401838	58.7835680921	-1559	1221	3.40E-016 ± 3.00E-017
350.8574434412	58.7909546022	-1017	717	9.80E-017 ± 8.65E-018

Table B.20. The blue shifted component of the [C II] 157 μm emission in the SP5 observations of Cas A measured by PACS-IFU

RA	Dec	Velocity	FWHM	Flux
350.8884399872	58.8367109184	4029	838	1.60E-016 ± 1.00E-017
350.890621377	58.83448768	4331	1286	4.30E-016 ± 3.00E-017
350.8926755235	58.8325779855	4559	711	3.00E-016 ± 2.00E-017
350.8826614911	58.8365566596	3380	595	9.00E-017 ± 1.00E-017
350.8847374178	58.8344247047	3938	860	2.30E-016 ± 2.00E-017
350.8700383774	58.8374457693	2029	681	2.50E-016 ± 1.00E-017
350.8659396337	58.8363326806	2282	755	2.30E-016 ± 2.00E-017

Table B.21. The red shifted component of the [O III] 88 μm emission in the SP7 observations of Cas A measured by PACS-IFU

RA	Dec	Velocity	FWHM	Flux
350.8884399872	58.8367109184	-1932	451	2.70E-016 ± 1.00E-017
350.890621377	58.83448768	-1964	653	3.50E-016 ± 2.00E-017
350.8926755235	58.8325779855	-2024	547	3.20E-016 ± 1.00E-017
350.8826614911	58.8365566596	-1552	550	8.00E-017 ± 1.00E-017
350.8847374178	58.8344247047	-1696	714	4.40E-016 ± 3.00E-017
350.8868988897	58.8322476487	-2037	658	4.90E-017 ± 2.00E-017
350.8887519343	58.8303905509	-2167	5113	5.10E-016 ± 3.00E-017
350.8770354436	58.8363917944	-1169	916	3.49E-016 ± 2.00E-017
350.8790856104	58.8342617396	-1620	9332	1.06E-015 ± 5.00E-017
350.8812020454	58.8321071293	-2086	580	4.20E-016 ± 4.00E-017
350.883123358	58.8300204889	-2434	569	2.20E-016 ± 2.00E-017
350.8720677503	58.8355092957	-1546	653	5.70E-016 ± 4.00E-017
350.8761425978	58.8311948793	-2156	575	2.85E-016 ± 7.00E-018
350.8780441564	58.8291442994	-2541	848	7.00E-016 ± 4.00E-017
350.8678495805	58.8342295703	-1350	657	4.00E-016 ± 2.00E-017
350.8697029339	58.8321075041	-1400	504	3.20E-016 ± 1.00E-017
350.8735146164	58.8277734357	-2557	632	1.60E-016 ± 2.00E-017

Table B.22. The blue shifted component of the [O III] 88 μm emission in the SP7 observations of Cas A measured by PACS-IFU

B.6 SP8

RA	Dec	Velocity	FWHM	Flux
350.890621377	58.83448768	4763	919	7.90E-16 ± 7.00E-17
350.8678495805	58.8342295703	3047	1320	2.30E-16 ± 1.00E-17

Table B.23. The red shifted component of the [O I] 63 μm emission in the SP7 observations of Cas A measured by PACS-IFU

RA	Dec	Velocity	FWHM	Flux
350.890621377	58.83448768	-3056	744	1.90E-16 ± 3.00E-17
350.8790856104	58.8342617396	-1755	632	5.20E-16 ± 2.00E-17
350.8812020454	58.8321071293	-2131	1195	6.34E-16 ± 3.00E-17
350.8720677503	58.8355092957	-1422	511	5.29E-17 ± 1.00E-17
350.8761425978	58.8311948793	-2158	918	7.20E-16 ± 4.00E-17
350.8780441564	58.8291442994	-2627	1134	6.00E-16 ± 4.00E-17
350.8678495805	58.8342295703	-1916	1089	3.25E-16 ± 2.00E-17
350.8697029339	58.8321075041	-1697	1220	3.00E-16 ± 2.00E-17
350.8735146164	58.8277734357	-2624	839	5.90E-16 ± 2.00E-17

Table B.24. The blue shifted component of the [O I] 63 μm emission in the SP7 observations of Cas A measured by PACS-IFU

RA	Dec	Velocity	FWHM	Flux
350.8236040659	58.7973977824	2943	797	2.40E-016 ± 2.00E-017
350.8260403057	58.79509426	2444	832	1.82E-016 ± 7.00E-018
350.8281278818	58.7929659927	1763	764	2.20E-016 ± 1.00E-017
350.818290374	58.796936098	3216	831	1.00E-016 ± 2.00E-017
350.820422112	58.7949193869	2680	433	2.30E-016 ± 2.00E-017
350.8224839402	58.7927929771	1986	943	8.20E-016 ± 3.00E-017
350.8246121337	58.7906421276	1657	728	4.90E-016 ± 1.00E-017
350.8134264889	58.795960913	3484	863	1.20E-016 ± 1.00E-017
350.8154662478	58.7940280537	2806	622	1.50E-016 ± 1.00E-017
350.8175763939	58.79185677	2265	763	2.90E-016 ± 2.00E-017
350.8195648182	58.7897208897	1863	940	6.30E-016 ± 3.00E-017

Table B.25. The red shifted component of the [O III] 88 μm emission in the SP8 observations of Cas A measured by PACS-IFU

RA	Dec	Velocity	FWHM	Flux
350.829526158	58.7974672769	-895	391	6.40E-016 ± 5.00E-017
350.8236040659	58.7973977824	-1320	613	2.04E-016 ± 8.00E-018
350.8260403057	58.79509426	-657	1008	5.30E-016 ± 1.00E-017
350.8281278818	58.7929659927	-413	702	3.10E-016 ± 2.00E-017
350.818290374	58.796936098	-1465	602	3.40E-016 ± 2.00E-017
350.820422112	58.7949193869	-878	626	4.60E-016 ± 2.00E-017
350.8134264889	58.795960913	-2013	576	1.20E-016 ± 1.00E-017
350.8154662478	58.7940280537	-1613	660	1.20E-016 ± 1.00E-017

Table B.26. The blue shifted component of the [O III] 88 μm emission in the SP8 observations of Cas A measured by PACS-IFU

B.7 SP9

RA	Dec	Velocity	FWHM	Flux
350.8260403057	58.79509426	2508	1132	3.50E-16 ± 2.00E-17
350.8281278818	58.7929659927	1786	963	3.70E-16 ± 2.00E-17
350.820422112	58.7949193869	2493	944	2.30E-16 ± 1.00E-17
350.8224839402	58.7927929771	2148	807	2.00E-16 ± 2.00E-17

Table B.27. The red shifted component of the [O I] 63 μm emission in the SP8 observations of Cas A measured by PACS-IFU

RA	Dec	Velocity	FWHM	Flux
350.8260403057	58.79509426	-686	1764	3.70E-16 ± 3.00E-17
350.8281278818	58.7929659927	-258	702	4.60E-16 ± 1.00E-17
350.820422112	58.7949193869	-967	1612	6.60E-16 ± 6.00E-17
350.8224839402	58.7927929771	-2464	810	5.00E-16 ± 1.00E-17

Table B.28. The blue shifted component of the [O I] 63 μm emission in the SP8 observations of Cas A measured by PACS-IFU

RA	Dec	Velocity	FWHM	Flux
350.8119013036	58.8023898812	1175	683	4.30E-016 ± 1.00E-017
350.8158887667	58.7982225351	2129	615	1.40E-016 ± 1.00E-017
350.8062201934	58.8023395694	1068	756	9.20E-016 ± 5.00E-017
350.8082356366	58.800207324	1353	1032	8.20E-016 ± 6.00E-017
350.8102679303	58.7980498646	1708	609	7.60E-016 ± 4.00E-017

Table B.29. The red shifted component of the [O III] 88 μm emission in the SP9 observations of Cas A measured by PACS-IFU

RA	Dec	Velocity	FWHM	Flux
350.811210103	58.8088119511	-720	512	4.55E-016 ± 9.00E-018
350.8134594132	58.8066811511	-929	670	3.10E-016 ± 1.00E-017
350.8157584073	58.8045989801	-1150	745	3.30E-016 ± 1.00E-017
350.8076881567	58.8066675773	-386	760	5.60E-016 ± 3.00E-017

Table B.30. The blue shifted component of the [O III] 88 μm emission in the SP9 observations of Cas A measured by PACS-IFU

RA	Dec	Velocity	FWHM	Flux
350.8042411615	58.8044410837	674	1565	3.40E-16 ± 5.00E-17
350.8082356366	58.800207324	1361	890	7.20E-16 ± 8.90E-17
350.8102679303	58.7980498646	1569	990	4.90E-16 ± 2.00E-16
350.7991018882	58.8036397956	897	1120	2.90E-16 ± 3.00E-17

Table B.31. The red shifted component of the [O I] 63 μm emission in the SP9 observations of Cas A measured by PACS-IFU

Appendix C

Appendix C

Table A1 lists the values of n and k measured by Uspenskii et al. (2006) between 2.8 nm and 30 nm for an amorphous carbon sample. It also lists extrapolated n and k values for the Zubko et al. (1996) ACAR and BE amorphous carbon samples, obtained by fitting power-laws to the short wavelength ends of their n and k distributions and then extrapolating these from their shortest wavelength points, at 40 nm and 54 nm, respectively, to shorter wavelengths until they intersected the n and k data of Uspenskii et al. (2006), which were then used from the intersection wavelength down to 2.8 nm. Power-law extrapolations of the Uspenskii et al. (2006) n and k data were then used from 2.8 nm down to 0.35 nm.

Wavelength (nm)	n Uspenskii	k Uspenskii	n Zubko ACAR	k Zubko ACAR	n Zubko BE	k Zubko BE
0.3			9.970E-01	1.72E-06	9.970E-01	1.72E-06
0.4			9.970E-01	3.26E-06	9.970E-01	3.26E-06
0.5			9.970E-01	5.36E-06	9.970E-01	5.36E-06
0.6			9.970E-01	8.04E-06	9.970E-01	8.04E-06
0.7			9.970E-01	1.13E-05	9.970E-01	1.13E-05
0.8			9.970E-01	1.52E-05	9.970E-01	1.52E-05
0.9			9.970E-01	1.98E-05	9.970E-01	1.98E-05
1.5			9.970E-01	6.16E-05	9.970E-01	6.16E-05
3.55	9.970E-01	4.477E-04	9.970E-01	4.477E-04	9.970E-01	4.477E-04
3.76	9.970E-01	5.226E-04	9.970E-01	5.226E-04	9.970E-01	5.226E-04
3.98	9.971E-01	6.004E-04	9.971E-01	6.004E-04	9.971E-01	6.004E-04
4.13	9.980E-01	2.000E-03	9.980E-01	2.000E-03	9.980E-01	2.000E-03
4.21	9.980E-01	1.700E-03	9.971E-01	1.700E-03	9.971E-01	1.700E-03
4.27	9.980E-01	1.000E-03	9.980E+00	1.000E-03	9.980E+00	1.000E-03
4.35	1.000E+00	3.000E-03	1.000E+00	3.000E-03	1.000E+00	3.000E-03
4.42	9.980E-01	1.000E-04	9.980E-01	1.000E-04	9.980E-01	1.000E-04
4.59	9.970E-01	1.000E-04	9.970E-01	1.000E-04	9.970E-01	1.000E-04
4.72	9.971E-01	1.062E-03	9.971E-01	1.062E-03	9.971E-01	1.062E-03
5.00	9.970E-01	1.062E-03	9.970E-01	1.062E-03	9.970E-01	1.062E-03
5.29	9.969E-01	1.062E-03	9.969E-01	1.062E-03	9.969E-01	1.062E-03
5.60	9.967E-01	1.174E-03	9.967E-01	1.174E-03	9.967E-01	1.174E-03
5.93	9.964E-01	1.297E-03	9.964E-01	1.297E-03	9.964E-01	1.297E-03
6.27	9.960E-01	1.433E-03	9.960E-01	1.433E-03	9.960E-01	1.433E-03
6.64	9.956E-01	1.586E-03	9.956E-01	1.586E-03	9.956E-01	1.586E-03
7.03	9.950E-01	1.755E-03	9.950E-01	1.755E-03	9.950E-01	1.755E-03
7.44	9.943E-01	1.949E-03	9.943E-01	1.949E-03	9.943E-01	1.949E-03
7.88	9.935E-01	2.174E-03	9.935E-01	2.174E-03	9.935E-01	2.174E-03
8.34	9.925E-01	2.431E-03	9.925E-01	2.431E-03	9.925E-01	2.431E-03
8.82	9.913E-01	2.731E-03	9.913E-01	2.731E-03	9.913E-01	2.731E-03
9.34	9.899E-01	3.087E-03	9.899E-01	3.087E-03	9.899E-01	3.087E-03
9.89	9.882E-01	3.511E-03	9.882E-01	3.511E-03	9.882E-01	3.511E-03
10.46	9.863E-01	4.009E-03	9.863E-01	4.009E-03	9.863E-01	4.009E-03
11.08	9.841E-01	4.612E-03	9.841E-01	4.612E-03	9.841E-01	4.612E-03
11.73	9.814E-01	5.333E-03	9.814E-01	5.333E-03	9.814E-01	5.333E-03
12.42	9.784E-01	6.209E-03	9.784E-01	6.209E-03	9.784E-01	6.209E-03
13.14	9.749E-01	7.251E-03	9.749E-01	7.251E-03	9.749E-01	7.251E-03
13.91	9.709E-01	8.519E-03	9.709E-01	8.519E-03	9.709E-01	8.519E-03
14.72	9.663E-01	1.005E-02	9.663E-01	1.005E-02	9.663E-01	1.005E-02
15.58	9.610E-01	1.192E-02	9.610E-01	1.192E-02	9.610E-01	1.192E-02
16.50	9.549E-01	1.417E-02	9.549E-01	1.417E-02	9.549E-01	1.417E-02
17.46	9.480E-01	1.691E-02	9.480E-01	1.691E-02	9.480E-01	1.691E-02
18.49	9.400E-01	2.022E-02	9.400E-01	2.022E-02	9.400E-01	2.022E-02
19.56	9.310E-01	2.422E-02	9.310E-01	2.422E-02	9.310E-01	2.422E-02
20.71	9.207E-01	2.909E-02	9.207E-01	2.909E-02	9.207E-01	2.909E-02
21.92	9.091E-01	3.496E-02	9.091E-01	3.496E-02	9.091E-01	3.496E-02
23.21	8.958E-01	4.206E-02	8.958E-01	4.206E-02	8.958E-01	4.206E-02
24.56	8.807E-01	5.064E-02	8.807E-01	5.064E-02	8.807E-01	5.064E-02
26.00	8.637E-01	6.101E-02	8.637E-01	6.101E-02	8.637E-01	6.101E-02
27.52	8.443E-01	7.350E-02	8.443E-01	7.350E-02	8.443E-01	7.350E-02
29.13	8.224E-01	8.860E-02	8.224E-01	8.860E-02	8.224E-01	8.860E-02
40.00			8.63800E-01	1.93800E-01	9.410E-01	9.780E-02
50.00			8.60100E-01	2.35100E-01	9.18300E-01	1.26400E-01

Table C.1. Values of n and k measured by Uspenskii et al. (2006) between 2.8 nm and 30 nm for an amorphous carbon sample and extrapolated n and k for Zubko et al. (1996) ACAR and BE amorphous carbon samples

Bibliography

- Adams, S., Seaton, M. J., Howarth, I. D., Auriere, M., & Walsh, J. R. 1984, MNRAS, 207, 471
- Ade, P. A. R., Aikin, R. W., Barkats, D., et al. 2014, Physical Review Letters, 112, 241101
- Arnett, D. 1996, Supernovae and Nucleosynthesis (Princeton University Press)
- Asplund, M., Grevesse, N., Sauval, A. J., & Scott, P. 2009, Ann. Rev. Astr. Astrophys., 47, 481
- Baade, W., & Minkowski, R. 1954, ApJ, 119, 206
- Baluja, K. L., & Zeippen, C. J. 1988, Journal of Physics B Atomic Molecular Physics, 21, 1455
- Barlow, M. J. 1978, MNRAS, 183, 417
- Barlow, M. J., Krause, O., Swinyard, B. M., et al. 2010, A&A, 518, L138
- Barlow, M. J., Swinyard, B. M., Owen, P. J., et al. 2013, Science, 342, 1343
- Bertoldi, F., Carilli, C. L., Cox, P., et al. 2003, A&A, 406, L55
- Bertoldi, F., & Cox, P. 2002, A&A, 384, L11
- Bianchi, S., & Schneider, R. 2007, MNRAS, 378, 973
- Boehler, Y., Dutrey, A., Guilloteau, S., & Piétu, V. 2013, MNRAS, 431, 1573
- Bohren, C. F., & Huffman, D. R. 1983, Absorption and scattering of light by small particles (Wiley)
- Bouchet, P., & Danziger, I. J. 1993, A&A, 273, 451

- Bouwens, R. J., Illingworth, G. D., Labbe, I., et al. 2011, *Nature*, 469, 504
- Bussoletti, E., Colangeli, L., Borghesi, A., & Orofino, V. 1987, *A&AS*, 70, 257
- Čadež, A., Carramiñana, A., & Vidrih, S. 2004, *ApJ*, 609, 797
- Cami, J., Bernard-Salas, J., Peeters, E., & Malek, S. E. 2010, *Science*, 329, 1180
- Cardelli, J. A., Clayton, G. C., & Mathis, J. S. 1989, *ApJ*, 345, 245
- Carilli, C. L., Bertoldi, F., Rupen, M. P., et al. 2001, *ApJ*, 555, 625
- Cesarsky, C. J., Abergel, A., Agnese, P., et al. 1996, *A&A*, 315, L32
- Cherchneff, I., & Dwek, E. 2009, *ApJ*, 703, 642
- . 2010, *ApJ*, 713, 1
- Chevalier, R. A. 1974, *ApJ*, 188, 501
- Chevalier, R. A., & Kirshner, R. P. 1978, *ApJ*, 219, 931
- Chiar, J. E., & Tielens, A. G. G. M. 2006, *ApJ*, 637, 774
- Chugai, N. N. 1991, *MNRAS*, 250, 513
- Clayton, D. D. 1978, *Moon and Planets*, 19, 109
- Clayton, D. D., Liu, W., & Dalgarno, A. 1999, *Science*, 283, 1290
- Clegg, P. E., Ade, P. A. R., Armand, C., et al. 1996, *A&A*, 315, L38
- Colangeli, L., Mennella, V., Palumbo, P., Rotundi, A., & Bussoletti, E. 1995, *A&AS*, 113, 561
- Cueto, M., Cernicharo, J., Barlow, M. J., et al. 2014, *ApJL*, 783, L5
- da Cunha, E., Charlot, S., & Elbaz, D. 2008, *MNRAS*, 388, 1595
- Davidson, K. 1987, *AJ*, 94, 964
- Davidson, K., & Fesen, R. A. 1985, *Ann. Rev. Astr. Astrophys.*, 23, 119
- de Graauw, T., Haser, L. N., Beintema, D. A., et al. 1996, *A&A*, 315, L49
- Docenko, D., & Sunyaev, R. A. 2010, *A&A*, 509, A59

- Draine, B. T. 2003, *ApJ*, 598, 1026
- . 2011, Physics of the Interstellar and Intergalactic Medium (Princeton University Press)
- Draine, B. T., & Lee, H. M. 1984, *ApJ*, 285, 89
- Dunne, L., Eales, S., Ivison, R., Morgan, H., & Edmunds, M. 2003, *Nature*, 424, 285
- Dwek, E., Galliano, F., & Jones, A. P. 2007, *ApJ*, 662, 927
- Dwek, E., & Scalo, J. M. 1980, *ApJ*, 239, 193
- Ercolano, B., Barlow, M. J., & Storey, P. J. 2005, *MNRAS*, 362, 1038
- Ercolano, B., Barlow, M. J., Storey, P. J., & Liu, X.-W. 2003, *MNRAS*, 340, 1136
- Ercolano, B., Barlow, M. J., & Sugerman, B. E. K. 2007, *MNRAS*, 375, 753
- Ercolano, B., Young, P. R., Drake, J. J., & Raymond, J. C. 2008, *ApJSS*, 175, 534
- Fabbri, J., Otsuka, M., Barlow, M. J., et al. 2011, *MNRAS*, 418, 1285
- Fazio, G. G., Hora, J. L., Allen, L. E., et al. 2004, *ApJSS*, 154, 10
- Fesen, R., & Blair, W. P. 1990, *ApJL*, 351, L45
- Fesen, R. A., & Kirshner, R. P. 1982, *ApJ*, 258, 1
- Fesen, R. A., Shull, J. M., & Hurford, A. P. 1997, *AJ*, 113, 354
- Fesen, R. A., Hammell, M. C., Morse, J., et al. 2006, *ApJ*, 645, 283
- Filippenko, A. V. 1988, *AJ*, 96, 1941
- . 1997, *Ann. Rev. Astr. Astrophys.*, 35, 309
- Filippenko, A. V. 2005, in Astronomical Society of the Pacific Conference Series, Vol. 332, The Fate of the Most Massive Stars, ed. R. Humphreys & K. Stanek, 33
- Finkbeiner, D. P., Langston, G. I., & Minter, A. H. 2004, *ApJ*, 617, 350
- Fitzpatrick, E. L. 1999, *PASP*, 111, 63
- Fritz, J., Gentile, G., Smith, M. W. L., et al. 2012, *A&A*, 546, A34
- Gall, C., Hjorth, J., Watson, D., et al. 2014, *Nature*, 511, 326

- Goldsmith, P. F., & Langer, W. D. 1999, ApJ, 517, 209
- Gomez, H., Krause, O., Barlow, M., et al. 2012, ApJ, 760, 96
- Gomez, H. L., Vlahakis, C., Stretch, C. M., et al. 2010, MNRAS, 401, L48
- Gomez, H. L., Clark, C. J. R., Nozawa, T., et al. 2012, MNRAS, 420, 3557
- Gotthelf, E. V., Koralesky, B., Rudnick, L., et al. 2001, ApJL, 552, L39
- Green, D. A., Tuffs, R. J., & Popescu, C. C. 2004, MNRAS, 355, 1315
- Grefenstette, B. W., Harrison, F. A., Boggs, S. E., et al. 2014, Nature, 506, 339
- Greif, T. H., & Bromm, V. 2006, MNRAS, 373, 128
- Griffin, M. J., Abergel, A., Abreu, A., et al. 2010, A&A, 518, L3
- Groenewegen, M. A. T., Waelkens, C., Barlow, M. J., et al. 2011, A&A, 526, A162
- Habing, H. J. 1996, Astronomy and Astrophysics Reviews, 7, 97
- Hanner, M. 1988, Infrared Observations of Comets Halley and Wilson and Properties of the Grains, 22
- Henry, R. B. C., MacAlpine, G. M., & Kirshner, R. P. 1984, ApJ, 278, 619
- Hester, J. J. 2008, Ann. Rev. Astr. Astrophys., 46, 127
- Hester, J. J., Mori, K., Burrows, D., et al. 2002, ApJL, 577, L49
- Hildebrand, R. H. 1983, QJRAS, 24, 267
- Hirashita, H., & Ferrara, A. 2002, MNRAS, 337, 921
- Houck, J. R., Roellig, T. L., van Cleve, J., et al. 2004, ApJSS, 154, 18
- Howarth, I. D. 1983, MNRAS, 203, 301
- Indebetouw, R., Matsuura, M., Dwek, E., et al. 2014, ApJL, 782, L2
- Jones, A. P., Fanciullo, L., Köhler, M., et al. 2013, A&A, 558, A62
- Kamenetzky, J., McCray, R., Indebetouw, R., & Barlow, M. J. e. a. 2013, ApJL, 773, L34
- Kemper, F., Vriend, W. J., & Tielens, A. G. G. M. 2004, ApJ, 609, 826

- Kessler, M. F., Steinz, J. A., Anderegg, M. E., et al. 1996, *A&A*, 315, L27
- Kirshner, R. P. 1974, *ApJ*, 194, 323
- Koike, C., Hasegawa, H., & Manabe, A. 1980, *Ap&SS*, 67, 495
- Kotak, R., Meikle, W. P. S., Farrah, D., et al. 2009, *ApJ*, 704, 306
- Krause, O., Birkmann, S. M., Rieke, G. H., et al. 2004, *Nature*, 432, 596
- Krause, O., Birkmann, S. M., Usuda, T., et al. 2008, *Science*, 320, 1195
- Launay, J. M., & Roueff, E. 1977, *A&A*, 56, 289
- Lawrence, S. S., MacAlpine, G. M., Uomoto, A., et al. 1995, *AJ*, 109, 2635
- Leger, A., & Puget, J. L. 1984, *A&A*, 137, L5
- Lemke, D., Klaas, U., Abolins, J., et al. 1996, *A&A*, 315, L64
- Lepp, S., Stancil, P. C., & Dalgarno, A. 2002, *Journal of Physics B Atomic Molecular Physics*, 35, 57
- Li, A., & Draine, B. T. 2001, *ApJ*, 554, 778
- . 2002, *ApJ*, 564, 803
- Li, D., Bancroft, G. M., Fleet, M., & Feng, X. H. 1995, *Physics and Chemistry of Minerals*, 22, 115
- Liseau, R., Justtanont, K., & Tielens, A. G. G. M. 2006, *A&A*, 446, 561
- Liu, X.-W., Barlow, M. J., Dalgarno, A., et al. 1997, *MNRAS*, 290, L71
- Loh, E. D., Baldwin, J. A., Curtis, Z. K., et al. 2011, *ApJSS*, 194, 30
- Loh, E. D., Baldwin, J. A., Ferland, G. J., et al. 2012, *MNRAS*, 421, 789
- MacAlpine, G. M., Lawrence, S. S., Sears, R. L., Sosin, M. S., & Henry, R. B. C. 1996, *ApJ*, 463, 650
- MacAlpine, G. M., & Satterfield, T. J. 2008, *AJ*, 136, 2152
- MacAlpine, G. M., & Uomoto, A. 1991, *AJ*, 102, 218

- Marsden, P. L., Gillett, F. C., Jennings, R. E., et al. 1984, ApJL, 278, L29
- Mathis, J. S., Rumpl, W., & Nordsieck, K. H. 1977, ApJ, 217, 425
- Matsuura, M., Woods, P. M., & Owen, P. J. 2013, MNRAS, 429, 2527
- Matsuura, M., Barlow, M. J., Zijlstra, A. A., et al. 2009, MNRAS, 396, 918
- Matsuura, M., Dwek, E., Meixner, M., et al. 2011, Science, 333, 1258
- Meixner, M., Panuzzo, P., Roman-Duval, J., et al. 2013, AJ, 146, 62
- Messenger, S., Keller, L. P., & Lauretta, D. S. 2005, Science, 309, 737
- Messenger, S., Keller, L. P., Stadermann, F. J., Walker, R. M., & Zinner, E. 2003, Science, 300, 105
- Mie, G. 1908, Annalen der Physik, 330, 377
- Miller, J. S. 1973, ApJL, 180, L83
- Min, M., Waters, L. B. F. M., de Koter, A., et al. 2007, A&A, 462, 667
- Moorhead, J. M., Lowe, R. P., Wehlau, W. H., Maillard, J.-P., & Bernath, P. F. 1988, ApJ, 326, 899
- Morgan, H. L., & Edmunds, M. G. 2003, MNRAS, 343, 427
- Muller, H. S., Schlader, F., Stutzki, J., & Winnewisser, G. 2005, Journal of Molecular Structure, 742, 215
- Nomoto, K., Tominaga, N., Umeda, H., Kobayashi, C., & Maeda, K. 2006, Nuclear Physics A, 777, 424
- Nozawa, T., Kozasa, T., Habe, A., et al. 2007, ApJ, 666, 955
- Omont, A., Cox, P., Bertoldi, F., et al. 2001, A&A, 374, 371
- Ott, S. 2010, in Astronomical Society of the Pacific Conference Series, Vol. 434, Astronomical Data Analysis Software and Systems XIX, ed. Y. Mizumoto, K.-I. Morita, & M. Ohishi, 139
- Owen, P. J., & Barlow, M. J. 2015, ApJ, 801, 141

- Persson, C. M., Maoli, R., Encrenaz, P., et al. 2010, A&A, 515, A72
- Pilbratt, G. L., Riedinger, J. R., Passvogel, T., et al. 2010, A&A, 518, L1
- Planck Collaboration. 2011, A&A, 536, A7
- . 2014, ArXiv e-prints, arXiv:1405.0871
- Poglitsch, A., Waelkens, C., Geis, N., et al. 2010, A&A, 518, L2
- Reed, J. E., Hester, J. J., Fabian, A. C., & Winkler, P. F. 1995, ApJ, 440, 706
- Rest, A., Prieto, J. L., Walborn, N. R., et al. 2012, Nature, 482, 375
- Rho, J., Jarrett, T. H., Reach, W. T., Gomez, H., & Andersen, M. 2009, ApJL, 693, L39
- Rho, J., Kozasa, T., Reach, W. T., et al. 2008, ApJ, 673, 271
- Richardson, C. T., Baldwin, J. A., Ferland, G. J., et al. 2013, MNRAS, 430, 1257
- Rieke, G. H., Young, E. T., Engelbracht, C. W., et al. 2004, ApJSS, 154, 25
- Roach, A. C., & Kuntz, P. J. 1970, J. Chem. Soc. D, 1336
- Roberge, W., & Dalgarno, A. 1982, ApJ, 255, 489
- Roueff, E., Alekseyev, A. B., & Le Bourlot, J. 2014, A&A, 566, A30
- Rouleau, F., & Martin, P. G. 1991, ApJ, 377, 526
- Rudy, R. J., Rossano, G. S., & Puetter, R. C. 1994, ApJ, 426, 646
- Sankrit, R., Hester, J. J., Scowen, P. A., et al. 1998, ApJ, 504, 344
- Sarangi, A., & Cherchneff, I. 2013, ApJ, 776, 107
- Savage, B. D., & Mathis, J. S. 1979, Ann. Rev. Astr. Astrophys., 17, 73
- Schilke, P., Neufeld, D. A., Mueller, H. S. P., et al. 2014, ArXiv e-prints, arXiv:1403.7902
- Schlegel, E. M. 1990, MNRAS, 244, 269
- Schneider, R., Ferrara, A., & Salvaterra, R. 2004, MNRAS, 351, 1379
- Seward, F. D., Schmidt, B., & Slane, P. 1995, ApJ, 453, 284

- Smartt, S. J. 2009, *Ann. Rev. Astr. Astrophys.*, 47, 63
- Smith, N. 2003, *MNRAS*, 346, 885
- . 2013, ArXiv e-prints, arXiv:1304.0689
- Smith, N., Chornock, R., Li, W., et al. 2008, *ApJ*, 686, 467
- Smith, N., Li, W., Foley, R. J., et al. 2007, *ApJ*, 666, 1116
- Speck, A. K., Barlow, M. J., & Skinner, C. J. 1997, *MNRAS*, 288, 431
- Sugerman, B. E. K., Croots, A. P. S., Kunkel, W. E., Heathcote, S. R., & Lawrence, S. S. 2005, *ApJ*, 627, 888
- Sugerman, B. E. K., Ercolano, B., Barlow, M. J., et al. 2006, *Science*, 313, 196
- Sutherland, R. S., & Dopita, M. A. 1995, *ApJ*, 439, 381
- Temim, T., & Dwek, E. 2013, ArXiv e-prints, arXiv:1302.5452
- Temim, T., Sonneborn, G., Dwek, E., et al. 2012, *ApJ*, 753, 72
- Temim, T., Gehrz, R. D., Woodward, C. E., et al. 2006, *AJ*, 132, 1610
- The Planck Collaboration. 2006, ArXiv Astrophysics e-prints, astro-ph/0604069
- Thielemann, F.-K., Nomoto, K., & Hashimoto, M.-A. 1996, *ApJ*, 460, 408
- Tielens, A. G. G. M. 2005, *The Physics and Chemistry of the Interstellar Medium* (Cambridge University Press)
- Todini, P., & Ferrara, A. 2001, *MNRAS*, 325, 726
- Trimble, V. 1968, *AJ*, 73, 535
- Trumpler, R. J. 1930, *PASP*, 42, 214
- Uspenskii, Y. A., Seely, J. F., Kjornrattanawanich, B., et al. 2006, in Society of Photo-Optical Instrumentation Engineers (SPIE) Conference Series, Vol. 6317, Society of Photo-Optical Instrumentation Engineers (SPIE) Conference Series
- van der Tak, F. F. S., Black, J. H., Schier, F. L., Jansen, D. J., & van Dishoeck, E. F. 2007, *AA*, 468, 627

- Wallström, S. H. J., Biscaro, C., Salgado, F., et al. 2013, A&A, 558, L2
- Weingartner, J. C., & Draine, B. T. 2001, ApJ, 548, 296
- Werner, M. W., Roellig, T. L., Low, F. J., et al. 2004, ApJSS, 154, 1
- Wesson, R., Barlow, M. J., Matsuura, M., & Ercolano, B. 2015, MNRAS, 446, 2089
- Wheeler, J. C., & Harkness, R. P. 1990, Reports on Progress in Physics, 53, 1467
- White, R. L., & Long, K. S. 1991, ApJ, 373, 543
- Woltjer, L., & Veron-Cetty, M.-P. 1987, A&A, 172, L7
- Wood-Vasey, W. M., Miknaitis, G., Stubbs, C. W., et al. 2007, ApJ, 666, 694
- Wooden, D. H., Rank, D. M., Bregman, J. D., et al. 1993, ApJSS, 88, 477
- Woosley, S. E., & Weaver, T. A. 1995, ApJSS, 101, 181
- Zubko, V., Dwek, E., & Arendt, R. G. 2004, ApJSS, 152, 211
- Zubko, V. G., Mennella, V., Colangeli, L., & Bussoletti, E. 1996, MNRAS, 282, 1321

French 75

30 ml Gin

20 ml Lemon Juice

10 ml Simple Syrup

95 ml Champagne

Shake the gin, lemon juice and simple sugar syrup over ice, double strain in to a champagne flute and then top up with champagne.